Supramolecular and Polymer Systems for Exciton Energy Transport

Dissertation

zur Erlangung des akademischen Grades

eines Doktors der Naturwissenschaften (Dr. rer. nat.)

in der Bayreuther Graduiertenschule für Mathematik und Naturwissenschaften

(BayNAT)

der Universität Bayreuth

vorgelegt von

Felix Alexander Wenzel

aus Magdeburg

Bayreuth, 2024

Der experimentelle Teil der vorliegenden Arbeit wurde in der Zeit von Januar 2019 bis November 2022 in Bayreuth am Lehrstuhl Makromolekulare Chemie I unter Betreuung von Herrn Professor Dr. Hans-Werner Schmidt angefertigt.

Vollständiger Abdruck der von der Bayreuther Graduiertenschule für Mathematik und Naturwissenschaften (BayNAT) der Universität Bayreuth genehmigten Dissertation zur Erlangung des akademischen Grades eines Doktors der Naturwissenschaften (Dr. rer. nat.).

Form der Dissertation: Kumulative Dissertation

Dissertation eingereicht am: 19.02.2024

Zulassung durch das Leitungsgremium: 19.03.2024

Wissenschaftliches Kolloquium: 17.12.2024

Amtierender Direktor: Prof. Dr. Jürgen Köhler

Prüfungsausschuss:

Prof. Dr. Hans-Werner Schmidt	(Gutachter)
Prof. Dr. Andreas Greiner	(Gutachter)
Prof. Dr. Jürgen Senker	(Vorsitz)
Prof. Dr. Anna Köhler	

Weiterer Gutachter: Prof. Dr. Pol Besenius

List of Publications

The most important results of my thesis are summarized and presented in the form of five manuscripts, three of which have been published in peer-reviewed journals. The following papers are the subject of this thesis:

[I] Bernd Wittmann, **Felix A. Wenzel**, Stephan Wiesneth, Andreas T. Haedler, Markus Drechsler, Klaus Kreger, Jürgen Köhler, E. W. Meijer, Hans-Werner Schmidt, and Richard Hildner
Enhancing Long-Range Energy Transport in Supramolecular Architectures by Tailoring Coherence Properties
Journal of the American Chemical Society, **2020**, *142 (18)*, 8323–8330.

[II] Asena Cerhan-Haink*, **Felix A. Wenzel***, Michael Buchhorn, Richard Kellnberger, Eric Schaible, Klaus Kreger, Hans-Werner Schmidt, Richard Hildner, and Eva Herzig
Temperature-induced inversion of circular dichroism in supramolecular polymers revisited: Structural vs. electronic helicity
to be submitted.

**These authors contributed equally to the work.*

[III] **Felix A. Wenzel**, Hannes Welz, Kasper P. van der Zwan, Sebastian Stäter, Klaus Kreger, Richard Hildner, Jürgen Senker, and Hans-Werner Schmidt
Highly Efficient Supramolecular Nucleating Agents for Poly(3-hexylthiophene)
Macromolecules, **2022**, *55(7)*, 2861–2871.

[IV] Sebastian Stäter, **Felix A. Wenzel**, Hannes Welz, Klaus Kreger, Jürgen Köhler, Hans-Werner Schmidt, and Richard Hildner
Directed Gradients in the Excited-State Energy Landscape of Poly(3-hexylthiophene) Nanofibers
Journal of the American Chemical Society, **2023**, *145(25)*, 13780–13787.

[V] **Felix A. Wenzel**, Sebastian Stäter, Padraic O'Reilly, Klaus Kreger, Jürgen Köhler, Richard Hildner, and Hans-Werner Schmidt
Isolated Hierarchical Superstructures with Highly Oriented P3HT Nanofibers
Macromolecules, **2024**, *57(21)*, 10389– 10398.

During my thesis, I was involved in further collaborations and co-authored the following peer-reviewed publications. As these publications are not in the focus of this thesis, they will not be discussed further:

[VI] Martin H. C. van Son, Anton M. Berghuis, Bas F. M. de Waal, **Felix A. Wenzel**, Klaus Kreger, Hans-Werner Schmidt, Jaime Gómez Rivas, Ghislaine Vantomme, and E. W. Meijer
Highly Ordered Supramolecular Materials of Phase-Separated Block Molecules for Long-Range Exciton Transport
Advanced Materials, **2023**, *35(25)*, 2300891.

[VII] Fabian Eller, **Felix A. Wenzel**, Richard Hildner, Remco W. A. Havenith, and Eva M. Herzig
Spark Discharge Doping—Achieving Unprecedented Control over Aggregate Fraction and Backbone Ordering in Poly(3-hexylthiophene) Solutions
Small, **2023***, 19(21)*, 2207537.

[VIII] Meike Kuhn, **Felix A. Wenzel**, Christopher Greve, Klaus Kreger, Matthias Schwartzkopf, Hans-Werner Schmidt, Helen Grüninger, and Eva M. Herzig
Tailored Supramolecular Additives to Control the Crystallization Process and Morphology of MAPbI3
Small, **2025***, 21*, 2410230.

Summary

In nature's light-harvesting units, chromophores and matrix molecules are precisely selected and positioned to efficiently steer exciton energy transport toward reactive centers. Model systems on a supramolecular level are still required to understand and manipulate exciton transport processes. This thesis contributes to this topic by presenting two robust model systems with unique exciton energy transport characteristics. In this context, this thesis focuses on the controlled preparation as well as the morphological, structural, and optical characterization of *supramolecular systems* based on carbonyl-bridged triarylamine trisamides and *polymer systems* consisting of N,N'-1,4-phenylenebis[4-pyridinecarboxamide] and poly (3-hexyl thiophene) (P3HT). For both systems, the delicate interplay between structural and optoelectronic, as well as exciton energy transport properties, will be investigated in close collaboration with the experimental physics group of Prof. Richard Hildner, University of Groningen.

In the *first part*, chromophores based on *carbonyl-bridged triarylamine trisamides* with chiral, bulky peripheral sidegroups are precisely self-assembled into supramolecular architectures. Selective preparation of either single supramolecular nanofibers or bundles of supramolecular nanofibers was achieved by controlling the self-assembly conditions from solution in *n-dodecane* or *anisole*. The structural arrangement in both architectures is comparable; however, significant spectroscopic and optical differences were found. In bundles of nanofibers, the peripheral side groups are closely packed and induce electronic disorder, resulting in localized excitons and trap-dominated exciton transport characteristics. For the single supramolecular nanofibers, the exciton energy landscape is level, and the excitons are more delocalized. These effects accelerate exciton diffusion in single nanofibers by over one order of magnitude, resulting in the highest reported exciton diffusion constant for H-aggregates.

Interestingly, the same building block features a temperature-dependent inversion of the circular dichroism signal for its dispersed supramolecular aggregates assembled from *toluene.* Investigating this effect is the focus of the *second part* of this thesis. The inversion of the circular dichroism signal occurs in conjunction with a decrease in the electronic coupling, as revealed by absorption spectroscopy. Measurements at the Advanced Light Source, Lawrence Berkeley National Laboratory, USA, show no structural changes in the objects except thermal compression. Notably, such building blocks feature an electronic C_4-symmetry but a structural C_3-symmetry. Therefore, a small twist of neighboring molecules in the columns around a critical angle can cause the inversion of the circular dichroism signals without requiring major structural rearrangements. We believe this also occurs for other supramolecular systems where inversion of the circular dichroism signal is reported.

Supramolecular aggregates are known to nucleate semi-crystalline polymers and to alter their physical properties. So far, supramolecular nucleating agents for conjugated semi-crystalline polymers are rarely investigated. Therefore, in the *third part* of this thesis, we explored supramolecular nucleating agents based on *bisamides* with peripheral *pyridine* groups. In particular, *N,N'-1,4-phenylenebis[4-pyridinecarboxamide],* was found to be a highly efficient supramolecular nucleating agent for *P3HT***Fehler! Textmarke nicht definiert.**. The supramolecular architecture provides an epitaxial match in combination with regular attractive donor-acceptor interactions between the surface of the supramolecular nucleating agent and *P3HT*. An outstanding nucleation efficiency of 98 % at a concentration of 0.1 wt % was achieved. In addition, the nucleating agent improves the stability of thin-films of *P3HT* without introducing trap-states. This approach is transferable to other *poly (3-alkyl thiophenes)* and is anticipated to be suitable for other semi-crystalline conjugated polymers.

The above-introduced supramolecular nucleating agent for the *P3HT* crystallization in the polymer melt can also be used in solution processes, which is investigated in the *fourth part* of this thesis. Here, to a dispersion of self-assembled nucleating agent, *P3HT* is added and dissolved. After aging, the dissolved *P3HT* crystallizes onto the surface of the supramolecular nucleating agent, forming hierarchical superstructures. After film casting and drying, such superstructures are embedded in a *P3HT* film. The superstructures consist of a central supramolecular ribbon of the nucleating agent and perpendicularly oriented nanofibers of *P3HT* of about 5 µm in length. This allows for spatially resolved absorption and photoluminescence imaging. It was found that a directed and continuous gradient in the excited-state energy landscape in the range of the thermal energy at room temperature is present. This is attributed to defect fragmentation during crystallization. Intriguingly, this concept could be used to achieve directed exciton energy transport in conjugated polymers.

In the *final part* of this thesis, a controlled two-step assembly, purification, and transfer procedure towards isolated hierarchical superstructures is developed. In a comprehensive manner, the mechanism, and kinetics of the self-assembly of the supramolecular nucleating agent and the polymer crystallization were investigated. After purification and transfer steps, hierarchical superstructures can be obtained with perpendicular-grown and highly oriented *P3HT*-based nanofibers. Such nanofibers feature an exceptional degree of orientation over 0.9 for distances up to 15 µm away from the central supramolecular ribbon. Photoluminescence imaging confirmed a continuous change in the excited-state energy landscape. These achievements may pave the way for artificial light-harvesting antennae or nanophotonic devices.

Zusammenfassung

In der Natur sind Chromophore und Matrixmoleküle genau so ausgewählt und positioniert, dass der Exzitontransport effizient zu den Reaktionszentren geleitet wird. Um diese Exzitontransportprozesse besser zu verstehen und manipulieren zu können, sind Modellsysteme auf supramolekularer Ebene erforderlich. Zu diesem Thema leistet diese Arbeit einen Beitrag, indem sie zwei robuste Modellsysteme mit einzigartigen Exzitonenergietransporteigenschaften behandelt. Dabei fokussiert sich die Arbeit auf die kontrollierte Herstellung sowie die morphologische, strukturelle und optische Charakterisierung von *supramolekularen Systemen* auf der Basis von Carbonyl-verbrückten Triarylamintrisamiden und von *polymeren Systemen*, die aus N,N'-1,4-Phenylenbis[4-pyridincarboxamid] und Poly(3-hexylthiophen) (P3HT) bestehen. Für beide Systeme wird die Beziehung zwischen strukturellen und optoelektronischen sowie Exziton-energietransporteigenschaften in enger Zusammenarbeit mit der Gruppe für Experimentalphysik von Prof. Richard Hildner, Universität Groningen, untersucht.

Der *erste Teil* dieser Arbeit thematisiert Chromophore auf der Basis von *Carbonyl-verbrückten Triarylamintrisamiden* mit chiralen, sterisch anspruchsvollen Seitengruppen, die zu supramolekularen Architekturen assembliert werden. Die selektive Herstellung von entweder einzelnen supramolekularer Nanofasern oder von supramolekularen Nanofaserbündeln wurde durch die Kontrolle der Bedingungen und die Wahl des Lösungsmittels erreicht. Obwohl die strukturelle Anordnung in beiden Architekturen vergleichbar ist, gibt es signifikante spektroskopische und optische Unterschiede. In den Nanofaserbündeln sind die Seitengruppen dicht gepackt und verursachen dadurch elektronische Unordnung, die zu lokalisierten Exzitonen und einem von Fallen dominierten Exzitontransport führen. Bei den einzelnen Nanofasern ist die Energielandschaft der Exzitonen flach und die Exzitonen sind stärker delokalisiert. Diese Effekte erhöhen die Exzitondiffusion in den einzelnen Nanofasern um mehr als eine Größenordnung, was zu der höchsten gemessenen Exzitondiffusionskonstante für H-Aggregate führt.

Interessanterweise zeigt derselbe molekulare Baustein eine temperaturabhängige Umkehrung des Zirkulardichroismus-Signals für in Toluol assemblierte und dispergierte supramolekularen Aggregate auf. Die Untersuchung dieses Effekts ist der Schwerpunkt des *zweiten Teils* dieser Arbeit. Die Umkehrung des Zirkulardichroismus-Signals geht mit einer Abnahme der elektronischen Kopplung einher, wie durch Absorptionsspektroskopie nachgewiesen wurde. Messungen an der Advanced Light Source, Lawrence Berkeley National Laboratory, USA, zeigen jedoch keine strukturellen Veränderungen in den Aggregaten außer die zu erwartende thermische Kompression beim Abkühlen. Wichtig ist, dass solche Bausteine eine elektronische C_4-Symmetrie, aber eine strukturelle C_3-

Symmetrie aufweisen. Daher kann eine kleine Verdrehung zwischen benachbarten Molekülen um einen kritischen Winkel die Umkehrung der Zirkulardichroismus-Signale bewirken, ohne dass größere strukturelle Veränderungen erforderlich sind. Wir gehen daher davon aus, dass dies auch bei ähnlichen supramolekularen Systemen der Fall sein kann, bei denen eine Inversion des Zirkulardichroismus-Signals beobachtet wurde.

Supramolekulare Aggregate können die Keimbildung von teilkristallinen Polymeren initiieren und deren physikalische Eigenschaften verändern. Bislang wurden solche supramolekulare Nukleierungsmittel für konjugierte teilkristalline Polymere kaum untersucht. Daher wurde im *dritten Teil* dieser Arbeit supramolekularen Nukleierungsmitteln auf Basis von *Bisamiden* mit peripheren *Pyridin*-Gruppen untersucht. Insbesondere *N,N'-1,4-Phenylenbis[4-pyridincarboxamid]* erwies sich als hocheffizientes supramolekulares Nukleierungsmittel für *P3HT*. Die supramolekularen Aggregate haben neben einer epitaktischen Übereinstimmung auch regelmäßige attraktive Donor-Akzeptor-Wechselwirkungen zwischen der Oberfläche des supramolekularen Nukleierungsmittels und *P3HT*. Bei einer Konzentration von 0,1 Gew.-% wurde eine hervorragende Nukleierungseffizienz von 98 % erreicht. Darüber hinaus verbessert das Nukleierungsmittel die Stabilität von dünnen *P3HT*-Filmen, ohne dass es zu optischen oder elektronischen Fallenzuständen kommt. Dieser Ansatz kann direkt auf andere *Poly(3-alkylthiophene)* übertragen werden, und es ist zu erwarten, dass er auch auf andere Arten von teilkristallinen konjugierten Polymeren übertragbar ist.

Das eben vorgestellte supramolekulare Nukleierungsmittel für die *P3HT*-Kristallisation in der Polymerschmelze kann auch in lösemittelbasierten Prozessen eingesetzt werden, was im *vierten Teil* dieser Arbeit untersucht wird. Dafür wird einer Dispersion mit Objekten aus supramolekularen Nukleierungsmitteln *P3HT* zugesetzt und dieses aufgelöst. Während der Alterung kristallisiert das gelöste *P3HT* auf der Oberfläche des supramolekularen Nukleierungsmittels, was zur Bildung von hierarchischen Überstrukturen führt. Nach der Filmherstellung und Trocknung sind solche Überstrukturen in einem *P3HT*-Film eingebettet. Die Überstrukturen bestehen aus einer zentralen bänderartigen Struktur des supramolekularen Nukleierungsmittels und senkrecht dazu orientierten Nanofasern von *P3HT*, die eine Länge von etwa 5 µm aufweisen. Dies ermöglicht räumlich-aufgelöste Absorptions- und Photolumineszenz Spektroskopie durchzuführen. Dabei wurde festgestellt, dass die angeregten Zustände einen gerichteten und kontinuierlichen Gradienten in ihrer Energielandschaft haben, der so groß ist wie die thermische Energie bei Raumtemperatur. Dieser Effekt wird auf die Defektfragmentierung während der Kristallisation zurückgeführt. Dieses Konzept birgt daher ein vielversprechendes Potential, um einen gerichteten Exzitonen-Energietransport in konjugierten Polymeren zu realisieren.

Im *letzten Teil* dieser Arbeit wird ein kontrolliertes zweistufiges Verfahren für den Aufbau, die Aufreinigung und den Transfer hinzu isolierten hierarchischen Überstrukturen entwickelt. Der Mechanismus sowie die Kinetik der Selbstorganisation des supramolekularen Nukleierungsmittels und der Polymerkristallisation wurden umfassend untersucht. Nach einem Reinigungs- und einem Transferschritt können hierarchische Überstrukturen mit senkrecht gewachsenen und hoch orientierten *P3HT* Nanofasern erhalten werden. Solche Nanofasern weisen einen außergewöhnlichen Orientierungsgrad von über 0,9 über eine Distanz von bis zu 15 µm weg vom ursprünglichen zentralen supramolekularen Nukleierungsmittel auf. Photolumineszenz Untersuchungen bestätigen eine kontinuierliche Veränderung der Energielandschaft der angeregten Zustände. Diese Befunde könnten zu künstlichen Lichtsammelantennen oder nanophotonischen Bauteilen führen.

Table of Contents

1 Introduction

Photosynthesis is a key process in nature enabling life as we know it. The process of photosynthesis is initiated by the absorption of light by a chromophore resulting in the excitation of the molecule. Subsequently, the excitation energy is transported towards reactive centers, where the energy is converted into chemical energy.[1–3] Importantly, this transport process needs to be fast as the lifetime of the relevant excited states *in vivo* is only around 4 ns.[4] Therefore, nature employs precisely arranged chromophore-protein complexes such as the light-harvesting complex II (see **Figure 1-1**) to enable fast and efficient exciton energy transport.[1–3]

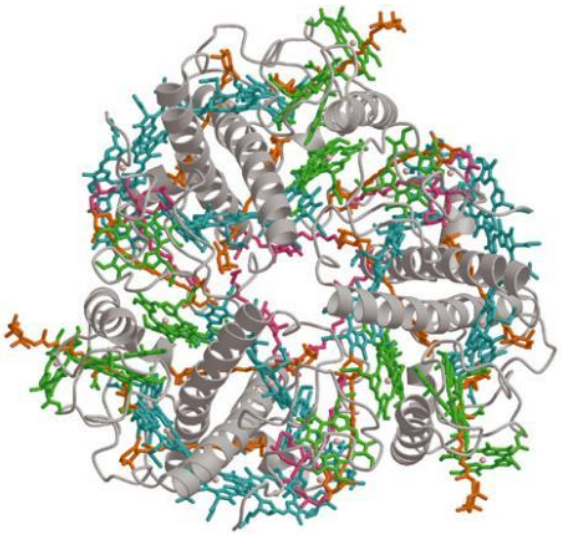

Figure 1-1: Model of light-harvesting complex II consisting of three *polypeptides* (grey), each binding eight *chlorophyll a* (green), six *chlorophyll b* (blue), four *carotenoids* (orange) and two *lipids* (violet). The precise arrangement of all components allows for the formation of delocalized excitons and a gradient in the exciton energy landscape ensuring efficient steering of the excitons towards reactive centers. *Reproduced with permission from Springer Nature.* [5]

The light-harvesting complex II, which is one of the most important arrangements for natural light absorption and exciton transport, consists of multiple precisely positioned components.[5,6] The complex comprises three *polypeptides* where each binds eight *chlorophyll a*, six *chlorophyll b*, four *carotenoids* and two *lipids*.[5] The delicate arrangement allows to maximize the absorption cross section and to tailor the absorption band as well as the excited state energy landscape by a multitude of weak and strong electronic interactions. Excitons in such complexes can be efficiently funneled through the surrounding molecules and then transported to an adjacent light-harvesting complex. For this, different quantum effects, such as coherence, are employed.[2,3,5–7] Importantly, such optimized exciton transfer dynamics are based on the cooperative properties of multiple building blocks mediated by their balanced positioning.[3,7–9] However, our knowledge with respect to the entire process of the exciton dynamics in such complex systems is incomplete as multiple

key factors are not fully understood.[2,3,7,10] Artificial model systems with unique optical properties to tailor and study these effects on the nano- and mesoscale are highly desirable, however, there is a lack of such systems at the current stage.[7,8] Only some approaches are known, which have demonstrated the potential of creating supramolecular systems or polymer systems as model systems to study exciton tranport.[11–16]

In the following, the fundamentals of supramolecular chemistry and polymer crystallization will be presented as these topics represent the basis for the formation of supramolecular and polymer systems for exciton energy transport which are later explored.

1.1 Supramolecular Systems

Supramolecular Interactions and Self-Assembly

Molecular self-assembly is the autonomous, spontaneous formation of molecules into stable and structurally well-defined aggregates by directed non-covalent secondary interactions.[17] This bottom-up approach towards supramolecular structures, i.e., structures beyond a single molecule, is based on a multitude of secondary interactions or a combination of these.[18] Common non-covalent interactions of non-charged structures include van-der-Waals forces, π- π interactions, dipole-dipole interactions, and hydrogen bonds.[19] Importantly, all the above are weaker compared to the covalent carbon-carbon bond.[20] As a result, this leads to the reversible and dynamic nature of such supramolecular structures under specific conditions, i.e., a constant exchange between aggregation and disaggregation.[21]

Each self-assembly process is governed by the delicate interplay of interactions as each supramolecular building block can interact with other building blocks and the medium.[22] Based on this competition, the system consists of single building blocks or supramolecular aggregates. Due to the relative weakness of the non-covalent interactions, activation barriers are usually low, and many supramolecular systems are in their thermodynamic equilibrium.[21]

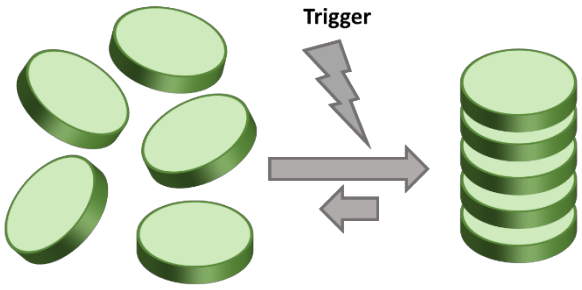

Figure 1-2: Schematic representation of a self-assembly process. Single discotic molecules in a disordered state (left) can self-assemble into an ordered columnar structure (right) promoted by a trigger, e.g., a temperature change. Any self-assembly process is dynamic in nature and the position of the equilibrium depends on the given conditions.

The self-assembly into supramolecular structures needs a driving force caused by the change of at least one parameter in the form of a trigger. Common triggers include changes in temperature, concentration, molecular conformation, or changes in the environment such as pH variations or adjustments to the solvent polarity or a combination of those.[21,23,24] Any such parameter change impacts the relative strength of the present interactions which can drive the system towards aggregation into a supramolecular structure or disaggregation(see **Figure 1-2**).

Even small variations in the set of conditions like the molecular design, the medium, temperature, or concentration determine the process and outcome of the self-assembly (see **Figure 1-3**). For example, Molla *et al.* showed that even slight variations in the molecular design impact the aggregation and, hence, macroscopic properties: They connected *naphthalene diimides* with an acid moiety over different long *alkyl* spacers. The length of this spacer impacts the supramolecular interactions and the stacking of the molecules resulting in different photoluminescence signals.[25] Blomenhofer *et al.* showed that slight variations in the molecular structure of substituted *1,3,5-benzene trisamides* result in different supramolecular structures capable of promoting the growth of different modifications of isotactic *poly(propylene)*.[26] Even traces of co-solvents such as water can significantly alter the aggregation process resulting in different nano and mesoscopic structures.[27] Some systems can show the formation of very different polymorphic nanostructures depending on the temperature or concentration. [28–30] This polymorphism is caused by the interplay of different interactions that allow, in general, a multitude of different structures to be formed.

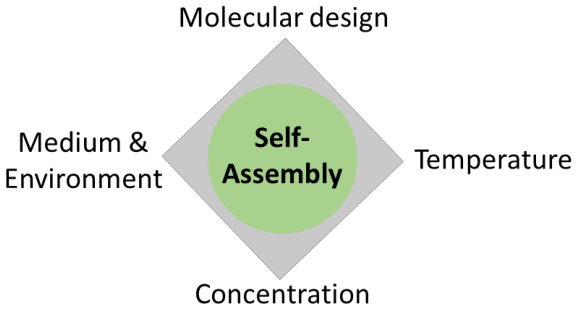

Figure 1-3: Overview of four key parameters controlling the self-assembly process. The combination of the molecular design at a specific concentration and temperature with the medium and environment determines the process and outcome of any self-assembly.

The realized supramolecular structure is determined by the specific set of conditions. A schematic but more detailed picture is given in **Figure 1-4** showing potential paths for aggregates of a supramolecular system within the free energy landscape. In the given example, a clear, thermodynamically stable structure of helical stacked molecules is shown at the bottom of the figure. However, the state of the monomer in the free energy landscape (shown at the top) cannot directly aggregate into these structures as the energy barrier is too large. Alternatively, it can first aggregate into stacks with a small offset (blue path). As this assembly process has a low energetic barrier, disassembly can also occur. Going from this state toward the thermodynamically stable structure also requires overcoming a significant energy barrier (red lines). Here, different external stimuli can be used to overcome this barrier or to reduce it enabling the formation of the thermodynamically stable structure. The monomer can also assemble using small additives to form cofacial stacked structures stabilized by the additives (solid green line). These structures are in a

deep trap state, i.e., the disassembly is hindered by a large energetic barrier.[31] Depending on the set of conditions, different kinetically or thermodynamically stable structures can, hence, be obtained from the same supramolecular building block underlining the importance of the control over the conditions to form the desired supramolecular aggregates.

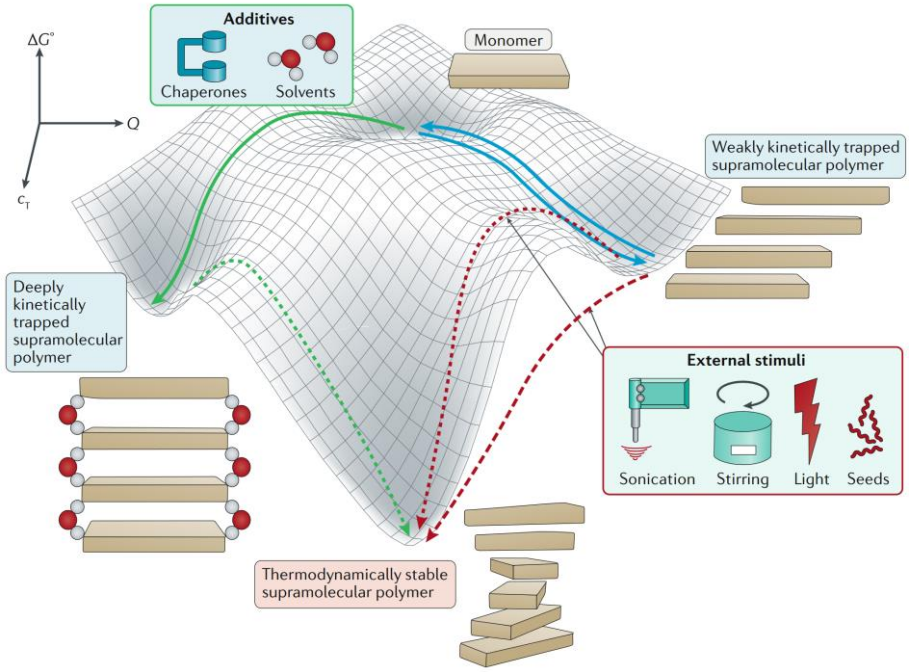

Figure 1-4: Schematic representation of a free energy landscape for the self-assembly of a supramolecular building block from solution (top). The molecule can follow different pathways along the energy landscape leading to different local or global minima. The global minimum represents the thermodynamic stable aggregate (bottom). However, during self-assembly, the pathway might lead towards a local minimum (left and right). Depending on the depth of each minimum relative to its surroundings, the aggregate might be trapped in the state (left) or can easily leave it towards a different state (right). *Reproduced with permission from Springer Nature* [31]

Molecular Design of Supramolecular Building Blocks

The molecular design of the supramolecular building block is crucial for the self-assembly process as the strength and directionality of the non-covalent interactions inside a supramolecular structure are based on the design. One common design principle consists of three parts and focuses around directed hydrogen bonds as the main driving force for self-assembly. The central core is the framework of the molecule and determines the symmetry - One of the most commonly used motifs is *benzene*, which can be either modified at the 1, 3, and 5 positions for a potentially C_3-symmetric molecule or on the 1 and 4 positions for a potentially C_2-symmetric building block (see **Figure 1-5**).[32–35]

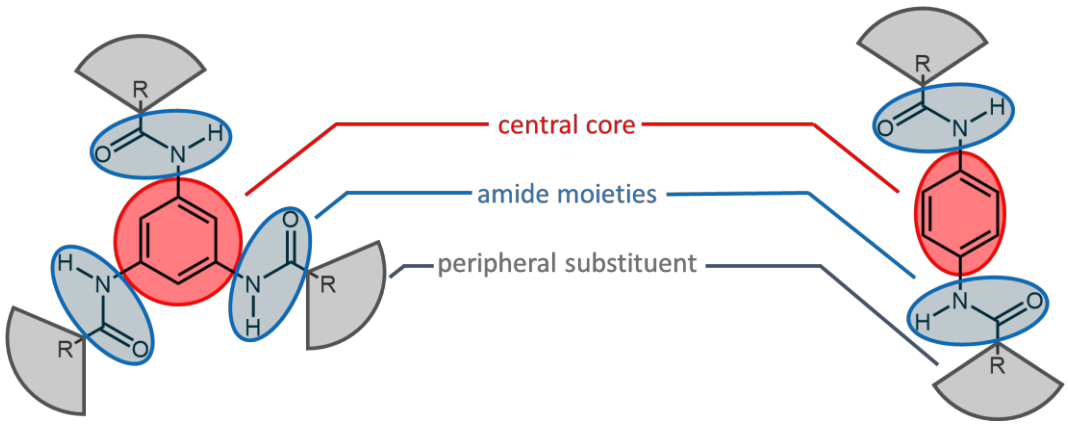

Figure 1-5: Chemical structure of two typical supramolecular building blocks based on directional hydrogen bonds with a C_3 symmetry (left) or a C_2 symmetry (right). The supramolecular building blocks consist of three parts. The usual planar core moieties determine the symmetry of the molecule. The amide moieties enable directional hydrogen bonds resulting in the formation of supramolecular aggregates. The peripheral substituents tailor the solubility and functionality of the molecule.

Amide moieties are attached to the core (see **Figure 1-5**) enabling the formation of directed hydrogen bonds. For the *benzene trisamide*, the three amide moieties switch out of the plane of the core to enable the formation of three hydrogen bonds to the next molecule. Therefore, the next molecule is typically cofacial stacked and rotated by 60° giving rise to three strands of helical hydrogen bonds resulting in the formation of supramolecular columns.[34,36,37] These dipole moments of the directed hydrogen bonds add up over the length of a column resulting in the formation of a macrodipole moment. This can be compensated by the anti-parallel alignment of additional columns leading to the formation of bundles.[38–40] The *benzene bisamide* usually forms two one-dimensional linear strands of hydrogen bonds. Typically, the aggregation inside a plane is preferred resulting in mesoscale morphologies of resembling platelets or ribbon-like structures.[32,41]

The third part of the molecular design encompasses the peripheral substituent. Here, a wide variety of moieties have been used including *alkyl* chains, chiral substituents, or chromophores.[26,33,35,36,42,43] The peripheries determine the solubility of the molecules as well as the interaction with neighboring building blocks in aggregates. Further, in columnar aggregates, which typically formed by *benzene trisamides*, the peripheries mostly make up the surface of the supramolecular structures. Therefore, the choice of the peripheries can also tailor the functionality of the formed structures. For example, certain *alkyl* sidechains enable the formation of nucleating agents for *poly(propylene)*[26] or can be used as air filter material[44]. *Terpyridine*-based peripheries allow for the binding of metal nanoparticles and hence catalysis.[45] *Benzoic acids* as peripheries allow the formation of pH-responsive hydrogelators[46] to name just a few examples.

A common pathway towards self-assembled structures of *benzene trisamides* and *benzene bisamides* is by a controlled heating and cooling approach. The supramolecular building block is molecular dissolved in a suitable solvent at elevated temperatures. Upon cooling, the solubility of the building blocks decreases, and self-assembly occurs. The structure and morphology of the supramolecular aggregates are directly linked to the applied process conditions. For example, *benzene trisamide*-based nanofibers showed different diameters depending on the stirring rate upon cooling. The stirring allows to control and establish a defined cooling rate over the entire system and thus influences the final morphology.[47]

Thermodynamic and Kinetic Aspects of Molecular Self-Assembly

The formation of supramolecular aggregates is strongly dependent on conditions such as the molecular design, the environment, the temperature, and the concentration. Depending on these conditions, different states such as molecular dissolved building blocks or aggregates of varying structures will be thermodynamically favored. Due to the dynamic nature of the self-assembly process, the system drives toward the energetically favored state adopting changes in the conditions. To describe the process of aggregation, the consecutive attachment of a single building block onto another single building block or onto an aggregate consisting of multiple building blocks can be considered. Every such aggregation step has an equilibrium constant *K* depending on the quotient of the product and educt concentrations for each step.[48] Such interaction between consecutive building blocks in supramolecular aggregates mainly follows one of two mechanisms:

If all aggregation steps are identical and, hence, independent of the size of the aggregate, the process is called isodesmic (see **Figure 1-6 A**). Here, all reactivities are the same, and the addition of each monomeric species onto another monomeric species or an aggregate yield the same energy. Modeling such a mechanism shows that the monomer is number-wise always the most common species in the solution. The dispersity of the aggregated species increases up to a value of two. Examples of this mechanism are aggregation processes that are only dependent on π-π interactions like in meta-linked *phenylacetylene macrocycles* or *hexa-perihexabenzocoronenes*.[49,50] However, examples for the isodesmic assembly of *benzene trisamides and perylene bisamides*-based building blocks as well as other systems have been reported.[48,51,52]

Alternatively, the associations of the monomeric species to small aggregates can differ from the association of single molecules to large aggregates. During nucleation, monomeric species follow an isodesmic mechanism until the aggregates reach a critical size. Then, the addition of each new molecule proceeds with a different association constant. (see **Figure 1-6 B**) If the second constant is larger, the process is referred to as a cooperative mechanism. If the second constant is smaller, the process is described as anti-cooperative. The cooperative mechanism can be further divided into a downhill and a nucleated process. If the aggregation of the seed is already energetically favorable, the mechanism is called downhill process. If the formation of the nucleus is energetically unfavored, this formation will be the bottleneck, and the process is referred to as nucleated process.[48] Most supramolecular building blocks based on *benzene trisamides* and multiple building blocks based on *perylene bisimides* aggregate in a cooperative way.[33,53–56] In *benzene trisamide*-based building blocks the cooperative nature was related to the helical three-fold hydrogen bonds. The interaction between two monomeric units is less than half as strong as the interaction of a unit

inside supramolecular columns with its neighbors. This is due to a combination of long-range dipole−dipole interactions, mutual polarizations, and resonance-assisted hydrogen bonding. [57]

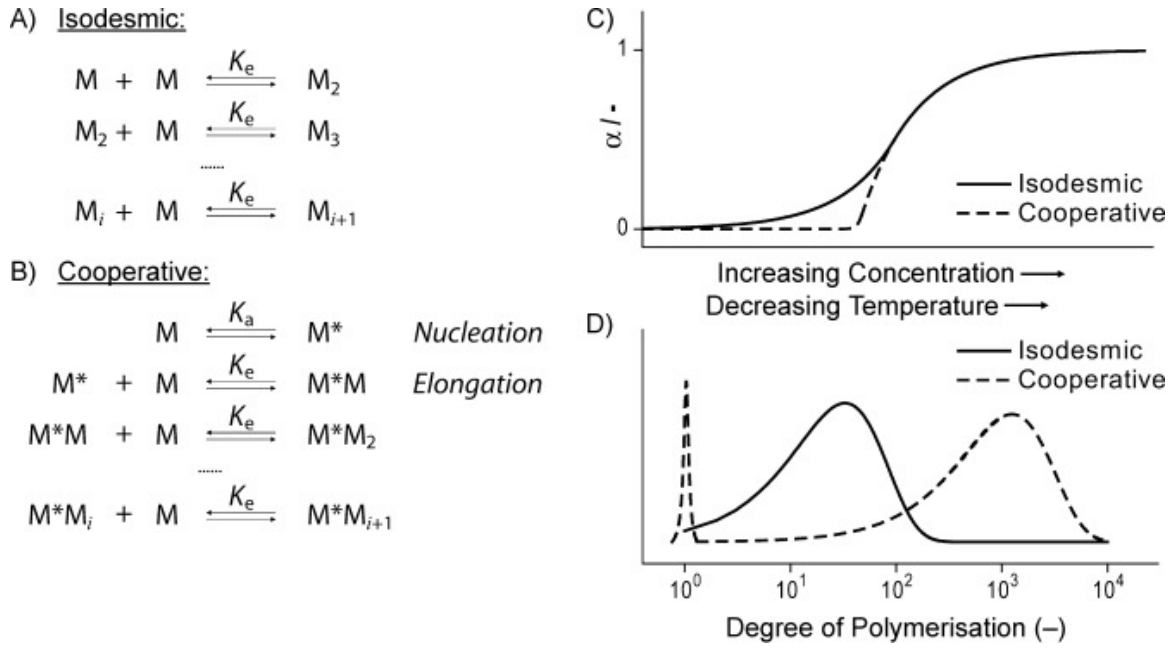

Figure 1-6: Overview of the two main mechanisms of self-assembly. A) In the isodesmic mechanism the addition of each monomeric species is identical and hence, only a single equilibrium constant K is sufficient to describe the system. B) In a cooperative system, the different equilibrium constants are necessary to describe the system depending on the size of the aggregate. C) Schematic progression of the degree of conversion for the isodesmic and cooperative mechanism. D) Schematic representation of the degree of aggregation for both mechanisms. Copyright 2009 Wiley. Used with permission from [58].

The mechanism of the self-assembly impacts the process as well as the final supramolecular structure. Upon aggregation, an isodesmic mechanism follows a sigmoidal shape for the degree of conversion α, i.e., a measure for the part of the building blocks in the system that are aggregated (see **Figure 1-6 C**). Here, 0 refers to a completely molecular dissolved state and 1 to a completely aggregated state. For most of the self-assembly process, only oligomers and monomers are present in such systems. Even at the end of the aggregation, mostly small aggregates are present as shown by the degree of aggregation, i.e., the average number of building blocks inside a supramolecular aggregate, in **Figure 1-6 D**. In contrast, a supramolecular system following a nucleated, cooperative mechanism stays almost exclusively in monomeric units until a critical parameter, such as the concentration or temperature, is reached (see **Figure 1-6 C**). This enables the formation of nuclei which can rapidly grow into large supramolecular structures due to the cooperativity-enhanced elongation process. Such a system features mostly large supramolecular aggregates as well as residual monomers.[48,58,59]

As the cooperative growth is limited by the nucleation process, it can be utilized to control the self-assembly process and the length of the aggregates using seeds. For example, Zhang *et al.* were able to achieve a seeded polymerization of π-conjugated small molecules, resulting in two different connected supramolecular semiconducting nanotubes. In this way, they produced a linear heterojunction. For this, they prepared in a first step a metastable monomer solution which is not capable of a spontaneous self-assembly. In the seconds step they added seeds to induce the elongation process by consuming the monomer, which ultimately end up in a heterojunction.[60]

In this context, the crystallization-driven self-assembly approach commonly applied using block-co-polymers is mentioned. In a first step, aggregates with high dispersity are assembled. These aggregates are then cut through ultrasonication to small seeds. These seeds can then be added to a metastable solution of supramolecular building blocks, initiating self-assembly in a controlled and similar manner as described above (see **Figure 1-7**). In the context of this thesis, an important feature of this approach is that these seeds can be heated and partly dissolved resulting in a self-seeding effect upon cooling.[15,61–63]

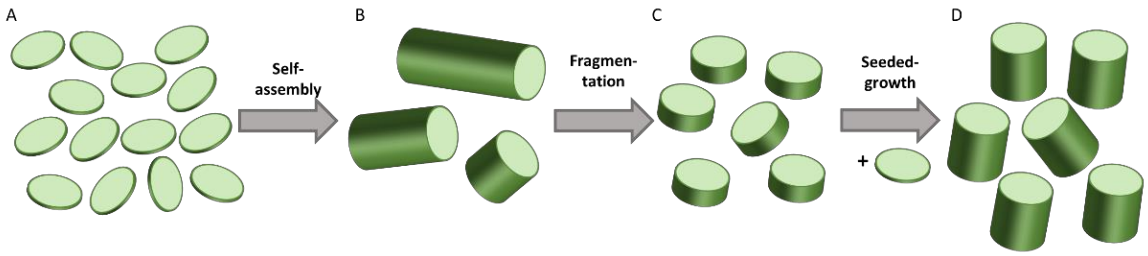

Figure 1-7: Schematic representation of an exemplary seeded-growth approach towards well-defined supramolecular aggregates. Molecular dissolved supramolecular building blocks (A) are self-assembled resulting in supramolecular structures of different lengths (B). These structures are fragmented into small aggregates (C). Upon addition of molecularly dissolved building blocks, the small aggregates act as seeds to initiate the formation of supramolecular structures of similar lengths (D).

A quite different, but equally important approach uses solutions of kinetically trapped monomers. In this context, Takeuchi *et al.* demonstrated for the first time by using *porphyrin*-based supramolecular building blocks that solutions of such kinetically trapped monomers features a long lag time. As a result, the *porphyrin* building blocks form different aggregates, depending on the set of conditions, which is referred to as pathway complexity. Takeuchi *et al.* described two types of aggregates. Initially, the molecules were assembled into the first form following an isodesmic mechanism. The subsequent transformation into a second form occurs over a couple of days by a cooperative mechanism. In another approach, they used sonication to overcome the energy barrier

to form seeds of the second form. These seeds were then added to a solution of the first form, initiating the growth of the second form immediately. They were also able to adjust the aggregate length by the ratio of seeds and monomers.[64]

In a similar approach, Würthner and coworkers assembled *perylene bisimide*-based building blocks but first in a less defined structure. Then they applied sonication to cut the fibers into short parts and added those seeds into a kinetically trapped monomer solution, immediately initiating the aggregation.[65]

Photophysics of π-conjugated Supramolecular Systems

The interaction of light with matter is a fundamental process and crucial for our life on Earth as it represents the basis for photosynthesis. The interaction of an electromagnetic wave with a molecule can be well described by a quantum mechanical approach using a perturbation.[66,67] In a simplified picture, a photon may be absorbed or emitted resulting in a transition between two states with the energy difference being equal to the energy of the photon. The transition dipole moment describes the interaction between the electromagnetic field and the electrons as well as the nuclei of the molecules. If it is non-zero a transition may occur, and the squared transition dipole moment is a measure of the intensity of the transition.[66,67]

If multiple molecules are in proximity as is the case for supramolecular aggregates, their excited states and transition dipole moments will interact resulting in changed photophysical properties. Scheibe[68] and Jelly[69] were the first to attribute such changes to the aggregation of molecules. Both analyzed the concentration-dependent absorption spectra of *pseudo isocyanine chloride* in water. For increasing concentrations, the spectrum of the molecule changes into a sharper, red-shifted absorption band attributed to the aggregation of molecules. However, other molecules showed the opposite effect, a hypsochromic shift (blue shift) of the absorption spectrum with an increasing concentration.

These differences were explained by Kasha who developed the basic concept for the relationship between photophysical properties and the structure of aggregates. He showed that the arrangement of the transition dipole moments determines the change in the photophysical properties.[70–73] In general, the interaction energies, i.e., the coupling J_{ij} between two closely arranged molecules i and j with their transition dipole moments μ can be described as:[66,70,74]

$$J_{ij} = \frac{\kappa_{ij}}{4\pi\varepsilon\varepsilon_0}\frac{|\mu_i||\mu_j|}{|R_{ij}|^3} \qquad (\mathbf{1})$$

with $\varepsilon\varepsilon_0$ being the permittivity of the medium, $|R_{ij}|$ the distance between the two molecules, μ_i and μ_j the transition dipole moments of the two molecules and κ the orientation factor defined by the unit vectors of the transition dipole moments as well as the unit vector along the intermolecular distance. κ_{ij} can range from -2 to 1 depending on the mutual arrangement of the molecules. The minimum of -2 is reached for a colinear head-tail arrangement defining a perfect J-aggregated, named after Jelly. Accordingly, the coupling is negative. If two molecules are stacked on top of each other, i.e., cofacial arranged, the orientation factor is 1 and the arrangement represents a perfect H-aggregate, where H refers to the commonly observed hypsochromic shift in such aggregates.[70,71]

The coupling results in the delocalization of the excited state over the molecular arrangement and the previously degenerated excited states of the individual molecules split up.[1,74] The energetic difference between the highest and lowest state is called the exciton bandwidth and is four times the coupling. The delocalization also impacts the transition dipole moments and multiple cases can be distinguished based on the phase of the transition dipole moments. If all molecular transition dipole moments oscillate in-phase, i.e., the wavevector k is zero, the total dipole moment will reach its maximum at $\sqrt{N}$ μ, where N is the number of individual molecules in the arrangement. If each transition dipole moment oscillates out of phase with its nearest neighbours, i.e., $k = \pi$ they cancel each other out and the total dipole moment is zero. For a positive coupling, i.e., an H-aggregate, the $k = 0$ state is at the top of the exciton band, and the $k = \pi$ state is at the bottom. Due to the opposite sign of the coupling for J-aggregates, the opposite is true.[71]

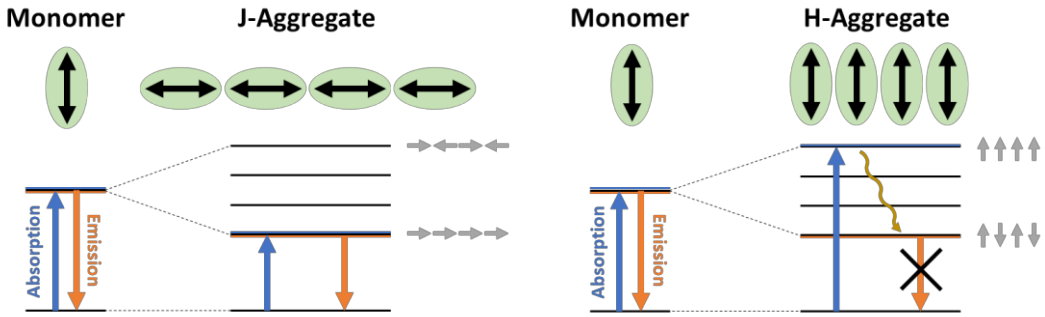

Figure 1-8: Schematic representation of energy levels in J-aggregates (left) and H-aggregates (right) based on the energy levels of a single molecule. In J-aggregates the transition dipole moments are aligned colinear. Therefore, the bottom of the exciton band has the highest total dipole moment and absorption and photoluminescence happen from this state. In contrast, the cofacial alignment of the transition dipole moment result in an accumulation of the total dipole moment at the top of the exciton band in which absorption happens. This is followed by quick non-radiative relaxations into the bottom of the exciton band. Here, the transition dipole moments of the molecules compensate each other prohibiting photoluminescence from this state.

As mentioned, the intensity of a transition is dependent on the transition dipole moment, and hence transitions to the state with $k = 0$ should feature the highest intensity, and transitions for $k = \pi$ will not occur.[70,71,73] This can be used to describe the original observations of the hypsochromic and bathochromic shift of the absorption due to aggregation. For H aggregates, the absorption will preferentially occur at the top of the exciton band as the dipole moment of this state is maximized. Compared to a single molecule, this state is located $2|J_0|$ above the excited state of an individual molecule. Therefore, the absorption is shifted to higher energies, resulting in a hypsochromic shift. In contrast, a J-aggregate is preferentially excited into the bottom of the exciton band as the dipole moment is maximized here. This state is located $2|J_0|$ below the excited state of an individual molecule and hence an absorption shift to lower energies, i.e., a bathochromic

shift, occurs.[70,71] It should be noted, that in addition an energy shift of the exciton band width compared to the excited state of an individual molecule occurs due to the changed polarizability of the environment in the aggregated state. This energy shift can be larger than $2|J_0|$ and hence overcompensate the effect of the exciton bandwidth.[75]

Equally important, the aggregates also significantly differ in their fluorescence. For J-aggregates, the absorption occurs into the bottom of the exciton bandwidth. Emission occurs from the same state, therefore, ideally no shift between absorption and emission, i.e., Stoke shift, occurs. In addition, the increased dipole moment of the aggregate compared to the individual monomer results in an N-fold increase of the likeliness for emission observed by an according increase in the radiative rate. Hence, J-aggregates feature super radiative states with very low lifetimes.[70,71]

In contrast, the absorption for H-aggregates occurs into the top of the exciton band and is followed by rapid non-radiative decays into the bottom of the exciton band. As this state has a total dipole moment of zero, emission from it is forbidden and no emission occurs, significantly increasing the lifetime of excited states. However, disorder and vibronic coupling result in an allowed emission.[70,71] It should be noted that this description is a simplification and more dedicated descriptions including vibronic progressions and disorder exist.

During the lifetime of an excited state, the excitation energy can be transferred between chromophores. The nature of this energy transport is directly linked to the excited-state energy landscape. In an ideal case, all excited-state energy levels of the chromophores are identical and in close proximity to each other. Here, the excited state can be delocalized over all chromophores, the coherent state (see **Figure 1-9 A**).[71,74]

However, interactions of the chromophores with the environment can induce disorder into the system resulting in perturbations in the excited energy landscape.[1,74,76] Such heterogeneities localize the excitation onto a single chromophore if the disorder is significantly larger than the electronic coupling.[1,76] However, the excited state can be transferred from one chromophore to the next via a Förster-type hopping mechanism, i.e., via Coulomb interactions between the chromophores (see **Figure 1-9 B**).[1,77] A simple description of this incoherent transport is in a random-walk type manner where the excited state hops without directionality.[8]

For an inhomogeneous excited energy landscape, i.e., a system with comparably large and local disorder, the excitation might be trapped by an energetic deep state. The large energy barrier to leave such a state can limit the transport of the excitation energy in the system (see **Figure 1-9 C**).[78]

If the excited energy landscape features a continuous gradient, the transport of the excitation energy along this gradient is preferred as hops opposing the direction of the gradients would be "uphill" energetically making such hops less probable. Such an energy gradient can, therefore, steer the excitation energy in a defined manner towards the lower lying energy states (see **Figure 1-9 D**).[79,80]

The final mechanism discussed here is present in the intermediate regime between coupling and disorder. Here, the exciton is delocalized over multiple chromophores.[1] Each hopping event between sets of chromophores results, therefore, in the advancement over multiple chromophores along an array. In other words, the exciton can be transferred further per consecutive hop which can significantly accelerate the exciton transport if all other parameters stay unchanged (see **Figure 1-9 E**).[8]

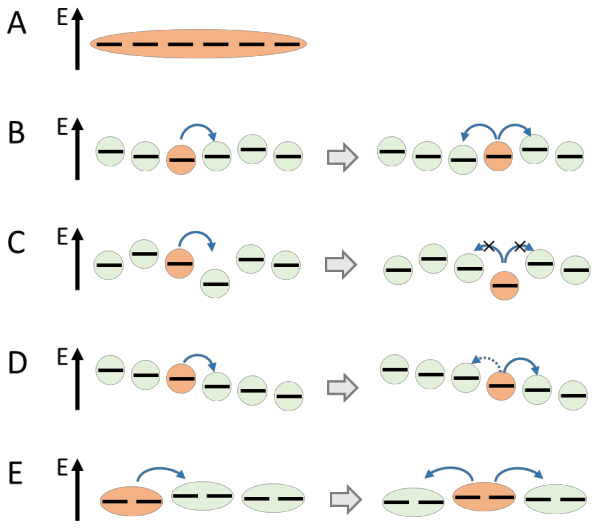

Figure 1-9: Schematic representation of five characteristic excited-state transport mechanisms. A) The exciton (orange) is delocalized over all chromophores – the coherent state. B) The excitation is localized onto a single chromophore (orange) in an arrangement of chromophores (green). The excitation can hop from chromophore to chromophore via Förster-type hopping. C) Similar to the previous state, the excited state is localized onto a single chromophore. However, the energy landscape is rough resulting in the presence of deep trap states limiting the transport. D) If the excited-state energy landscape features a continuous energy gradient, the transport of the excited state along the gradient is preferred. E) Here, the exciton is delocalized onto two chromophores. Each consecutive hop can therefore move the exciton by two chromophores.

Supramolecular Systems for Long-Range Exciton Energy Transport

Supramolecular aggregation represents an attractive way to precisely arrange chromophores enabling long-range exciton transport. For example, supramolecular building blocks based on *perylene bisimides* can be self-assembled into one-dimensional assemblies featuring exciton diffusion over one hundred molecules - corresponding to exciton transport distances up to 100 nm.[81,82] Different *perylene bisamides*-based building blocks can be assembled into two-strand or four-strand helices featuring exciton diffusion lengths of 188 nm and 77 nm, respectively.[83] Single nanotubes as well as bundles of nanotubes based on *meso-tetra(4-sulfonatophenyl) porphyrin* can be formed and have exciton diffusion lengths of 370 nm for the bundles and 160 nm in the nanotubes.[84,85] A third well-investigated system is based on double-walled nanotubes of amphiphilic *carbocyanine* dyes with exciton diffusion lengths of 140 nm and 790 nm, respectively.[12] Optimizations allowed the preparation of double-walled aggregates with further exciton transport distances in the range of 1.6 µm.[86] In addition, an emerging model system based on *carbonyl-bridged triarylamine trisamides* has enabled the formation of nanofibers with exciton transport over up to 4 µm.[11]

The supramolecular design of these building blocks is inspired by the previously mentioned *benzene trisamide*. However, instead of a *benzene* ring, a *carbonyl bridged triarylamine* (*CBT*) is used as core (see **Figure 1-10 A**). This aromatic π-system is a planar and discotic chromophore enabling a C_3-symmetric modification at the 2, 6 and 10 position with three amide moieties enabling the supramolecular aggregation. Under appropriate conditions the supramolecular nanofibers are capable of forming a gel at very low concentrations.[87]

Different molecules were designed with peripheries based on *naphthalimides* (*NI*) or *4-(5-hexyl-2,2'-bithiophene)naphthalimide* (*NIBT*). Importantly, these peripheries differ in their relative energy level compared to the central unit enabling exciton energy transport phenomena inside a single molecule. Excitation of the *naphthalimides* using light of 340 nm results in photoluminescence stemming from the *CBT* core, although the core does not absorb at this wavelength. Therefore, the *NI* absorbs the light, and the excitation is transferred to the central *CBT* unit where fluorescence occurs. The opposite is true for the *NIBT*-based building block. Here, the *CBT* core is excited using light with a wavelength of 440 nm and the fluorescence characteristics of the *NIBT* peripheries can be observed.[87]

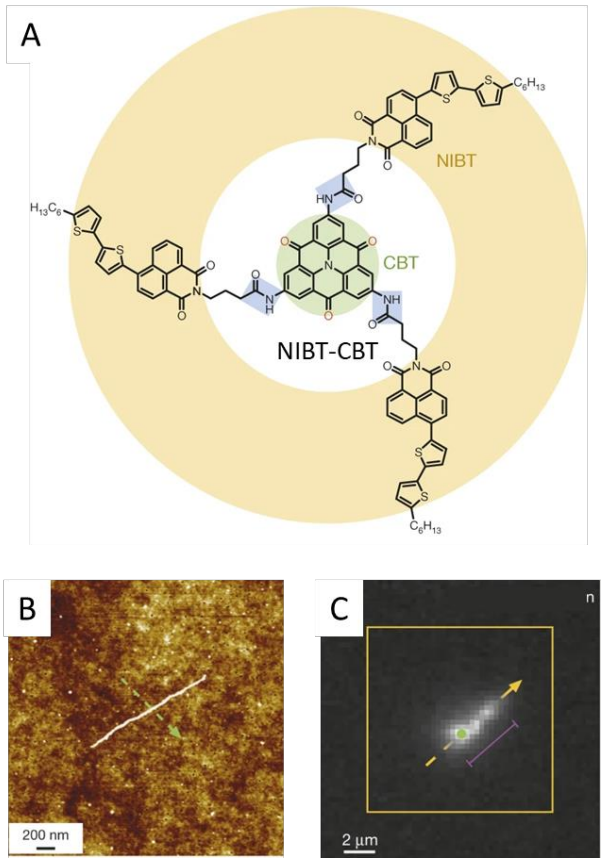

Figure 1-10: A) Chemical structure a supramolecular building block based on *carbonyl bridged triarylamine* (*CBT*) linked at the 2, 6 and 10 position via amide moieties to *4-(5-hexyl-2,2'-bithiophene)naphthalimide* (*NIBT*). B) Atomic force microscopy showing the formation of separated, single nanofibers based of *NIBT-CBT*. C) Confocal excitation showing the long-range exciton energy transfer properties. The green dot indicates the point of illumination. Over distances, up to 4 µm photoluminescence of the supramolecular nanofiber can be detected. *Reproduced with permission from Springer Nature.*[11]

Intriguingly, exciton energy transport between different molecules can also be observed in supramolecular aggregates of the same molecule. Therefore, building blocks of *NIBT-CBT* are assembled into single supramolecular nanofibers at concentrations of 7 µM in *ortho-dichlorobenzene*. Spin-coated samples reveal isolated, single nanofibers (see **Figure 1-10 B**) of around 2.5 nm in height and multiple micrometers in length. Excitation of the nanofiber at one spot results in detectable fluorescence over the whole fiber length as shown in **Figure 1-10 C**. In other words, the excitation is transported through the whole fiber over remarkable distances up to 4 µm moving over 10000 molecules.[11]

To further study the self-assembly process of such *CBT*-based supramolecular building blocks, new molecules were designed with chiral peripheries (see **Figure 1-11**). The self-assembly of the S chiral building block (*S-CBT*) was probed via temperature-dependent circular dichroism (CD) spectroscopy. The building block can form aggregates via an isodesmic pathway upon cooling to

7 °C. Further cooling result is the formation of a different aggregate (state B) with an inverse CD signal via a nucleation-elongation mechanism. Interestingly, aggregates of state B can be used as seeds to induce the transformation of state A into B indicating that state A is kinetically trapped and state B is the thermodynamic stable form.[88]

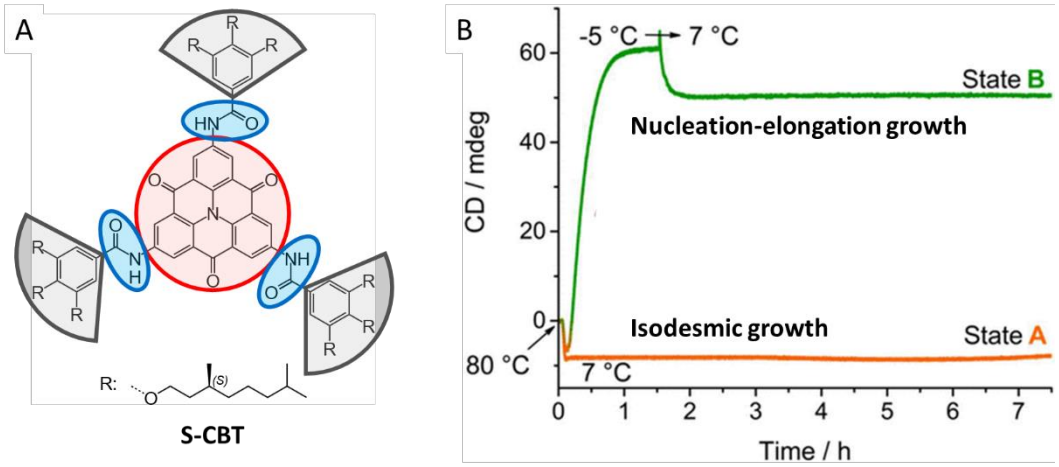

Figure 1-11: A) Molecular structure of a supramolecular building block based on *carbonyl-bridged triarylamine trisamide* with (*S*)-chiral bulky side-groups (*S-CBT*). B) Circular dichroism (CD) signal at 490 nm of S-CBT in *ortho-dichlorobenzene* shows that two stable structures can be formed at 7 °C depending on the thermal history. If the sample is cooled from 80°C to 7 °C (orange) the kinetically trapped state A is formed via an isodesmic mechanism with a negative CD signal at 490 nm. In contrast, if the sample is cooled to -5 °C and then heated to 7 °C, the thermodynamically stable state B is formed via a nucleation- elongation mechanism with a positive CD signal at 490 nm. Adopted with permission from reference [88]. © 2016 American Chemical Society.

1.2 Polymer Systems

Crystallization of Polymers

Polymers are an essential class of materials in our daily lives which is linked to their mechanical properties and ease of processing. These mechanical properties of crystallizable polymer, which make up the majority of all synthetic polymer products produced worldwide, are dominated by their semicrystalline morphology, i.e., the interplay between the crystalline and amorphous part of the material.[89–91] The crystallization of polymers is a complex topic, due to diffusion, adsorption, resorption, entanglements of chains, exclusion of defect, and further processes. There are multiple different crystallization theories, and the complete mechanism is still not completely understood.[91,92]

In general, any system tries to move towards the energetically favored state. Importantly, the free enthalpy of the amorphous state and the crystalline state have different temperature dependencies due to their different entropies. Therefore, a specific temperature exists, where the free enthalpies of both states is identical – the melting point. Above this temperature, the amorphous or molten state is energetically favored and below this point, the crystalline state is energetically favored. A temperature change crossing the melting point, hence, creates an energetical driving force for a phase transition. [93–95]

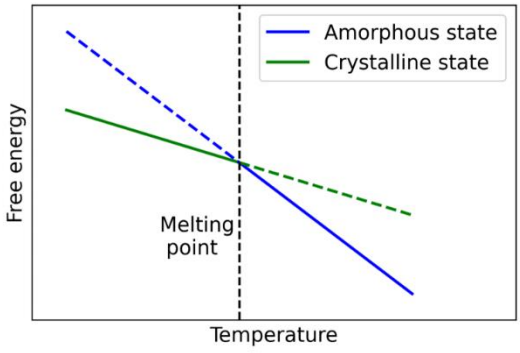

Figure 1-12: Schematic representation of the free energy in a polymeric system. At high temperatures, the free energy of the amorphous state (blue) is lower while at lower temperatures the free energy of the crystalline state is preferred.

Although the crystalline state is energetically favored upon cooling below the melting point, the formation of the crystal is retarded (see **Figure 1-13**). In general, the crystallization process follows a nucleation and growth mechanism. Forming a crystal generates an interface towards the surrounding amorphous phase which is energetically unfavored. However, the free energy inside the forming crystal is favorable compared to the amorphous phase. Therefore, the formation of crystals is governed by the rise in surface energy and the energy gain due to the volume of the

crystal. Importantly, the surface energy-related term scales with the surface of the crystal, so the square of the crystal size, and the volume-related term scales with the cube of the crystal size. The formation of very small crystals is dominated by the surface term and, therefore, energetically hindered while the further growth of the crystals would be energetically beneficial. Consequently, a critical exists upon further growth is beneficial (see **Figure 1-13**), and an energetic barrier to reach this critical size needs to be overcome resulting in the nucleation and growth mechanism.[92,93,96–98]

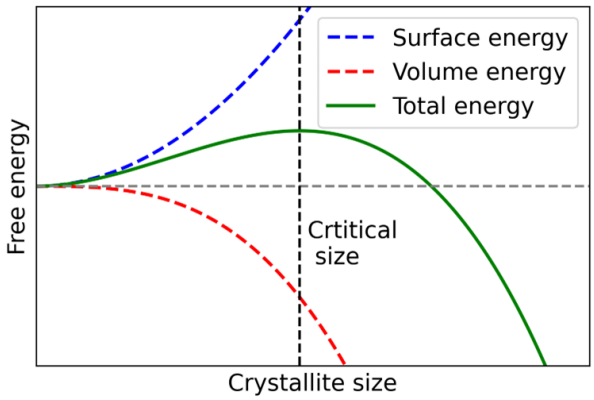

Figure 1-13: Schematic representation of the free energy dependent on the crystal size as well as the contributions from the surface (blue) and volume of the crystal (red). The formation of crystals is hampered by an energetic barrier until a critical crystal size is reached. Further grows is energetically beneficial for the system.

Although the formation of nuclei is energetically unfavorable, thermal fluctuations can result in the spontaneous formation of nuclei of the necessary critical size. However, this chance process becomes more unlikely the larger the critical size is. Therefore, most systems need to be cooled below their melting point enhancing the volume-driven energetical gain, effectively reducing the critical size of the crystallization to make nucleation more likely.

Nucleation can be differentiated by the dimensions in which new surfaces are created due to the nucleation. The two most important classes are primary nucleation which describes the formation of a new nucleus with new surfaces in all three dimensions and secondary nucleation which is the growth onto the surface of a crystal or nucleus and, therefore, only creates new surfaces in two-dimensions. Due to the reduced surface creation in secondary crystallization, this process is significantly accelerated.[91–93,99,100]

The crystallization of polymers is even more complex as the long polymer chains are usually randomly coiled and entangled in the amorphous state but need to align to form crystals. As this alignment and disentanglement is very slow, it is usually incomplete for long polymer chains. Therefore, aligned parts of nearby polymer chains are incorporated into the growing crystal. The remaining polymer chain might be trapped in a non-aligned state and form an amorphous part next

to the crystal. Alternatively, the non-aligned parts might back-fold and be incorporated into the crystal directly or at a later stage or they can be incorporated into a different growing crystal giving rise to tie molecules. Usually, polymer crystals form spherulites consisting of multiple lamellae with amorphous parts in between – giving rise to the semi-crystalline nature of polymers. [93,101,102]

Supramolecular Nucleating Agents

To accelerate the crystallization process of polymers, nucleating agents can be introduced. Such materials can act as a basis for the nucleation of polymers, therefore, skipping the slow primary nucleation step and utilizing faster secondary nucleation directly. In a practical sense, this results in the crystallization conducting faster and at higher temperatures – both are highly beneficially for industrial processes. Further, the use of nucleating agents determines the amount of nuclei in the systems enabling control over the number of crystals and, hence, the crystal size in the system impacting the solid-state morphology and allowing for the tuning of the final properties of the material.[26,95,103,104]

Insoluble inorganic compounds such as silica, talc, titan dioxide, or potassium phosphates were initially used as nucleating agents for semi-crystalline polymers.[95,103,105] Such additives are dispersed in the polymer melt and can then assist the nucleation upon cooling. However, due to the insoluble character, a homogenous distribution of these in the melt is not a given.[95,104] A different class of nucleating agent relies on the reversible structure formation to solve this issue. Such supramolecular nucleating agents are small organic molecules that dissolve in the polymer melt at elevated temperatures ensuring a homogenous distribution (see **Figure 1-14**). Upon cooling, these molecules can self-assembly into small, but solid structures above the crystallization temperature of the polymer. These structures can then provide surfaces for the secondary nucleation of the polymer accelerating the crystallization process. Further, such supramolecular nucleating agents can be very efficient even at minuscule concentrations due to the small size of the formed aggregates and the resulting very high surface to volume ratio.[26,95,104,106,107]

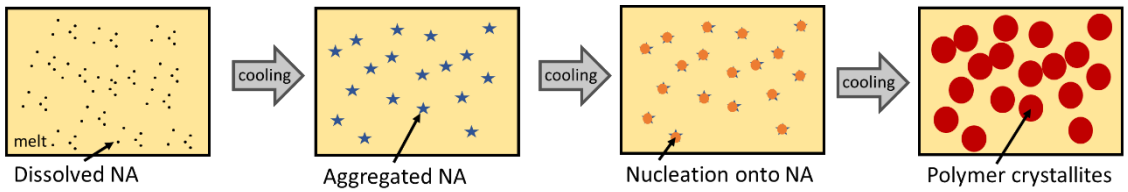

Figure 1-14: Schematic representation of the mechanism behind supramolecular nucleating agents (NA). The supramolecular nucleating agent is dissolved in the polymer melt at elevated temperatures. Upon cooling, supramolecular aggregates of the NA are formed. Upon further cooling, the polymer can use the supramolecular structures of NA for secondary nucleation initiating the crystallization. Finally, polymer crystals are formed based on the aggregated nucleation agent.

Supramolecular nucleating agents must fulfill multiple requirements that need to be considered for their molecular design. First, such additives need to be thermally stable as polymer melts are usually processed at high temperatures. The additives must be soluble in the polymer melt at high

temperatures, but they also have to aggregate into supramolecular structures at temperatures above the melting point requiring a delicate equilibrium of the supramolecular interactions. Finally, the aggregates should feature an epitaxial surface, i.e., a surface that fits the crystalline structure of the polymer allowing for the direct attachment of the polymer onto the surface of the nucleating agent.[26,95,104,106,108]

The nucleating agents can increase the crystallization temperature by reducing the energy barrier of the nucleation. This effect can be tracked via dynamic scanning calorimetry where the cooling curves of polymer melts are investigated. Efficient nucleating agents can shift the crystallization temperature even at very low concentrations. Hence, a figure of merit was developed to assess the abilities of different nucleating agents – the nucleation efficiency NE. Here, the crystallization temperature with the nucleating agent T_c is related to the maximal achievable crystallization temperature $T_{c,max}$ and the crystallization temperature of the neat polymer $T_{c,min}$ (see **Equation 2**).[109]

$$NE = \frac{T_c - T_{c,0}}{T_{c,max} - T_{c,0}} \qquad (\mathbf{2})$$

The maximal achievable crystallization temperature is determined using self-seeding experiments. Here, the polymer is only partly molten upon heating. Thus, small crystallites remain in the sample. Upon cooling, these small crystallites can act as perfect nuclei as they are just small crystals of the desired structure.[110] The nucleation efficiency can be used to quantify and compare the effects of different nucleating agents.

Two important groups of supramolecular nucleating agents are based on *benzene trisamides*[26,106,108] and *sorbitol* derivatives[111,112] and have been extensively studied for their use in isotactic *poly(propylene)*. Here, both groups of structures can achieve outstanding nucleation efficiencies.[26,108,112] Further, the addition of such nucleating agents can accelerate the crystallization process speeding up the processing times as well as improving the optical and mechanical properties.[111,113–116] In some cases it is even possible to change the crystal modification with supramolecular nucleating agents.[26,108] Nowadays, supramolecular nucleating agents are well established in industry, and for multiple semi-crystalline polymers efficient supramolecular nucleating agents have been designed. [95,104,106]

Crystallization of *Poly (3-hexyl thiophene)*

After the discovery of conducting polymers, i.e., *poly(acetylene)*, by Shirakawa, Heeger, and MacDiarmid in 1977[117] conjugated polymers have become an extensive research field. Regio-regular *poly (3-hexyl thiophene)* (*P3HT*), which was first synthesized in the early 1990s, in this context became quickly one of the most investigated semiconducting polymers due to its use in organic electronic devices. Still, this polymer is used as a model system to understand and tailor the solid-state morphology of conjugated polymer and polymer blends.[118–120]

Due to the asymmetry of the monomeric unit, *3-hexyl thiophene*, different regio-isomers can be obtained during the polymerization of *P3HT*. However, only consecutive head to tail connections lead to a regio-regular polymer where the polymer backbone can planarize enhancing the conjugation and π- π interactions between the backbones.[119,121,122] It should be noted that most polymerization methods towards *P3HT* start with a tail-to-tail coupling and hence a regio-defect.[123–125] Although new methods have emerged to create completely regio-regular *P3HT*. [126,127]

The crystallization of *P3HT* is driven by the rigid backbone and the π-π–interaction of the *thiophene* units between the backbones. However, the creation of single crystals of *P3HT* is only rarely possible.[128] Most characterizations have been made based on semi-crystalline films. A schematic representation of the typical microstructure is shown in **Figure 1-15**. *P3HT* can crystallize into different modifications. In the most stable form 1, the side chains of individual backbones do not interdigitate and the polymer crystallizes in the anisotropic P2/1c space group.[129–131] Upon crystallization, *P3HT* forms a lamellar structure along the c-direction with alternating crystalline and amorphous areas. The amorphous areas are formed due to regio defects, non-aligned polymer backbones, as well as entanglements and back-folding of the polymer chains. In general, larger molecular weights and, hence, longer polymer chains, increase the width of the lamellar until a maximum is reached at around 12 000 g mol^{-1}, resulting in a lamellar width of about 20 nm. Longer polymer chains show increased back-folding and entanglements. Therefore, the width of the crystalline part remains constant or even decreases slightly with further increasing molecular weight.[132] The height of the *P3HT* crystals (see a direction in **Figure 1-15**) is reported to be only two to four molecules, corresponding to 3 to 6 nm.[133] The *P3HT* fiber length, which propagates along the b-direction, varies on the preparation method. It is possible to form *P3HT* nanofibers up to multiple micrometers in length, where each micrometer corresponds to stacks of over 2500 molecules.[134]

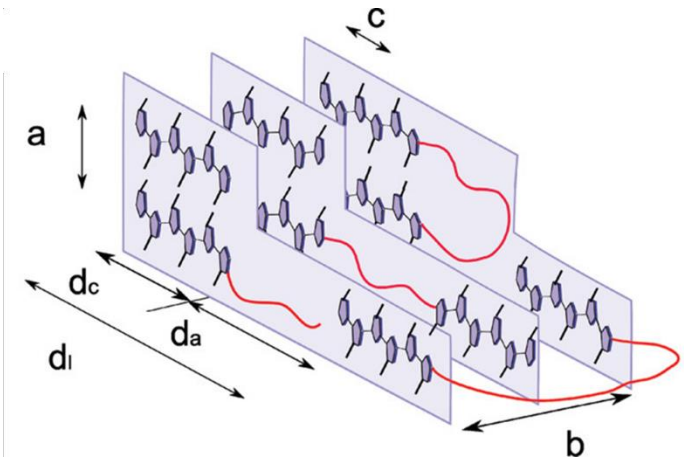

Figure 1-15: Schematic representation of the crystal structure of *P3HT* in form I. *P3HT* crystallizes in the anisotropic P2/1c space group. The red lines indicate the amorphous part between the crystalline structures. Reprinted with permission from reference [131]. © 2010 American Chemical Society.

P3HT is of great interest as the conjugated polymer combines interesting optical and electronic properties with ease of processing. For the preparation of organic photovoltaics and organic field-effect transistors, the preparation of thin-films with defined morphologies is of great importance as the properties and hence the device performance is directly linked to the solid-state properties of *P3HT* thin-films.[119,120,135] Besides molecular variations, such as regio-regularity and molecular weight changes, the processing is crucial to tailor the morphology of conjugated polymers. Different strategies have evolved to achieve such control via modifications to the nucleation or crystal growth process including thermal[136] or solvent vapor annealing[137], the use of antisolvents[138] or processing additives[139], or preforming of crystals. For example, pre-formed *P3HT* nanofibers can improve the performance of devices.[140,141] The effect can even be enhanced by a pre-orientation of the nanofibers.[142]

An interesting approach in this regard is the use of nucleating agents. Examples are based on *carbon nanotubes*[143], *graphene*[144,145] as well as *thiophene*-based copolymer[146,147] to name a few. Commercially available nucleating agents, originally developed for the nucleation of isotactic *poly (propylene)* have also been successfully used to tailor the nucleation of for conjugated polymers.[148–150] For example, Stingelin and coworkers used supramolecular nucleating agents to nucleate *poly (3-alkyl thiophenes)*. The addition of 1 wt % of a *sorbitol* based supramolecular nucleating agent increased the crystallization temperature of *poly (3-dodecyl thiophene)* by 24 °C. They could also show that 1 wt % of a *benzene trisamide* based supramolecular nucleating agent can increase the crystallization temperature of *P3HT* from solution by 7 °C indicating the general functionality of supramolecular nucleating agents for conjugated polymers.[150] However, tailored supramolecular nucleating agents for conjugated polymers are rare.

Isolated Superstructures based on *Poly (3-hexyl thiophene)*

Detailed studies of isolated *P3HT*-based structures are of great interest to understand structure-property relationships and as an approach to form components for nanophotonic devices or artificial light harvesting machineries. One of the first works in this regard was conducted by Smith and coworkers. They showed in 1993 the formation of one dimensional P3HT nanofibers. These fibers were about 15 nm wide, 5 nm high and about 10 µm long. These one-dimensional crystals were prepared out of a 0.05 wt % solution of *P3HT* in *cyclohexanone*. For this, they heated the solution to 50 °C to dissolve the *P3HT* and slowly cooled it to room temperature. After deposition of the solution and solvent evaporation, *P3HT* fibers could be observed.[134] Since then multiple methods have been developed to create nanofibers of *P3HT* including mixed solvent[151], temperature variation[141,152] or UV-light radiation[153] approaches.

Interestingly, different research groups were able to form superstructures featuring numerous nanofibers of *P3HT*. For example, Brinkmann *et al.* used *trichlorobenzene* fibers and *pyridine* as nucleation agents. They first drop-casted a 1 wt % solution of *P3HT* in *chloroform* on a glass slide and then added *trichlorobenzene* powder. They subsequently heated the sample to melt the *trichlorobenzene* and dissolve the *P3HT*. After the addition of *pyridine*, they cooled the sample. In the following, *trichlorobenzene* crystallizes into thin and long fibers and *P3HT* subsequently crystallizes in an epitaxial fashion on the fiber. This process resulted in the formation of shish-kebab-like superstructures (see **Figure 1-16 A**) for conjugated polymers for the first time with the *trichlorobenzene* as central shish and *P3HT* nanofibers with lengths up to 200 nm as kebabs. The nanofibers feature a high orientation due to the epitaxial growth as shown by polarized photoluminescence.[154]

Single-walled and multi-walled *carbon nanotubes* were also used to induce the crystallization of *P3HT* in anisole upon cooling. However, the *P3HT* nanofibers are only very thinly attached to the carbon nanotubes or less than 200 nm long (see **Figure 1-16 B**).[155] Later studies used chemically modified multi-walled *carbon nanotubes* to induce the crystallization of P3HT.[156] They modified the *carbon nanotubes* with *3-alkyl thiophene* oligomers. However, such *carbon nanotube*s are either covered only sparely with *P3HT* nanofiber or the *P3HT* nanofibers are less than 200 nm long. Nonetheless, a later study by the same group showed the potential of such structures for photovoltaics.[157]

Hayward and coworkers demonstrated an approach based on supramolecular aggregated structures. They used a substituted *perylene diimides* and *P3HT* in solution. The *P3HT* kinetically stabilizes the supersaturated *perylene diimides* solution and enables the assembly of long and thin

perylene diimides aggregates. In return, those can act as heterogeneous nucleation sites for *P3HT* resulting in the formation of acceptor-donor shish kebabs with nanofibers of up to 500 nm in length (see **Figure 1-16 C**).[158] Similarly, Zhang *et al.* also employed supramolecular structures to induce the crystallization of *P3HT*. They form supramolecular nanowires based on a *sorbitol* derivative on which *P3HT* crystallizes into nanofibers (see **Figure 1-16 D**). Further, they showed that such structures increase the mobilities in thin-films by one order of magnitude.[159]

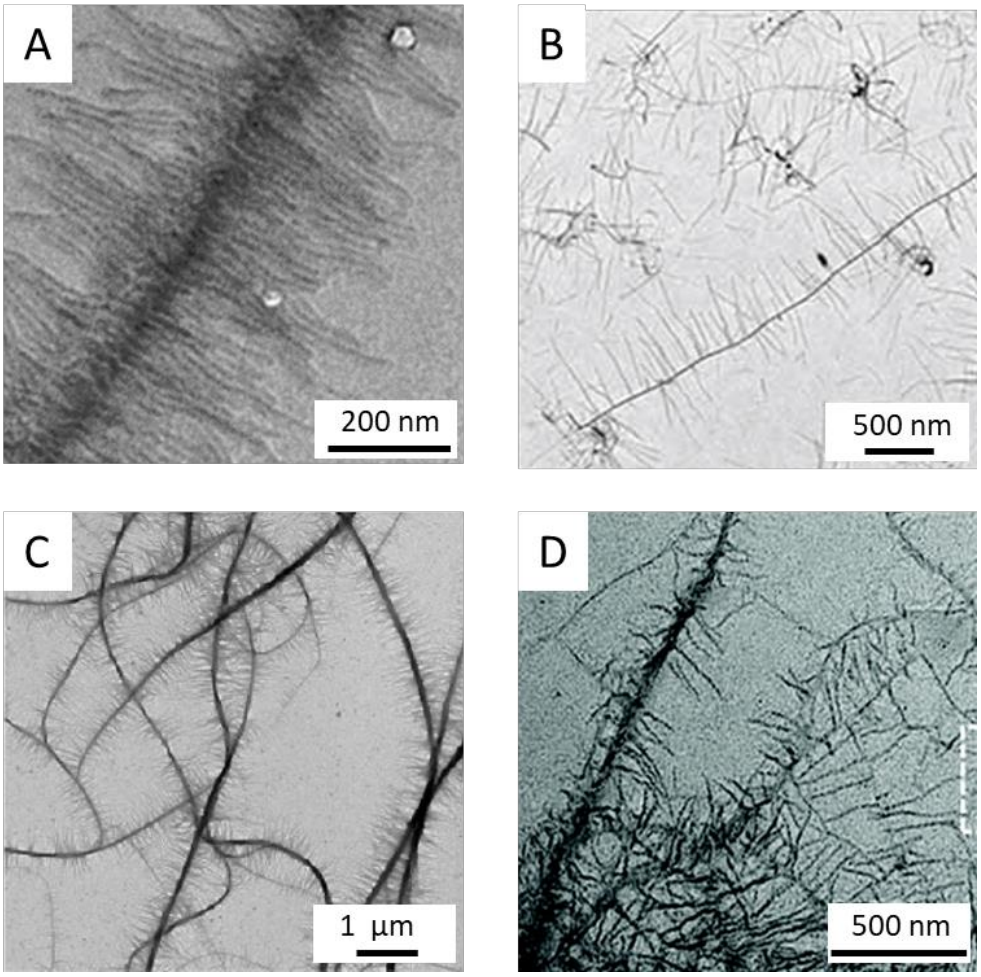

Figure 1-16: Overview of selected *P3HT*-based superstructures in literature using different components as the core. A) *P3HT*-based shish-kebab structures based on *trichlorobenzene* and *pyridine* as core. © 2009 Wiley. Used with permission from reference [154]. B) *P3HT*-based superstructures using multi-walled *carbon nanotubes* as cores. © 2009 Wiley. Used with permission from reference [155]. C) *P3HT*-based superstructures using supramolecular aggregates based on substituted *perylene diimides* as core. Reprinted with permission from reference [158]. © 2012 American Chemical Society. D) *P3HT*-based superstructures using supramolecular aggregates based on derivatives of *sorbitol* as core. Reproduced from Ref. [159] with permission from the Royal Society of Chemistry.

Such superstructures demonstrate an interesting path to further understand structure-property relationships in conjugated polymer and to form functional components for nanophotonic devices or as collecting wires.[154,155,159] However, the limited length of the *P3HT* nanofibers hampers spatially resolved investigations. Therefore, achieving multiple micrometer long *P3HT* nanofibers as shown by Smith *et al.*[134] but inside a superstructure would open new pathways for their investigations. In addition, the shown superstructure features oriented *P3HT* nanofibers for the samples with a high nucleation density (see **Figure 1-16 A & C**). Therefore, a high nucleation density to achieve superstructures with highly oriented P3HT nanofibers is also desired.

1.3 References

[1] Fassioli, F.; Dinshaw, R.; Arpin, P. C.; Scholes, G. D. *Photosynthetic light harvesting: excitons and coherence.* Journal of the Royal Society, Interface **2014**, *11* (*92*), 20130901.

[2] Mirkovic, T.; Ostroumov, E. E.; Anna, J. M.; van Grondelle, R.; Govindjee; Scholes, G. D. *Light Absorption and Energy Transfer in the Antenna Complexes of Photosynthetic Organisms.* Chemical Reviews **2017**, *117* (*2*), 249–293.

[3] Strümpfer, J.; Sener, M.; Schulten, K. *How Quantum Coherence Assists Photosynthetic Light Harvesting.* The Journal of Physical Chemistry Letters **2012**, *3* (*4*), 536–542.

[4] Mullineaux, C. W.; Pascal, A. A.; Horton, P.; Holzwarth, A. R. *Excitation-energy quenching in aggregates of the LHC II chlorophyll-protein complex: a time-resolved fluorescence study.* Biochimica et Biophysica Acta (BBA) - Bioenergetics **1993**, *1141* (*1*), 23–28.

[5] Standfuss, J.; van Terwisscha Scheltinga, A. C.; Lamborghini, M.; Kühlbrandt, W. *Mechanisms of photoprotection and nonphotochemical quenching in pea light-harvesting complex at 2.5 A resolution.* The EMBO journal **2005**, *24* (*5*), 919–928.

[6] Liguori, N.; Periole, X.; Marrink, S. J.; Croce, R. *From light-harvesting to photoprotection: structural basis of the dynamic switch of the major antenna complex of plants (LHCII).* Scientific Reports **2015**, *5* (*1*), 15661.

[7] Kreger, K.; Schmidt, H.-W.; Hildner, R. *Tailoring the excited-state energy landscape in supramolecular nanostructures.* Electronic Structure **2021**, *3* (*2*), 23001.

[8] Brédas, J.-L.; Sargent, E. H.; Scholes, G. D. *Photovoltaic concepts inspired by coherence effects in photosynthetic systems.* Nature Materials **2016**, *16* (*1*), 35–44.

[9] Scholes, G. D.; Fleming, G. R.; Chen, L. X.; Aspuru-Guzik, A.; Buchleitner, A.; Coker, D. F.; Engel, G. S.; van Grondelle, R.; Ishizaki, A.; Jonas, D. M.; Lundeen, J. S.; McCusker, J. K.; Mukamel, S.; Ogilvie, J. P.; Olaya-Castro, A.; Ratner, M. A.; Spano, F. C.; Whaley, K. B.; Zhu, X. *Using coherence to enhance function in chemical and biophysical systems.* Nature **2017**, *543* (*7647*), 647–656.

[10] Scholes, G. D. *Coherence from Light Harvesting to Chemistry.* The Journal of Physical Chemistry Letters **2018**, *9* (*7*), 1568–1572.

[11] Haedler, A. T.; Kreger, K.; Issac, A.; Wittmann, B.; Kivala, M.; Hammer, N.; Köhler, J.; Schmidt, H.-W.; Hildner, R. *Long-range energy transport in single supramolecular nanofibres at room temperature.* Nature **2015**, *523* (*7559*), 196–199.

[12] Clark, K. A.; Krueger, E. L.; Vanden Bout, D. A. *Direct Measurement of Energy Migration in Supramolecular Carbocyanine Dye Nanotubes.* The Journal of Physical Chemistry Letters **2014**, *5* (*13*), 2274–2282.

[13] Winiger, C. B.; Li, S.; Kumar, G. R.; Langenegger, S. M.; Häner, R. *Long-distance electronic energy transfer in light-harvesting supramolecular polymers.* Angewandte Chemie International Edition **2014**, *53* (*49*), 13609–13613.

[14] Eisele, D. M.; Knoester, J.; Kirstein, S.; Rabe, J. P.; Vanden Bout, D. A. *Uniform exciton fluorescence from individual molecular nanotubes immobilized on solid substrates.* Nature Nanotechnology **2009**, *4* (*10*), 658–663.

[15] Jin, X.-H.; Price, M. B.; Finnegan, J. R.; Boott, C. E.; Richter, J. M.; Rao, A.; Menke, S. M.; Friend, R. H.; Whittell, G. R.; Manners, I. *Long-range exciton transport in conjugated polymer nanofibers prepared by seeded growth.* Science **2018**, *360* (*6391*), 897–900.

[16] Kim, J.; McQuade, D. T.; Rose, A.; Zhu, Z.; Swager, T. M. *Directing energy transfer within conjugated polymer thin films.* Journal of the American Chemical Society **2001**, *123* (*46*), 11488–11489.

[17] Whitesides, G. M.; Mathias, J. P.; Seto, C. T. *Molecular self-assembly and nanochemistry: a chemical strategy for the synthesis of nanostructures.* Science **1991**, *254* (*5036*), 1312–1319.

[18] Lehn, J.-M. *Supramolecular Chemistry—Scope and Perspectives Molecules, Supermolecules, and Molecular Devices (Nobel Lecture).* Angewandte Chemie International Edition **1988**, *27* (*1*), 89–112.

[19] Varshey, D. B.; Sander, J. R. G.; Friščić, T.; MacGillivray, L. R. *Supramolecular Interactions*; Supramolecular Chemistry; John Wiley & Sons, Ltd, **2012**.

[20] Luo, Y.-R. *Comprehensive handbook of chemical bond energies*; CRC Press, **2007**.

[21] Mattia, E.; Otto, S. *Supramolecular systems chemistry.* Nature Nanotechnology **2015**, *10* (*2*), 111–119.

[22] Hoeben, F. J. M.; Jonkheijm, P.; Meijer, E. W.; Schenning, Albertus P. H. J. *About supramolecular assemblies of pi-conjugated systems.* Chemical Reviews **2005**, *105* (*4*), 1491–1546.

[23] Besenius, P. *Controlling supramolecular polymerization through multicomponent self-assembly.* Journal of Polymer Science Part A: Polymer Chemistry **2017**, *55* (*1*), 34–78.

[24] Qin, B.; Yin, Z.; Tang, X.; Zhang, S.; Wu, Y.; Xu, J.-F.; Zhang, X. *Supramolecular polymer chemistry: From structural control to functional assembly.* Progress in Polymer Science **2020**, *100*, 101167.

[25] Molla, M. R.; Gehrig, D.; Roy, L.; Kamm, V.; Paul, A.; Laquai, F.; Ghosh, S. *Self-assembly of carboxylic acid appended naphthalene diimide derivatives with tunable luminescent color and electrical conductivity.* Chemistry – A European Journal **2014**, *20* (*3*), 760–771.

[26] Blomenhofer, M.; Ganzleben, S.; Hanft, D.; Schmidt, H.-W.; Kristiansen, M.; Smith, P.; Stoll, K.; Mäder, D.; Hoffmann, K. *"Designer" Nucleating Agents for Polypropylene.* Macromolecules **2005**, *38* (*9*), 3688–3695.

[27] van Zee, N. J.; Adelizzi, B.; Mabesoone, M. F. J.; Meng, X.; Aloi, A.; Zha, R. H.; Lutz, M.; Filot, I. A. W.; Palmans, A. R. A.; Meijer, E. W. *Potential enthalpic energy of water in oils exploited to control supramolecular structure.* Nature **2018**, *558* (*7708*), 100–103.

[28] Korevaar, P. A.; George, S. J.; Markvoort, A. J.; Smulders, M. M. J.; Hilbers, P. A. J.; Schenning, Albert P. H. J.; Greef, T. F. A. de; Meijer, E. W. *Pathway complexity in supramolecular polymerization.* Nature **2012**, *481* (*7382*), 492–496.

[29] Tantakitti, F.; Boekhoven, J.; Wang, X.; Kazantsev, R. V.; Yu, T.; Li, J.; Zhuang, E.; Zandi, R.; Ortony, J. H.; Newcomb, C. J.; Palmer, L. C.; Shekhawat, G. S.; La Cruz, M. O. de; Schatz, G. C.; Stupp, S. I. *Energy landscapes and functions of supramolecular systems.* Nature Materials **2016**, *15* (*4*), 469–476.

[30] Wehner, M.; Röhr, M. I. S.; Bühler, M.; Stepanenko, V.; Wagner, W.; Würthner, F. *Supramolecular Polymorphism in One-Dimensional Self-Assembly by Kinetic Pathway Control.* Journal of the American Chemical Society **2019**, *141* (*14*), 6092–6107.

[31] Wehner, M.; Würthner, F. *Supramolecular polymerization through kinetic pathway control and living chain growth.* Nature Reviews Chemistry **2020**, *4* (*1*), 38–53.

[32] van der Zwan, K. P.; Steinlein, C.; Kreger, K.; Schmidt, H.-W.; Senker, J. *Crystal Engineering of Supramolecular 1,4-Benzene Bisamides by Side-Chain Modification - Towards Tuneable Anisotropic Morphologies and Surfaces.* ChemPhysChem **2021**, *22* (*24*), 2585–2593.

[33] Cantekin, S.; Greef, T. F. A. de; Palmans, A. R. A. *Benzene-1,3,5-tricarboxamide: a versatile ordering moiety for supramolecular chemistry.* Chemical Society Reviews **2012**, *41* (*18*), 6125–6137.

[34] Lightfoot, M. P.; Mair, F. S.; Pritchard, R. G.; Warren, J. E. *New supramolecular packing motifs: π-stacked rods encased in triply-helical hydrogen bonded amide strands.* Chemical Communications **1999**, *0* (*19*), 1945–1946.

[35] Markvoort, A. J.; Eikelder, H. M. M. ten; Hilbers, P. A. J.; Greef, T. F. A. de; Meijer, E. W. *Theoretical models of nonlinear effects in two-component cooperative supramolecular copolymerizations.* Nature Communications **2011**, *2* (*1*), 509.

[36] Palmans, A. R. A.; Meijer, E. W. *Amplification of chirality in dynamic supramolecular aggregates.* Angewandte Chemie International Edition **2007**, *46* (*47*), 8948–8968.

[37] Smulders, M. M. J.; Filot, I. A. W.; Leenders, J. M. A.; van der Schoot, P.; Palmans, A. R. A.; Schenning, Albertus P. H. J.; Meijer, E. W. *Tuning the extent of chiral amplification by temperature in a dynamic supramolecular polymer.* Journal of the American Chemical Society **2010**, *132* (*2*), 611–619.

[38] Zehe, C. S.; Hill, J. A.; Funnell, N. P.; Kreger, K.; van der Zwan, K. P.; Goodwin, A. L.; Schmidt, H.-W.; Senker, J. *Mesoscale Polarization by Geometric Frustration in Columnar Supramolecular Crystals.* Angewandte Chemie International Edition **2017**, *56* (*16*), 4432–4437.

[39] Wegner, M.; Dudenko, D.; Sebastiani, D.; Palmans, A. R. A.; Greef, T. F. A. de; Graf, R.; Spiess, H. W. *The impact of the amide connectivity on the assembly and dynamics of benzene-1,3,5-tricarboxamides in the solid state.* Chemical Science **2011**, *2* (*10*), 2040.

[40] Albuquerque, R. Q.; Timme, A.; Kress, R.; Senker, J.; Schmidt, H.-W. *Theoretical investigation of macrodipoles in supramolecular columnar stackings.* Chemistry – A European Journal **2013**, *19* (*5*), 1647–1657.

[41] Schmidt, M.; Zehe, C. S.; Siegel, R.; Heigl, J. U.; Steinlein, C.; Schmidt, H.-W.; Senker, J. *NMR-crystallographic study of two-dimensionally self-assembled cyclohexane-based low-molecular-mass organic compounds.* CrystEngComm **2013**, *15* (*43*), 8784.

[42] Kulkarni, C.; Meijer, E. W.; Palmans, A. R. A. *Cooperativity Scale: A Structure-Mechanism Correlation in the Self-Assembly of Benzene-1,3,5-tricarboxamides.* Accounts of Chemical Research **2017**, *50* (*8*), 1928–1936.

[43] Bernet, A.; Albuquerque, R. Q.; Behr, M.; Hoffmann, S. T.; Schmidt, H.-W. *Formation of a supramolecular chromophore: a spectroscopic and theoretical study.* Soft Matter **2012**, *8* (*1*), 66–69.

[44] Weiss, D.; Skrybeck, D.; Misslitz, H.; Nardini, D.; Kern, A.; Kreger, K.; Schmidt, H.-W. *Tailoring Supramolecular Nanofibers for Air Filtration Applications.* ACS Applied Materials & Interfaces **2016**, *8* (*23*), 14885–14892.

[45] Drummer, M.; Liang, C.; Kreger, K.; Rosenfeldt, S.; Greiner, A.; Schmidt, H.-W. *Stable Mesoscale Nonwovens of Electrospun Polyacrylonitrile and Interpenetrating Supramolecular 1,3,5-Benzenetrisamide Fibers as Efficient Carriers for Gold Nanoparticles.* ACS Applied Materials & Interfaces **2021**, *13* (*29*), 34818–34828.

[46] Howe, R. C. T.; Smalley, A. P.; Guttenplan, A. P. M.; Doggett, M. W. R.; Eddleston, M. D.; Tan, J. C.; Lloyd, G. O. *A family of simple benzene 1,3,5-tricarboxamide (BTA) aromatic carboxylic acid hydrogels.* Chemical Communications **2013**, *49* (*39*), 4268–4270.

[47] Weiss, D.; Kreger, K.; Schmidt, H.-W. *Self-Assembly of Alkoxy-Substituted 1,3,5-Benzenetrisamides Under Controlled Conditions.* Macromolecular Materials and Engineering **2017**, *302* (*1*), 1600390.

[48] Greef, T. F. A. de; Smulders, M. M. J.; Wolffs, M.; Schenning, Albert P. H. J.; Sijbesma, R. P.; Meijer, E. W. *Supramolecular polymerization.* Chemical Reviews **2009**, *109* (*11*), 5687–5754.

[49] Zhao, D.; Moore, J. S. *Shape-persistent arylene ethynylene macrocycles: syntheses and supramolecular chemistry.* Chemical Communications **2003** (*7*), 807–818.

[50] Kastler, M.; Pisula, W.; Wasserfallen, D.; Pakula, T.; Müllen, K. *Influence of alkyl substituents on the solution- and surface-organization of hexa-peri-hexabenzocoronenes.* Journal of the American Chemical Society **2005**, *127* (*12*), 4286–4296.

[51] Metzroth, T.; Hoffmann, A.; Martín-Rapún, R.; Smulders, M. M. J.; Pieterse, K.; Palmans, A. R. A.; Vekemans, J. A. J. M.; Meijer, E. W.; Spiess, H. W.; Gauss, J. *Unravelling the fine structure of stacked bipyridine diamine-derived C_3 -discotics as determined by X-ray diffraction, quantum-chemical calculations, Fast-MAS NMR and CD spectroscopy.* Chemical Science **2011**, *2* (*1*), 69–76.

[52] Würthner, F.; Chen, Z.; Dehm, V.; Stepanenko, V. *One-dimensional luminescent nanoaggregates of perylene bisimides.* Chemical Communications **2006** (*11*), 1188–1190.

[53] Aparicio, F.; García, F.; Sánchez, L. *Supramolecular polymerization of C_3-symmetric organogelators: cooperativity, solvent, and gelation relationship.* Chemistry – A European Journal **2013**, *19* (*9*), 3239–3248.

[54] Kulkarni, C.; Bejagam, K. K.; Senanayak, S. P.; Narayan, K. S.; Balasubramanian, S.; George, S. J. *Dipole-moment-driven cooperative supramolecular polymerization.* Journal of the American Chemical Society **2015**, *137* (*11*), 3924–3932.

[55] Kulkarni, C.; Meijer, E. W.; Palmans, A. R. A. *Cooperativity Scale: A Structure-Mechanism Correlation in the Self-Assembly of Benzene-1,3,5-tricarboxamides.* Accounts of Chemical Research **2017**, *50* (*8*), 1928–1936.

[56] Smulders, M. M. J.; Schenning, Albertus P. H. J.; Meijer, E. W. *Insight into the mechanisms of cooperative self-assembly: the "sergeants-and-soldiers" principle of chiral and achiral C_3-symmetrical discotic triamides.* Journal of the American Chemical Society **2008**, *130* (*2*), 606–611.

[57] Filot, I. A. W.; Palmans, A. R. A.; Hilbers, P. A. J.; van Santen, R. A.; Pidko, E. A.; Greef, T. F. A. de. *Understanding cooperativity in hydrogen-bond-induced supramolecular polymerization: a density functional theory study.* The journal of physical chemistry. B **2010**, *114* (*43*), 13667–13674.

[58] Smulders, M. M. J.; Nieuwenhuizen, M. M. L.; Greef, T. F. A. de; van der Schoot, P.; Schenning, Albertus P. H. J.; Meijer, E. W. *How to distinguish isodesmic from cooperative supramolecular polymerisation.* Chemistry – A European Journal **2010**, *16* (*1*), 362–367.

[59] Bruckner, E. P.; Stupp, S. I. *Designing supramolecular polymers with nucleation and growth processes.* Polymer International **2022**, *71* (*5*), 590–595.

[60] Zhang, W.; Jin, W.; Fukushima, T.; Saeki, A.; Seki, S.; Aida, T. *Supramolecular linear heterojunction composed of graphite-like semiconducting nanotubular segments.* Science **2011**, *334* (*6054*), 340–343.

[61] Tao, D.; Feng, C.; Cui, Y.; Yang, X.; Manners, I.; Winnik, M. A.; Huang, X. *Monodisperse Fiber-like Micelles of Controlled Length and Composition with an Oligo(p-phenylenevinylene) Core via "Living" Crystallization-Driven Self-Assembly.* Journal of the American Chemical Society **2017**, *139* (*21*), 7136–7139.

[62] Tao, D.; Feng, C.; Lu, Y.; Cui, Y.; Yang, X.; Manners, I.; Winnik, M. A.; Huang, X. *Self-Seeding of Block Copolymers with a π-Conjugated Oligo(p -phenylenevinylene) Segment: A Versatile Route toward Monodisperse Fiber-like Nanostructures.* Macromolecules **2018**, *51* (*5*), 2065–2075.

[63] Hudson, Z. M.; Boott, C. E.; Robinson, M. E.; Rupar, P. A.; Winnik, M. A.; Manners, I. *Tailored hierarchical micelle architectures using living crystallization-driven self-assembly in two dimensions.* Nature Chemistry **2014**, *6* (*10*), 893–898.

[64] Ogi, S.; Sugiyasu, K.; Manna, S.; Samitsu, S.; Takeuchi, M. *Living supramolecular polymerization realized through a biomimetic approach.* Nature Chemistry **2014**, *6* (*3*), 188–195.

[65] Ogi, S.; Stepanenko, V.; Sugiyasu, K.; Takeuchi, M.; Würthner, F. *Mechanism of self-assembly process and seeded supramolecular polymerization of perylene bisimide organogelator.* Journal of the American Chemical Society **2015**, *137* (*9*), 3300–3307.

[66] Köhler, A.; Bässler, H. *Electronic processes in organic semiconductors*:*An introduction*; Wiley-VCH GmbH, **2022**.

[67] Myers Kelley, A. *Condensed-phase molecular spectroscopy and photophysics*, Second edition; Wiley, **2023**.

[68] Scheibe, G. *Über die Veränderlichkeit des Absorptionsspektrums einiger Sensibilisierungsfarbstoffe und deren Ursache.* Angewandte Chemie **1936** (*49*), 563.

[69] Jelley, E. E. *Spectral Absorption and Fluorescence of Dyes in the Molecular State.* Nature **1936**, *138* (*3502*), 1009–1010.

[70] Brixner, T.; Hildner, R.; Köhler, J.; Lambert, C.; Würthner, F. *Exciton Transport in Molecular Aggregates – From Natural Antennas to Synthetic Chromophore Systems.* Advanced Energy Materials **2017**, *7* (*16*), 1700236.

[71] Hestand, N. J.; Spano, F. C. *Expanded Theory of H- and J-Molecular Aggregates: The Effects of Vibronic Coupling and Intermolecular Charge Transfer.* Chemical Reviews **2018**, *118* (*15*), 7069–7163.

[72] Hestand, N. J.; Spano, F. C. *Molecular Aggregate Photophysics beyond the Kasha Model: Novel Design Principles for Organic Materials.* Accounts of Chemical Research **2017**, *50* (*2*), 341–350.

[73] Spano, F. C.; Silva, C. *H- and J-aggregate behavior in polymeric semiconductors.* Annual review of physical chemistry **2014**, *65*, 477–500.

[74] May, V.; Kühn, O. *Charge and energy transfer dynamics in molecular systems*; Wiley-VCH, **2023**.

[75] Hildner, R.; Köhler, A.; Müller-Buschbaum, P.; Panzer, F.; Thelakkat, M. *π-Conjugated Donor Polymers: Structure Formation and Morphology in Solution, Bulk and Photovoltaic Blends.* Advanced Energy Materials **2017**, *7* (*16*).

[76] Moix, J. M.; Khasin, M.; Cao, J. *Coherent quantum transport in disordered systems: I. The influence of dephasing on the transport properties and absorption spectra on one-dimensional systems.* New Journal of Physics **2013**, *15* (*8*), 85010.

[77] Bondarenko, A. S.; Knoester, J.; Jansen, T. L. *Comparison of methods to study excitation energy transfer in molecular multichromophoric systems.* Chemical Physics **2020**, *529*, 110478.

[78] Vlaming, S. M.; Malyshev, V. A.; Eisfeld, A.; Knoester, J. *Subdiffusive exciton motion in systems with heavy-tailed disorder.* The Journal of Chemical Physics **2013**, *138* (*21*), 214316.

[79] Baldwin, A.; Delport, G.; Leng, K.; Chahbazian, R.; Galkowski, K.; Loh, K. P.; Stranks, S. D. *Local Energy Landscape Drives Long-Range Exciton Diffusion in Two-Dimensional Halide Perovskite Semiconductors.* The Journal of Physical Chemistry Letters **2021**, *12* (*16*), 4003–4011.

[80] Davidson, S.; Pollock, F. A.; Gauger, E. *Eliminating Radiative Losses in Long-Range Exciton Transport.* PRX Quantum **2022**, *3* (*2*), 20354.

[81] Lin, H.; Camacho, R.; Tian, Y.; Kaiser, T. E.; Würthner, F.; Scheblykin, I. G. *Collective fluorescence blinking in linear J-aggregates assisted by long-distance exciton migration.* Nano Letters **2010**, *10* (*2*), 620–626.

[82] Marciniak, H.; Li, X.-Q.; Würthner, F.; Lochbrunner, S. *One-dimensional exciton diffusion in perylene bisimide aggregates.* The journal of physical chemistry. A **2011**, *115* (*5*), 648–654.

[83] Rehhagen, C.; Stolte, M.; Herbst, S.; Hecht, M.; Lochbrunner, S.; Würthner, F.; Fennel, F. *Exciton Migration in Multistranded Perylene Bisimide J-Aggregates.* The Journal of Physical Chemistry Letters **2020**, *11* (*16*), 6612–6617.

[84] Wan, Y.; Stradomska, A.; Knoester, J.; Huang, L. *Direct Imaging of Exciton Transport in Tubular Porphyrin Aggregates by Ultrafast Microscopy.* Journal of the American Chemical Society **2017**, *139* (*21*), 7287–7293.

[85] Kim, T.; Ham, S.; Lee, S. H.; Hong, Y.; Kim, D. *Enhancement of exciton transport in porphyrin aggregate nanostructures by controlling the hierarchical self-assembly.* Nanoscale **2018**, *10* (*35*), 16438–16446.

[86] Caram, J. R.; Doria, S.; Eisele, D. M.; Freyria, F. S.; Sinclair, T. S.; Rebentrost, P.; Lloyd, S.; Bawendi, M. G. *Room-Temperature Micron-Scale Exciton Migration in a Stabilized Emissive Molecular Aggregate.* Nano Letters **2016**, *16* (*11*), 6808–6815.

[87] Haedler, A. T.; Beyer, S. R.; Hammer, N.; Hildner, R.; Kivala, M.; Köhler, J.; Schmidt, H.-W. *Synthesis and photophysical properties of multichromophoric carbonyl-bridged triarylamines.* Chemistry – A European Journal **2014**, *20* (*37*), 11708–11718.

[88] Haedler, A. T.; Meskers, S. C. J.; Zha, R. H.; Kivala, M.; Schmidt, H.-W.; Meijer, E. W. *Pathway Complexity in the Enantioselective Self-Assembly of Functional Carbonyl-Bridged Triarylamine Trisamides.* Journal of the American Chemical Society **2016**, *138* (*33*), 10539–10545.

[89] Ehrenstein, G. W. *Polymeric Materials*:*Structure, Properties, Applications*; Hanser eLibrary; Hanser, Carl, **2012**.

[90] N.M. Nurazzi; M.N.F. Norrrahim; S.S. Shazleen; M.M. Harussani; F.A. Sabaruddin; M.R.M. Asyraf. *Introduction to Polymer Crystallization*. In *Polymer Crystallization*; Parameswaranpillai, J., Jacob, J., Krishnasamy, S., Jayakumar, A., Hameed, N., Eds.; John Wiley & Sons, Ltd, **2023**; pp 1–12.

[91] Saalwächter, K.; Thurn-Albrecht, T.; Paul, W. *Recent Progress in Understanding Polymer Crystallization.* Macromolecular Chemistry and Physics **2023**, *224* (*7*).

[92] Zhang, M.; Guo, B.-H.; Xu, J. *A Review on Polymer Crystallization Theories.* Crystals **2017**, *7* (*1*), 4.

[93] Guo, Q., Ed. *Polymer morphology*:*Principles, characterization, and processing*; Wiley Blackwell, **2016**.

[94] Hu, W.; Zha, L. *Thermodynamics and Kinetics of Polymer Crystallization*. In *Polymer morphology*:*Principles, characterization, and processing*; Guo, Q., Ed.; Wiley Blackwell, **2016**; pp 242–258.

[95] Zweifel, H.; Maier, R.-D.; Schiller, M., Eds. *Plastics additives handbook*, 6th ed.; Hanser Publishers; Hanser Publications, **op. 2009**.

[96] Kelton, K. F. *Crystal Nucleation in Liquids and Glasses*. In ; pp 75–177.

[97] Ehrenreich, H.; Turnbull, D., Eds. *Solid State Physics*; Academic Press, **1991**.

[98] Gedde, U. W.; Hedenqvist, M. S. *Crystallization Kinetics.* Fundamental Polymer Science **2019**, 327–386.

[99] Lindenmeyer, P. H. *Surface area and secondary nucleation theory.* Nature **1977**, *269* (*5627*), 396–397.

[100] Zhao, X.; Han, S.; Song, W.; Liu, L.; Men, Y. *Self-nucleation and heterogeneous nucleation in ethylene/1-octene random copolymer and its linear polyethylene blends.* Thermochimica Acta **2022**, *718*, 179392.

[101] Sperling, L. H. *Introduction to Physical Polymer Science*; John Wiley & Sons, **2005**.

[102] Milner, S. T. *Polymer crystal–melt interfaces and nucleation in polyethylene.* Soft Matter **2011**, *7* (*6*), 2909.

[103] Fairgrieve, S. *Nucleating Agents*; Smithers Rapra Publishing, **2007**.

[104] Wypych, G. *Handbook of Nucleating Agents*; Chemtec Publishing, **2021**.

[105] Menczel, J.; Varga, J. *Influence of nucleating agents on crystallization of polypropylene.* Journal of Thermal Analysis **1983**, *28* (*1*), 161–174.

[106] Richter, F.; Schmidt, H.-W. *Supramolecular Nucleating Agents for Poly(butylene terephthalate) Based on 1,3,5-Benzenetrisamides.* Macromolecular Materials and Engineering **2013**, *298* (*2*), 190–200.

[107] Thierry, A.; Straupé, C.; Wittmann, J.-C.; Lotz, B. *Organogelators and Polymer Crystallisation.* Macromolecular Symposia **2006**, *241* (*1*), 103–110.

[108] Abraham, F.; Kress, R.; Smith, P.; Schmidt, H.-W. *A New Class of Ultra-Efficient Supramolecular Nucleating Agents for Isotactic Polypropylene.* Macromolecular Chemistry and Physics **2013**, *214* (*1*), 17–24.

[109] Fillon, B.; Thierry, A.; Lotz, B.; Wittmann, J. C. *Efficiency scale for polymer nucleating agents.* Journal of Thermal Analysis **1994**, *42* (*4*), 721–731.

[110] Fillon, B.; Wittmann, J. C.; Lotz, B.; Thierry, A. *Self-nucleation and recrystallization of isotactic polypropylene (α phase) investigated by differential scanning calorimetry.* Journal of Polymer Science Part B: Polymer Physics **1993**, *31* (*10*), 1383–1393.

[111] Kristiansen, M.; Werner, M.; Tervoort, T.; Smith, P.; Blomenhofer, M.; Schmidt, H.-W. *The Binary System Isotactic Polypropylene/Bis(3,4-dimethylbenzylidene)sorbitol: Phase Behavior, Nucleation, and Optical Properties.* Macromolecules **2003**, *36* (*14*), 5150–5156.

[112] Shepard, T. A.; Delsorbo, C. R.; Louth, R. M.; Walborn, J. L.; Norman, D. A.; Harvey, N. G.; Spontak, R. J. *Self-organization and polyolefin nucleation efficacy of 1,3:2,4-di-p-*

methylbenzylidene sorbitol. Journal of Polymer Science Part B: Polymer Physics **1997**, *35* (*16*), 2617–2628.

[113] Mohmeyer, N.; Behrendt, N.; Zhang, X.; Smith, P.; Altstädt, V.; Sessler, G. M.; Schmidt, H.-W. *Additives to improve the electret properties of isotactic polypropylene.* Polymer **2007**, *48* (*6*), 1612–1619.

[114] Behrendt, N.; Mohmeyer, N.; Hillenbrand, J.; Klaiber, M.; Zhang, X.; Sessler, G. M.; Schmidt, H.-W.; Altstädt, V. *Charge storage behavior of isotropic and biaxially-oriented polypropylene films containing α- and β-nucleating agents.* Journal of Applied Polymer Science **2006**, *99* (*3*), 650–658.

[115] Kersch, M.; Schmidt, H.-W.; Altstädt, V. *Influence of different beta-nucleating agents on the morphology of isotactic polypropylene and their toughening effectiveness.* Polymer **2016**, *98*, 320–326.

[116] Liu, L.; Zhao, Y.; Zhang, C.; Dong, Z.; Wang, K.; Wang, D. *Morphological Characteristics of β-Nucleating Agents Governing the Formation of the Crystalline Structure of Isotactic Polypropylene.* Macromolecules **2021**, *54* (*14*), 6824–6834.

[117] Chiang, C. K.; Fincher, C. R.; Park, Y. W.; Heeger, A. J.; Shirakawa, H.; Louis, E. J.; Gau, S. C.; MacDiarmid, A. G. *Electrical Conductivity in Doped Polyacetylene.* Physical Review Letters **1977**, *39* (*17*), 1098–1101.

[118] Dang, M. T.; Hirsch, L.; Wantz, G. *P3HT:PCBM, best seller in polymer photovoltaic research.* Advanced Materials **2011**, *23* (*31*), 3597–3602.

[119] Ludwigs, S., Ed. *P3HT Revisited – From Molecular Scale to Solar Cell Devices*; Springer Berlin Heidelberg, **2014**.

[120] Berger, P. R.; Kim, M. *Polymer solar cells: P3HT:PCBM and beyond.* Journal of Renewable and Sustainable Energy **2018**, *10* (*1*).

[121] Aiyar, A. R.; Hong, J.-I.; Reichmanis, E. *Regioregularity and Intrachain Ordering: Impact on the Nanostructure and Charge Transport in Two-Dimensional Assemblies of Poly(3-hexylthiophene).* Chemistry of Materials **2012**, *24* (*15*), 2845–2853.

[122] Snyder, C. R.; Henry, J. S.; DeLongchamp, D. M. *Effect of Regioregularity on the Semicrystalline Structure of Poly(3-hexylthiophene).* Macromolecules **2011**, *44* (*18*), 7088–7091.

[123] Sheina, E. E.; Liu, J.; Iovu, M. C.; Laird, D. W.; McCullough, R. D. *Chain Growth Mechanism for Regioregular Nickel-Initiated Cross-Coupling Polymerizations.* Macromolecules **2004**, *37* (*10*), 3526–3528.

[124] Miyakoshi, R.; Yokoyama, A.; Yokozawa, T. *Catalyst-transfer polycondensation. mechanism of Ni-catalyzed chain-growth polymerization leading to well-defined poly(3-hexylthiophene).* Journal of the American Chemical Society **2005**, *127* (*49*), 17542–17547.

[125] Yamamoto, T.; Uemura, T.; Tanimoto, A.; Sasaki, S. *Synthesis and Chemical Properties of π-Conjugated Poly(imidazole-2,5-diyl)s.* Macromolecules **2003**, *36* (*4*), 1047–1053.

[126] Bronstein, H. A.; Luscombe, C. K. *Externally initiated regioregular P3HT with controlled molecular weight and narrow polydispersity.* Journal of the American Chemical Society **2009**, *131* (*36*), 12894–12895.

[127] Chavez, C. A.; Choi, J.; Nesterov, E. E. *One-Step Simple Preparation of Catalytic Initiators for Catalyst-Transfer Kumada Polymerization: Synthesis of Defect-Free Polythiophenes.* Macromolecules **2014**, *47* (*2*), 506–516.

[128] Rahimi, K.; Botiz, I.; Stingelin, N.; Kayunkid, N.; Sommer, M.; Koch, F. P. V.; Nguyen, H.; Coulembier, O.; Dubois, P.; Brinkmann, M.; Reiter, G. *Controllable Processes for Generating Large Single Crystals of Poly(3-hexylthiophene).* Angewandte Chemie **2012**, *124* (*44*), 11293–11297.

[129] Wu, Z.; Petzold, A.; Henze, T.; Thurn-Albrecht, T.; Lohwasser, R. H.; Sommer, M.; Thelakkat, M. *Temperature and Molecular Weight Dependent Hierarchical Equilibrium Structures in Semiconducting Poly(3-hexylthiophene).* Macromolecules **2010**, *43* (*10*), 4646–4653.

[130] Dudenko, D.; Kiersnowski, A.; Shu, J.; Pisula, W.; Sebastiani, D.; Spiess, H. W.; Hansen, M. R. *A strategy for revealing the packing in semicrystalline π-conjugated polymers: crystal structure of bulk poly-3-hexyl-thiophene (P3HT).* Angewandte Chemie International Edition **2012**, *51* (*44*), 11068–11072.

[131] Pascui, O. F.; Lohwasser, R.; Sommer, M.; Thelakkat, M.; Thurn-Albrecht, T.; Saalwächter, K. *High Crystallinity and Nature of Crystal−Crystal Phase Transformations in Regioregular Poly(3-hexylthiophene).* Macromolecules **2010**, *43* (*22*), 9401–9410.

[132] Singh, C. R.; Gupta, G.; Lohwasser, R.; Engmann, S.; Balko, J.; Thelakkat, M.; Thurn-Albrecht, T.; Hoppe, H. *Correlation of charge transport with structural order in highly ordered melt-crystallized poly(3-hexylthiophene) thin films.* Journal of Polymer Science Part B: Polymer Physics **2013**, *51* (*12*), 943–951.

[133] Guo, Y.; Jiang, L.; Ma, X.; Hu, W.; Su, Z. *Poly(3-hexylthiophene) monolayer nanowhiskers.* Polymer Chemistry **2013**, *4* (*16*), 4308.

[134] Ihn, K. J.; Moulton, J.; Smith, P. *Whiskers of poly(3-alkylthiophene)s.* Journal of Polymer Science Part B: Polymer Physics **1993**, *31* (*6*), 735–742.

[135] Shubham Dadhich; A. D. D. Dwivedi; Arun Kumar Singh. *Fabrication, characterization, numerical simulation and compact modeling of P3HT based organic thin film transistors.* Journal of Semiconductors **2021**, *42* (*7*), 74102.

[136] Verploegen, E.; Mondal, R.; Bettinger, C. J.; Sok, S.; Toney, M. F.; Bao, Z. *Effects of Thermal Annealing Upon the Morphology of Polymer–Fullerene Blends.* Advanced Functional Materials **2010**, *20* (*20*), 3519–3529.

[137] Verploegen, E.; Miller, C. E.; Schmidt, K.; Bao, Z.; Toney, M. F. *Manipulating the Morphology of P3HT–PCBM Bulk Heterojunction Blends with Solvent Vapor Annealing.* Chemistry of Materials **2012**, *24* (*20*), 3923–3931.

[138] Cha, W.-Y.; Lee, J.; Park, J.; Koo, Y. H.; Park, J.; Seki, S.; Kim, W.-S.; Park, J. *Poly(3-hexylthiophene) Crystalline Cubes: A Facile Preparation of Polymer Particles Featuring Long-range Ordering.* Chemistry Letters **2020**, *49* (*12*), 1494–1496.

[139] Xu, B.; Sai-Anand, G.; Unni, G. E.; Jeong, H.-M.; Kim, J.-S.; Kim, S.-W.; Kwon, J.-B.; Bae, J.-H.; Kang, S.-W. *Pyridine-based additive optimized P3HT:PC61BM nanomorphology for improved performance and stability in polymer solar cells.* Applied Surface Science **2019**, *484*, 825–834.

[140] McBride, M.; Bacardi, G.; Morales, C.; Risteen, B.; Keane, D.; Reichmanis, E.; Grover, M. A. *Control of Nucleation Density in Conjugated Polymers via Seed Nucleation.* ACS Applied Materials & Interfaces **2019**, *11* (*41*), 37955–37965.

[141] Oh, J. Y.; Shin, M.; Lee, T. I.; Jang, W. S.; Min, Y.; Myoung, J.-M.; Baik, H. K.; Jeong, U. *Self-Seeded Growth of Poly(3-hexylthiophene) (P3HT) Nanofibrils by a Cycle of Cooling and Heating in Solutions.* Macromolecules **2012**, *45* (*18*), 7504–7513.

[142] Chu, P.-H.; Kleinhenz, N.; Persson, N.; McBride, M.; Hernandez, J. L.; Fu, B.; Zhang, G.; Reichmanis, E. *Toward Precision Control of Nanofiber Orientation in Conjugated Polymer Thin Films: Impact on Charge Transport.* Chemistry of Materials **2016**, *28* (*24*), 9099–9109.

[143] Dias, Y.; Yerushalmi-Rozen, R. *Entropic effects in carbon nanotubes-templated crystallization of Poly(3-alkyl thiophenes, P3HT, P3OT).* Polymer **2013**, *54* (*23*), 6399–6405.

[144] Yang, Z.; Lu, H. *Nonisothermal crystallization behaviors of poly(3-hexylthiophene)/reduced graphene oxide nanocomposites.* Journal of Applied Polymer Science **2013**, *128* (*1*), 802–810.

[145] Acevedo-Cartagena, D. E.; Zhu, J.; Trabanino, E.; Pentzer, E.; Emrick, T.; Nonnenmann, S. S.; Briseno, A. L.; Hayward, R. C. *Selective Nucleation of Poly(3-hexyl thiophene) Nanofibers on Multilayer Graphene Substrates.* ACS Macro Letters **2015**, *4* (*5*), 483–487.

[146] Bechara, R.; Leclerc, N.; Lévêque, P.; Richard, F.; Heiser, T.; Hadziioannou, G. *Efficiency enhancement of polymer photovoltaic devices using thieno-thiophene based copolymers as nucleating agents for polythiophene crystallization.* Applied Physics Letters **2008**, *93* (*1*).

[147] Deribew, D.; Pavlopoulou, E.; Fleury, G.; Nicolet, C.; Renaud, C.; Mougnier, S.-J.; Vignau, L.; Cloutet, E.; Brochon, C.; Cousin, F.; Portale, G.; Geoghegan, M.; Hadziioannou, G. *Crystallization-Driven Enhancement in Photovoltaic Performance through Block Copolymer Incorporation into P3HT:PCBM Blends.* Macromolecules **2013**, *46* (*8*), 3015–3024.

[148] Shan, H.; He, J.; Zhu, B.; Zhou, J.; Huo, H. *Synergistic effects of ultrasonication and the addition of a nucleating agent on improving the crystallization and performance of P3HT.* Organic Electronics **2023**, *114*, 106733.

[149] Shan, H.; He, J.; Zhu, B.; Zhou, J.; Huo, H. *The role of the commercial nucleating agent HPN-68L in the stretchable and electrical properties of solvent vapor annealed P3HT.* Journal of Materials Chemistry C **2022**, *10* (*46*), 17583–17593.

[150] Treat, N. D.; Nekuda Malik, J. A.; Reid, O.; Yu, L.; Shuttle, C. G.; Rumbles, G.; Hawker, C. J.; Chabinyc, M. L.; Smith, P.; Stingelin, N. *Microstructure formation in molecular and polymer semiconductors assisted by nucleation agents.* Nature Materials **2013**, *12* (*7*), 628–633.

[151] Kiriy, N.; Jähne, E.; Adler, H.-J.; Schneider, M.; Kiriy, A.; Gorodyska, G.; Minko, S.; Jehnichen, D.; Simon, P.; Fokin, A. A.; Stamm, M. *One-Dimensional Aggregation of Regioregular Polyalkylthiophenes.* Nano Letters **2003**, *3* (*6*), 707–712.

[152] Berson, S.; De Bettignies, R.; Bailly, S.; Guillerez, S. *Poly(3-hexylthiophene) Fibers for Photovoltaic Applications.* Advanced Functional Materials **2007**, *17* (*8*), 1377–1384.

[153] Persson, N. E.; Chu, P.-H.; McBride, M.; Grover, M.; Reichmanis, E. *Nucleation, Growth, and Alignment of Poly(3-hexylthiophene) Nanofibers for High-Performance OFETs.* Accounts of Chemical Research **2017**, *50* (*4*), 932–942.

[154] Brinkmann, M.; Chandezon, F.; Pansu, R. B.; Julien-Rabant, C. *Epitaxial Growth of Highly Oriented Fibers of Semiconducting Polymers with a Shish-Kebab-Like Superstructure.* Advanced Functional Materials **2009**, *19* (*17*), 2759–2766.

[155] Liu, J.; Zou, J.; Zhai, L. *Bottom-up Assembly of Poly(3-hexylthiophene) on Carbon Nanotubes: 2D Building Blocks for Nanoscale Circuits.* Macromolecular Rapid Communications **2009**, *30* (*16*), 1387–1391.

[156] Charoughchi, S.; Agbolaghi, S.; Aghapour, S.; Sarvari, R.; Abbasi, F. *Polymer wrapping versus well-oriented crystal growth of polythiophenes onto multi-wall carbon nanotubes via surface chemical modification and regioregularity deliberation.* New Journal of Chemistry **2018**, *42* (*17*), 14469–14480.

[157] Agbolaghi, S.; Charoughchi, S.; Aghapour, S.; Abbasi, F.; Bahadori, A.; Sarvari, R. *Bulk heterojunction photovoltaics with improved efficiencies using stem-leaf, shish-kebab and double-fibrillar nano-hybrids based on modified carbon nanotubes and poly(3-hexylthiophene).* Solar Energy **2018**, *170*, 138–150.

[158] Bu, L.; Pentzer, E.; Bokel, F. A.; Emrick, T.; Hayward, R. C. *Growth of polythiophene/perylene tetracarboxydiimide donor/acceptor shish-kebab nanostructures by coupled crystal modification.* ACS Nano **2012**, *6* (*12*), 10924–10929.

[159] Zhang, X.; Yuan, N.; Ding, S.; Wang, D.; Li, L.; Hu, W.; Bo, Z.; Zhou, J.; Huo, H. *Growth and carrier-transport performance of a poly(3-hexylthiophene)/1,2,3,4-bis(p-methylbenzylidene) sorbitol hybrid shish-kebab nanostructure.* Journal of Materials Chemistry C **2017**, *5* (*16*), 3983–3992.

2 Objective

Nature achieves directed exciton energy transport in natural light-harvesting units by the precise positioning of chromophores and matrix molecules. Versatile model systems on a supramolecular level are still required to understand and manipulate exciton transport processes. In this context, this thesis aims to provide and study model systems with unique exciton energy transport characteristics. This thesis will focus on the controlled preparation as well as the morphological, structural, and optical characterization of ***supramolecular systems*** based on *carbonyl-bridged triarylamine trisamides* and ***polymer systems*** consisting of *N,N'-1,4-phenylenebis[4-pyridinecarboxamide]* and *poly (3-hexyl thiophene)*. For both systems, the delicate interplay between structural and optoelectronic as well as exciton energy transport properties will be investigated in close collaboration with the experimental physics group of Prof. Dr. Richard Hildner, University of Groningen, The Netherlands.

Supramolecular Systems

Supramolecular chemistry allows for the precise alignment of chromophores enabling the formation of structures with long-range exciton energy transport properties. In this regard, nanofibers based on *carbonyl-bridged triarylamine trisamide* derivatives have emerged as a promising artificial model system for exciton energy transport over exceptional large distances. In spite this fact, fundamental questions regarding structure-property relations with respect to the supramolecular structure and their influences on the exciton transport remain.

Therefore, the influence of the hierarchical level of supramolecular architectures on the exciton energy transport properties is in the focus of the *first part* of this thesis. In this respect, the self-assembly behavior of a supramolecular building block based on *carbonyl-bridged triarylamine trisamides* has to be explored to find self-assembly conditions to prepare single supramolecular nanofibers and bundles of supramolecular nanofibers, selectively. These two supramolecular architectures are compared regarding their morphological, structural, spectroscopical and optical properties. In cooperation with the experimental physics group of Prof. Richard Hildner, University of Groningen, the exciton energy landscapes, and the exciton energy transport dynamics of these architectures are explored.

Curiously, supramolecular aggregates based on *carbonyl-bridged triarylamine trisamides* as well as building blocks based on other large C_3-symmetric core moieties can feature a temperature-dependent inversion in their circular dichroism signal, which is usually assigned to an inversion in their helical chirality.

Therefore, the *second part* of this thesis focusses on elucidating this process. Here, the self-assembly process as well as the inversion of the circular dichroism for such a supramolecular architecture has to be explored using temperature-dependent circular dichroism, UV/vis absorption, and photoluminescence spectroscopy. In cooperation with the experimental physics group of Prof. Eva Herzig, University of Bayreuth, temperature-dependent wide-angle x-ray spectroscopy should be performed. These investigations are conducted at the Advanced Light Source, Lawrence Berkeley National Laboratory, USA. In addition, based on spectroscopic measurements conclusions should be complemented by investigations and calculations of the group of Prof. Richard Hildner, University of Groningen.

Polymer Systems

The solid state of semi-crystalline polymers can be influenced by nucleating agents. One type of nucleating agents are supramolecular nucleating agents. Here the nucleating agent is soluble in the polymer melt and self-assembles into supramolecular architectures upon cooling which can then induce the polymer crystallization. Supramolecular nucleating agents are a well-established approach to nucleate commodity polymers such as *isotactic poly (propylene)* but are rarely investigated for conjugated polymers.

In this context, the aim of the *third part* of this thesis is to investigate the concept of supramolecular nucleating agents for *poly (3-hexyl thiophene) (P3HT)*, one of the most investigated conjugated polymers. For this, supramolecular nucleating agents based on *bisamides* with peripheral *pyridine* groups will be synthesized and studied with respect to the nucleation of *P3HT*. The nucleation efficiencies and mechanism of the nucleation process should be elucidated. Furthermore, the effect of the supramolecular nucleating agents on the properties and stability of thin-films of *P3HT* should be explored.

As next step, the possibility of creating hierarchical superstructures with oriented nanofibers of *P3HT* at the micrometer scale will be explored. Therefore, a solution process needs to be tested in the *fourth part* of the thesis to establish an approach of controlling the nucleation process of *P3HT* nanofibers onto the supramolecular nucleating agents resulting in hierarchical superstructures. The formed superstructures need to be transferrable from solution to substrates. The lengths of the *P3HT* nanofibers have to be in the micrometer range to enable investigations by spatially resolved absorption and photoluminescence imaging. These experiments are conducted at the experimental physics group of Prof. Richard Hildner, University of Groningen.

The previously introduced hierarchical superstructures show unique features in their excited-state energy landscape. However, open questions regarding the controlled preparation, purification, and

transfer of such structures to substrates remain. The *fifth part* of this thesis focuses on these aspects. The self-assembly of the supramolecular nucleating agent from solution as well as the crystallization process of *P3HT* onto the nucleating agent is explored in a comprehensive manner. A purification procedure needs to be developed to remove the residual polymer without dissolving the superstructure. Further such superstructure needs to be transferred to substrates while keeping their structural integrity to enable detailed investigations of the structural and morphological features. In cooperation with the experimental physics group of Prof. Richard Hildner, University of Groningen, the spectroscopic features of isolated superstructures should be explored.

3 Synopsis

3.1 Overview of the Thesis

Delicately positioned chromophores in natural light-harvesting units can steer exciton transport towards reactive centers. The precise supramolecular interactions between the chromophores and the protein matrix in these light-harvesting units are crucial for the control of this exciton energy transport. Elucidating such exciton energy transport phenomena is hampered by a lack of robust model systems. Different approaches toward such model systems, i.e., based on supramolecular systems and polymer systems, are presented in this thesis. This work focuses on the formation, manipulation, and characterization of such model systems. With the support of the experimental physics group of Prof. Dr. Hildner, the structural and optoelectronic properties of these systems are related to their exciton energy landscape as well as exciton transport characteristics.

Key results of this thesis have been summarized in five manuscripts - three are published in peer-reviewed journals, one manuscript is under revision and the final manuscript will be submitted to an appropriate peer-reviewed journal. The general overview of the thesis is shown in **Figure 3-1**.

Supramolecular Systems

Supramolecular interactions are tailored in the *first publication* of this thesis to form distinct supramolecular architectures. Supramolecular building blocks based on *carbonyl-bridged triarylamine trisamides* are utilized to form either single supramolecular nanofibers or bundles of supramolecular nanofibers depending on the conditions of the self-assembly process. The structural and optoelectronic properties of these structures are compared, and the exciton energy transport characteristics identified.

Interestingly, supramolecular aggregates based on *carbonyl-bridged triarylamine trisamides* can feature a temperature-dependent inversion in their circular dichroism signal. This process is elucidated in the second publication of this thesis using temperature-dependent circular dichroism, UV/vis absorption, and photoluminescence spectroscopy in conjunction with temperature-dependent wide-angle x-ray spectroscopy.

Polymer Systems

Supramolecular nucleating agents are a well-established approach to nucleate commodity polymers such as *isotactic poly (propylene)* but are rarely investigated for conjugated polymers. Therefore, the third publication of this thesis introduces an approach to tailor the crystallization process of the conjugated polymer, *poly (3-hexyl thiophene)* (*P3HT*) using the supramolecular nucleating agent, *N,N'-1,4-phenylenebis[4-pyridinecarboxamide].* The nucleation mechanism is elucidated and the effects of the nucleating agent onto thin-films of *P3HT* are investigated.

This system of *P3HT* and supramolecular nucleating agent is transferred from a polymer melt process to a solution-based process in the *fourth publication*. A process is developed to form hierarchical superstructures based on supramolecular *microribbons of N,N'-1,4-phenylenebis[4-pyridinecarboxamide] and* perpendicular oriented *P3HT* nanofibers. The excited-state energy landscape of these superstructures is revealed and related to the directed crystallization approach.

In the *final publication* of this thesis, a controlled process is developed to form isolated hierarchical superstructures. Therefore, the self-assembly of the supramolecular nucleating agent and the trans-crystallization of *P3HT* are investigated in detail. In addition, a purification and transfer step is introduced to yield isolated hierarchical superstructures. Their detailed morphological and structural features are investigated.

A more detailed summary of the obtained results is presented in **sections 3.2 to 3.6**. The complete publications are given in **chapters 4**.

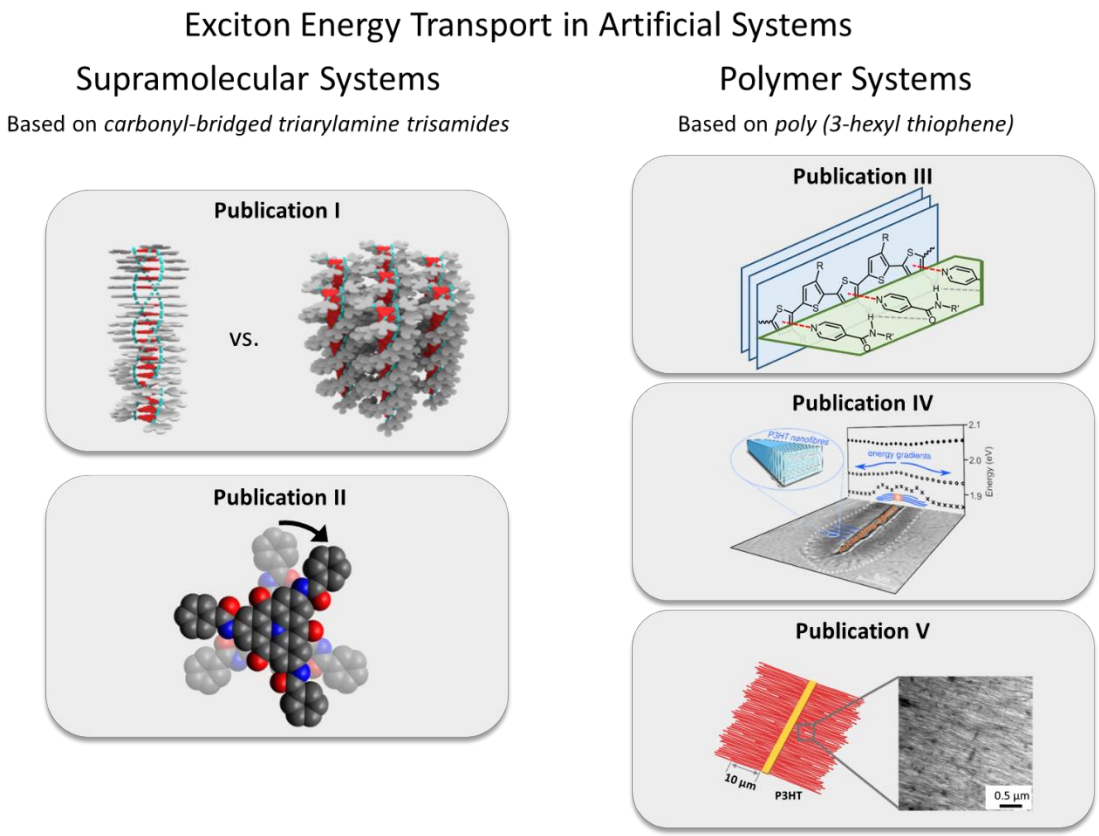

Figure 3-1: Overview of the key results of this thesis summarized into five publications. The first two publications focus on supramolecular systems based on *carbonyl-bridged triarylamine trisamides* as the central motif of the supramolecular building blocks (left). The impact of the hierarchical level on the exciton energy transport is analyzed (Publication I) and the detailed structure inside a supramolecular column is investigated (Publication II). Adapted with permission from reference II. © 2020 American Chemical Society. Polymer systems are designed and investigated in the second half of this thesis (right). First, the interaction between *poly (3-hexyl thiophene)* and the supramolecular nucleating agent, *N,N'-1,4-phenylenebis[4-pyridinecarboxamide]* is elucidated (Publication III). Reprinted with permission from reference III. © 2022 American Chemical Society. The system is transferred from bulk to solution enabling the formation of hierarchical superstructures with a continuous energy gradient in the exciton landscape (Publication IV). Adapted with permission from reference IV. © 2023 American Chemical Society. Finally, the controlled formation and isolation of such superstructures is investigated (Publication V). Reprinted with permission from reference V. © 2024 American Chemical Society.

3.2 Exciton Energy Transport in Supramolecular Architectures of Different Hierarchical Levels

In previous works at the department of Macromolecular Chemistry I, distinct C_3-symmetric building blocks of *carbonyl-bridged triarylamine* derivatives, in which a chromophoric periphery was linked via *amide* moieties to the core was successfully synthesized and analyzed. Self-assembly of these building blocks to single supramolecular nanofibers showed exceptional long-range exciton transport properties.[a] However, exciton transport through the H-aggregated cores was reported by the fluorescence of the periphery limiting detailed studies of the exciton transport characteristics. Also, no information with respect to the influence of the hierarchical levels of such aggregates were known.

In this work, we investigated the self-assembly of *carbonyl-bridged triarylamines* without fluorescent peripheries to achieve and study the impact of different supramolecular architectures, i.e., isolated, µm-long single supramolecular nanofibers and bundles of supramolecular nanofibers. In cooperation with the experimental physics group of Prof. Dr. Richard Hildner, University of Groningen, this allows us to gain insight into the exciton energy landscape and coherence properties as well as the exciton transport characteristics. The key results are published in the Journal of the American Chemical Society.[I]

As molecular building block a *carbonyl-bridged triarylamine* linked in the 2, 6 and 10 position via *amide* groups with non-chromophoric sidegroups was chosen. As bulky side groups we selected *3,4,5-tri((S)-3,7-dimethyloctyloxy) benzoic acid* resulting in the (*S*)-chiral supramolecular building block *S-CBT.* Controlled self-assembly procedures were designed and established to selectively form either single supramolecular nanofibers or supramolecular bundles of nanofibers (see **Figure 3-2**). To control the hierarchical level of the supramolecular aggregates the interaction of the supramolecular column to the solvent needs to be tailored in relation to the interactions of the supramolecular columns among each other. For the formation of single nanofibers an *aliphatic* solvent was selected to favor interactions between the *(S)-3,7-dimethyloctyloxy* groups of the peripheries with the solvent over interactions between the peripheries among each other. However, *S-CBT* is insoluble in such solvents due to the limited interactions of the amide moieties and conjugated systems of *S-CBT* with the *aliphatic* solvent. Therefore, we selected *n-dodecane* with its very high boiling temperature above 200°C allowing us to thermally force open the supramolecular interactions and, hence, control the self-assembly process. In contrast, we chose *anisole* for the formation of bundles of nanofibers. The weak polarity and π- π interactions enable

[a] Haedler, A. T.; Kreger, K.; Issac, A.; Wittmann, B.; Kivala, M.; Hammer, N.; Köhler, J.; Schmidt, H.-W.; Hildner, R. *Long-range energy transport in single supramolecular nanofibres at room temperature*. Nature **2015**, *523 (7559).*

the dissolution of *S-CBT* at lower temperatures. However, *anisole* can only weakly interact with the aliphatic *(S)-3,7-dimethyloctyloxy* groups of the peripheries resulting in the formation of bundles to reduce the interactions of the periphery with the solvent.

By using suitable self-assembly procedures, single supramolecular nanofibers can be obtained from *n-dodecane* while mostly supramolecular bundles of nanofibers are obtained in *anisole* as well as some residual monomers. The different morphologies were revealed by atomic force microscopy (see **Figure 3-2**). Here, single supramolecular nanofibers feature heights of about 2 nm which is in agreement with previous works, while bundles of nanofibers feature heights of about 100 nm corresponding to over 2000 aligned columns.

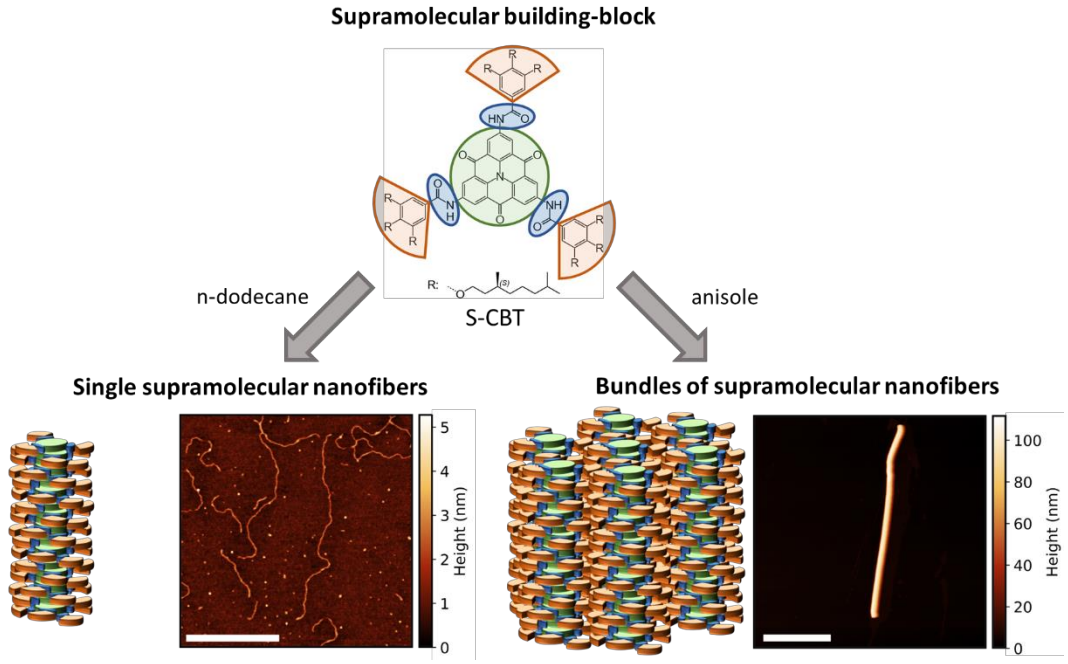

Figure 3-2: Chemical structure of the *carbonyl-bridged triarylamine trisamide* with (*S*)-chiral bulky side-groups (*S-CBT*) used to form different supramolecular structures. Self-assembly in *n-dodecane* results in the formation of single supramolecular nanofibers with heights of about 2 nm as shown in the atomic force microscopy image. In contrast, self-assembly in *anisole* results in the formation of bundles of supramolecular nanofibers with heights of about 100 nm as shown in the respective atomic force microscopy image. Reprinted with permission from reference II. © 2020 American Chemical Society.

Another important finding is that the circular dichroism spectra recorded from dispersion of the single nanofibers and the bundles of nanofibers feature the same shape indicating a similar structural arrangement inside the columns of the different architectures. This is further evidenced by identical π-π distances of 0.33 nm as probed by selected area electron diffraction performed on isolated structures. In addition, electron diffraction reveals an inter-columnar distance in the bundles of nanofiber of around 3.2 nm which is lower than the calculated diameter of 4.4 nm for the supramolecular building block with an extended conformation.

The UV/vis absorption spectra of dispersions of both supramolecular structures are shown in **Figure 3-3 A & C** (blue circles). The lowest energy absorption at around 520 nm is very weakly visible for both supramolecular architectures. For H-aggregates with strong electronic couplings, the oscillator strength of the excited states is mostly present in the higher energy bands resulting in a strongly reduced lowest energy (highest wavelength) absorption. Therefore, both aggregates show features attributed to H-aggregates with strong electronic coupling.

For H-aggregates, the lowest energy excited state has no oscillator strength, and hence emission from this state is forbidden. This can be seen in the PL spectra of the single supramolecular nanofibers (see **Figure 3-3 A**, red), where the 0-0 transition at 535 nm is mostly suppressed and predominantly the 0-1 transition at 600 nm is visible. This indicates electronic order and hence coherence in the excited states. In contrast, the PL spectrum of the bundles of nanofibers (see **Figure 3-3 C**, red) is dominated by the 0-0 transition indicating localized excited states.

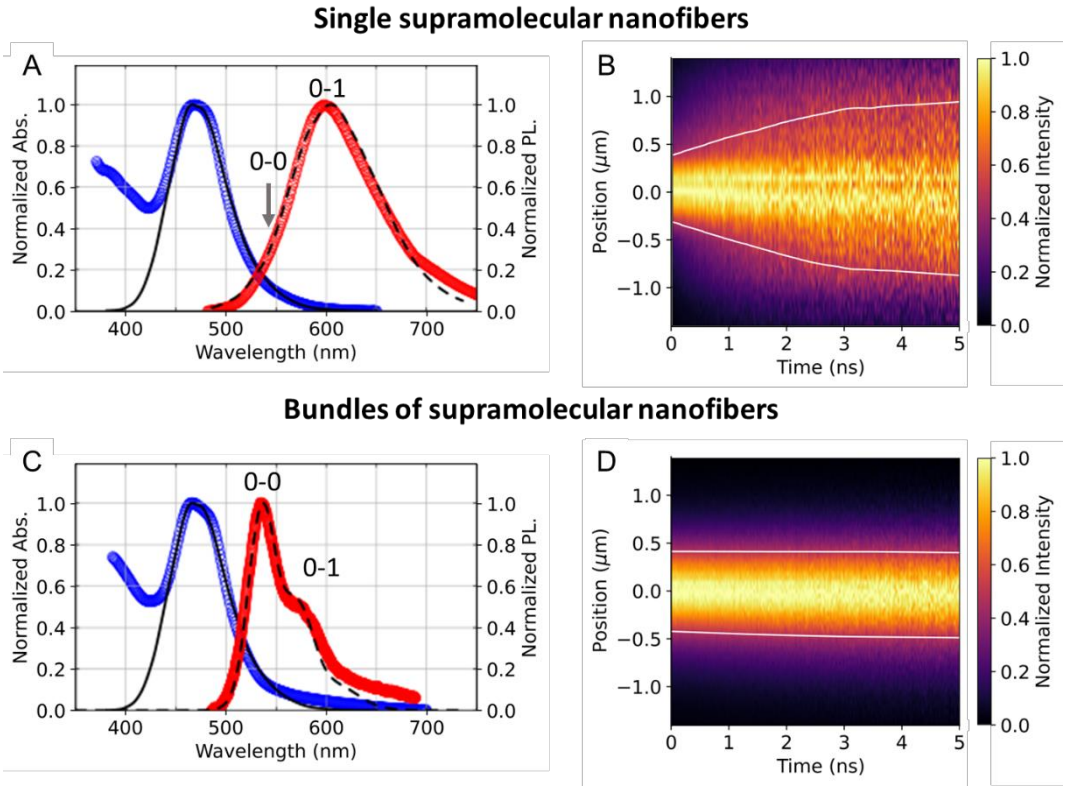

Figure 3-3: A & C) Normalized absorption (blue circles) and photoluminescence spectra (red circles) as well as numerical simulations (black lines). Single supramolecular nanofibers (top) feature high order resulting in an almost completely suppressed 0-0 transition. B & D) Normalized photoluminescence intensity evolutions over space and time relative to excitation for single supramolecular nanofibers (top) and bundles of supramolecular nanofibers (bottom). The white lines indicate the temporal evolution of the full width at half-maximum. For the single nanofibers are clear broadening of the PL over time can be observed. Reprinted with permission from reference II. © 2020 American Chemical Society.

Numerical simulations are also shown in **Figure 3-3 A & C** (black lines). They reveal a comparable electronic coupling for both architectures. The excited energy landscape of the single supramolecular nanofibers is smooth, and the excitons are delocalized on over 5 cores. In contrast, the excited energy landscape of bundles of nanofibers is rougher and the excitons are more localized. We attribute these differences to the interacting peripheries in the bundle resulting in local electronic perturbations.

These differences in the delocalization of the excitons and the uniformity of the excited energy landscape do significantly alter the exciton transport properties. In **Figure 3-3 B & D** the evolution in space and time of the normalized photoluminescence relative to the excitation is shown along a single supramolecular nanofiber (**B**) and a bundle of supramolecular nanofibers (**D**). Upon excitation, the normalized photoluminescence of the single nanofibers widens significantly visualizing the efficient transport of excitons along the nanofiber (see **Figure 3-3 B**) while the normalized photoluminescence shows only a slight widening along the bundle of nanofibers (see **Figure 3-3 D**). Based on these findings, the exciton diffusivities (D) can be calculated and were found to be up to one order of magnitude higher for the single nanofibers. The exciton diffusion for the nanofiber shown in **Figure 3-3 B** is with D = 1.03 cm^2/s the highest reported value for the diffusivity of H-aggregates in literature.

In summary, in this publication we demonstrated how the excited energy landscape in supramolecular architectures is influenced by the level of hierarchy. In bundles of nanofibers, the interacting peripheries of the supramolecular columns result in energetic disorders limiting coherence and exciton diffusion. For single nanofibers, the uniformity of the excited energy landscape results in an efficient exciton energy transport with high diffusivities. Therefore, this work provides guidelines to design H-type supramolecular architectures to achieve long-range exciton transport with tailored coherence properties.

3.3 Temperature-dependent Inversion of the Circular Dichroism in Supramolecular Aggregates

Intriguingly, supramolecular aggregates of *carbonyl-bridged triarylamine trisamides* with bulky, (*S*)-chiral side-groups, *S-CBT,* show a temperature-dependent inversion of their circular dichroism (CD) spectra.[b] Such an unexpected effect was also recently observed for other systems based on chiral, C_3-symmetric supramolecular building blocks. However, the mechanism of this inversion is under debate with several theories in discussion.

In this work, we revisited the inversion of the circular dichroism for *S-CBT* and investigated the phenomena by combining complementary methods, i.e., temperature-dependent optical and x-ray spectroscopy. In cooperation with the experimental physics groups of Prof. Eva Herzig, University of Bayreuth, and Prof. Richard Hildner, University of Groningen, we were able to provide a rational explanation for this inversion. Key results of this work are summarized in a manuscript and will be submitted to an appropriate peer-reviewed journal.[II]

*S-CBT (*see **Figure 3-2** for the chemical structure) can be self-assembled in several nonpolar solvents to nanoobjects depending on the set of conditions. For this study we selected *toluene* as solvent resulting in bundles of supramolecular nanofibers upon cooling a solution at a concentration of 100 ppm. Circular dichroism spectroscopy, which is based on the difference in left and right-handed circular polarized light , is commonly used to track the formation of supramolecular structures with chiral molecular building blocks, such as *S-CBT*, in dispersions (see **Figure 3-4**). At high temperatures where monomeric building blocks are present, no significant CD signal is observed. Upon cooling and subsequent aggregation of the *S-CBT* monomer species into twisted and helical structures, a negative cotton signature arises, which is indicative for a counterclockwise arrangement of the transition dipole moments (see **Figure 3-4**). Consequently, this signature demonstrates the formation of supramolecular aggregates with a preferred helicity and is often observed for the self-assembly of chiral building blocks. However, in the case of *S-CBT*, further cooling results in the reduction of the cotton effect until it vanishes at around 20 °C. Intriguingly, at lower temperatures, a positive cotton effect emerges, i.e. the CD signal inverts upon further cooling (see **Figure 3-4**). In this situation, that a negative cotton effect changes to a positive cotton effect, the transition dipole moments have to switch from a counterclockwise to a clockwise arrangement. Here, one is tempted to assume, that the supramolecular columns change from a left-handed to a right-handed helical structure and, hence, the observed inversion of the CD signal is attributed to an inversion of the

[b] Haedler, A. T.; Meskers, S. C. J.; Zha, R. H.; Kivala, M.; Schmidt, H.-W.; Meijer, E. W. *Pathway Complexity in the Enantioselective Self-Assembly of Functional Carbonyl-Bridged Triarylamine Trisamides*. Journal of the American Chemical Society **2016**, *138 (33),* 10539–10545.

structural helicity of the supramolecular aggregates. However, the mechanism behind this structural inversion remains unclear because it would either require significant rearrangements in the supramolecular column including the breakage of the hydrogen bonds or an extensive disassembly and reassembly process into a supramolecular structure with the opposite helicity. To explore the mechanism, we have conducted a series of experiments in the relevant temperature range including absorption and photoluminescence spectroscopy as well as x-ray spectroscopy.

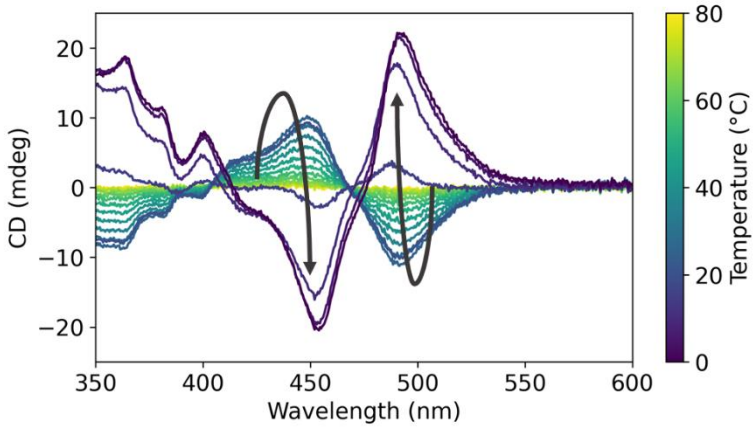

Figure 3-4: Temperature-dependent circular-dichroism (CD) spectra of supramolecular aggregates based on S-CBT upon cooling in toluene. The color code depicts the temperature. At high temperatures, no CD signal is present. Upon cooling, a negative cotton effect emerges which vanishes upon further cooling. Finally, a positive cotton effect emerges at the lowest temperatures. This process is also indicated by the black arrows.

The supramolecular aggregates of *S-CBT* feature two distinct vibronic progressions at 460 nm and 485 nm. The ratio of these two transitions (A_{485}/A_{460}) (see **Figure 3-5**, blue triangles) is directly linked to the magnitude of the electronic Coulomb coupling in the system. An increase in this ratio is observed for temperatures below 20°C indicating a reduction in the electronic coupling upon cooling. In fact, the electronic coupling decreases between 20°C and 0°C by about 20% which can be only caused by changes in the distance between the building blocks, i.e. the π-π distance, or changes to the respective orientation of the building blocks.

As shown in detail in Publication I, supramolecular bundles of nanofibers feature an emission with a maximum at about 545 nm. The progression of the relative PL intensity at 545 nm is plotted in **Figure 3-5**, (red circles) and shows only minor variations between 80°C and 20°C. Further cooling results in a steep decrease in the PL intensity attributed to a reduction in the structural disorder of the supramolecular aggregates leading to a significant reduction in the radiative rates of the emission for these H-aggregates. In addition, the PL spectra show a continuously decreasing signal at 480 nm upon cooling caused by molecularly dissolved *S-CBT*, indicating a continuous decrease in the concentration of molecular dissolved *S-CBT* which provides no evidence for a disassembly

process below 20°C. The photoluminescence at 545 nm (red circles) and the ratio of the absorption at 485 nm and 460 nm (blue triangles) are shown in **Figure 3-5** together with the CD intensity at 490 nm (green squares). Remarkably, all spectroscopic data show significant changes between 10 °C and 20 °C (indicated by the dashed grey lines), the temperature range where the inversion of the CD signal occurs.

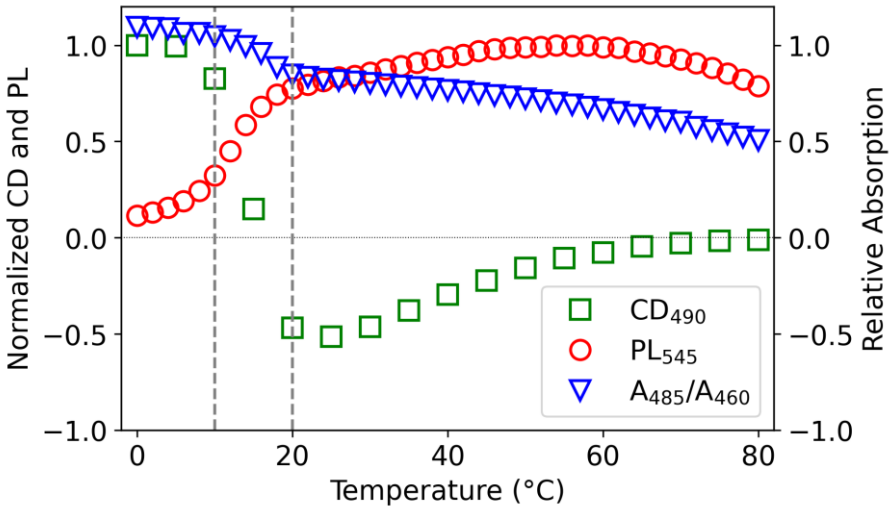

Figure 3-5: Normalized temperature-dependent circular-dichroism at 490 nm (green squares) and normalized photoluminescence at 545 nm (red circles) as well the ratio of the absorption at 485 nm and 460 nm (blue triangles) for a dispersion of *S-CBT* upon cooling. All optical properties show significant changes between 10 °C and 20 °C (indicated by the dashed grey lines) when the inversion of the CD intensity occurs.

To elucidate structural changes during cooling, we performed temperature-dependent wide-angle x-ray scattering at the Advanced Light Source, Lawrence Berkeley National Laboratory, USA. The bundles of supramolecular nanofibers feature a hexagonal packaging where the intercolumnar distance between the individual nanofibers is smaller than the diameter of a fully extended *S-CBT* molecule. Hence, the sidegroups of the molecules interact with each other, which is in agreement with our previous work. Upon cooling, the intercolumnar distance and the π-π distance between the molecules show only thermal contraction. We found that the π-π distance decreases by 0.5 % between 50°C and 10°C, which should be accompanied by an increase of the electronic coupling – the opposite effect compared to the observed changes based on the absorption spectroscopy. Therefore, the reduction of the electronic coupling, retrieved from the absorption spectra, can only be caused by a change in the orientation between the transition dipole-moments and hence, by a change in the rotational angle of the *S-CBT* molecules in a column. As the electronic coupling depends on the cosine of the rotational degree, a decrease of the coupling by 20% can be caused by relatively small rotational angle change between two S-CBT molecules of about 10°.

To provide a rational explanation for the findings of the CD experiments, one has to note that the CD signal relates to the orientation of the transition dipole moments of the chromophores, which is in our case the *carbonyl bridged triarylamine* core. Importantly, C_3-symmteric discotic chromophores features two degenerate and perpendicular oriented transition dipole moments. For *S-CBT* this results in an electronically C_4-symmetric helical chirality with a critical angle at 45°. Even small changes in the rotational angle passing this critical angle result in an inversion of the electronic chirality (see **Figure 3-6**) explaining the inversion of the CD signal. Notably, as known for the well-investigated class of *1,3,5-benzenetricarboxamides*, the *S-CBT* molecules are held together by three helical strands of hydrogen bonds formed by the three amide groups of the *S-CBT*. Since all amide groups are tilted in one direction, the thermal compression of the discotic molecules can only perform a rotational movement in the same direction, e.g., from 40° to 50°. Such a small rotation would not result in major structural changes as the structural chirality would stay unchanged which agrees with the wide-angle x-ray scattering data.

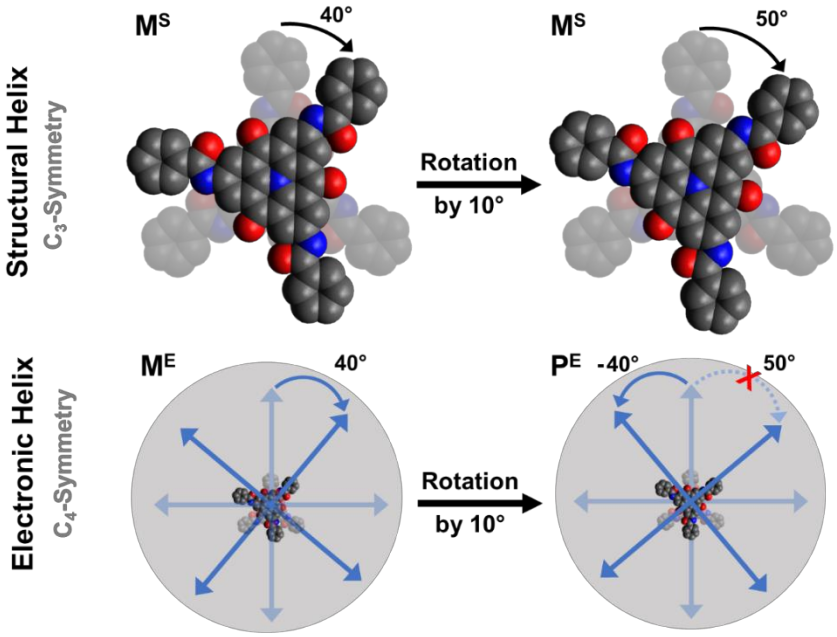

Figure 3-6: Sketch of the structural (top) and electronic chirality (bottom) for supramolecular aggregates based on *S-CBT* with rotational degrees of 40° (left) and 50° (right). Changing the rotational degree by just 10° from 40° to 50° results in no change in the structural chirality - in both cases an M helix is present. However, the same change results in an inversion of the electronic chirality from an M to a P helix because the critical angle for a C_4-symmetric structure of 45° is passed.

In summary, in this publication we showed that the temperature-dependent inversion of the CD signal is caused by slight changes in the rotational angle resulting in an inversion of the electronic chirality, which does not relate to an inversion in the structural chirality of the aggregates.

3.4 Supramolecular Nucleating Agents for Poly(3-hexyl thiophene)

In a previous work at the department of Macromolecular Chemistry I, supramolecular building blocks based on *benzene* and *cyclohexane* with different *amide* linkages and *pyridine* sidegroups *were* studied as supramolecular nucleating agents for the well-investigated conjugated polymer, *poly (3-hexyl thiophene)* (*P3HT)*.[c] It was found that only the C_2-symmetric building blocks, i.e., based on modifications in the 1 and 4 positions of benzene and cyclohexane that are linked to peripheral 4-*pyridine* sidegroups showed high efficiencies as supramolecular nucleating agents. However, only limited information regarding the mechanism of the nucleation and the effects of the supramolecular nucleating agents on the solid-state morphology were known.

In this work, we present how *N,N'-1,4-phenylenebis[4-pyridinecarboxamide]* is acting as supramolecular nucleating agent for *P3HT* and elucidate details of the nucleation mechanism. Therefore, we combined microscopy and differential scanning calorimetry together with structure elucidation performed by the inorganic chemistry group of Prof. Jürgen Senker, University of Bayreuth. We deviate a general design approach for supramolecular nucleating agents for conjugated polymers and explore the effects of the nucleating agent on optical properties of *P3HT*-based thin-films in cooperation with the experimental physics group of Prof. Dr. Richard Hildner, University of Groningen, and on the charge-carrier mobility. Key results of this work are published in *Macromolecules*.[III]

The molecular design of the supramolecular nucleating agent, *N,N'-1,4-phenylenebis[4-pyridinecarboxamide]* (NA **1,** see **Figure 3-7**), combines the C_2-symmetrical *1,4-benzene bisamide* as the core with peripheral *4-pyridine* units. Supramolecular building blocks of *1,4-benzene bisamide* can form oriented strands of hydrogen bonds resulting in platelets or ribbon-like structures with at least two opposite surfaces with outward-facing peripheries. We chose *4-pyridine* units as the periphery due to their potential to give rise to attractive acceptor-donor interactions with the *thiophene* cores of the polymer, i.e., *P3HT*.

[c] Welz, H. *Morphology control of poly(3-hexylthiophene) with tailored supramolecular nucleating agents*, Dissertation, Universität Bayreuth **2020**.

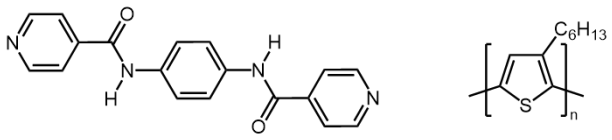

NA **1** P3HT

Figure 3-7: Chemical structure of *N,N'-1,4-phenylenebis [4-pyridinecarboxamide]* (NA **1**, left) and *poly (3-hexyl thiophene)* (*P3HT*, right). The molecular design of NA **1** combines *1,4-benzenebisamide* as the symmetry-defining core and for directed hydrogen bonds with *4-pyridine* units as peripheries to ensure attractive interactions with the thiophene cores of *P3HT*.

The operating principle of supramolecular nucleating agents in the polymer bulk relies on a multi-step mechanism. Upon melting and further heating the polymer, the supramolecular nucleating agent dissolves in the polymer melt ensuring a homogenous distribution, which we could observed via temperature-dependent polarized light microscopy. Upon cooling, the dissolved supramolecular building blocks self-assemble into small but solid structures in the melt. This is indicated by small but distinct exothermic features in the differential scanning calorimetry cooling curves of *P3HT* with different amounts of NA **1** between 240°C and 270°C shown in **Figure 3-8 A**. In addition, polarized light microscopy of similarly prepared samples do not show the formation of birefringent structures at these temperatures, indicating the formation of very small aggregates.

Initiating polymer crystallization without nucleating agents relies on the formation of nuclei of above a critical size, which requires a distinct activation energy and thus typically supercooling of the melt. Heterogeneous nucleating agents reduces this energetic barrier, which is accomplished by offering epitaxial surfaces for the polymer resulting in a polymer crystal growth at higher temperatures. This effect is shown in **Figure 3-8 B** for different concentrations of NA **1** in *P3HT*. The red curve at the bottom of the graph shows the crystallization of neat *P3HT* taking place below 200°C. The addition of different amounts of NA **1** to *P3HT* significantly increases the crystallization temperature, which is visible by a shift of the exothermic crystallization peak to higher temperatures, even at very low concentrations. Comparing the efficiency of NA **1** with the ideal nucleation sites, which is known as self-nucleation, i.e., very small crystallites of *P3HT* (see top red curve in **Figure 3-8 B**), NA **1** achieves outstanding nucleation efficiencies of 98% for a concentration of just 0.1 wt % - the highest reported value for the nucleation of *P3HT*.

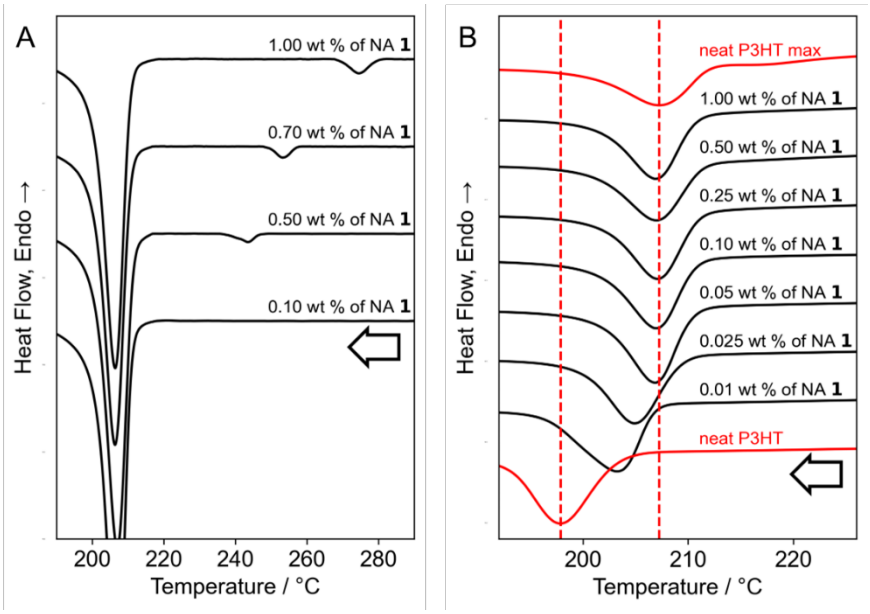

Figure 3-8: A) Differential scanning calorimetry cooling curves of *P3HT* with different concentrations of NA **1**. All samples show an exothermic peak at 207°C due to the crystallization of *P3HT*. The samples with high concentrations of NA **1** have a weak but distinct exothermic peak at high temperatures caused by the aggregation of NA **1**. B) Differential scanning calorimetry cooling curves of *P3HT* with different concentrations of NA **1** (black lines). In addition, the cooling curve of neat P3HT as a reference and for self-nucleated *P3HT*, which corresponds to the maximal achievable crystallization temperature, are shown (red lines). With increasing concentrations of NA **1**, the crystallization rapidly shifts close to the maximum. Reprinted with permission from reference III. © 2022 American Chemical Society.

Within this research, we were able to correlate this outstanding nucleation efficiency to the crystal structure of NA **1**. The periodic distance of *P3HT* along the polymer backbone has an almost 99% match to the periodic distance of NA **1** between neighboring nitrogen atoms of the *pyridine* units. In other words, the nitrogen atoms of the *pyridine* moieties do almost perfectly fit into every second *thiophene* unit along the *P3HT* polymer backbone. To get a deeper insight, we designed structurally very similar supramolecular building blocks based on *1,4-benezene bisamide* with *benzene* and *cyclohexane* peripheries featuring the same epitaxial match. However, these reference structures did show no or only very low nucleation efficiencies even at very high concentrations of 1 wt %. Consequently, the efficiency cannot simply be attributed to an epitaxial match. Therefore, we concluded that the combination of the epitaxial match together with attractive donor-acceptor interactions is essential to achieve supramolecular nucleation agents with outstanding nucleation efficiencies for conjugated polymers (see **Figure 3-9**).

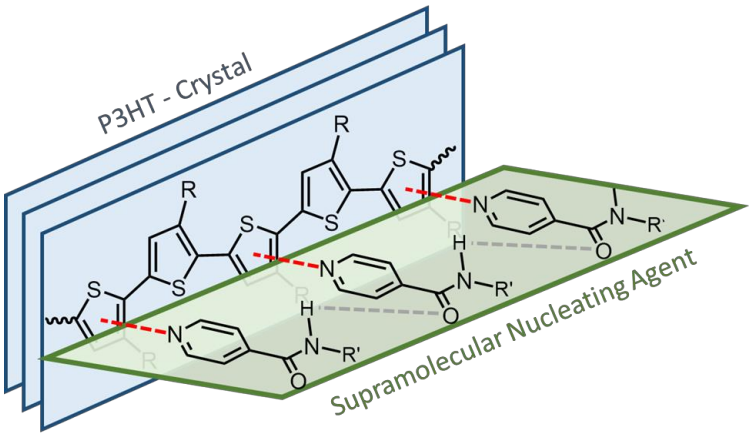

Figure 3-9: Schematic representation of the interaction between NA **1** and *P3HT*. The hydrogen bonds mediated (dashed grey lines) supramolecular structures of the nucleation agent (green) feature regular outwards facing *4-pyridine* units on its surface. Due to the epitaxial match, the distance between the *nitrogen* atoms of the *pyridine* units almost perfectly matches with every second thiophene core. The dashed red lines indicate the resulting attractive interactions due to the acceptor-donor behavior. The combination of epitaxial match and regular attractive interactions results in outstanding nucleation efficiency. Reprinted with permission from reference III. © 2022 American Chemical Society.

As this design concept requires epitaxy and attractive interactions between the nucleating agent and the polymer, we can directly transfer it towards other *poly (alkyl thiophenes)* as the relevant periodic distances and the type of the *thiophene* array and appearance in the crystals is the same Thus, we were able to show that NA **1** can efficiently nucleate *poly (3-butyl thiophene)* and *poly (3-octyl thiophene)* with nucleation efficiencies over 90% showing the potential of this approach.

The addition of NA **1** does influence the nucleation step of the *P3HT* crystallization and, hence, the final solid-state morphology. This was evidenced by spatially resolved photoluminescence spectroscopy for which thin-films of *P3HT* with and without NA **1** were prepared and measured. Importantly, the addition of NA **1** does not result in spectroscopic inhomogeneities of the thin-films and no trap states were induced. We also determined charge-carrier mobilities in thin films in organic field effect transistor geometry before and after aging for four weeks at room-temperature. Importantly, the charge carrier mobility of thin-films of P3HT containing NA **1** showed no changes upon aging while the sample without NA1 significantly deteriorates.

In essence, this work presents an approach to realize efficient supramolecular nucleating agents for conjugated polymers, i.e. *P3HT*, by combining epitaxy with regular attractive interactions. This concept can be transferred to other *poly (3-alkyl thiophenes)* resulting in outstanding nucleation efficiencies. It is therefore expected that this approach can be used to realize supramolecular nucleating agents for other semi-crystalline conjugated polymers.

3.5 Excited-State Energy Landscape of Poly(3-hexyl thiophene)-based Superstructures

Controlling the crystallization process of *poly(3-hexyl thiophene)* (*P3HT*) into nanofibers is known to result in a defect-fractionation within the nanofibers rendering those to a fundamentally very interesting model system.[d] However, a detailed investigation of this effect is limited either to very small scales of the crystalline objects or by the random distribution of the nanofibers during the deposition process. In this context, nucleating agents can be beneficially used, because the solid objects provide a predefined starting point for the polymer crystallization process. This allows for a precise control of the crystallization-driven defect-fractionation and to realize single mesoscale superstructures required for spatially resolved photophysical characterizations. Previous works at the department of Macromolecular Chemistry I showed the potential of achieving such structures using the supramolecular nucleating agent *N,N'-1,4-phenylenebis[4-pyridinecarboxamide]* (NA **1**) and solutions of *poly(3-hexyl thiophene)* (*P3HT*).[c]

In this work, the approach of using supramolecular nucleating agents to control the crystallization of *P3HT* is transferred from the melt to solution resulting in the formation of hierarchical superstructures consisting of a central supramolecular ribbon of NA **1** and perpendicular grown nanofibers of *P3HT.* The excited-state energy landscape of such superstructures is described by the experimental physics group of Prof. Dr. Richard Hildner, University of Groningen, and related to structural investigations. The key results of this work are published in the *Journal of the American Chemical Society*.

As shown in the previous part, the supramolecular nucleating agent *N,N'-1,4-phenylenebis[4-pyridinecarboxamide]* (NA **1**) can efficiently nucleate the crystallization of *poly(3-hexyl thiophene)* (*P3HT*) from the melt. However, the resulting superstructures consisting of the supramolecular aggregates of NA **1** and nucleated nanofibers of *P3HT* are formed within the bulk of the *P3HT* and can, therefore, not be easily distinguished from the semi-crystalline *P3HT* microstructure nor isolated. Thus, a transfer of the trans-crystallization concept from a bulk-based approach to a solution-based approach has to be developed. Such a solution-based approach was initially evaluated by temperature-dependent UV/vis absorption spectroscopy using solutions of dissolved *P3HT* in *chlorobenzene* with and without solid objects of NA **1**. Upon cooling, *P3HT* starts to aggregate resulting in a change in its absorption spectrum. Importantly, this change occurs at higher

[c] Welz, H. *Morphology control of poly(3-hexylthiophene) with tailored supramolecular nucleating agents*, Dissertation, Universität Bayreuth **2020**.

[d] Roehling, J. D.; Arslan, I.; Moulé, A. J. *Controlling microstructure in poly(3-hexylthiophene) nanofibers*. Journal of Material Chemistry **2012**, *22* (6), 2498–2506.

temperatures for the samples with solid objects of NA **1** present indicating that the epitaxial surface of NA **1** can also initiate the crystallization of *P3HT* from solution.

Based on these results, a two-step self-assembly process was designed (see **Figure 3-10**). At first, NA **1** is self-assembled via a heating and cooling process in *chlorobenzene* into supramolecular ribbons (see **Figure 3-10 A & B**). By adding and dissolving *P3HT,* supramolecular structures of NA **1** can subsequently nucleate the crystallization of *P3HT* from solution at room temperature (see **Figure 3-10 C**). During aging, hierarchical superstructures are formed consisting of a supramolecular ribbon of NA **1** in the center and perpendicular-oriented *P3HT* nanofibers of about 5 µm. The dispersion can then be deposited onto substrates yielding hierarchical superstructures embedded in a film of the residual P3HT (see **Figure 3-10 D**).

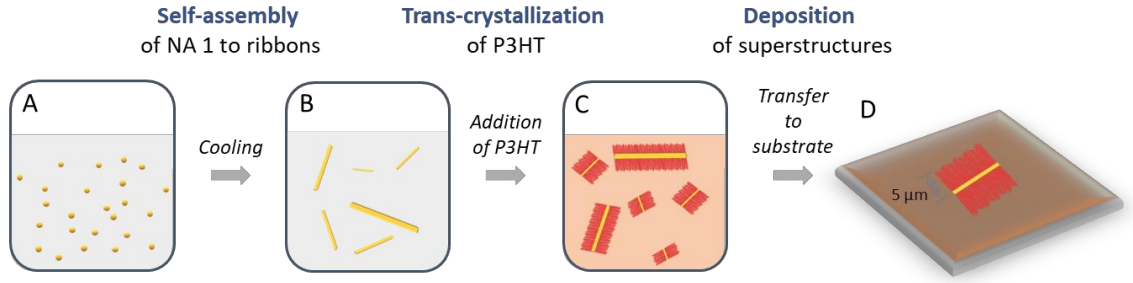

Figure 3-10: Schematic overview of the two-step self-assembly process to form hierarchical superstructures with oriented *P3HT* nanofibers. At first, *N,N'-1,4-phenylenebis [4-pyridinecarboxamide]* (NA **1**, yellow) at elevated temperatures in *chlorobenzene* (A) is cooled to self-assemble NA **1** into supramolecular ribbons (B). *P3HT* is added and dissolved to the dispersion and trans-crystallization of *P3HT* (red) occurs onto the ribbons forming hierarchical superstructures (C). The dispersion can be deposited onto substrates to yield hierarchical superstructures embedded in a film of residual *P3HT* (D).

A key parameter of this process is the choice of solvent. Here, we selected chlorobenzene as *solvent*. The solubility of NA **1** in chlorobenzene at room temperature is very low but the relatively high boiling point of *the solvent* allows to dissolve low concentrations of NA **1** at high temperatures. Consequently, this allows to form supramolecular structures of NA **1** in form of micro ribbons upon cooling. *Chlorobenzene* is also able to dissolve *P3HT* at only slightly elevated temperatures, hence, the crystallization of *P3HT* from solution occurs slowly over multiple days. This low crystallization speed allows for a high control over the superstructure formation process, that is, the nucleation and crystallization of *P3HT* nanofibers onto the surface of micro ribbons of NA **1**. Importantly, the *P3HT-chlorobenzene* system is fairly dynamic at these conditions, resulting in a controlled crystal growth process, in which the *P3HT* chains with the lowest number of defects incorporate into the growing *P3HT* nanofibers first. During aging, polymer chains with increasingly more defects are incorporated into the *P3HT* nanofibers of the growing superstructure.

Light microscopy reveals the composition of the superstructure with the supramolecular ribbon of NA **1** in the center and perpendicularly grown *P3HT* nanofibers of about 5 µm in length to both sides (see **Figure 3-11 A**) of the microribbon. Spatially resolved absorption and photoluminescence spectra at various positions were measured. Exemplary, three positions with different distances to the central ribbon are marked in **Figure 3-11 A.** The absorption spectra (see **Figure 3-11,** continuous lines in **B**) at the three positions show the same general shape. The structured absorption in the low energy region is caused by the aggregated polymer and the broad absorption in the high energy region is caused by the amorphous part of the structure. However, the relative intensity of the highest-energy absorption (depicted as A_1 in **Figure 3-11 B**) decreases with increasing distance from the central supramolecular ribbon.

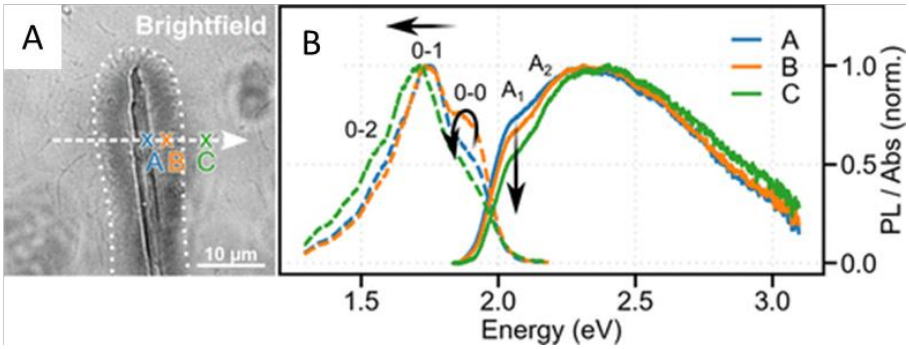

Figure 3-11: A) Brightfield light microscopy image of a hierarchical superstructure embedded in a film of *P3HT*. The dotted line indicates the length of the *P3HT* nanofibers. B) Normalized absorption (continuous lines) and photoluminescence spectra (dashed lines) at three positions (marked in A) with different distances to the central ribbon. The first absorption peak decreases with increasing distance to the central ribbon as indicated by the right arrow. The relative intensity of the 0-0 photoluminescence peak indicates changes in the disorder. Reprinted with permission from reference IV. © 2023 American Chemical Society.

We found that the free exciton bandwidth varies continuously and thus the Coulomb interaction between the polymer chains must do so, too. However, spatially resolved selected area electron diffraction (SAED) of a similarly prepared superstructure reveals no variations in the π- π distance between the aggregated *P3HT* backbones. Therefore, the change in the Coulomb interaction is attributed to an increasingly pronounced exciton localization on a single polymer chain, which occurs increasingly when moving away from the microribbon. This change in exciton localization can be attributed to an increasing number of defects, which is increasingly incorporated in the crystalline P3HT nanofiber structure during the directed crystallization of the superstructure formation.

The photoluminescence spectra (see **Figure 3-11 B**, dashed lines) show a partially suppressed highest energy peak (0-0) typically found for H-aggregates. However, variations in the relative intensity of the 0-0 peak dependent on the position along the nanofiber length are visible. The

increase of the relative intensity from spot A to B is in line with an increased disorder as mentioned above. To visualize the resulting exciton energy landscape, 40 spectra along the white dashed arrow in **Figure 3-11 A** were recorded and evaluated (see **Figure 3-12**).

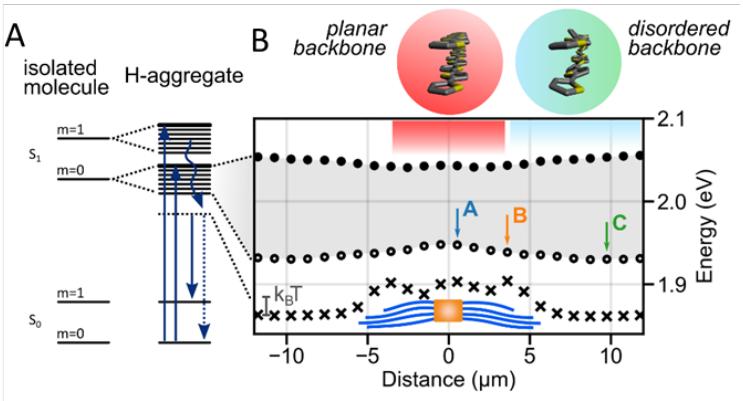

Figure 3-12: A) Energy level scheme for an isolated molecule (left) and an H-aggregate (right). The straight arrows indicate absorption and emission while the curved arrow indicates relaxation. B) Exciton energy landscape of a hierarchical superstructure. The lowest energy vibronic state is colored in grey with the upper and lower limit indicated with filled and open circles, respectively. Emission in the system occurs from the torsional relaxed, lowest-energy exciton state indicated by crosses. The data points stem from spatially resolved absorption and photoluminescence spectra and the position from **Figure 3-11** are indicated. The lower edge of the exciton band shows a continuous decrease with increasing distance to the central ribbon of NA **1** of about 20 meV. Reprinted with permission from reference IV. © 2023 American Chemical Society.

Most importantly, the maximum of the lower exciton band can be found at the supramolecular ribbon and with increasing distance to it, the energy level of the lower limits continuously decreases until it levels off. This energy gradient roughly amounts to the thermal energy at room temperature (k_BT) and is continuously stretched over multiple micrometers. We can attribute this energy gradient to a systematic decrease in the chain planarity and hence an increase in disorder. Importantly, we find such systematic variations along the whole width of the superstructure.

In conclusion, in this publication we presented for the first time an elegant approach to form hierarchical superstructures with a continuous gradient in the excited-state energy landscape over several micrometers. The observation of this gradient was only possible by establishing a well-defined starting point for the crystallization of *P3HT* into highly oriented nanofibers with increasing number of defects by a crystallization-driven defect-fractionation We envision that this approach can be transferred to other superstructures based on semi-crystalline conjugated polymers and supramolecular nucleating agents to realize long-range directed exciton energy transport.

3.6 Isolated Hierarchical Superstructures based on Poly(3-hexyl thiophene)

The previous part demonstrated an intriguing approach to realize hierarchical superstructures based on the supramolecular nucleating agent, *N,N'-1,4-phenylenebis[4-pyridinecarboxamide]* (NA **1**), and *P3HT*, which features an intrinsic energy gradient in the excited-state energy landscape.[IV] However, these superstructures are still embedded in a film of residual *P3HT* hampering structural investigations and further modifications. Moreover, full control over the two-step self-assembly process was not yet demonstrated.

In this work, we investigated the controlled formation of such hierarchical superstructures in detail. Further, a new purification step is introduced enabling detailed morphological and structural investigations. In cooperation with the experimental physics group of Prof. Dr. Richard Hildner, University of Groningen, the spectroscopic features of isolated superstructures are investigated. Key results of this work are published in *Macromolecules*. [V]

The two-step self-assembly towards hierarchical superstructures as schematically depicted in **Figure 3-13** is based on the process shown in the previous chapter. A first major difference is that self-assembly of NA **1** to supramolecular ribbons is now controlled via heating and cooling process employing an *in-situ* seeded-growth approach in *chlorobenzene* (see **Figure 3-13 A & B**). Subsequently, dissolved *P3HT* is added and the formation of highly oriented *P3HT* nanofibers is controlled in a way to yield nanofibers exceeding 20 µm in length onto the surface of NA **1** (see **Figure 3-13 C**). The superstructures are then purified by removing the excessive *P3HT* of the dispersion without disassembling the superstructures significantly. Finally, the superstructures are transferred to substrates yielding isolated hierarchical superstructures where the structural integrity remains intact. (see **Figure 3-13 D & E**)

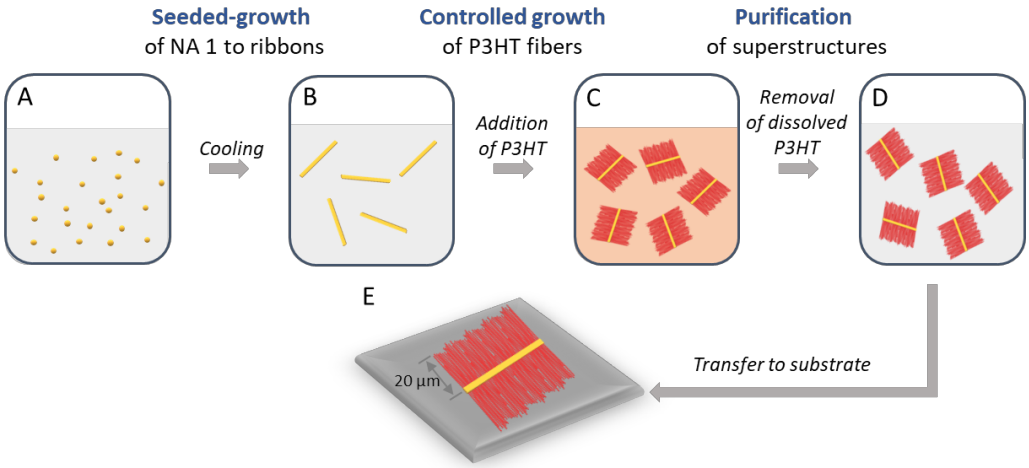

Figure 3-13: Schematic overview of the controlled two-step self-assembly and purification process to form hierarchical superstructures with oriented *P3HT* nanofibers. At first, *N,N'-1,4-phenylenebis [4-pyridinecarboxamide]* (NA **1**, yellow) at elevated temperatures in *chlorobenzene* (A) is cooled to self-assemble NA **1** into well-defined supramolecular ribbons (B). *P3HT* is added and dissolved to the dispersion and trans-crystallization of *P3HT* (red) occurs onto the ribbons forming hierarchical superstructures (C). Finally, the excessive, dissolved *P3HT* is removed, and the purified hierarchical superstructures can be redispersed (D) and transferred to substrates to yield isolated superstructures (E). Adapted with permission from reference V. © 2024 American Chemical Society.

The self-assembly of NA **1** is analyzed via temperature-dependent UV/vis absorption spectroscopy. For a concentration of 20 ppm the self-assembly behavior can be well described via a cooperative mechanism with an enthalpy of aggregation of about -59 kJ/mol and a critical temperature of about 94°C. This can also be regarded as a nucleation-elongation mechanism and can be used to tailor the number and size of the formed structures by controlling the number of seeds. We achieve this using an incomplete dissolving step for a given concentration at elevated temperatures. Upon heating the dispersion of NA **1** in *chlorobenzene* to a specific maximal temperature, NA **1** dissolves to a large extent, while some aggregates remain intact. These aggregates can act as seeds upon cooling and the number of seeds can, hence, determine the length of the final formed aggregates.

In the next step, the crystallization of dissolved *P3HT* in chlorobenzene on the surface of the supramolecular ribbons of NA **1** is initiated. The crystallization process of *P3HT* is monitored and evaluated over the range of hours to weeks. Here, the length of these nanofibers can be controlled by the aging time of the system reaching a remarkable fiber length of more than 20 µm (see **Figure 3-14 A**). Notably, under these conditions even after 50 days of trans-crystallization only a small amount of the P3HT in the system is crystallized. Most of the *P3HT* in the samples is not aggregated, i.e., either dissolved *or located in the* amorphous domains between the crystalline *P3HT* fibers in the superstructures. Upon drop-casting or spin-coating such a dispersion, the superstructures are embedded in a film microcrystalline *P3HT* hampering detailed investigations (see **Figure 3-14 A**).

Subsequently, a purification and isolation procedures is established comprising a filtration and washing step of the superstructure with *chlorobenzene* to remove almost the entirety of the remaining dissolved *P3HT*. The superstructures can then be redispersed in *chlorobenzene without re-dissolving the aggregated P3HT*. As analyzed by absorption spectroscopy, the purified superstructures comprise almost 30% of crystalline *P3HT* (see **Figure 3-14 B**). These superstructures can then be transferred to different substrates resulting in isolated superstructures. (see **Figure 3-14 C**). A significant feature of isolated superstructures is the strong increase in contrast when observed between crossed polarizers (compare **Figure 3-14 A** and **C**).

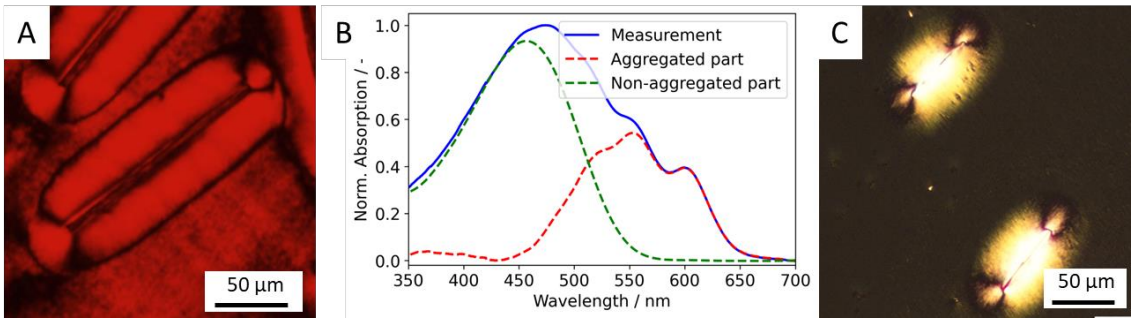

Figure 3-14: A) Polarized light microscopy image of a hierarchical superstructure embedded in a film of residual *P3HT*. B) Normalized absorption spectrum of a purified superstructure dispersion including fits of the aggregated and non-aggregated part. After purification almost 30% of the *P3HT* in the sample is aggregated. C) Polarized light microscopy image of isolated hierarchical superstructures. Importantly, such superstructures feature a significantly enhanced contrast (compare to A) under crossed polarizers as they are not embedded in a microcrystalline *P3HT* film. Adapted with permission from reference V. © 2024 American Chemical Society.

Performing selected area electron diffraction on isolated superstructures reveal that close to the initial *P3HT* crystallization point, the lattice planes of the NA **1** and of the *P3HT* nanofibers features the same direction indicating a direct contact plane between NA **1** and *P3HT.* Intriguingly, transmission electron microscopy images along the *P3HT* nanofibers are highly oriented. In **Figure 3-15** transmission electron microscopy images at different distances to the supramolecular ribbon (the dark structure on the left part of **Figure 3-15 A**) are shown. Especially in **Figure 3-15 B**, the dense nanofibers and their high alignment can be seen. We utilized an algorithm[e] to fit the orientation of the nanofiber. The resulting orientation parameter of the nanofibers in such images reveals an almost perfect alignment with values above 0.9 over distances up to 15 µm. (see **Figure 3-15 E**)

[e] Persson, N. E.; McBride, M. A.; Grover, M. A.; Reichmanis, E. *Automated Analysis of Orientational Order in Images of Fibrillar Materials*, Chemistry of Materials **2017**, *29*, 3.

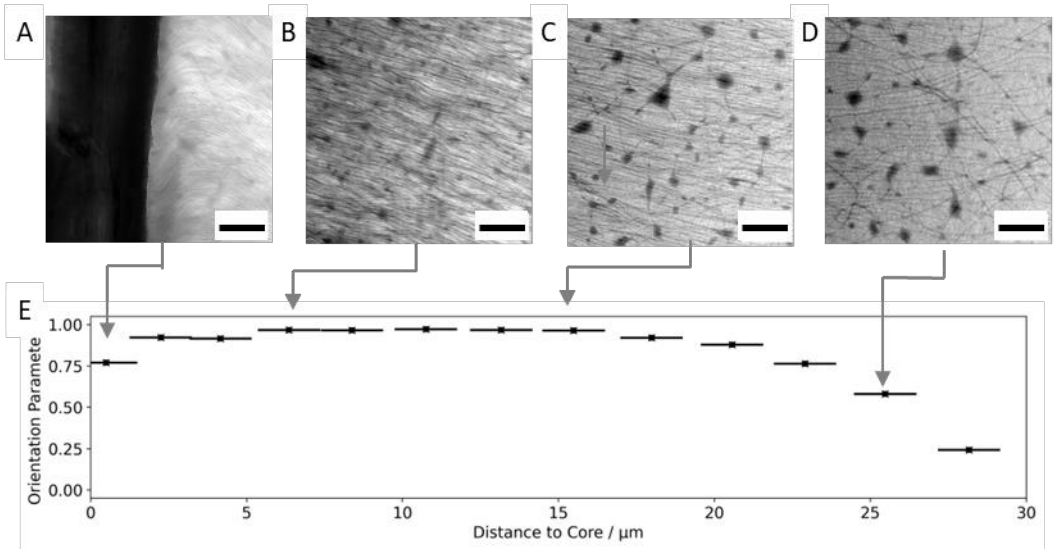

Figure 3-15: Spatially resolved transmission electron microscopy reveals the high orientation of *P3HT* nanofibers in isolated superstructures. A - D) Representative TEM images of isolated superstructures at different distances to the central ribbon (the scale bar corresponds to 0.5 µm). With increasing distance to the microribbon of NA 1 (from A at 0 µm to D at 25 µm), the density of the nanofibers decreases. Over the first 15 µm, the orientation of the nanofibers is very high. This is further evidenced by the very high orientation parameter of the nanofibers over large distances above 0.9 (E). Reprinted with permission from reference V. © 2024 American Chemical Society.

In addition, we performed spatially resolved photoluminescence spectroscopy in an area of 80 µm x 80 µm. In agreement with our previous work, we find systematic variations in the photoluminescence peak ratios indicating an increase of disorder with increasing distance to the central ribbon due to the crystallization-driven defect-fractionation. This resembles an important finding, because in the previous work the role of the surrounding *P3HT* film on the photophysical properties cannot be entirely ruled out.

In conclusion, a robust and controlled multi-step self-assembly procedure towards isolated hierarchical superstructures with densely packed and perpendicularly oriented *P3HT* nanofibers over distances of more than 20 µm in length was presented. Both the dense *P3HT* nanofiber mat as well as the high orientation of the *P3HT* nanofibers is attributed to the highly efficient epitaxial surface of the microribbon, which allows transfer to substrates without compromising structural integrity. The *P3HT* nanofibers of the isolated superstructures feature an exceptionally high orientation order parameter up to distances of15 µm. Photophysical investigations provide further evidence, that defects are exceedingly incorporated at the end of the nanofibers confirming our previous results. We envision that such isolated superstructures based on conjugated polymers may find use as an artificial light harvesting antennae or in nanophotonic devices.

4 Publications

4.1 Individual contributions to joint publications

All publications included in this thesis are the result of close collaborative work of several researchers across multiple disciplines. The individual contributions of each author and coauthor are given in this section.

Publication I: Enhancing Long-Range Energy Transport in Supramolecular Architectures by Tailoring Coherence Properties

Journal of the American Chemical Society **2020**, *142 (18)*, 8323–8330

Bernd Wittmann, Felix A. Wenzel, Stephan Wiesneth, Andreas T. Haedler, Markus Drechsler, Klaus Kreger, Jürgen Köhler, E. W. Meijer, Hans-Werner Schmidt, and Richard Hildner

Publication I focuses on the impact of the hierarchical level on the exciton energy transport and is published as a communication. I performed the majority of the controlled self-assembly studies. I performed the initial circular-dichroism spectroscopy during my research stay in the laboratory of E. W. Meijer at the TU Eindhoven. I supported Bernd Wittmann with the absorption and photoluminescence spectroscopy as well as the sample preparation for the transmission electron microscopy and selected area electron diffraction measurements. Bernd Wittmann with support from Stefan Wiesneth performed the atomic force microscopy as well as the optical and spectroscopic measurements of deposited supramolecular architectures on substrates. Bernd Wittmann evaluated the spectroscopic data and performed the numerical simulations. Markus Drechsler performed the electron microscopy and electron diffraction. Bernd Wittmann led detailed scientific discussions with me regarding the experiments. Bernd Wittmann prepared the figures and wrote the initial manuscript. Klaus Kreger, Hans-Werner Schmidt, and Richard Hildner were involved in scientific discussions during the project and contributed to the interpretation of the results. All authors were involved in finalizing the manuscript.

Publication II: Temperature-induced inversion of circular dichroism in supramolecular polymers revisited: Structural vs. electronic helicity

Manuscript to be submitted

Asena Cerhan-Haink*, Felix A. Wenzel*, Michael Buchhorn, Richard Kellnberger, Eric Schaible, Klaus Kreger, Hans-Werner Schmidt, Richard Hildner, and Eva Herzig

**These authors contributed equally to the work.*

Publication II covers the investigation and understanding of the chirality inversion of supramolecular aggregates and will be submitted as a communication in an appropriate peer-reviewed journal. I performed and optimized the self-assembly-experiments and conducted the temperature-dependent absorption, photoluminescence, and circular dichroism spectroscopy measurements. I evaluated the spectroscopic data with the help of Richard Hildner. Michael Buchhorn and I performed the temperature-dependent wide-angle x-ray scattering experiments at the Advanced Light Source, Lawrence Berkeley National Laboratory, USA, under the supervision of Richard Kellnberger and Eric Schaible. Asena Cerhan-Haink and Eva Herzig analyzed the scattering data. Richard Hildner performed the calculations of the electronic coupling. Asena Cerhan-Haink, Klaus Kreger, Hans-Werner Schmidt, Richard Hildner, Eva Herzig, and I jointly wrote the initial manuscript. All authors were involved in finalizing the manuscript.

Publication III: Highly Efficient Supramolecular Nucleating Agents for Poly(3-hexylthiophene)

Macromolecules, **2022**, *55(7)*, 2861–2871

Felix A. Wenzel, Hannes Welz, Kasper P. van der Zwan, Sebastian Stäter, Klaus Kreger, Richard Hildner, Jürgen Senker, and Hans-Werner Schmidt

Publication III focuses on *N,N'-1,4-phenylenebis[4-pyridinecarboxamide]* as an efficient supramolecular nucleating agent for *poly(3-hexyl thiophene)* in bulk and is published as a full paper. Hannes Welz performed the initial selection of the molecules as well as dynamic differential scanning calorimetry measurements. I conducted extensively dynamic and isothermal differential scanning calorimetry measurements for *N,N'-1,4-phenylenebis[4-pyridinecarboxamide]* as well as for the reference substances and the other *poly (3-alkyl thiophenes)*. I also performed the temperature-dependent polarized light microscopy and the OFET mobility measurements. I prepared the samples for the spectroscopy measurements as well as the single crystals of *N,N'-1,4-phenylenebis[4-pyridinecarboxamide]* for the structure elucidation. Kasper P. van der Zwan performed the structure elucidation and was involved in detailed discussions regarding the epitaxial concept. Sebastian Stäter measured and evaluated the spatially resolved absorption and photoluminescence spectroscopy. I wrote the initial draft of the manuscript. Klaus Kreger, Richard Hildner, Jürgen Senker, and Hans-Werner Schmidt were involved in scientific discussions during the project and contributed to the interpretation of the results. All authors were involved in finalizing the publication.

Publication IV: Directed Gradients in the Excited-State Energy Landscape of Poly(3-hexylthiophene) Nanofibers

Journal of the American Chemical Society, **2023**, *145(25)*, 13780–13787

Sebastian Stäter, Felix A. Wenzel, Hannes Welz, Klaus Kreger, Jürgen Köhler, Hans-Werner Schmidt, and Richard Hildner

Publication IV focuses on the continuous gradient in the excited-state energy landscape of hierarchical *P3HT*-based superstructures and is published as a communication. Based on the initial process developed by Hannes Welz, I performed most of the self-assembly studies and established a robust procedure to prepare and deposit superstructures. I measured and evaluated the temperature-dependent crystallization of *P3HT* in solution. I supported the transmission electron microscopy and selected area electron diffraction measurements. Sebastian Stäter performed the spatially resolved spectroscopy as well as the atomic force and light microscopy. He also performed the analysis of the absorption and photoluminescence spectroscopy and calculated the excited-state energy landscape. Sebastian Stäter wrote the initial manuscript. Klaus Kreger, Hans-Werner Schmidt, Jürgen Köhler, and Richard Hildner were involved in scientific discussions during the project and contributed to the interpretation of the results. All authors were involved in finalizing the manuscript.

Publication V: Micrometer-long highly oriented P3HT nanofibers in isolated hierarchical superstructures

Macromolecules, **2024**, *57(21)*, 10389– 10398.

Felix A. Wenzel, Sebastian Stäter, Padraic O'Reilly, Klaus Kreger, Richard Hildner, and Hans-Werner Schmidt

In Publication V, the controlled preparation, purification, and transfer of hierarchical superstructures with highly aligned *P3HT* nanofibers is investigated. The results are published as a full paper. I performed comprehensive self-assembly studies of the nucleating agent and the trans-crystallization of P3HT including absorption spectroscopy studies as well as electron microscopy and light microscopy studies. I developed the purification and transfer steps to substrates. I conducted the scanning electron microscopy and the scanning transmission electron microscopy. I performed the transmission electron microscopy and selected area electron diffraction with the support of Markus Drechsler. Sebastian Stäter measured the spatially resolved photoluminescence imaging and performed their evaluation. Padraic O'Reilly conducted photo-induced force microscopy imaging and performed their evaluation. I wrote the initial manuscript. Klaus Kreger, Richard Hildner, and Hans-Werner Schmidt were involved in scientific discussions during the project and contributed to the interpretation of the results. All authors were involved in finalizing the manuscript.

4.2 Publication I: Enhancing Long-Range Energy Transport in Supramolecular Architectures by Tailoring Coherence Properties

JACS
JOURNAL OF THE AMERICAN CHEMICAL SOCIETY

pubs.acs.org/JACS

Article

Enhancing Long-Range Energy Transport in Supramolecular Architectures by Tailoring Coherence Properties

Bernd Wittmann, Felix A. Wenzel, Stephan Wiesneth, Andreas T. Haedler, Markus Drechsler, Klaus Kreger, Jürgen Köhler, E. W. Meijer, Hans-Werner Schmidt,* and Richard Hildner*

Cite This: J. Am. Chem. Soc. 2020, 142, 8323−8330

Read Online

ACCESS | Metrics & More | Article Recommendations | Supporting Information

ABSTRACT: Efficient long-range energy transport along supramolecular architectures of functional organic molecules is a key step in nature for converting sunlight into a useful form of energy. Understanding and manipulating these transport processes on a molecular and supramolecular scale is a long-standing goal. However, the realization of a well-defined system that allows for tuning morphology and electronic properties as well as for resolution of transport in space and time is challenging. Here we show how the excited-state energy landscape and thus the coherence characteristics of electronic excitations can be modified by the hierarchical level of H-type supramolecular architectures. We visualize, at room temperature, long-range incoherent transport of delocalized singlet excitons on pico- to nanosecond time scales in single supramolecular nanofibers and bundles of nanofibers. Increasing the degree of coherence, i.e., exciton delocalization, via supramolecular architectures enhances exciton diffusivities up to 1 order of magnitude. In particular, we find that single supramolecular nanofibers exhibit the highest diffusivities reported for H-aggregates so far.

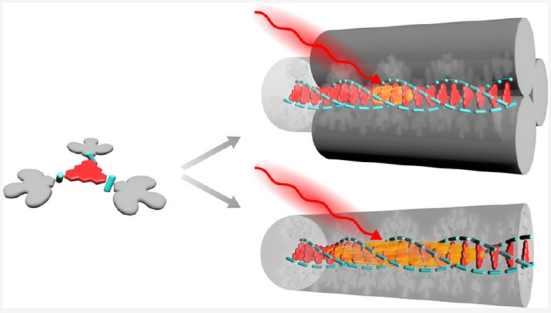

INTRODUCTION

Supramolecular chemistry provides intriguing opportunities to create nano- to mesoscale assemblies with unprecedented optical and electronic functionalities owing to cooperative interactions between the constituent building blocks.[1−7] A key functionality for potential applications is, for example, efficient long-range excitation energy transport.[4,8−14] In general, energy transport in organic materials is governed by the delicate interplay between electronic Coulomb coupling between densely packed molecules and electronic and structural disorder. On the one hand, electronic coupling leads to the formation of delocalized exciton states; that is, electronic excitations are coherently shared by many molecules, which we refer to as (quantum) coherent transport. On the other hand, electronic and structural disorder leads to a localization of excitons on small domains of supramolecular assemblies.[15,16] If disorder dominates, long-range transport cannot be realized, because incoherent Förster-type hopping of strongly localized excitons limits transport to some tens of nanometers.[17] In contrast, reducing disorder increases exciton delocalization, and thus the degree of coherence.[15,18−20] Such combined incoherent−coherent transport, i.e., incoherent hops of delocalized excitons,[12,21−24] with a strong contribution of coherence, indeed allowed achieving distances beyond 1 μm.[12,23] However, a full understanding and control of long-range energy transport is still highly complex, because in supramolecular nanostructures the electronic coupling and disorder are typically of the same order of magnitude. This so-called intermediate regime renders disentangling the different contributions to energy transport difficult, on both the theoretical and experimental side.[16] Since transport efficiencies and distances are predicted to be largest in this regime,[21,25,26] a unique picture is desirable for the design of novel excitonic materials and devices.[2,4,5,7−9]

A straightforward approach to modify electronic coupling and disorder makes use of the self-assembly of defined nanostructures based on the same building blocks. In this context, so-called pathway complexity can be exploited to form thermodynamically and kinetically stable supramolecular aggregates with different structural order[6,27,28] and thus with significantly altered photophysical and energy transport properties. In contrast, supramolecular aggregates with different hierarchical levels[11,29−31] feature the same structural arrangement of the building blocks, i.e., the same electronic coupling, with only subtle variations in the local electronic

Received: February 7, 2020
Published: April 11, 2020

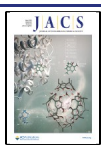

https://dx.doi.org/10.1021/jacs.0c01392
J. Am. Chem. Soc. 2020, 142, 8323−8330

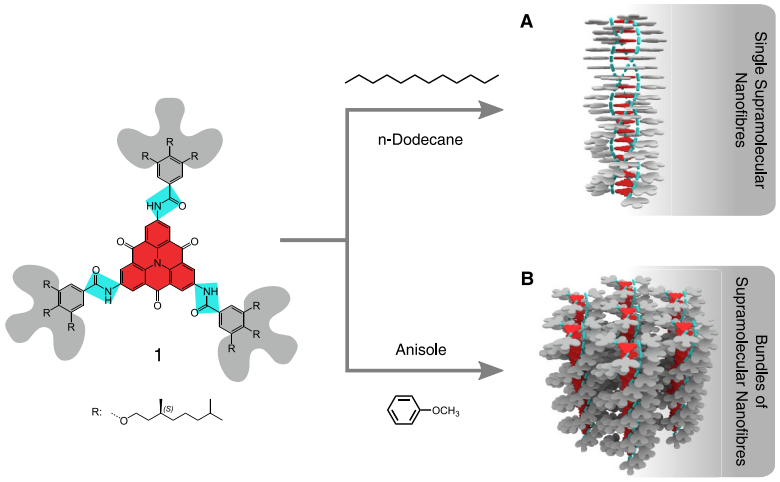

Figure 1. Supramolecular architectures of compound **1** with different hierarchical levels. Left: Compound **1** comprising a carbonyl-bridged triarylamine core (red), three amide moieties (blue), and chiral bulky peripheries (gray). Self-assembly in *n*-dodecane results in single supramolecular nanofibers (A) and in anisole in bundles of supramolecular nanofibers (B).

environment. Such structures are therefore ideal candidates to reveal the interplay between the electronic coupling and disorder.

Here we present stable and robust supramolecular architectures based on a carbonyl-bridged triarylamine trisamide (CBT, compound **1**, see ref 32) with different hierarchical levels depending on the solvent, i.e., single supramolecular nanofibers and bundles of supramolecular nanofibers (Figure 1). The molecular design of compound **1** results in columnar structures with a well-defined, cofacial H-type arrangement of the CBT cores that is driven by directed hydrogen bonding between amide groups. Excitons in these supramolecular architectures possess different degrees of coherence (delocalization), tuned by bundling-induced electronic disorder. We are thus able to resolve the competition between coherence and disorder and to demonstrate its impact on long-range, pico- to nanosecond, incoherent transport of singlet excitons in supramolecular architectures on the level of single nanostructures at room temperature. In contrast to previous work on nanotubular assemblies,[11,30] we find a higher degree of coherence and thus enhanced exciton diffusivities in single supramolecular nanofibers.

■ RESULTS AND DISCUSSION

Controlled Self-Assembly of Single Nanofibers and Bundles of Nanofibers. Using two selected solvents, we are able to self-assemble compound **1** into distinct supramolecular morphologies (see Supporting Information section 1). In *n*-dodecane, compound **1** forms single supramolecular nanofibers of several micrometers in length (Figures 2A and S1) and uniform heights of about 2 nm (Figure 2B), as shown by atomic force microscopy (AFM), which is consistent with our previous work on single CBT-nanofibers.[23,32] Transmission electron microscopy (TEM, Figure 2C) reveals single supramolecular nanofibers and nanofibers partially located next to each other due to sample preparation. The selected area electron diffraction (SAED) pattern features a signal corresponding to a distance of 0.33 nm (Figure 2D) caused by cofacial stacking of CBT cores along the supramolecular nanofibers.[23,32]

Self-assembly of compound **1** in anisole results in bundles of supramolecular nanofibers with widths and heights on the order of 100 nm, as shown by AFM and TEM measurements (Figure 2E,F,G and Figure S1). The SAED pattern yields the characteristic cofacial stacking distance of 0.33 nm between CBT cores (Figure 2H). Additionally, SAED at smaller angles (Figure S2) reveals defined signals corresponding to a distance of 2.8 nm. Assuming a columnar hexagonal packing of the nanofibers,[32] we obtain an intercolumnar spacing of 3.2 nm. This distance is substantially smaller than the calculated diameter of about 4.4 nm for the extended compound **1**.[32] In bundles the peripheries of adjacent nanofibers therefore strongly interact. Based on these data, we estimate that one bundle consists of approximately 2000 nanofibers.

Optical Properties of Nanofibers and Bundles. UV–vis and photoluminescence (PL) spectra of dissolved compound **1** in THF (Figure 3A) exhibit the characteristic vibronic progression of an aromatic molecule (see Supporting Information section 4, Table S1). The maxima at 460 nm and 490 nm, respectively, are attributed to the electronic (0–0) $\pi-\pi^*$ transition of the CBT core.[33,34]

The absorption spectra of supramolecular nanofibers and bundles of nanofibers are shown in Figure 3B and C, respectively (see also Figure S3). Both feature a substantially reduced intensity of the highest-wavelength (lowest-energy) peak around 520 nm (labeled A_1) compared to the spectrum of dissolved compound **1**. This spectral change is characteristic for delocalized absorbing excitons in H-aggregates, formed by substantial electronic Coulomb coupling between adjacent CBT cores.[35] Circular-dichroism spectra of dispersions of both supramolecular morphologies feature nearly identical signatures (Figure S4) indicating no significant difference in the structural arrangement of the CBT cores in supramolecular nanofibers and bundles of nanofibers.

After absorption rapid, subpicosecond relaxation within the exciton bands takes place toward lower-energy, relaxed exciton states,[22] from where emission occurs (see Supporting

https://dx.doi.org/10.1021/jacs.0c01392
J. Am. Chem. Soc. 2020, 142, 8323–8330

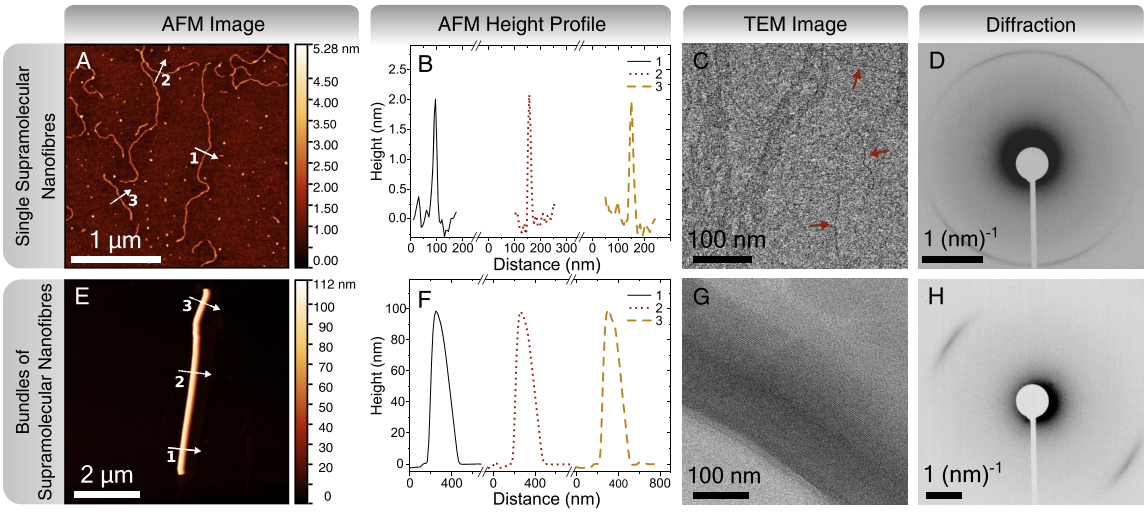

Figure 2. Morphological and structural characterization of the supramolecular architectures. (A) AFM image (topographical scan) of single supramolecular nanofibers prepared from a dispersion of compound **1** in *n*-dodecane (4 μM, ~10 ppm). (B) Height profiles along the arrows labeled in A. (C) TEM image of single nanofibers partially located next to each other (40 μM, ~100 ppm). Arrows indicate isolated single nanofibers. (D) SAED pattern corresponds to a stacking distance of 0.33 nm between CBT cores. (E) AFM image of a bundle of supramolecular nanofibers prepared from a dispersion of compound **1** in anisole (40 μM, ~100 ppm). (F) Height profiles along the arrows labeled in E. (G) TEM image of a bundle of nanofibers. (H) SAED pattern corresponds to a stacking distance of 0.33 nm.

Information section 4, Figure S5). In the PL spectrum of supramolecular nanofibers the 0−0 peak seems to be absent at room temperature (Figure 3B, see also Supporting Information section 4, Figure S6). These data suggest a large degree of electronic order and thus of coherence with a pronounced delocalization of relaxed emitting excitons[35] along nanofibers. In contrast, the corrected PL spectrum of bundles of nanofibers (Figures 3C and S7) features a 0−0 peak that is only slightly suppressed compared to that of dissolved compound **1**. This observation indicates strong localization of the relaxed emitting exciton over only a few CBT cores and thus a small degree of coherence. The localization must result predominantly from electronic disorder, because the structural order within the columns of both architectures appears to be comparable (Figure S4). Our data for bundles of nanofibers thus demonstrate a rapid disorder-induced localization of initially delocalized absorbing excitons prior to emission.[21]

The influence of electronic disorder on the relaxed emitting excitons in our supramolecular architectures is further confirmed by the trend in the excited-state lifetimes (PL quantum yields), which increase (decrease) from 2.7 ns (13.8%) for the dissolved compound **1** to 3.5 ns (2.6%) for bundles and 5.4 ns (1.3%) for single nanofibers (see Table S2 and Figure S8). This enhancement in lifetimes is highly beneficial for long-range energy transport,[15] as we previously reported.[23]

To quantify the electronic Coulomb coupling and the electronic disorder between CBT cores from the spectra in Figure 3B,C, we performed numerical simulations based on the theory of Spano and co-workers using a disordered Holstein Hamiltonian (ref 35 and Supporting Information section 5). The intercolumnar distance of 3.2 nm within bundles prevents delocalization of electronic excitations between columns. A bundle is thus modeled as an arrangement of independent nanofibers. Electronic (energy) disorder is included by taking the CBT cores' transition energy offsets from a Gaussian distribution with a width σ. Moreover, we include a correlation length l_0 that accounts for differences in the spatial distribution of disorder in the transition energies (Figure S5).

The simulations (Figure 3B,C, black lines) agree very well with the experimental data in the relevant spectral region. The absorption spectra of both architectures are well described by a common set of parameters, i.e., by an electronic coupling of J_0 = 735 cm^{-1} (91 meV) and an electronic disorder of σ = 1036 cm^{-1} (130 meV, see Figure S9 and Supporting Information section 5), which places both morphologies in the intermediate coupling regime.

The differences between the PL spectra of nanofibers and bundles can only be modeled using different correlation lengths. The absence of the 0−0 PL peak in the spectrum of nanofibers requires a correlation length of $l_0 \geq 10$ CBT cores with a disorder of σ = 1076 cm^{-1} (134 meV, see Supporting Information section 5). Due to this spatial correlation in the transition energies, a nanofiber is segmented into domains that possess a rather uniform excited-state energy landscape (Figure 3E). The delocalization of the relaxed, emitting singlet excitons can then be quantified by the coherence number of $N_{coh} \geq 5.4$ CBT cores. In contrast, the strong 0−0 PL peak intensity in the PL spectrum of bundles of nanofibers requires a vanishing correlation length (l_0 = 0). The relaxed emitting exciton in bundles is thus localized on approximately 2.9 CBT cores due to the rough excited-state energy landscape along nanofibers in bundles (Figure 3F). The different excited-state energy landscapes along one column (single nanofiber and within a bundle, respectively) due to the distinct spatial transition energy correlations is visualized in Figure 3E,F. We note that these realizations are directly taken from the numerical simulations.

Direct Visualization of Exciton Transport. Our optical spectroscopy data demonstrate that we are able to tune the

https://dx.doi.org/10.1021/jacs.0c01392
J. Am. Chem. Soc. 2020, 142, 8323−8330

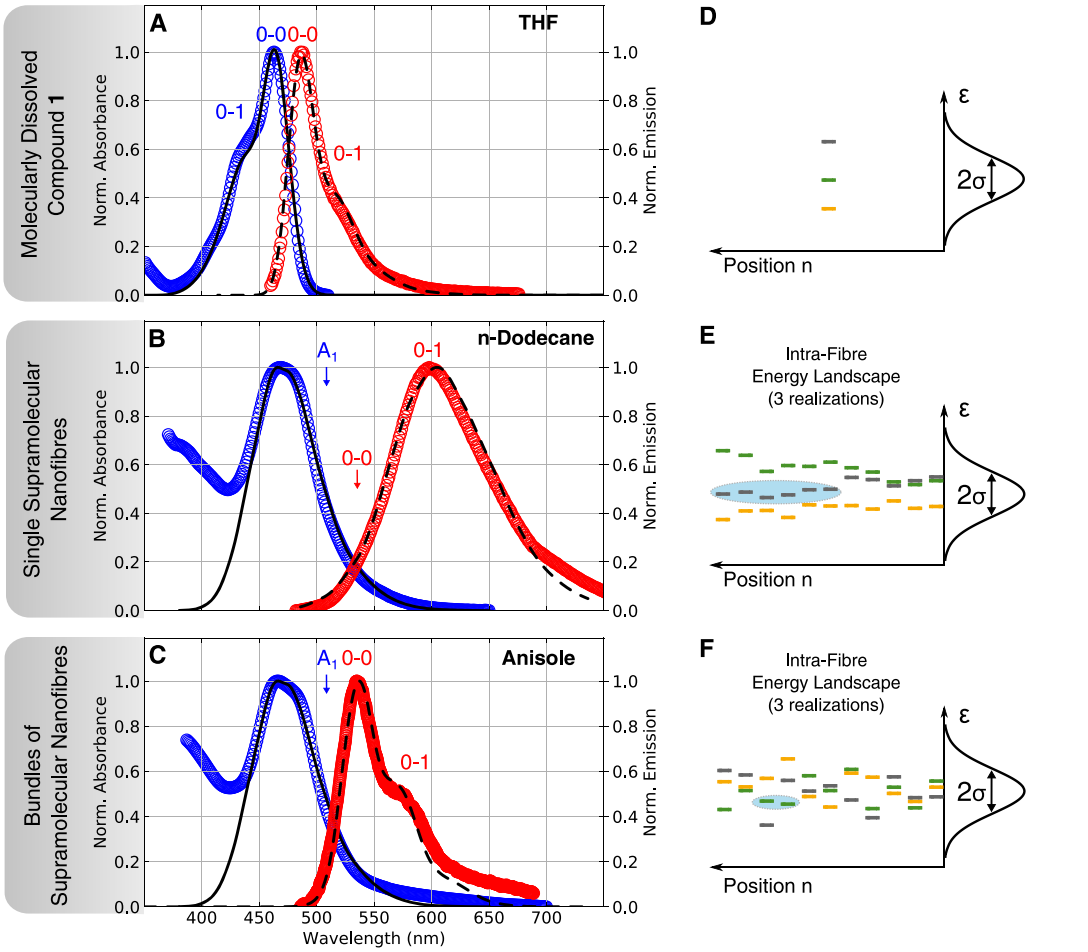

Figure 3. Optical properties of compound **1** and supramolecular architectures. (A) Normalized absorption (blue) and photoluminescence spectra (red) of dissolved compound **1** in THF (40 μM) with the corresponding Franck−Condon analysis (black lines). (B, C) Normalized absorption (blue) and photoluminescence spectra (red) of single supramolecular nanofibers in *n*-dodecane (40 μM) (B) and bundles of supramolecular nanofibers in anisole (200 μM) (C), together with simulated spectra based on a Frenkel−Holstein Hamiltonian (black lines). (D) Illustration of the inhomogeneous distribution of transition energies of dissolved compound **1** for three realizations. (E, F) Representation of three simulated realizations of transition energies of the building block at position n within one single column for the simulated spectra in B and C. The spatial correlation length of transition energies for single nanofibers is $l_0 \geq 10$ and for bundles of nanofibers $l_0 = 0$ (left, intracolumn energy landscape), while the corresponding ensemble averages, with a Gaussian width σ, over all columns (right) are almost identical. The ellipses indicate the delocalization of relaxed emitting states.

coherence characteristics of the relaxed excitons along the H-type columns by altering the hierarchical level of our architectures. These relaxed excitons are responsible for incoherent long-range transport, since they perform many hopping steps within their substantial excited-state lifetime in our H-aggregates. Importantly, the hopping rates of delocalized excitons have to be described by a generalized Förster theory, in which optically dark exciton states contribute to the hopping rates.[36−38] These systems are thus ideal to resolve the interplay between morphology, correlated electronic disorder, and coherence (delocalization) in the long-range incoherent transport of excitons along individual, spatially isolated nanostructures on pico- to nanosecond time scales. Figure 4A and B display representative wide-field PL images of isolated nanostructures, both with lengths of several micrometers, in agreement with the AFM data (Figure 2A,E). The single nanofiber shows a small PL signal (Figure 4A), which demonstrates the weakly optically allowed nature of the emitting excitons and thus the high degree of coherence within the nanofiber. The signal from the bundle of nanofibers is significantly stronger mainly owing to the large number of columns within the bundle (Figure 4B) and to a lesser extent due to the higher PL quantum efficiency of one column in a bundle (see Table S2).

Having located isolated nanostructures, we switched the microscope to confocal illumination and centered each nanostructure in the diffraction-limited focus of a pulsed laser (red dashed circles, Figure 4A,B). Combining detection-beam scanning with time-correlated single-photon counting[39] (see Supporting Information sections 1 and 6), we measured

https://dx.doi.org/10.1021/jacs.0c01392
J. Am. Chem. Soc. 2020, 142, 8323−8330

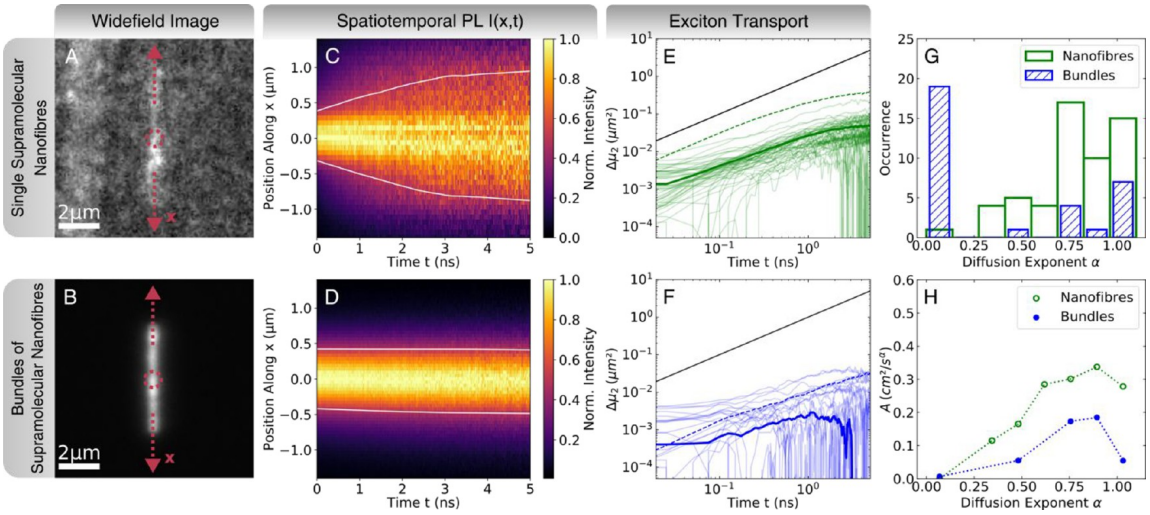

Figure 4. Direct visualization of long-range energy transport along supramolecular architectures. (A, B) Wide-field photoluminescence image of a single supramolecular nanofiber and a bundle of supramolecular nanofibers, respectively. Red dashed arrows indicate the scanning axis x; dashed circles label the position $x = 0$ of the excitation spot. (C, D) Normalized PL intensity distributions and their evolution in space and time for the single nanofiber in A and the bundle in B. The white contour lines indicate the time evolution of the full width at half-maximum. (E, F) Temporal changes of the second moments of the spatial intensity profiles for 56 nanofibers and 32 bundles of nanofibers (thin green and blue solid lines). The thick lines represent the average of all curves, and the dashed lines the evolution of the second moment for the data in C and D. The black lines indicate a linear scaling in time, i.e., normal diffusion, as a guide for the eye. (G) Distribution of the diffusion exponent α for all nanofibers (green) and bundles (blue) in E and F, evaluated for $t < 1$ ns. (H) Averaged hopping coefficients A as a function of α for nanofibers (green) and bundles (blue).

PL decay curves while scanning the detection position along the long axis of the nanostructures (dashed arrows in Figure 4A,B). Figure 4C and D show the resulting PL intensity distributions, $I(x, t)$, as a function of the distance x relative to the center of the excitation spot and time t after laser excitation. Normalization of the spatial intensity distributions at each point in time (Figure S13) reveals the broadening of the PL signal along the nanostructures' long axes on (sub-) nanosecond time scales. Hence, the initial singlet exciton population, created by the diffraction-limited excitation pulse, is transported away from the excitation spot prior to (radiative) decay. This energy transport is significantly more pronounced for the single nanofiber compared to the bundle of nanofibers (Figure 4C,D, white contour lines). We attribute this difference to the distinct excited-state energy landscapes (Figure 3E,F). We rule out artifacts due to saturation and technical issues, since we operate under very low excitation fluences, and we have performed an independent control experiment on a system that does not show long-range energy transport (see Supporting Information, Materials and Methods, and Figure S12).

To quantitatively describe the time-dependent broadening of the spatial intensity distributions, we calculated the second moments $\mu_2(t)$[22] at time t as a measure for their widths (Figure S13). We evaluated changes of $\mu_2(t)$ with respect to the second moment (width) of the initial distribution $\mu_2(0)$:

$$\Delta\mu_2(t) = \mu_2(t) - \mu_2(0) \tag{1}$$

The $\Delta\mu_2(t)$ curves retrieved from the data in Figure 4C,D are shown as thick dashed lines in Figure 4E,F. At short times ($t \leq$ 1 ns), we find similar slopes for both curves. However, the $\Delta\mu_2(t)$ values for the single nanofiber are larger by more than 1 order of magnitude compared to those for the bundle. This observation reflects the faster and more pronounced broadening of the initial exciton population in the single nanofiber due to more efficient energy transport. For longer times ($t \geq$ 2.5 ns) the broadening slows down and a plateau is reached for both architectures. We confirmed the same trend for in total 56 single nanofibers and 32 bundles, illustrated with thin solid green and blue lines in Figure 4E,F.

The second moments $\Delta\mu_2(t)$ follow to a good approximation a power law for $t < 1$ ns. We can thus fit the transport dynamics with a diffusion model[11,17,22,39−41] (see Supporting Information section 7):

$$\Delta\mu_2(t) = At^{\alpha} \tag{2}$$

Here α is the diffusion exponent and A is the exciton hopping coefficient, which is related to the time-dependent diffusivity $D(t) = \frac{1}{2}A_\alpha t^{\alpha-1}$. Figure 4G shows the exponents for nanofibers (green bars) and bundles (blue hatched bars) for all curves in Figure 4E,F. We find a broad distribution with $0 \leq \alpha \leq 1$ (for $t < 1$ ns) due to the intrinsic electronic disorder in deposited supramolecular nanostructures. For single nanofibers the mean exponent is $\overline{\alpha}_{\text{Fiber}} = 0.78 \pm 0.24$, and a significant fraction exhibits $\alpha \approx 1$, which indicates normal diffusion visualized in Figure 4E,F with black solid lines. In contrast, the mean exponent for bundles is smaller with $\overline{\alpha}_{\text{Fiber}} = 0.37 \pm 0.47$, which is characteristic for strongly subdiffusive transport due to the disordered energy landscape.[22] Notably, for bundles the highest occurrence of exponents is at $\alpha \approx 0$. This behavior is expected for a system with strong local electronic perturbations (Figure 3F), in which trapping hinders exciton transport.[22] For the single nanofibers the average exciton hopping coefficients A as a function of the exponent α are larger (Figure 4H). This

https://dx.doi.org/10.1021/jacs.0c01392
J. Am. Chem. Soc. 2020, 142, 8323−8330

translates into higher diffusivities $D(t)$ for single nanofibers: For example, for the nanofiber shown in Figure 4C we find $D_{Fiber}(t = 1\ ns) = 1.03\ cm^2/s$, which is the largest value reported for an H-aggregate and is more than 1 order of magnitude larger than the diffusivity for the bundle shown in Figure 4D with D_{Bundle} $(t = 1\ ns) = 0.05\ cm^2/s$ (see also Figure S14).

CONCLUSION

Our H-type supramolecular architectures with different hierarchical levels represent a versatile system to understand the subtle interplay between electronic coupling, disorder, and coherence for efficient long-range, incoherent transport of delocalized singlet excitons. We have demonstrated remarkable differences in the spectroscopic properties as well as in the energy transport characteristics of single supramolecular nanofibers and bundles of nanofibers. The transition energies of adjacent CBT cores in single supramolecular nanofibers are spatially correlated, resulting in smooth excited-state energy landscapes. The concomitant high degree of coherence (exciton delocalization) facilitates long-range incoherent energy transport. In contrast, in bundles of nanofibers spatial correlations in the transition energies are found to be absent. This gives rise to a disordered excited-state energy landscape with strongly localized excitons. Hence, exciton transport is hindered by trapping in local energy minima.[22] The uncorrelated transition energies in bundles of nanofibers can be explained by very subtle local electronic perturbations due to interacting peripheries.[30] Alternatively, disorder on a local scale between columns may arise from a geometric frustration in a hexagonal packing due to compensation of macrodipoles.[42] Both effects can destroy shared electronic environments. Our observations are a manifestation of coherence-enhanced diffusivities of excitons[15,18,43] and highlight the critical role of spatially correlated transition energies of the supramolecular building blocks for long-range energy transport.[44] The present data therefore add a new dimension to the development of a detailed theoretical understanding of energy transport in columnar H-type supramolecular nanostructures[45] as well as for the design of novel, optimized nanophotonic applications.

ASSOCIATED CONTENT

Supporting Information

The Supporting Information is available free of charge at https://pubs.acs.org/doi/10.1021/jacs.0c01392.

Materials and methods; additional characterization of supramolecular architectures by AFM, electron diffraction, and optical spectroscopy; numerical simulations of optical spectra and exciton diffusion model (PDF)

AUTHOR INFORMATION

Corresponding Authors

Hans-Werner Schmidt − *Macromolecular Chemistry and Bavarian Polymer Institute, University of Bayreuth, 95447 Bayreuth, Germany;* orcid.org/0000-0002-1761-1153; Email: hans-werner.schmidt@uni-bayreuth.de

Richard Hildner − *Spectroscopy of Soft Matter, University of Bayreuth, 95447 Bayreuth, Germany; Zernike Institute for Advanced Materials, University of Groningen, 9747 AG Groningen, The Netherlands;* orcid.org/0000-0002-7282-3730; Email: r.m.hildner@rug.nl

Authors

Bernd Wittmann − *Spectroscopy of Soft Matter, University of Bayreuth, 95447 Bayreuth, Germany*

Felix A. Wenzel − *Macromolecular Chemistry and Bavarian Polymer Institute, University of Bayreuth, 95447 Bayreuth, Germany; Institute for Complex Molecular Systems, Laboratory of Macromolecular and Organic Chemistry, Eindhoven University of Technology, 5612, AZ, Eindhoven, The Netherlands*

Stephan Wiesneth − *Spectroscopy of Soft Matter, University of Bayreuth, 95447 Bayreuth, Germany*

Andreas T. Haedler − *Macromolecular Chemistry and Bavarian Polymer Institute, University of Bayreuth, 95447 Bayreuth, Germany; Institute for Complex Molecular Systems, Laboratory of Macromolecular and Organic Chemistry, Eindhoven University of Technology, 5612, AZ, Eindhoven, The Netherlands*

Markus Drechsler − *Bavarian Polymer Institute, University of Bayreuth, 95447 Bayreuth, Germany*

Klaus Kreger − *Macromolecular Chemistry and Bavarian Polymer Institute, University of Bayreuth, 95447 Bayreuth, Germany;* orcid.org/0000-0003-3021-1311

Jürgen Köhler − *Spectroscopy of Soft Matter, University of Bayreuth, 95447 Bayreuth, Germany;* orcid.org/0000-0002-4214-4008

E. W. Meijer − *Institute for Complex Molecular Systems, Laboratory of Macromolecular and Organic Chemistry, Eindhoven University of Technology, 5612, AZ, Eindhoven, The Netherlands;* orcid.org/0000-0003-4126-7492

Complete contact information is available at: https://pubs.acs.org/10.1021/jacs.0c01392

Notes

The authors declare no competing financial interest.

ACKNOWLEDGMENTS

We acknowledge financial support from the German Research Foundation (DFG) through the research training group GRK1640 and from the Bavarian State Ministry of Science and the Arts through the Collaborative Research Network "Solar Technologies go Hybrid". We acknowledge support by the Elite Network of Bavaria (ENB) through the study programs "Macromolecular Science" (F.A.W.) and "Biological Physics" (R.H.) as well as the Max-Weber program (F.A.W.). We are grateful to Doris Hanft and Sandra Ganzleben (Macromolecular Chemistry, University of Bayreuth) for their help with syntheses. We thank Markus Hund (KeyLab Surface and Interface Characterization) of the Bavarian Polymer Institute for support with AFM measurements and Sooruban Shanmugaratnam (Biochemistry, University of Bayreuth) for help with CD spectroscopy.

REFERENCES

(1) Sengupta, S.; Würthner, F. Chlorophyll J-Aggregates: From Bioinspired Dye Stacks to Nanotubes, Liquid Crystals, and Biosupramolecular Electronics. *Acc. Chem. Res.* **2013**, *46* (11), 2498−2512.

(2) Liess, A.; Arjona-Esteban, A.; Kudzus, A.; Albert, J.; Krause, A. M.; Lv, A.; Stolte, M.; Meerholz, K.; Würthner, F. Ultranarrow Bandwidth Organic Photodiodes by Exchange Narrowing in Merocyanine H- and J-Aggregate Excitonic Systems. *Adv. Funct. Mater.* **2019**, *29* (21), 1−9.

(3) Aida, T.; Meijer, E. W.; Stupp, S. I. Functional Supramolecular Polymers. *Science* **2012**, *335* (6070), 813−817.
(4) Boulais, E.; Sawaya, N. P. D.; Veneziano, R.; Andreoni, A.; Banal, J. L.; Kondo, T.; Mandal, S.; Lin, S.; Schlau-Cohen, G. S.; Woodbury, N. W.; Yan, H.; Aspuru-Guzik, A.; Bathe, M. Programmed Coherent Coupling in a Synthetic DNA-Based Excitonic Circuit. *Nat. Mater.* **2018**, *17* (2), 159−166.
(5) Moulin, E.; Armao, J. J.; Giuseppone, N. Triarylamine-Based Supramolecular Polymers: Structures, Dynamics, and Functions. *Acc. Chem. Res.* **2019**, *52* (4), 975−983.
(6) Korevaar, P. A.; George, S. J.; Markvoort, A. J.; Smulders, M. M. J.; Hilbers, P. A. J.; Schenning, A. P. H. J.; De Greef, T. F. A.; Meijer, E. W. Pathway Complexity in Supramolecular Polymerization. *Nature* **2012**, *481* (7382), 492−496.
(7) Ciesielski, A.; Palma, C.-A.; Bonini, M.; Samori, P. Towards Supramolecular Engineering of Functional Nanomaterials: Pre-Programming Multi-Component 2D Self-Assembly at Solid-Liquid Interfaces. *Adv. Mater.* **2010**, *22*, 3506−3520.
(8) Scholes, G. D.; Fleming, G. R.; Chen, L. X.; Aspuru-Guzik, A.; Buchleitner, A.; Coker, D. F.; Engel, G. S.; Van Grondelle, R.; Ishizaki, A.; Jonas, D. M.; Lundeen, J. S.; McCusker, J. K.; Mukamel, S.; Ogilvie, J. P.; Olaya-Castro, A.; Ratner, M. A.; Spano, F. C.; Whaley, K. B.; Zhu, X. Using Coherence to Enhance Function in Chemical and Biophysical Systems. *Nature* **2017**, *543* (7647), 647−656.
(9) Jin, X. H.; Price, M. B.; Finnegan, J. R.; Boott, C. E.; Richter, J. M.; Rao, A.; Matthew Menke, S.; Friend, R. H.; Whittell, G. R.; Manners, I. Long-Range Exciton Transport in Conjugated Polymer Nanofibers Prepared by Seeded Growth. *Science* **2018**, *360* (6391), 897−900.
(10) Winiger, C. B.; Li, S.; Kumar, G. R.; Langenegger, S. M.; Häner, R. Long-Distance Electronic Energy Transfer in Light-Harvesting Supramolecular Polymers. *Angew. Chem., Int. Ed.* **2014**, *53* (49), 13609−13613.
(11) Clark, K. A.; Krueger, E. L.; Vanden Bout, D. A. Direct Measurement of Energy Migration in Supramolecular Carbocyanine Dye Nanotubes. *J. Phys. Chem. Lett.* **2014**, *5* (13), 2274−2282.
(12) Caram, J. R.; Doria, S.; Eisele, D. M.; Freyria, F. S.; Sinclair, T. S.; Rebentrost, P.; Lloyd, S.; Bawendi, M. G. Room-Temperature Micron-Scale Exciton Migration in a Stabilized Emissive Molecular Aggregate. *Nano Lett.* **2016**, *16* (11), 6808−6815.
(13) Lin, H.; Camacho, R.; Tian, Y.; Kaiser, T. E.; Würthner, F.; Scheblykin, I. G. Collective Fluorescence Blinking in Linear J-Aggregates Assisted by Long-Distance Exciton Migration. *Nano Lett.* **2010**, *10* (2), 620−626.
(14) Wan, Y.; Stradomska, A.; Knoester, J.; Huang, L. Direct Imaging of Exciton Transport in Tubular Porphyrin Aggregates by Ultrafast Microscopy. *J. Am. Chem. Soc.* **2017**, *139* (21), 7287−7293.
(15) Brédas, J. L.; Sargent, E. H.; Scholes, G. D. Photovoltaic Concepts Inspired by Coherence Effects in Photosynthetic Systems. *Nat. Mater.* **2017**, *16* (1), 35−44.
(16) Fassioli, F.; Dinshaw, R.; Arpin, P. C.; Scholes, G. D. Photosynthetic Light Harvesting: Excitons and Coherence. *J. R. Soc., Interface* **2014**, *11* (92), 20130901.
(17) Menke, S. M.; Holmes, R. J. Exciton Diffusion in Organic Photovoltaic Cells. *Energy Environ. Sci.* **2014**, *7* (2), 499−512.
(18) Scholes, G. D. Designing Light-Harvesting Antenna Systems Based on Superradiant Molecular Aggregates. *Chem. Phys.* **2002**, *275* (1−3), 373−386.
(19) Topczak, A. K.; Roller, T.; Engels, B.; Brütting, W.; Pflaum, J. Nonthermally Activated Exciton Transport in Crystalline Organic Semiconductor Thin Films. *Phys. Rev. B: Condens. Matter Mater. Phys.* **2014**, *89* (20), 201203.
(20) Sung, J.; Kim, P.; Fimmel, B.; Würthner, F.; Kim, D. Direct Observation of Ultrafast Coherent Exciton Dynamics in Helical π-Stacks of Self-Assembled Perylene Bisimides. *Nat. Commun.* **2015**, *6* (1), 8646.
(21) Moix, J. M.; Khasin, M.; Cao, J. Coherent Quantum Transport in Disordered Systems: I. the Influence of Dephasing on the Transport Properties and Absorption Spectra on One-Dimensional Systems. *New J. Phys.* **2013**, *15* (8), 085010.
(22) Vlaming, S. M.; Malyshev, V. A.; Eisfeld, A.; Knoester, J. Subdiffusive Exciton Motion in Systems with Heavy-Tailed Disorder. *J. Chem. Phys.* **2013**, *138* (21), 214316.
(23) Haedler, A. T.; Kreger, K.; Issac, A.; Wittmann, B.; Kivala, M.; Hammer, N.; Köhler, J.; Schmidt, H. W.; Hildner, R. Long-Range Energy Transport in Single Supramolecular Nanofibres at Room Temperature. *Nature* **2015**, *523* (7559), 196−199.
(24) Spano, F. C.; Clark, J.; Silva, C.; Friend, R. H. Determining Exciton Coherence from the Photoluminescence Spectral Line Shape in Poly(3-Hexylthiophene) Thin Films. *J. Chem. Phys.* **2009**, *130* (7), 074904.
(25) Mohseni, M.; Aspuru-Guzik, A.; Rebentrost, P.; Shabani, A.; Lloyd, S.; Huelga, S. F.; Plenio, M. B. Environment-Assisted Quantum Transport. In *Quantum Effects in Biology*; Cambridge University Press, 2014; pp 159−176.
(26) Novo, L.; Mohseni, M.; Omar, Y. Disorder-Assisted Quantum Transport in Suboptimal Decoherence Regimes. *Sci. Rep.* **2016**, *6* (1), 18142.
(27) Fukui, T.; Kawai, S.; Fujinuma, S.; Matsushita, Y.; Yasuda, T.; Sakurai, T.; Seki, S.; Takeuchi, M.; Sugiyasu, K. Control over Differentiation of a Metastable Supramolecular Assembly in One and Two Dimensions. *Nat. Chem.* **2017**, *9* (5), 493−499.
(28) Wagner, W.; Wehner, M.; Stepanenko, V.; Würthner, F. Supramolecular Block Copolymers by Seeded Living Polymerization of Perylene Bisimides. *J. Am. Chem. Soc.* **2019**, *141* (30), 12044−12054.
(29) Eisele, D. M.; Arias, D. H.; Fu, X.; Bloemsma, E. A.; Steiner, C. P.; Jensen, R. A.; Rebentrost, P.; Eisele, H.; Tokmakoff, A.; Lloyd, S.; Nelson, K. A.; Nicastro, D.; Knoester, J.; Bawendi, M. G. Robust Excitons Inhabit Soft Supramolecular Nanotubes. *Proc. Natl. Acad. Sci. U. S. A.* **2014**, *111* (33), E3367−E3375.
(30) Kim, T.; Ham, S.; Lee, S. H.; Hong, Y.; Kim, D. Enhancement of Exciton Transport in Porphyrin Aggregate Nanostructures by Controlling the Hierarchical Self-Assembly. *Nanoscale* **2018**, *10* (35), 16438−16446.
(31) Marty, R.; Szilluweit, R.; Sánchez-Ferrer, A.; Bolisetty, S.; Adamcik, J.; Mezzenga, R.; Spitzner, E.-C.; Feifer, M.; Steinmann, S. N.; Corminboeuf, C.; Frauenrath, H. Hierarchically Structured Microfibers of "Single Stack" Perylene Bisimide and Quaterthiophene Nanowires. *ACS Nano* **2013**, *7* (10), 8498−8508.
(32) Haedler, A. T.; Meskers, S. C. J.; Zha, R. H.; Kivala, M.; Schmidt, H. W.; Meijer, E. W. Pathway Complexity in the Enantioselective Self-Assembly of Functional Carbonyl-Bridged Triarylamine Trisamides. *J. Am. Chem. Soc.* **2016**, *138* (33), 10539−10545.
(33) Valera, J. S.; Gómez, R.; Sánchez, L. Tunable Energy Landscapes to Control Pathway Complexity in Self-Assembled N-Heterotriangulenes: Living and Seeded Supramolecular Polymerization. *Small* **2018**, *14* (3), 1702437.
(34) Haedler, A. T.; Beyer, S. R.; Hammer, N.; Hildner, R.; Kivala, M.; Köhler, J.; Schmidt, H. W. Synthesis and Photophysical Properties of Multichromophoric Carbonyl-Bridged Triarylamines. *Chem. - Eur. J.* **2014**, *20* (37), 11708−11718.
(35) Hestand, N. J.; Spano, F. C. Expanded Theory of H- and J-Molecular Aggregates: The Effects of Vibronic Coupling and Intermolecular Charge Transfer. *Chem. Rev.* **2018**, *118* (15), 7069−7163.
(36) Sumi, H. Bacterial Photosynthesis Begins with Quantum-Mechanical Coherence. *Chem. Rec.* **2001**, *1* (6), 480−493.
(37) Scholes, G. D.; Jordanides, X. J.; Fleming, G. R. Adapting the Förster Theory of Energy Transfer for Modeling Dynamics in Aggregated Molecular Assemblies. *J. Phys. Chem. B* **2001**, *105* (8), 1640−1651.
(38) Beljonne, D.; Curutchet, C.; Scholes, G. D.; Silbey, R. J. Beyond Förster Resonance Energy Transfer in Biological and Nanoscale Systems. *J. Phys. Chem. B* **2009**, *113* (19), 6583−6599.

https://dx.doi.org/10.1021/jacs.0c01392
J. Am. Chem. Soc. 2020, 142, 8323−8330

(39) Akselrod, G. M.; Deotare, P. B.; Thompson, N. J.; Lee, J.; Tisdale, W. A.; Baldo, M. A.; Menon, V. M.; Bulovic, V. Visualization of Exciton Transport in Ordered and Disordered Molecular Solids. *Nat. Commun.* **2014**, *5* (1), 3646.
(40) Havlin, S.; Ben-Avraham, D. Diffusion in Disordered Media. *Adv. Phys.* **2002**, *51* (1), 187−292.
(41) Wu, J.; Berland, K. M. Propagators and Time-Dependent Diffusion Coefficients for Anomalous Diffusion. *Biophys. J.* **2008**, *95* (4), 2049−2052.
(42) Zehe, C. S.; Hill, J. A.; Funnell, N. P.; Kreger, K.; van der Zwan, K. P.; Goodwin, A. L.; Schmidt, H.-W.; Senker, J. Mesoscale Polarization by Geometric Frustration in Columnar Supramolecular Crystals. *Angew. Chem., Int. Ed.* **2017**, *56* (16), 4432−4437.
(43) Lloyd, S.; Mohseni, M. Symmetry-Enhanced Supertransfer of Delocalized Quantum States. *New J. Phys.* **2010**, *12* (7), 075020.
(44) Lee, C. K.; Shi, L.; Willard, A. P. Modeling the Influence of Correlated Molecular Disorder on the Dynamics of Excitons in Organic Molecular Semiconductors. *J. Phys. Chem. C* **2019**, *123* (1), 306−314.
(45) Saikin, S. K.; Shakirov, M. A.; Kreisbeck, C.; Peskin, U.; Proshin, Y. N.; Aspuru-Guzik, A. On the Long-Range Exciton Transport in Molecular Systems: The Application to H-Aggregated Heterotriangulene Chains. *J. Phys. Chem. C* **2017**, *121* (45), 24994−25002.

https://dx.doi.org/10.1021/jacs.0c01392
J. Am. Chem. Soc. 2020, 142, 8323−8330

Supporting Information

for

Enhancing Long-Range Energy Transport in Supramolecular Architectures by Tailoring Coherence Properties

Bernd Wittmann[1], Felix A. Wenzel[2,3], Stephan Wiesneth[1], Andreas T. Haedler[2,3], Markus Drechsler[4], Klaus Kreger[2], Jürgen Köhler[1], E. W. Meijer[3], Hans-Werner Schmidt*[2], Richard Hildner*[1,5]

Affiliations:

[1]Spectroscopy of Soft Matter, University of Bayreuth, Universitätsstraße 30, 95447 Bayreuth, Germany.

[2]Macromolecular Chemistry and Bavarian Polymer Institute, University of Bayreuth, Universitätsstraße 30, 95447 Bayreuth, Germany.

[3]Institute for Complex Molecular Systems, Laboratory of Macromolecular and Organic Chemistry, Eindhoven University of Technology, 5612 AZ Eindhoven, The Netherlands.

[4]Bavarian Polymer Institute, University of Bayreuth, Universitätsstraße 30, 95447 Bayreuth, Germany.

[5]Zernike Institute for Advanced Materials, University of Groningen, Nijenborgh 4, 9747 AG Groningen, The Netherlands.

*Correspondence to: r.m.hildner@rug.nl and hans-werner.schmidt@uni-bayreuth.de.

Table of Content

1. Materials and Methods

Materials. The synthesis, purification and characterization of compound **1** is described in detail elsewhere [1]. All solvents were of HPLC grade and used as received.

*Molecularly dissolved solution of compound **1***. A 40 µM solution of compound **1** in THF (boiling point: 66 °C) was refluxed for 20 minutes under stirring and allowed to cool to room temperature.

*Self-assembly of compound **1***. Compound **1** was added at a concentration of 40 µM (~100 p.p.m., 0.01 wt%) in n-dodecane (bp.: 216 °C) or anisole (bp.: 154 °C), respectively. A homogeneous dispersion was ensured by ultrasonication for 15 minutes. The dispersions were refluxed for 30 minutes under stirring and then allowed to cool to room temperature. The self-assembly process was monitored via UV/vis and PL spectroscopy until no spectral changes were detected. Subsequently, all samples were stored for 24 hours prior investigation.

AFM. For AFM measurements, we used silicon wafers as substrate. The self-assembled 40 µM dispersions were either spin-coated directly or spin-coated after dilution to a concentration of 4 µM. All samples were dried under vacuum. AFM images were recorded on a Dimension 3100 NanoScope V (Veeco Metrology Group). Scanning was performed in tapping mode using silicon nitride (Si_3N_4) cantilevers (OTESPA-R3, Bruker) with a typical spring constant of 26 N m^{-1} and a typical resonance frequency of 300 kHz. Image processing and analysis was conducted with the Gwyddion 2.52 software.

TEM and SAED. The self-assembled 40 µM dispersions were drop-cast on a carbon-coated copper grid and the solvent was removed with a filter paper. Finally, all samples were dried under vacuum. TEM images were recorded with a Zeiss / LEO EM922 Omega and a JEOL JEM-2200FS energy filtering transmission electron microscope (EFTEM) both operated at 200 kV in bright-field and diffraction mode. Zero-loss filtered micrographs ($\Delta E \sim 0$ eV) were recorded with bottom mounted camera systems. The Zeiss microscope was equipped with a CCD camera system (Ultrascan 1000, Gatan) and the JEOL microscope with a CMOS camera system (OneView, Gatan). Both camera systems were operated with an image acquisition and processing software (Digital Micrograph GMS 1.9 resp. 3.3).

UV/vis, photoluminescence and circular dichroism spectroscopy in solution. UV/vis absorption spectra were recorded on a Perkin Elmer Lambda750 spectrophotometer. Photoluminescence (PL) spectra were measured on a Varian Cary Eclipse at excitation wavelengths of 430 nm for n-dodecane dispersions and THF solutions and 380 nm for anisole dispersions. All PL spectra were corrected for reabsorption with the factor $\boldsymbol{k_{abs} = 10^{0.5\,OD(\lambda)}}$, where $\boldsymbol{OD(\lambda)}$ is the wavelength dependent absorbance. The PL quantum efficiency was measured on a JASCO FP-8600 spectrofluorometer equipped with an integrating sphere (ILF-835). Circular dichroism spectra were recorded on a Jasco J-715 spectrophotometer. All measurements were conducted with Hellma QS quartz-glass cuvettes.

Optical imaging and spectroscopy of single supramolecular nanofibres and bundles. The 40 µM-dispersions were either diluted to 4 µM before spin-coating, or spin-coated undiluted on microscopy cover slips (borosilicate glass; thickness 0.17 µm; Carl Roth). All samples were dried under vacuum. Optical imaging and spectroscopy was performed using a home-built microscope (Fig. S11). The excitation source was a pulsed diode laser (LDH-P-C-450B, Picoquant; 2.5 MHz repetition rate, 70 ps pulse duration) that operates at a wavelength of 450 nm. The laser light was spatially filtered and directed to the microscope, which was equipped

with an infinity-corrected high-numerical aperture oil-immersion objective (PlanApo, 60×, numerical aperture 1.45; Olympus). The sample was placed in the focal plane of the objective, and the sample position was controlled by a piezo-stage (Tritor 102 SG, from piezosystem jena). Photoluminescence was collected by the same objective and passed a set of dielectric filters (dichroic beam splitter z460RDC, long-pass filter LP467; AHF Analysentechnik) to suppress scattered or reflected laser light.

The detection beam path is equipped with a closed-loop piezo scan mirror (S-335.2.SH, PI) and a single-photon-counting avalanche photodiode (MPD, Picoquant) to position the detection spot independently from the confocal excitation spot (Fig. S11). The electrical signal of the photodiode was fed into a time-correlated single-photon-counting module (TimeHarp 260 PICO, Picoquant).

In imaging mode, the photoluminescence signal was imaged onto a CMOS camera (Zyla 4.2 sCMOS, Andor). In this mode, we used two illumination methods. First, for widefield illumination we flipped an additional lens (widefield lens) into the excitation beam path to focus the laser light into the back-focal plane of the microscope objective. This allows for nearly uniform illumination of a large area with ∼70 µm diameter in the sample plane, to acquire overview PL images of our samples and to identify elongated nanostructures (Fig. 4A and 4B). Second, for confocal illumination the widefield lens was removed and the laser light was tightly focused to a spot with a half width at half maximum of ∼170 nm in the sample plane. A flip-mirror allows to switch between imaging and single-photon counting mode of the setup.

For measurements on single supramolecular nanofibres and bundles, the excitation intensities were below 140 W cm^{-2} for confocal illumination and 1.3 W cm^{-2} for widefield illumination These intensities correspond to a maximum excitation probability of 0.1 absorbed photon per pulse per 3000 CBT-cores along a column and confirm that our experiments are conducted in a regime where annihilation does not play a role. All experiments were carried out at room temperature under ambient conditions.

Numerical Simulations. For the numerical simulation of the absorption and PL spectra shown in Fig. 3B,C we used home-written Matlab-scripts. The electronic Coulomb coupling between CBT-cores along a column was treated in nearest-neighbour approximation. The transition energies of the CBT-cores were taken from a Gaussian distribution with width σ. To account for different degrees of intra-column electronic disorder, a correlation length l_0 was introduced, i.e., with increasing l_0, the distribution of transition energies within a column becomes smoother (see Fig. 3D). To model the experimental spectra we averaged over 10^4 realisations of electronic disorder and performed a residual analysis. Further details are outlined in the Supplementary Materials, Fig. S9 and S10 and section 5.

2. Characterisation of Supramolecular Architectures of Compound 1

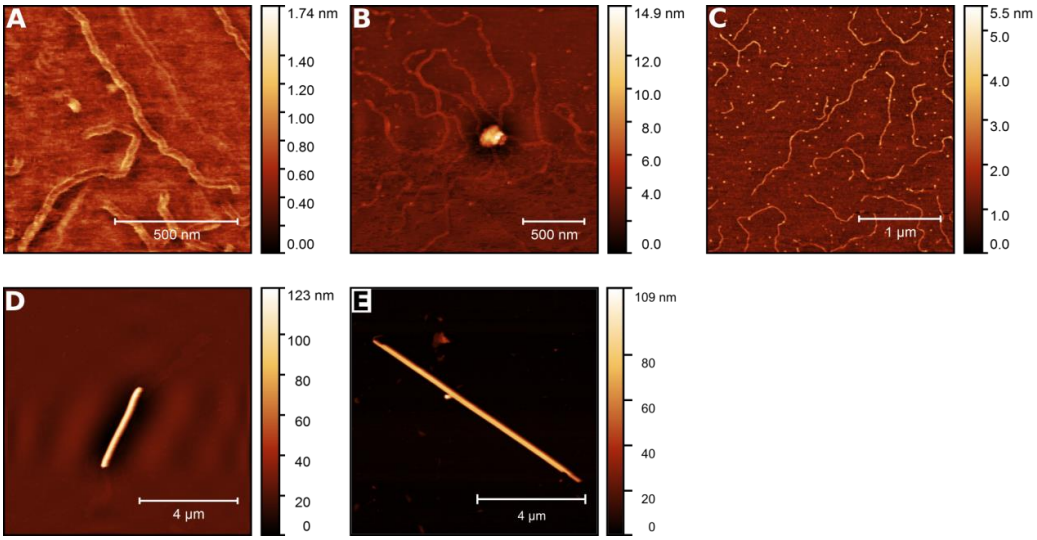

Fig. S1: AFM images of single supramolecular nanofibres and bundles of nanofibres. A-C) AFM images (topographical scan) of single nanofibres spin-coated from a dispersion of compound **1** in n-dodecane (**A,B**: 40 µM; **C**: 4 µM) demonstrating the presence of single nanofibres at concentrations of 4 µM as well as of 40 µM. The discrepancy between the heights and the diameters of the nanofibres, as determined by AFM (2–2.5 nm) and molecular modelling (4.4 nm) [2], respectively, is a known phenomenon [3,4]. **D,E)** AFM images (topographical scan) of bundles of nanofibres spin-coated from a dispersion of compound **1** in anisole at a concentration of 40 µM.

3. Selected Area Electron Diffraction of Bundles of Supramolecular Nanofibres

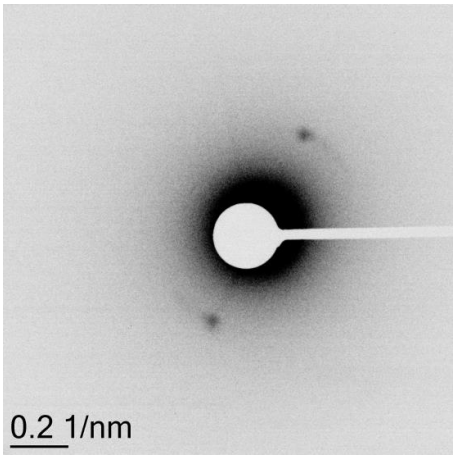

Fig. S2: Selected Area Electron Diffraction (SAED) at smaller angles. SAED pattern from a sample as in Fig. 2G (prepared from a dispersion of self-assembled compound **1** in anisole, concentration 40 μM), which reveals sharp signals corresponding to a distance of 2.8 nm. Assuming a columnar hexagonal packing of nanofibres within bundles [1], this plane-plane distance corresponds to an intercolumnar spacing of 3.23 nm.

4. Optical Spectroscopy and Spectroscopic Characteristics of H-Aggregates

Franck-Condon Analysis of Absorption and PL Spectra

For the Franck-Condon analysis of the PL and absorption spectra of molecularly dissolved compound **1** in THF (Fig. 3A) we assume coupling of the electronic transition to a single effective vibrational mode (carbon-bond stretch). In this situation, the normalized spectra for PL $I_{PL}(\omega)$ and for absorption $I_{Abs}(\omega)$ can be described by [5]

$$\frac{I_{PL}(\omega)}{n^3\omega^3} \propto \sum_m \frac{S^m}{m!} e^{-S} \Gamma[\omega - (\omega_{0-0} - m\omega_0)] \qquad (1)$$

$$\frac{I_{Abs}(\omega)}{n\omega} \propto \sum_m \frac{S^m}{m!} e^{-S} \Gamma[\omega - (\omega_{0-0} + m\omega_0)] \qquad (2)$$

Here S is the Huang–Rhys factor for the effective vibrational mode with energy ω_0, $\omega_{0\text{-}0}$ is the energy of the purely electronic 0–0 transition, $m = (1,2,\dots)$ denotes the vibrational quantum number and n is the refractive index. Γ is the Gaussian (inhomogeneous) line width function with a standard deviation σ, which we allow to be different for the electronic and vibronic transitions (the effective mode is typically a superposition of several modes that are closely spaced and that give rise to a larger "effective" inhomogeneous line width for the ensemble vibronic transition).

To describe both the absorption and the PL with the same Huang-Rhys factor S and vibrational energy ω_0, we fit absorption and PL simultaneously. The parameters for the best fit are shown in Tab. S1.

Tab. S1: Franck-Condon analysis of the absorption and PL spectra of molecularly dissolved compound 1 in THF.

	S	ω_{0-0}/eV	ω_0/eV	σ_{0-0}/eV	$\sigma_{0-1,2..}/eV$
Abs.	0.54 ± 0.02	2.664 ± 0.003	0.157 ± 0.005	0.090 ± 0.002	0.133 ± 0.008
PL	0.54 ± 0.02	2.544 ± 0.003	0.157 ± 0.005	0.082 ± 0.003	0.105 ± 0.008

Concentration-Dependent Absorption Spectra of Compound 1 in Anisole

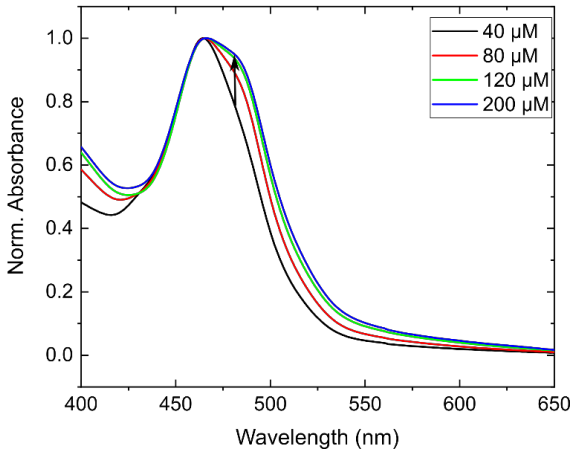

Fig. S3: Concentration-dependent absorption spectra of compound 1 in anisole. Due to the remaining solubility of compound **1** at low concentrations (40 µM, black) in anisole, the absorption is a superposition of the absorption of molecularly dissolved compound **1** and of bundles of nanofibres. We therefore increased the concentration until no further spectral changes occurred (at 200 µM, blue), i.e., mainly bundles of nanofibres exist in the anisole dispersion.

Circular-Dichroism Spectroscopy

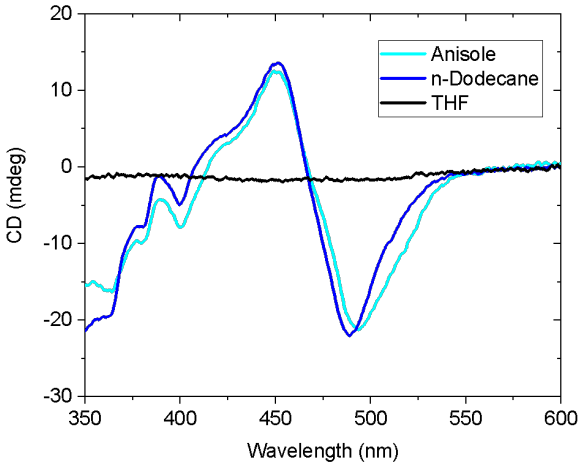

Fig. S4: Circular dichroism spectroscopy of compound 1. Circular dichroism spectra of compound **1** in THF (molecularly dissolved, black), n-dodecane (single supramolecular nanofibres, blue) and anisole (bundles of supramolecular nanofibres, cyan), each recorded at a concentration of about 40 µM (~100 ppm) at room temperature. While there is no circular-dichroism signal for the molecularly dissolved building block in THF, aggregates formed in n-dodecane and anisole exhibit a nearly identical circular-dichroism activity, which suggests a comparable structural arrangement within the columns of the supramolecular aggregates [6].

Optical Absorption and PL Spectra of Molecular Aggregates

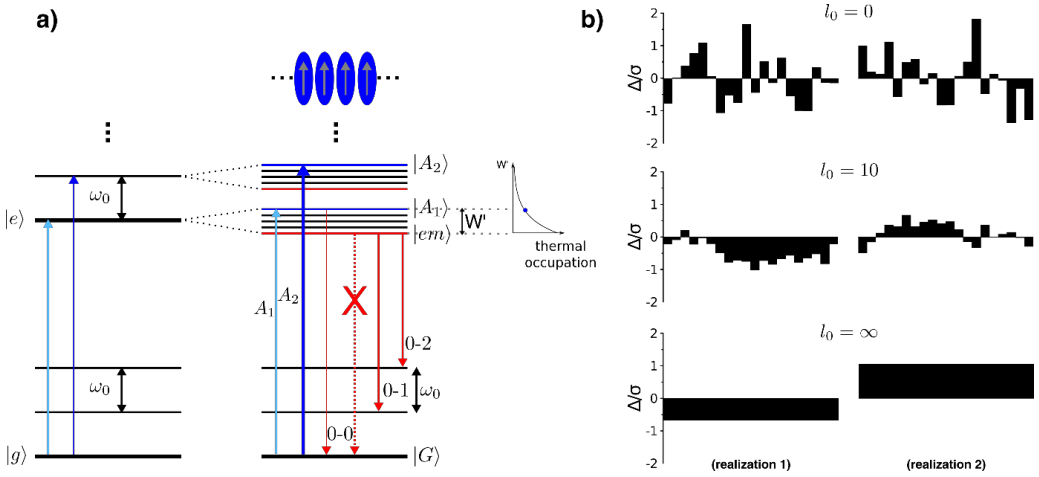

Fig. S5: Spano model of H-type assemblies. a) Left: Energy level scheme for a molecule with an intra-molecular vibrational mode of energy w_0, coupling to the electronic transition between electronic ground $|g\rangle$ and excited electronic state $|e\rangle$. Right: Upon electronic Coulomb coupling between molecules a progression of vibronic exciton bands is formed, separated in energy by the vibrational energy w_0 and with an exciton bandwidth W'. The optically accessible exciton states, labelled $|A_1\rangle, |A_2\rangle, ...$, are located at the top of each band (blue solid lines), while emission occurs only from the lowest-energy exciton state $|em\rangle$ (red solid line). In a perfect H-aggregate the 0-0 transition from $|em\rangle$ into the ground state $|G\rangle$ is optically forbidden, while the 0-1, 0-2, … transitions are still allowed. Thermal energy populates (optically allowed) higher-energy exciton states in the lowest-energy exciton band. Hence, with increasing temperature an increasing intensity of the 0-0 PL intensity is observed. Solid coloured arrows indicate the allowed optical transitions [7,8]. **b)** Six realisations of correlated site-energy disorder along an aggregate. Left and right column depict two different realisations of transition energy offsets Δ_n of an aggregate consisting of N=20 monomers for three correlation lengths l_0 (increasing from the top to the bottom) [7,9].

The optical spectra of organic molecules show a pronounced vibronic progression (Fig. 3A). This electron-phonon coupling of intra-molecular vibrations (typically carbon-bond stretch modes with energies $\omega_0 \approx 1400 - 1600\ cm^{-1}$) to electronic transitions is characterised by the Huang-Rhys parameter *S*. In the simplest picture, each molecule is described as a two level system, which couples to one (effective) intra-molecular vibration with the vibrational energy ω_0 (Fig. S5a, left).

If organic molecules are densely assembled in an aggregate, their transition dipole moments interact via electronic Coulomb coupling J_0 (in nearest-neighbour approximation). To include the influence of electron-phonon coupling on the aggregate spectra, Spano *et al.* [6–9] introduced one- and two-particle states. A one-particle state $|n, \tilde{v}\rangle$ consist of one vibronically excited molecule n, i.e., molecule n is in its electronically excited state with $\tilde{v} \geq 0$ vibrational quanta, and all other molecules of the aggregate are in their vibrationless electronic ground state. For two-particle states $|n, \tilde{v}, n', v'\rangle$, in addition to the vibronic excitation of molecule n, molecule $n'(\neq n)$ is in a vibrational excited state $v' \geq 1$ of its electronic ground state. The αth eigenstate of the aggregate can then be written as a superposition of one- and two-particle states,

$$|\Psi^{\alpha}\rangle = \sum_{n,\tilde{\nu}} c^{\alpha}_{n,\tilde{\nu}} \; |n,\tilde{\nu}\,\rangle + \sum_{n,\tilde{\nu}} \; \sum_{n',\nu'} c^{\alpha}_{n,\tilde{\nu},n',\nu'} \; |n,\tilde{\nu},\, n',\nu'\rangle, \qquad (3)$$

where the wave function coefficients c_j^i are obtained via diagonalization of the Hamiltonian of the system.

Now a series of vibronic exciton bands form (Fig. S5a, right) that feature a reduced bandwidth W' compared to the free exciton bandwidth $W = 4|J_0|$ due to electron-phonon coupling. In perfect, disorder-free systems, vibronic excitons are delocalised over the entire aggregate. For H-aggregates only transitions from the ground state to the highest-energy exciton of each band are allowed. These optically accessible states are labelled $|A_{i+1}\rangle$ $(i = 0,1, \dots)$ and correlate to the $0 - i$ transitions of the isolated molecule (Fig. S5 a). Consequently, the optically accessible vibronic exciton states show up as a progression of peaks with an energy difference of ω_0 in the absorption spectrum. Furthermore, as the coupling J_0 rises, the oscillator strength is increasingly redistributed towards higher energy bands (e.g. from $|A_1\rangle \; to, |A_2\rangle, \dots$), leading to a decreased $|A_1\rangle$ intensity compared to the monomer 0-0-intensity in absorption. Hence, the relative intensity of the $|A_1\rangle$ absorption is a direct measure for the magnitude of the electronic Coulomb coupling.

PL takes place from the lowest-energy exciton state $|em\rangle$ of the lowest-energy vibronic exciton band. Absence of disorder leads to a highly symmetric exciton wave function for this state with alternating sign of wavefunction coefficients between consecutive monomers, leading to destructive interference of the 0-0-intensity compared to the monomer PL spectrum. Hence, in ideal H-aggregates the 0-0-peak in emission is completely suppressed, while the remaining progression (0-1, 0-2, etc.) is still visible, because momentum conservation is satisfied by simultaneously exciting a vibration in the electronic ground state.

If PL spectra are recorded at temperatures $T \neq 0$K, states above the lowest-energy exciton state become thermally accessible (thermally activated emission), i.e., PL stems no longer exclusively from the lowest-energy exciton state $|em\rangle$. For ideal H-aggregates, increasing temperature thus leads to an enhanced 0-0 PL intensity. As the bandwidth *W'* of the lowest-energy exciton band rises, thermal occupation of higher-energy exciton states becomes less likely (for a given temperature, see Fig. S5a, right, thermal occupation of states), i.e., the 0-0 PL intensity is determined by the ratio between the thermal energy and the exciton bandwidth *W*.

Until now we considered disorder-free aggregates with excitons being delocalised over the entire aggregate ($N_{coh} = N$, N_{coh} is the number of coherently coupled molecules). In real aggregates, structural and electronic disorder is present, which localises excitons ($N_{coh} < N$).

Because of electronic disorder, the transition energies of the individual molecules of the aggregate are distributed around an average transition energy ϵ_0. For a description of this distribution, the individual transition energy offsets Δ_n are chosen from a joint Gaussian distribution [9]

$$P(\Delta_1, \dots, \Delta_N) = \left[\frac{1}{\sqrt{2\pi}}\right]^N \frac{1}{\sqrt{det\, A}} exp[-0.5 \sum_{n.m=1} (A^{-1})_{nm} \Delta_n \Delta_m \,] \qquad (4)$$

where $(A^{-1})_{nm}$ are the elements of the inverse of the covariance matrix A. The matrix elements are given by

$$A_{nm} = \sigma^2 e^{-\frac{|n-m|}{l_0}}, \qquad (5)$$

where σ is a measure for the disorder strength, defined as $\sigma \equiv \sqrt{\langle \Delta_n^2 \rangle}$ ($\langle \dots \rangle$ denotes the mean over all realizations). l_0 describes the spatial correlation of transition energies in units of monomers. For $l_0 = 0$ each transition energy offset Δ_n is chosen independently from a Gaussian distribution. In the opposite limit of infinite spatial correlation ($l_0 = \infty$) each monomer within one aggregate exhibits the same energy and disorder is entirely inter-aggregate, see Fig. S5b. By means of correlated energy disorder, inter-aggregate (disorder between aggregates, parameter σ) as well as intra-aggregate electronic disorder (within one aggregate, parameter l_0) is taken into account.

Qualitatively, at $T = 0K$ and for increasing disorder (increasing σ and/or decreasing l_0) the 0-0 PL intensity increases, due to the broken symmetry in the exciton wave function. Moreover, the 0-0 PL intensity is a strong function of N_{coh}, in contrast to the sideband PL 0-1, 0-2, etc. [9]. Therefore, the 0-0 PL-intensity reports on the degree of coherence of the emitting exciton, in particular, the number of coherently coupled molecules N_{coh} can be determined from

$$N_{coh} \equiv \frac{1}{\langle C^{em}(0) \rangle} \sum_{s=-(N-1)}^{N-1} |\langle C^{em}(s) \rangle| . \quad (6)$$

Here, the coherence function for the emitting exciton $|em\rangle$, i.e., the delocalisation of the vibronically excited centre of mass of the exciton, is defined as [9]

$$C^{em}(s) = \sum_n \sum_{\tilde{\nu},\tilde{\nu}'} f_{\tilde{\nu},0}\, f_{\tilde{\nu}',0}\, c_{n,\tilde{\nu}}^{em}\, c_{n+s,\tilde{\nu}'}^{em}, \quad (7)$$

where $f_{\tilde{\nu},\nu}$ are the vibrational overlap factors, $c_{n,\tilde{\nu}}^{em}$ are the one-particle coefficients and n counts the monomers along the aggregate.

For example, for aggregates without disorder ($\sigma = 0\ and/or\ l_0 = \infty$) and periodic boundary conditions $N_{coh} = N$.

Note that motional narrowing should be in principle observable in our data. However, motional narrowing affects mainly the 0-0 PL peak line width, which is largely suppressed in our supramolecular nanofibres. Also the probability of the presence of energetically low-lying states in an aggregate decreases with increasing correlation length l_0 [9]. Consequently, the linewidths in emission decrease only slightly with increasing size of the aggregates.

Temperature-Dependent PL Spectroscopy of Compound 1 in n-Dodecane

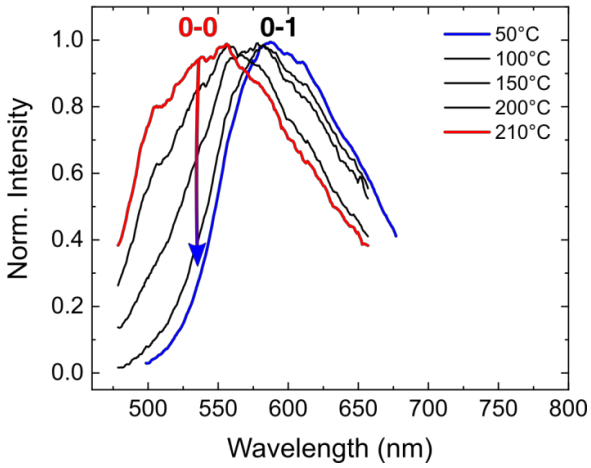

Fig. S6: Temperature-dependent PL spectra of compound 1 in n-dodecane. To support our assignment of the 0-0 and 0-1-peak in the PL spectrum taken from a dispersion of compound **1** in n-dodecane at room temperature (Fig. 3B), we performed temperature dependent PL-spectroscopy on this dispersion. Upon cooling from 210 °C to room temperature, the 0-0 peak decreases continuously. For these measurements, the dispersions are filled in Hellma QS quartz-glass cuvettes at a concentration of 40 µM (100 ppm). The cuvettes were placed inside an aluminium block on a heating plate. The excitation source was a continuous-wave laser that operates at a wavelength of 405 nm. The PL passed a dielectric filter (long-pass filter LP467; AHF Analysentechnik) and was focussed onto the entrance slit of a spectrograph (SpectraPro 2150, Princeton, 300 grooves per millimetre, blaze wavelength 500 nm) equipped with a CCD camera (pco.pixelfly usb, PCO).

Correction of Bundle PL Spectra

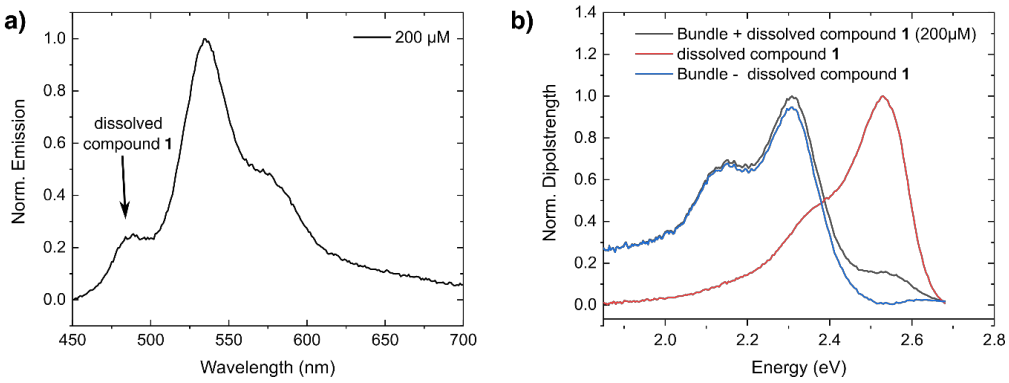

Fig. S7: Correction of the PL spectrum of compound 1 in anisole. a) Raw PL-spectrum of compound **1** in anisole at a concentration of 200 µM at room temperature. The peak at 490 nm stems from molecularly dissolved compound **1** in the dispersion due to some degree of remaining solubility. The stronger signal at longer wavelengths (> 510 nm) corresponds to PL from bundles of nanofibres. **b)** To obtain exclusively the PL spectrum of bundles (without monomer contribution), we converted the PL spectrum to an energy scale $I_{PL}(E)$ and to dipole strength via $I_{DP}(E) \propto I_{PL}(E)/E^3$, black curve. We then subtracted a converted, scaled and slightly shifted (0.01 eV) molecularly dissolved spectrum of compound **1** (red curve) from the measured and converted PL. The blue curve shows the resulting dipole strength of bundles of nanofibres.

Excited-State Lifetimes, Radiative Rates and PL Quantum Yields (PL-QY)

The PL decay was recorded by time-correlated single-photon counting (Fig. S8). For bundles an additional long-pass filter LP545 (AHF Analysentechnik) was used to suppress the monomer emission. The PL decay of dissolved compound **1** (THF) shows an exponential behaviour, see table S2.

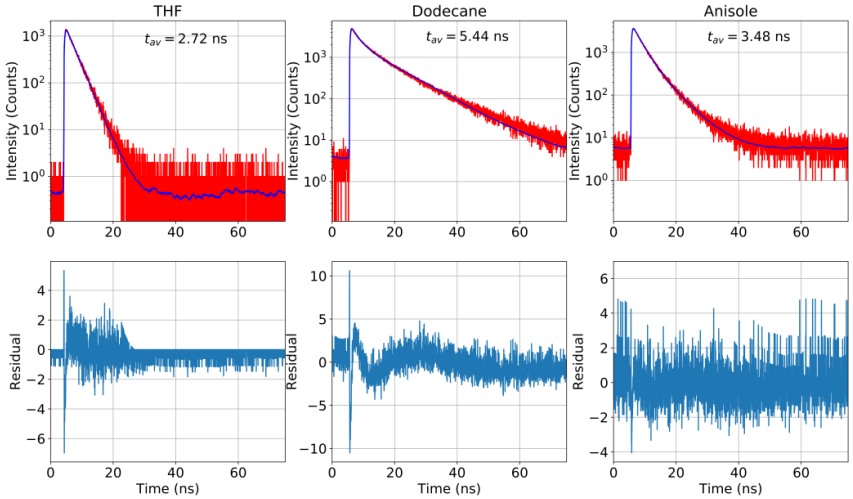

Fig. S8: PL-lifetime measurements. Left: Molecularly dissolved compound **1** in THF, middle: Single nanofibres in n-dodecane, right: Bundles of nanofibres in anisole. Top row: Time-correlated single-photon counting data (red) with fit function (blue). Bottom row: Weighted residuals. For all measurements, the concentration was 40 µM.

For both single supramolecular nanofibres (in n-dodecane) and for bundles of nanofibres (anisole) we found a bi-exponential PL decay with time constants t_i (relative amplitudes F_i) of $t_1 = 2.26\,ns$ ($F_1 = 3705.7$) and $t_2 = 10.45\,ns$ ($F_2 = 2353.59$), respectively $t_1 = 2.65\,ns$ ($F_1 = 3470.49$) and $t_2 = 5.97\,ns$ ($F_2 = 1144.86$). From these numbers we calculated the amplitude-averaged lifetime

$$t_{av} = \frac{\sum F_i t_i}{\sum F_i}. \qquad (8)$$

Tab. S2: PL-QY, excited-state lifetime and radiative lifetimes of (self-assembled) compound 1 in THF, n-dodecane and anisole (concentration: 40 µM).

	PL-QY	Excited state lifetime t_{av}	Radiative lifetime τ_r
THF	13.79 %	2.72 ns	19.72 ns
n-Dodecane	1.30 %	5.44 ns	418.46 ns
Anisole	2.58 %	3.48 ns	134.88 ns

5. Numerical Simulations of Experimental Spectra

To determine the electronic Coulomb coupling J_0 between the CBT-cores, the electronic disorder σ and the correlation length l_0 along the columns (single nanofibres as well as in bundles), we simulated the optical spectra of self-assembled compound **1** based on the numerical solution of a disordered Holstein Hamiltonian [6–9] and a residual analysis between simulation and data (Fig. 3B,C). The size of each nanofibre was limited for most of the cases to N = 20 CBT-cores for two reasons: First, this reduces the computational effort if combined with a truncation of the two-particle basis set (i.e., the position of the vibrationally excited molecule with respect to the vibronically excited molecule, see Fig. S5a; e.g. CutOff = 3: the vibrationally excited molecule sits at most three units away). Second, the 0-0 PL intensity is almost independent of N [9] and for N > 20 the absorption spectra remain unchanged [6]. Finally, we shifted the calculated spectra in energy to fit the measurements, which accounts for the (unknown) change of non-resonant dispersive interactions [8] when going from molecularly dissolved compound **1** to self-assembled compound **1**.

Usually, absorption spectra are used to determine the exciton bandwidth $W = 4J_0$. Unfortunately, our broad absorption spectra (Fig. 3B,C) made an unambiguous retrieval of all parameters (σ, J_0, l_0) impossible. We started therefore with the PL spectrum of isolated supramolecular nanofibres with its unique feature - the largely suppressed 0-0 peak intensity (Fig. 3B), which is approximately a function of $(l_0, \frac{\sigma}{W})$ [9]. We obtained then a *lower bound* for W for a maximised correlation length, i.e., $l_0 = \infty$ (see below for details). Based on these values for W the parameters W, σ and l_0 were further refined to reproduce all measured spectra of the different supramolecular morphologies. We exploited that the electronic Coulomb coupling J_0 (and thus the exciton bandwidth W) must be very similar in both isolated nanofibres and bundles of nanofibres, because the $\pi - \pi$-distance between CBT-cores (Fig. 2), the absorption spectra (Fig. 3B,C) as well as the circular dichroism spectra (Fig. S4) are almost identical for both morphologies.

Overall, we were able to reproduce the experimental spectra in Fig. 3 with good agreement using the following set of parameters:

$$W \approx 4.3\, S\omega_0\,,$$
$$\sigma \approx 0.85\, \omega_0,$$

$l_0 \approx 10$	for single nanofibres in n-dodecane,
$l_0 \approx 0$	for bundles of nanofibres in anisole.

The parameters $S = 0.54$ and $\omega_0 = 0.157$ were determined by a Franck-Condon analysis of the PL and absorption spectra of molecularly dissolved compound **1** in THF (see Tab. S1).

Simulation of the PL of isolated nanofibres:
We varied W within the interval $W = S\omega_0\,[2, 2.5, \ldots, 6]$ to reproduce the suppressed 0-0 PL peak of the isolated nanofibres, and the energy disorder σ within the interval $\sigma = \omega_0[0.75, 0{,}8, \ldots, 1.05\,]$ to reproduce the linewidth. Smaller values of W did not describe the suppressed 0-0 PL intensity of isolated nanofibres at room temperature. For a correlation length of $l_0 = \infty$ the smallest residual for a truncation CutOff = 3 was obtained for $W = 5.5\ \omega_0\ S$ and $\sigma = 0.85\ \omega_0$ (Fig. S9a and black dashed curve in Fig. 3B). Also a more accurate calculation with a truncation of CutOff = 6 (Fig. S9b) led to nearly identical results, and the residuals ran

into a minimum for $W \geq 4.0\ \omega_0 S$ and $0.80\ \omega_0 \leq \sigma \leq 0.90\ \omega_0$. Note that *the values for W represent lower bounds*, because the correlation length was maximised.

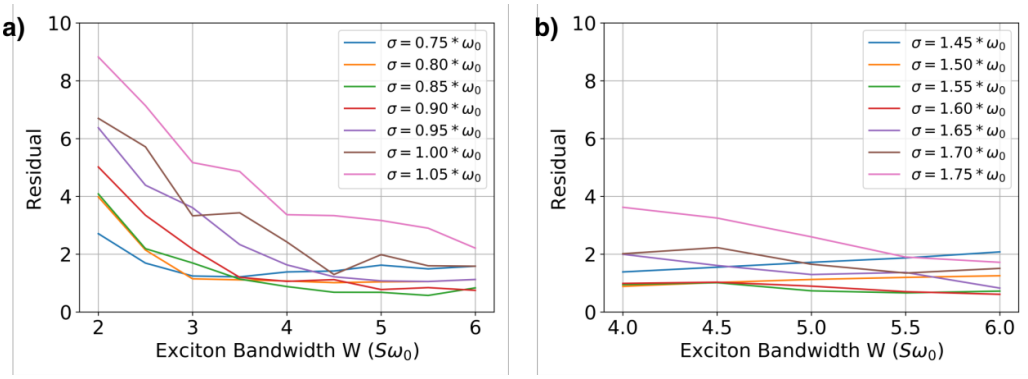

Figure S9: Residual analysis for the PL-spectrum of isolated nanofibres. a) Residuals for a calculation with truncation of CutOff = 3. b) Residuals for a calculation with a truncation of CutOff = 6**.**

Simulation of the absorption of isolated nanofibres and bundles of nanofibres:
Since the absorption depends only weakly on l_0 (because σ is of the order of W [10]), we also set $l_0 = \infty$ for the simulation of the absorption spectra and performed a residual analysis for W and σ. To be consistent with the simulation of the PL we limit the intervals to $W = S\omega_0\ [4, 4.1, \ \ldots, 5.5]$ and $\sigma = \omega_0 [0.75, 0.76, \ldots, 0.85\ ]$. For both single nanofibres and bundles the smallest residual was obtained for $W = 4.3\ \omega_0\ S$ and $\sigma = 0.84\ \omega_0$, see Fig. 3B,C (black lines).

Simulation of the PL of bundles of nanofibres:
Here, the challenge was to reproduce a "monomer-like" PL spectrum with a relatively large value of $W = 4.3\ \omega_0\ S$ for the exciton bandwidth. We took two steps: (i) We increased the disorder within the nanofibres in bundles by setting $l_0 = 0$, and (ii) we increased the number of monomers to N = 60 to increase the probability of finding monomers with site energies in the bottom tail of the Gaussian inhomogeneous distribution. For computational reasons, we chose a truncation of CutOff = 1. The PL spectrum in anisole, in particular the pronounced 0-0 PL intensity, can then be reproduced with the parameters $W = 4.3\ \omega_0\ S$ and $\sigma = 0.8$. Note, in order to get a good fit for higher values of σ, i.e. $\sigma = 0.85\ \omega_0$, the size of the nanofibres N have to be increased further. Importantly, a heavy-tailed Levy-type disorder [11] is not required to produce "monomer-type" PL spectra from molecular aggregates.

Coherence length* $\mathbf{N_{coh}}$ *for nanofibres and bundles of nanofibres:

Finally, we refined the value of l_0 to obtain an estimate for the coherence length N_{coh} in isolated nanofibres in n-dodecane. We chose the values determined above for $W = 4.3\ \omega_0\ S$ and $\sigma = 0.85\ \omega_0$ and performed a residual analysis for the PL spectrum with respect to l_0. To describe the suppresses 0-0 PL peak we restricted the spectral region to 486 nm - 600 nm (Fig. S10a). Furthermore, we used N = 40 monomers per nanofibre to minimize boundary effects and a truncation of CutOff = 3 to minimize computational efforts. From the best fit we found that $l_0 \approx 10$ CBT-cores, which leads to the coherence number $N_{coh} = 5.44$ CBT-cores (Fig. S10 b). Note, that as a consequence of our underestimated value for the coupling, this correlation length and coherence number itself is *a lower limit only*.

We obtained a coherence number for the bundles of $N_{coh} = 2.94$ CBT-cores, using $W = 4.3\ \omega_0\ S$; $\sigma = 0.85\ \omega_0$; $l_0 = 0$ and $N = 60$ CBT-cores from the simulation of the of the bundle PL (see above). Note, that this coherence number decreases with increasing N.

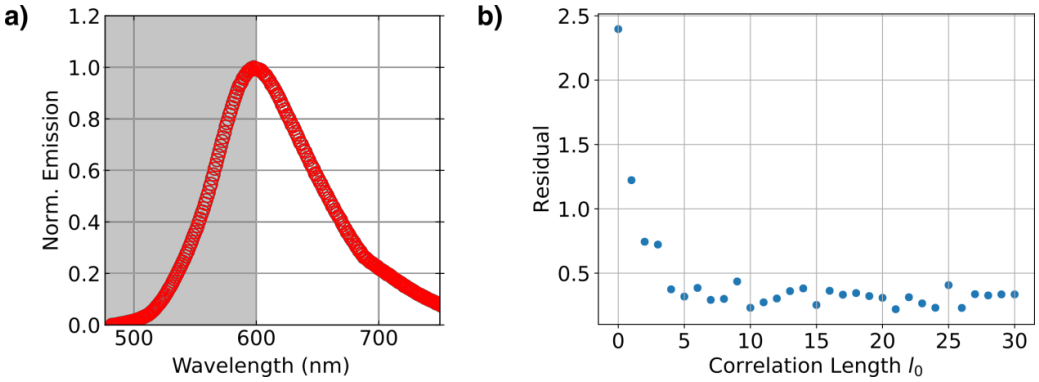

Figure S10: Coherence length in isolated nanofibres. a) PL spectrum of single supramolecular nanofibres in n-dodecane. The area highlighted in grey indicates the spectral region used for the residual analysis. **b)** Results of the residual analysis for the area highlighted in grey in a). The correlation length is given in units of CBT-cores along a nanofibre.

6. Experimental Setup

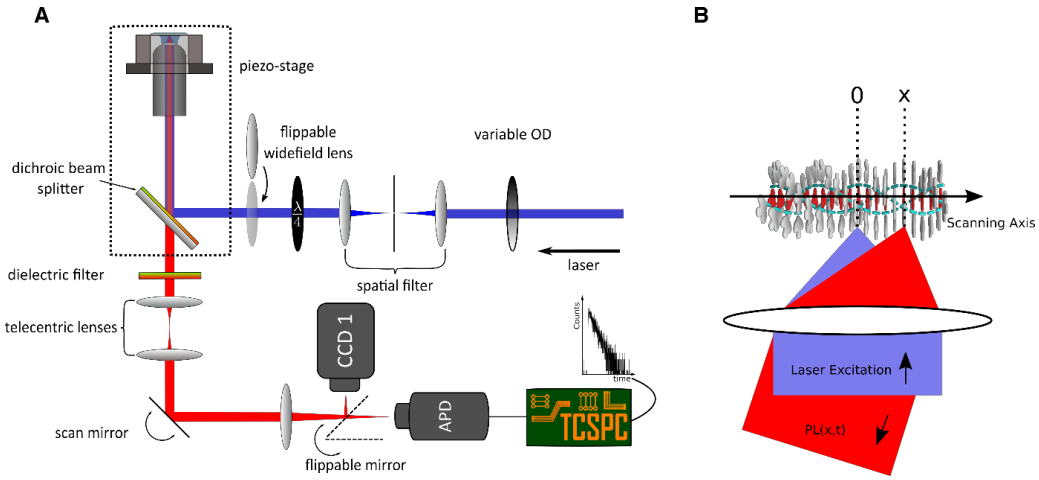

Fig S11: Experimental Setup. A) Optical setup with detection-beam scanning capabilities. For details, see 1. Materials and Methods. **B)** Schematic illustration of detection-beam scanning [modified, [12]]. During the entire detection-beam scan, the confocal excitation spot remains at the same position of the nanostructure, while the detection position imaged onto the APD is independently moved with the scan mirror.

To characterise the setup in Fig. S11, we used agglomerated SiOx-nanobeads (Corpuscular, diameter 52 nm), because energy transport between the nanobeads is negligible and a time-dependent broadening of the PL profile is not expected. Fig. S12 displays the results of detection-beam scanning on these nanobeads.

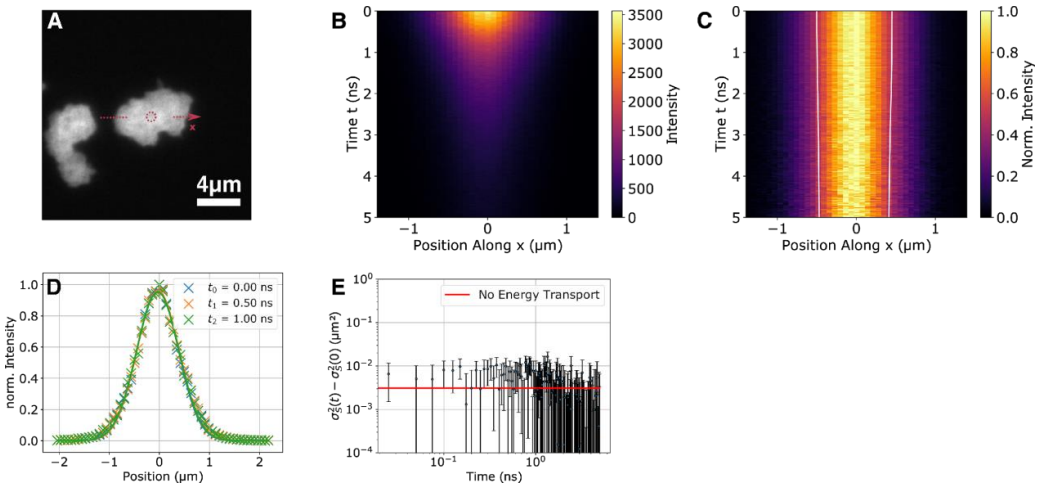

Fig. S12: Control experiment. A) Widefield PL image of agglomerated SiOx-nanobeads. The dashed red circle and arrow illustrate the position of confocal excitation and the direction of the detection scanning (x-axis), respectively. **B)** Spatio-temporal PL intensity distribution $I(x,t)$. **C)** Normalized PL intensity distribution as it evolves in space and time, measured along the axis illustrated by the red dashed arrow in A). The position x denotes the distance relative to the excitation position (x=0) along the arrow in A), and t = 0 ns corresponds to the arrival time of the excitation pulse. To emphasize changes in the width of the distribution, it is normalized at each time step. The contour lines indicate the time evolution of the full width at half maximum. **D)** Illustration of the normalized spatial intensity distribution $I(x,t_i)$ for three times t_i and the corresponding Gaussian fits, yielding e.g. a standard deviation of $\sigma_I\,(t=0) = 411\,nm$. Note that this number is determined by the convolution of the Gaussian excitation profile, the detection point-spread function and the detector chip size. **E)** Temporal changes of the second moments of the singlet excitons, revealing no resolvable energy transport in agglomerated SiOx-nanobeads.

7. Incoherent Exciton Diffusion Model

The extended diffusion equation for 1-dimensional incoherent transport with an exponential decay of the excitations reads [13–15]

$$\frac{\partial n(x,t)}{\partial (t)} = D(t)\frac{\partial^2 n(x,t)}{\partial x^2} - kn(x,t), \qquad (9)$$

where $n(x,t)$ is the exciton distribution that depends on both space and time. $D(t)$ is the time-dependent diffusivity that is related to an exciton hopping coefficient A by $D(t) = \frac{1}{2}A_\alpha t^{\alpha-1}$ with fractional time units for A [16]. Finally, k is the constant exciton decay rate.

Superdiffusive transport is characterized by $\alpha > 1$. For normal diffusion, $\alpha = 1$, the diffusivity $D = \frac{1}{2}A$ is time independent with units of cm^2s^{-1}. Subdiffusion is characterized by $\alpha < 1$ and occurs for exciton motion in a disordered excited-state energy landscape [17,18].

In our experiments the diffraction-limited confocal excitation spot creates to a good approximation an exciton population with a Gaussian profile and a standard deviation of σ. The solution to equation (9) is given then

$$n(x,t) \propto exp\left(-\frac{x^2}{2\sigma^2+2At^\alpha}\right) exp\,(-k\,t)\,. \qquad (10)$$

Note that the exponential decay ($exp\,(-kt)$) for the exciton population in equation (10) only changes the magnitude of this distribution at any point in time (and not its shape) and vanishes upon normalization to its maximum value at a given time, see Fig. 4C,D.

Equation (10) shows that the variance of the exciton distribution, which is also called the mean square displacement MSD $\langle x(t)^2\rangle$, evolves in time as [13,14]

$$\langle x(t)^2\rangle = \sigma_n^2(t) = \sigma^2 + At^\alpha, \qquad (11)$$

In a general situation with electronic disorder in the excited-state energy landscape the time-dependent diffusivity $D(t) = \frac{1}{2}A_\alpha t^{\alpha-1}$ decreases with time [15,16] (Fig. S14).

For normal diffusion ($\alpha = 1$), equation (12) transforms to

$$\langle x(t)^2\rangle = \sigma_n^2(t) = \sigma^2 + 2Dt. \qquad (12)$$

In general, the measured spatial intensity distribution (e.g. Fig. 4C,D) is a convolution of the exciton distribution $n(x,t)$, the detection point spread function $PSF(x)$ and the function of the APD detector size $C(x)$

$$I(x,t) = n(x,t) * PSF(x) * C(x). \qquad (13)$$

The PSF can be well approximated by a Gaussian function. The APD detector size is 50 µm and if the magnification of the setup of 83.9 is considered, the convolution of the PSF and the APD function can be well approximated with a Gaussian function with a time-independent variance σ_{setup} (see above Fig. S12). Therefore, the variance of the resulting Gaussian function is

$$\sigma_I^2(t) = \sigma_n^2(t) + \sigma_{setup}^2. \qquad (14)$$

The temporal changes in the variance of the spatial intensity distributions, i.e., the changes in the MSD, are calculated using the difference of the Gaussian variance (Eq. (14)) at a time t and the Gaussian variance at a fixed reference time $t = 0$. Using Eq. (11), the changes in the MSD due to diffusion with a Gaussian initial condition is then given by [13,14]

$$\Delta MSD = \sigma_I^2(t) - \sigma_I^2(0) = At^{\alpha}. \qquad (15)$$

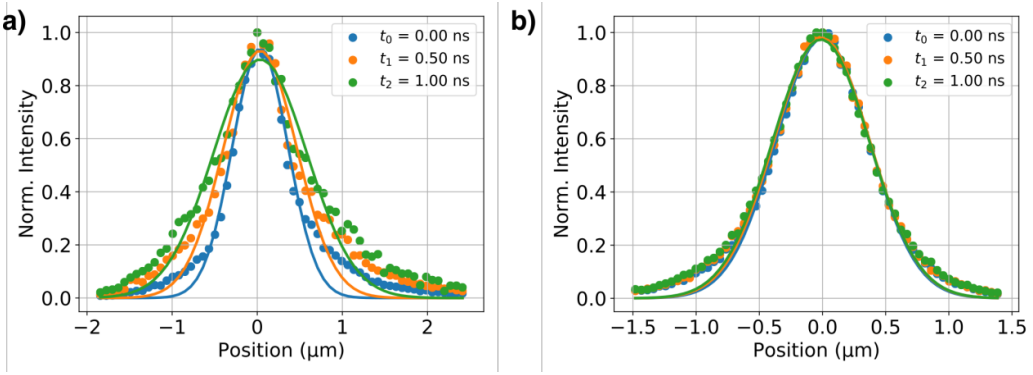

Fig. S13: Normalized spatial intensity distributions. a,b) Profiles from the normalized spatial intensity distributions $I(x, t_i)$ for the single nanofibre and the bundle of nanofibres, respectively, shown in Fig. 4C,D. The profiles were extracted at three times t_i and the solid lines show fits with Gaussian functions.

Fig. S13a,b show three profiles from the normalised spatial intensity distributions in Fig. 4C,D at different times. While Gaussian fits can roughly reproduce the intensity distribution of bundles, the profiles for the single nanofibre are very clearly non-Gaussian. This observation is related to the fact that each single nanofibre possesses its own unique excited-state energy landscape, which we directly probe in our single nanofibre experiment. In other words, we do not perform an ensemble average, and thus do not average out the specifics of each individual system. Thus, $n(x, t)$ does not evolve in time according to a Gaussian function.

To account for the non-Gaussian profiles, we evaluated the changes of the second moments (a measure for the widths) of our spatial intensity distributions, i.e.,

$$\Delta\mu_2(t) = \mu_2(t = 0) - \mu_2(t) = At^{\alpha}. \qquad (16)$$

For our spatial intensity distribution $I(x, t)$ the second moment at each point in time is defined as

$$\mu_2 = \frac{1}{N} \int (x - \mu_1)^2 I(x, t) dx \qquad (17)$$

where $N = \int I(x, t) dx$ is the integrated PL intensity and $\mu_1(t) = \frac{1}{N} \int x I(x, t) dx$ is the corresponding first moment (i.e., a measure for the centre of mass of the profile).

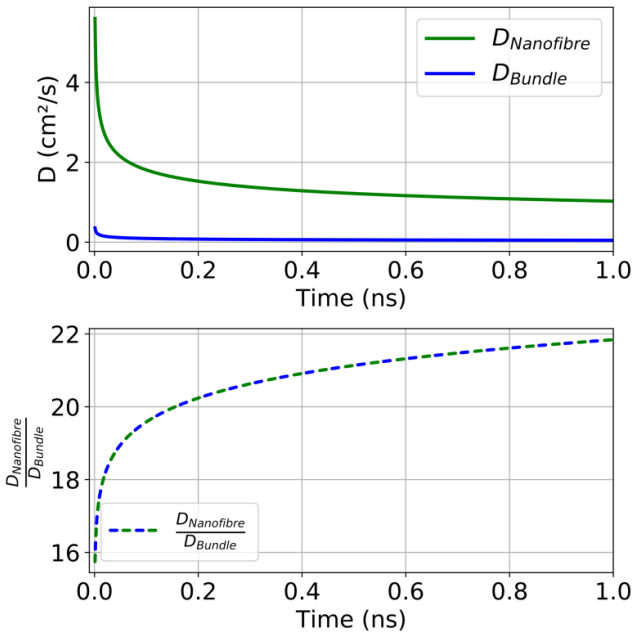

Fig. S14: Time-dependent diffusivities. Time-dependent diffusivity D of the single supramolecular nanofibre (green) and bundle (blue) shown in Fig. 4A,B.

8. References

(1) Haedler, A. T.; Meskers, S. C. J.; Zha, R. H.; Kivala, M.; Schmidt, H. W.; Meijer, E. W. Pathway Complexity in the Enantioselective Self-Assembly of Functional Carbonyl-Bridged Triarylamine Trisamides. *J. Am. Chem. Soc.* **2016**, *138* (33), 10539–10545. https://doi.org/10.1021/jacs.6b05184.

(2) Haedler, A. T.; Kreger, K.; Issac, A.; Wittmann, B.; Kivala, M.; Hammer, N.; Köhler, J.; Schmidt, H. W.; Hildner, R. Long-Range Energy Transport in Single Supramolecular Nanofibres at Room Temperature. *Nature* **2015**, *523* (7559), 196–199. https://doi.org/10.1038/nature14570.

(3) Eisele, D. M.; Knoester, J.; Kirstein, S.; Rabe, J. P.; Vanden Bout, D. A. Uniform Exciton Fluorescence from Individual Molecular Nanotubes Immobilized on Solid Substrates. *Nat. Nanotechnol.* **2009**, *4* (10), 658–663. https://doi.org/10.1038/nnano.2009.227.

(4) Zhang, W.; Jin, W.; Fukushima, T.; Saeki, A.; Seki, S.; Aida, T. Supramolecular Linear Heterojunction Composed of Graphite-like Semiconducting Nanotubular Segments. *Science* **2011**, *334* (6054), 340–343. https://doi.org/10.1126/science.1210369.

(5) Köhler, A.; Bässler, H. *Electronic Processes in Organic Semicond*uctors: An Introduction*. Wiley-VCH*; 2015.

(6) Spano, F. C.; Meskers, S. C. J.; Hennebicq, E.; Beljonne, D. Probing Excitation Delocalization in Supramolecular Chiral Stacks by Means of Circularly Polarized Light: Experiment and Modeling. *J. Am. Chem. Soc.* **2007**, *129* (22), 7044–7054. https://doi.org/10.1021/ja067321g.

(7) Hestand, N. J.; Spano, F. C. Expanded Theory of H- and J-Molecular Aggregates: The Effects of Vibronic Coupling and Intermolecular Charge Transfer. *Chem. Rev.* **2018**, *118* (15), 7069–7163. https://doi.org/10.1021/acs.chemrev.7b00581.

(8) Spano, F. C. The Spectral Signatures of Frenkel Polarons in H- and J-Aggregates. *Acc. Chem. Res.* **2010**, *43* (3), 429–439. https://doi.org/10.1021/ar900233v.

(9) Spano, F. C.; Clark, J.; Silva, C.; Friend, R. H. Determining Exciton Coherence from the Photoluminescence Spectral Line Shape in Poly(3-Hexylthiophene) Thin Films. *J. Chem. Phys.* **2009**, *130* (7), 074904. https://doi.org/10.1063/1.3076079.

(10) Clark, J.; Silva, C.; Friend, R. H.; Spano, F. C. Role of Intermolecular Coupling in the Photophysics of Disordered Organic Semiconductors: Aggregate Emission in Regioregular Polythiophene. *Phys. Rev. Lett.* **2007**, *98* (20), 206406. https://doi.org/10.1103/PhysRevLett.98.206406.

(11) Merdasa, A.; Jiménez, Á. J.; Camacho, R.; Meyer, M.; Würthner, F.; Scheblykin, I. G. Single Lévy States-Disorder Induced Energy Funnels in Molecular Aggregates. *Nano Lett.* **2014**, *14* (12), 6774–6781. https://doi.org/10.1021/nl5021188.

(12) Ciesielski, R.; Schäfer, F.; Hartmann, N. F.; Giesbrecht, N.; Bein, T.; Docampo, P.; Hartschuh, A. Grain Boundaries Act as Solid Walls for Charge Carrier Diffusion in Large Crystal MAPI Thin Films. *ACS Appl. Mater. Interfaces* **2018**, *10* (9), 7974–7981. https://doi.org/10.1021/acsami.7b17938.

(13) Clark, K. A.; Krueger, E. L.; Vanden Bout, D. A. Direct Measurement of Energy Migration in Supramolecular Carbocyanine Dye Nanotubes. *J. Phys. Chem. Lett.* **2014**, *5* (13), 2274–2282. https://doi.org/10.1021/jz500634f.

(14) Akselrod, G. M.; Deotare, P. B.; Thompson, N. J.; Lee, J.; Tisdale, W. A.; Baldo, M. A.; Menon, V. M.; Bulovic, V. Visualization of Exciton Transport in Ordered and Disordered Molecular

Solids. *Nat. Commun.* **2014**, *5* (1), 3646. https://doi.org/10.1038/ncomms4646.

(15) Akselrod, G. M.; Prins, F.; Poulikakos, L. V.; Lee, E. M. Y.; Weidman, M. C.; Mork, A. J.; Willard, A. P.; Bulović, V.; Tisdale, W. A. Subdiffusive Exciton Transport in Quantum Dot Solids. *Nano Lett.* **2014**, *14* (6), 3556–3562. https://doi.org/10.1021/nl501190s.

(16) Wu, J.; Berland, K. M. Propagators and Time-Dependent Diffusion Coefficients for Anomalous Diffusion. *Biophys. J.* **2008**, *95* (4), 2049–2052. https://doi.org/10.1529/biophysj.107.121608.

(17) Havlin, S.; Ben-Avraham, D. Diffusion in Disordered Media. *Adv. Phys.* **2002**, *51* (1), 187–292. https://doi.org/10.1080/00018730110116353.

(18) Vlaming, S. M.; Malyshev, V. A.; Eisfeld, A.; Knoester, J. Subdiffusive Exciton Motion in Systems with Heavy-Tailed Disorder. *J. Chem. Phys.* **2013**, *138* (21), 214316. https://doi.org/10.1063/1.4808155.

4.3 Publication II: Temperature-induced inversion of circular dichroism in supramolecular polymers revisited: Structural vs. electronic helicity

Temperature-induced inversion of circular dichroism in supramolecular polymers revisited: Structural vs. electronic helicity

Asena Cerhan-Haink[1,4,†], Felix A. Wenzel[2,†], Michael Buchhorn[1], Richard Kellnberger[1], Eric Schaible[3], Klaus Kreger[2], Hans-Werner Schmidt[2]*, Richard Hildner[4]*, Eva M. Herzig[1]*

[*] *Corresponding authors. Email: eva.herzig@uni-bayreuth.de, r.m.hildner@rug.nl, hans-werner.schmidt@uni-bayreuth.de*
[†] *Both authors contributed equally*

1 Dynamics and Structure formation – Herzig Group, University of Bayreuth, 95447 Bayreuth, Germany

2 Macromolecular Chemistry I and Bavarian Polymer Institute, University of Bayreuth, 95447 Bayreuth, Germany

3 Lawrence Berkeley National Laboratory, 1 Cyclotron Road, Berkeley, CA 94720, USA

4 Zernike Institute for Advanced Materials, University of Groningen, Nijenborgh 3, 9747 AG Groningen, The Netherlands

Abstract:

Controlling the helicity of supramolecular polymers by external stimuli is key to create tailored chiral systems. In particular, supramolecular polymers based on disk-like, aromatic building blocks with structural C_3-symmetry feature an intriguing temperature-induced inversion of electronic circular-dichroism (CD) spectra. However, the mechanism of this inversion is not yet fully understood. Here, we combine temperature-dependent optical spectroscopy with wide-angle X-ray scattering to study a model system, supramolecular nanofibers in toluene dispersion that form by cofacial stacking of a C_3-symmetric carbonyl-bridged triarylamine with (S)-chiral aliphatic side groups. We show that only minor structural rearrangements of the building blocks within supramolecular nanofibers are responsible for the inversion of the electronic CD spectra. Importantly, this inversion does not result from an inversion in the structural helicity of the supramolecular nanofibers. Already a minor change in rotation angle of the stacked building blocks induces an inversion in the helicity of the electronically coupled transition dipole moments, which is responsible for the CD signal of our supramolecular nanofibers.

Keywords: supramolecular polymers, chirality inversion, transition dipole moment, excitons, optical spectroscopy, x-ray scattering

1. INTRODUCTION

Chiral molecular (nano)structures are ubiquitous in nature and are of fundamental importance for life. An intriguing feature is enantioselectivity which is related to functional groups in chiral molecules and/or chiral molecular assemblies. Research on such systems is often carried out in a combined effort between chemistry, physics, and biology[1] with the aim to control the chirality of (nano)structures and ultimately their functionality. In particular, supramolecular polymers, formed by self-assembly of molecular building blocks via non-covalent, directional and reversible interactions, represent flexible platforms to create systems with defined chiral properties[2–4]. Possible applications include circularly polarised (hybrid) light-emitting diodes[5–8] and sensors for identifying chirality[9,10]. Chiral supramolecular polymers also appear to support extraordinary longevity of charge carriers[11].

In recent efforts to control chiral properties of supramolecular polymers, for several systems an inversion of their chirality from a M- to a P-helix, or vice versa, was induced by external stimuli during supramolecular polymerisation[12,13]. This inversion was achieved, for instance by illumination with appropriately circularly polarised light,[14] by applying an external static electric field,[15] by exploiting specific (chiral) solvents,[16–20] by addition of (chiral) auxiliary molecules,[21–24] by temperature cycling or ageing at different temperatures,[16,17,25–32] and by exploiting pathway complexity to form thermodynamically or kinetically stable supramolecular polymers with inverse chirality[18,32,33].

A particularly interesting situation is the temperature-induced chirality inversion in supramolecular polymers based on C_3-symmetrical molecular building blocks with a discotic aromatic core, such as N-heterotriangulene[33], triphenylamine[20] and triphenylene[16,17,20,27], linked to three amide groups with peripheral side chains. The hydrogen-bonding amide groups allow for the formation of supramolecular nanofibers with cofacially arranged and densely packed core molecules, which results in reasonably strong electronic coupling between the cores. Thus, such structures optically represent H-type aggregates[34,35]. The hydrogen-bond formation between the building blocks to three helical strands along the columnar axis is an

important feature, since it enforces and locks the cofacial stacking of the aromatic cores, making a dynamic slipping of the cores impossible (see Supporting Information Fig. S1 and Fig. 1). The limited length of the hydrogen bonds formed between two amide groups of neighboring building blocks is equally important, because it defines and restricts the rotation between two core structures of the building block. Consequently, larger core structures result in a reduced core-core rotation and a larger pitch of the supramolecular nanofibers. Introducing (S)- or (R)-chiral peripheral side groups, the formation of one helical species, i.e. either M- or P-helical supramolecular nanofibers, becomes predominant as evidenced by a corresponding bisignate signal in electronic circular-dichroism (CD) spectra. For the systems featuring the temperature-induced chirality inversion, the bisignate structure in CD spectra changes sign at a critical inversion temperature T_{inv}, which has accordingly been attributed to the formation of the inverted P- or M-helices or vice versa. As one possible mechanism a temperature-dependent supramolecular depolymerisation/polymerisation process, i.e., a disassembly/self-assembly process, has been suggested: Upon cooling, depolymerisation takes place when approaching T_{inv} and below T_{inv}, polymerisation is initiated resulting in supramolecular nanofibers with an inverted structural helicity[20]. As alternative mechanism a rearrangement of molecules within nanofibers was proposed, specifically a rotation about a large angle, to allow for a full structural inversion in the helical assembly of the molecular building blocks[16,20,27]. In special cases, additional rotations of peripheral hydrogen-bonding amide groups are involved[20,25]. Since the critical inversion temperature was found to depend on the solvent, solvent-solute interactions seem to be of great importance to stabilise the different helical states by temperature-dependent solvation effects[16,17,27].

Here we revisit the temperature-induced chirality inversion in supramolecular polymers based on a structurally C_3-symmetric carbonyl-bridged triarylamine bearing (S)-chiral aliphatic side groups (s-CBT) and reveal the mechanism behind the chirality inversion (Fig. 1). The self-assembly of this compound is driven by directed hydrogen bonds of three amide groups, giving rise to a cofacial stacking of s-CBT molecules into helical, H-type nanofibers that can form bundles under a suitable set of conditions[33,36–38]. Using temperature-dependent CD, UV/Vis absorption and photoluminescence (PL) spectroscopy in combination with temperature-dependent wide-angle x-ray scattering (WAXS), we find that only a minor rotation of self-assembled s-CBT molecules within the nanofibers occurs upon cooling below the inversion temperature T_{inv}. Already such a small rotation inverts the helicity of the electronically coupled transition dipole moments of the s-CBT molecules stacked along the nanofibers, i.e., an

inversion of the electronic helicity takes place, which is related to the specific electronic properties of structurally C_3-symmetric molecules.

2. RESULTS AND DISCUSSION

Self-assembly of s-CBT into bundles of supramolecular nanofibers was performed in toluene (see Supporting Information, section S2, and Fig. S3). For optical spectroscopy we prepared toluene dispersions at a concentration of ~40 μM (~100 p.p.m.) and recorded spectra as a function of temperature during cooling from 80°C to 0°C (Fig. 2). The CD spectra in Fig. 2A generally feature a bisignate structure in the spectral range of the π-π* absorption band of s-CBT between 400 nm and 550 nm. This shape of CD spectra is characteristic for electronically coupled transition dipole moments of molecules that are helically arranged and perfectly stacked[39–44]. This observation is in line with our previous work, where we have shown that s-CBT self-assembles by cofacial stacking into supramolecular nanofibers with a preferred helicity due to the chiral centres in the peripheral side groups[33,38]. However, upon cooling we observe a pronounced inversion of the bisignate CD spectra from a negative to a positive Cotton-effect at a critical temperature of T_{inv} = 16°C (Figs. 2B and S4), implying an inversion in the helical arrangement of s-CBT molecules within nanofibers. Upon heating, the inversion of the bisignate CD spectra is fully reversible with a small hysteresis (Fig. S5). We also find that the sample is stable over several hours upon ageing at a constant temperature, independent of the thermal history (Figs. S6 and S7). These findings agree with data on self-assembled structures of chemically different C_3-symmetric building blocks that also show an inversion in CD spectra[16,20,33].

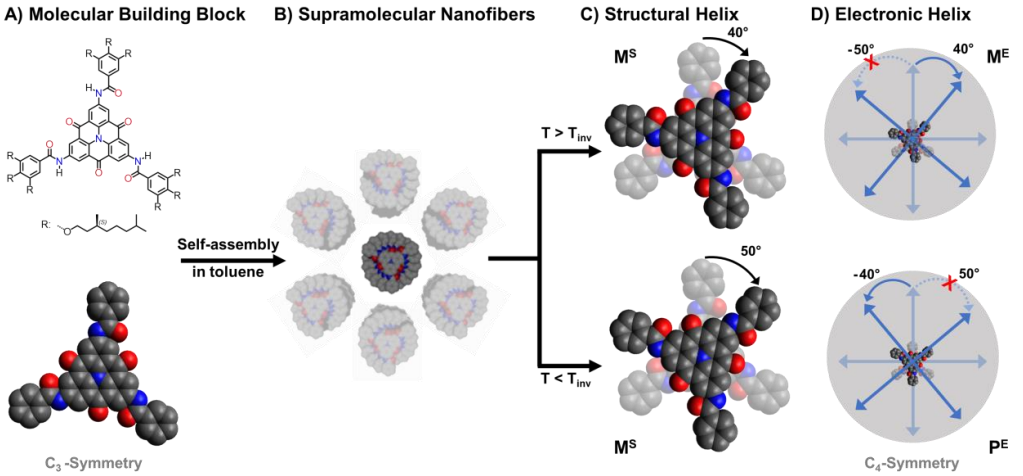

Fig. 1 | Illustration of the temperature-induced electronic chirality inversion in supramolecular polymers based on the structurally C_3-symmetric s-CBT. A) Chemical structure of s-CBT with (S)-chiral side groups. B) Schematic of self-assembled s-CBT into hexagonally packed bundles of supramolecular nanofibers in toluene. Chiral aliphatic side groups are not shown for clarity. C) Upon cooling a slight rotation of s-CBT within supramolecular nanofibers occurs at the critical inversion temperature T_{inv}, here illustrated by a change in rotation angle from 40° (top) to 50° (bottom, for a justification of the choice of those angles, see text and SI, Fig. S1 and section S6). Due to the structural C_3-symmetry, structurally a M-helix (M^S) prevails independent of the temperature. D) Electronically the s-CBT molecule possesses C_4-symmetry with two degenerate, perpendicularly oriented transition dipole moments (double-headed arrows). The same change in rotation angle as in C) inverts the helicity of the stacked transition dipole moments along nanofibers from an electronic M-helix (M^E) to a P^E-helix, since rotation occurs over the critical angle of 45°.

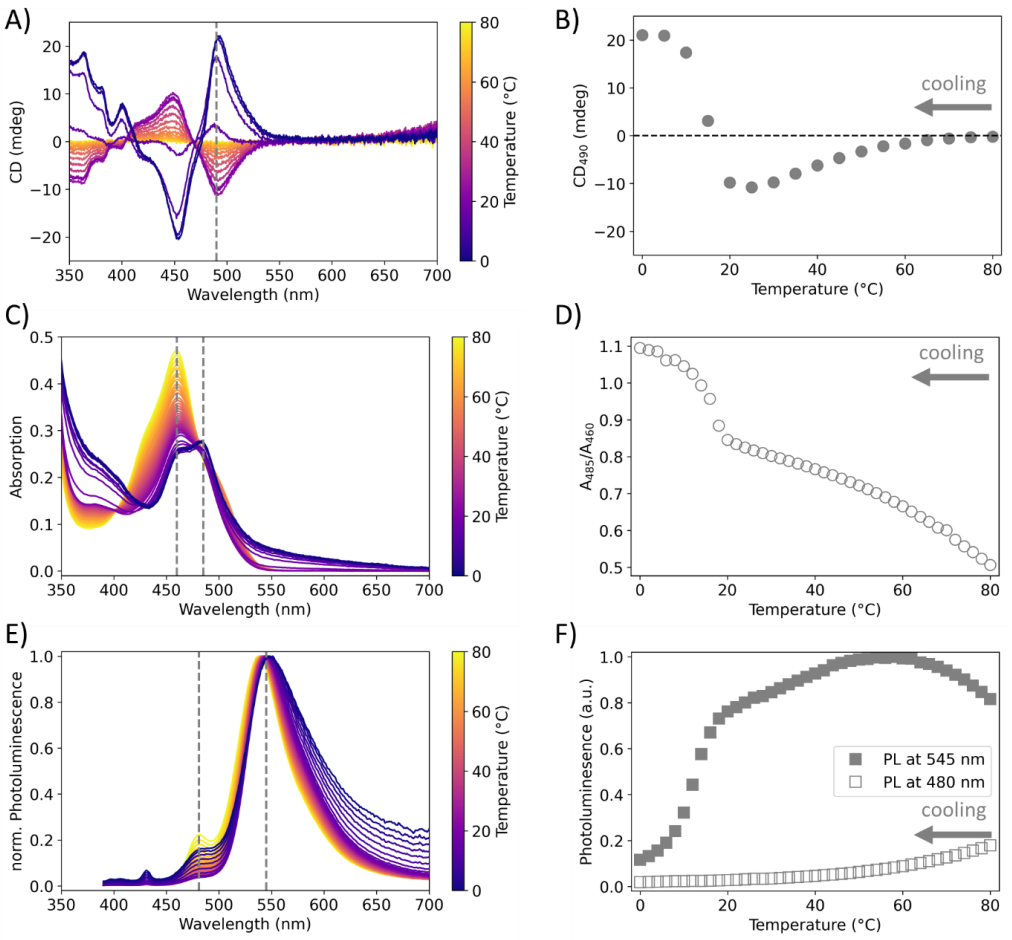

Fig. 2 | Temperature-dependent optical characterisation of supramolecular polymers based on s-CBT upon cooling in toluene. A) Circular-dichroism (CD) spectra. B) CD-signal at 490 nm. C) Linear UV/Vis absorption spectra. D) Ratio A_{485}/A_{460} of the absorption at 485 nm and 460 nm. E) Normalised PL spectra excited at a wavelength of 380 nm. F) PL signals at 480 nm (relative contribution of molecularly dissolved s-CBT, see also Fig. S9) and at 545 nm (relative contribution of bundles of nanofibers). For all measurements the s-CBT concentration is 40 µM (100 p.p.m.) and all spectra are acquired after 10 min equilibration at each temperature upon cooling from 80°C to 0°C. The colour code in A), C) and E) depicts temperature. The data in B), D), F) are obtained from the positions marked by the dashed vertical lines in A), C) and E), respectively.

The linear UV/Vis absorption spectra upon cooling (Fig. 2C) exhibit a distorted vibronic progression above 20°C with the highest-wavelength absorption A_{485} around 485 nm being weaker compared to the absorption A_{460} around 460 nm ($A_{485}/A_{460} < 1$). Below a temperature of 20°C, the ratio rapidly increases towards $A_{485}/A_{460} > 1$ (Fig. 2D). This spectral shape is

characteristic of H-aggregated, cofacially stacked s-CBT building blocks within the supramolecular nanofibers. Reasonably strong electronic coupling between transition dipole moments of adjacent molecules emerges, which delocalises electronic excitations along nanofibers and gives rise to the formation of (vibronic) excitons[37,38]. The magnitude of this electronic coupling is directly reflected in the A_{485}/A_{460} ratio: The increase of the ratio upon cooling demonstrates that the electronic coupling decreases[45]. Moreover, we find a continuous red-shift of the absorption spectra upon cooling (see especially the A_{460} peak in Fig. 2C), which implies increasing non-resonant dispersive interactions between s-CBT molecules. Thermal compression upon cooling reduces the distance between s-CBT molecules and thus increases van-der-Waals binding energies in the ground and excited states, which gives rise to an overall continuous red-shift of the optical transition[46–48]. Below 20°C a broad tail appears in the absorption spectra between 550 and 600 nm. We attribute this tail to increasing scattering due to an increase in the number and size of scattering centres in the toluene dispersion at low temperature, i.e., the bundles of supramolecular nanofibers continue to grow in size upon cooling.

Temperature-dependent normalised PL spectra upon cooling are displayed in Fig. 2E (see Fig. S8 for raw PL spectra). Between 80°C and about 20°C the spectral shape of the PL with its maximum around 545 nm changes only weakly. Below 16°C the relative PL signal at wavelengths around 600 nm increases. Those broad and unstructured PL spectra are consistent with emission from H-aggregated s-CBT molecules[38]. The PL signal at 480 nm with low intensity results from the emission of some residual molecularly dissolved s-CBT molecules (see Fig. S8)[37]. Below 16°C the integrated PL signal rapidly decreases (Figs. 2F and S8), although the absorption at the excitation wavelength of 380 nm continuously increases. This indicates an overall improved structural order within the bundled H-type nanofibers[38], that diminishes the radiative rates of H-aggregate emission[45] in this temperature window. In analogy to the absorption data, the maximum of the PL signal around 545 nm shows a continuous red-shift upon cooling that we ascribe to the increasing non-resonant dispersive interactions between s-CBT molecules (see above).

The CD, absorption and PL spectra in Fig. 2 demonstrate that the optical response of our s-CBT-based supramolecular polymers is determined by vibronic excitons delocalised along H-type nanofibers arranged within bundles[33,38]. Vibronic excitons arise from substantial electronic coupling between transition dipole moments of adjacent molecules, which prevails

in the entire temperature range, including at T_{inv} = 16°C where the CD signal vanishes (Fig. S9). The presence of bundles of H-type nanofibers is highlighted by the UV/Vis absorption and PL spectra at T_{inv} = 16°C in Fig. S9 by comparison with the spectra of molecularly dissolved s-CBT. We note that excitons do not delocalise across nanofibers within a bundle, because the long aliphatic side groups of s-CBT ensure a distance of several nm between nanofibers[33,38] (see also below). The CD spectra with their characteristic bisignate shape (Fig. 2A) imply a helical assembly of perfectly cofacially stacked s-CBT molecules with a rotation with respect to each other within nanofibers, rather than a twisted helical arrangement of nanofibers within a bundle, i.e., a superhelix (see also Fig. S3)[39–44]. The temperature-dependent change from a negative to a positive Cotton effect in the CD spectra is commonly interpreted to arise from an inversion from an M- to a P-helix in the structural arrangement of s-CBT molecules within a nanofiber. Such structural chirality inversion is proposed to arise either from a depolymerisation-polymerisation process or by intra-fiber rearrangements (rotations) of molecules around the critical inversion temperature[16–18,20,27]. However, our temperature-dependent absorption and PL data clearly show that depolymerisation-polymerisation is unlikely to occur, since we do not observe a larger fraction of molecularly dissolved monomers around T_{inv} (see Fig. 2C-F). In fact, the contribution of molecularly dissolved s-CBT to the PL signal continuously decreases towards lower temperatures (Fig. S8) and can be estimated to be ~1% only at T_{inv} = 16°C (Fig. S9). Moreover, large rotations of s-CBT molecules within bundles of supramolecular nanofibers seem implausible. In particular, the sterically demanding aliphatic side chains of s-CBT tend to interact and interpenetrate within the bundles[38] and render substantial rotations energetically very costly.

To resolve the structural changes responsible for the strong changes observed in CD, we investigate the bundles of supramolecular nanofibers by temperature-dependent wide angle X-ray scattering (WAXS) experiments during cooling from 50°C to 10°C (Fig. 3A,B, and Supporting Information, section S2). We structurally investigate both, the solvent toluene by itself as well as dispersions of bundles of supramolecular nanofibers. Toluene itself shows a linear compression of the solvent due to the reduction in temperature (Fig. 3C). The nearest-neighbour distance of toluene molecules is reduced by about 2.0% over the examined temperature range. For the dispersions with s-CBT-based bundles of supramolecular nanofibers we measured at a concentration of ~2000 μM (~5000 p.p.m., see Fig. S10) to obtain a sufficiently strong scattering signal. An example of a 2D transmission pattern taken during the WAXS measurements at 20°C is shown in Fig. 3A. Multiple, relatively sharp concentric

rings are recorded that indicate the presence of well-ordered structures oriented isotropically in space[49]. For a quantitative analysis we radially integrated the scattering signal for all temperatures and corrected for capillary and solvent contributions (Fig. 3B). Several peaks are observed in the low-q region ($q < 7$ nm^{-1}), while a broad peak appears in the high-q region (~ 18.5 nm^{-1}). The peaks in the low-q region feature a specific distance ratio in reciprocal space of 1: $\sqrt{3}$: $\sqrt{4}$: $\sqrt{7}$: $\sqrt{9}$: $\sqrt{12}$: $\sqrt{13}$. This ratio is characteristic for a hexagonal arrangement of columns[49]. Peaks were indexed (Fig. 3B) based on allowed reflections in reciprocal space (see Supporting Information, section S3), which are in excellent agreement with theoretical q-values (see Supporting Information, table S1) of hexagonally packed cylinders. Hence, the supramolecular nanofibers are hexagonally packed within bundles (Fig. 1B) throughout the cooling process.

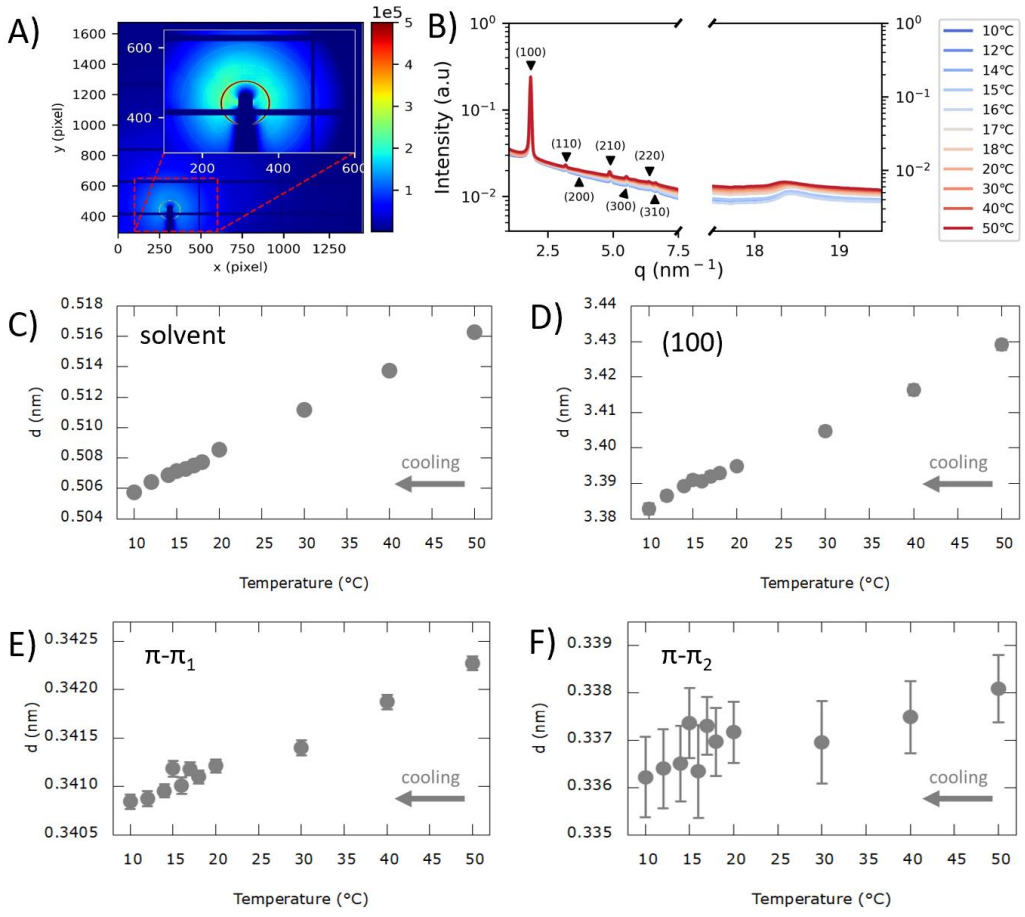

Fig. 3 | Temperature-dependent WAXS measurements on bundles of supramolecular nanofibers in toluene dispersion. A) 2D WAXS pattern measured at 20°C. B) Radially

integrated intensity of scattering patterns for all temperatures cooled from 50°C down to 10°C as shown in the legend next to A). Indices show hexagonally packed nanofibers within bundles. C) Nearest-neighbour distances of toluene molecules as a function of temperature obtained from the solution scattering peak measuring the neat solvent. D) Hexagonal distance obtained from the (100) scattering peak as a function of temperature on dispersions of s-CBT-based bundles of supramolecular nanofibers. E) First and F) second contribution to π-π-stacking fitted with Lorentzian contributions. For A)-B) and D)-F) the concentration of s-CBT was 2000 μM (5000 p.p.m.). All data were acquired during cooling with 10 min equilibration at each temperature.

The fiber-fiber separation within the bundles of supramolecular nanofibers as a function of temperature is extracted by fitting the (100) peak of the WAXS measurements for all temperatures (Fig. 3D). The hexagonal lattice parameter of d = 3.4 nm translates into a column-column distance of d_c = 3.9 nm (see Supporting Information, section S4), which is smaller than the size of a fully extended s-CBT molecule and thus indicates interactions between side groups of neighbouring nanofibers within a bundle[33,38]. The hexagonal lattice parameter decreases by about 1.4% upon cooling which is in accordance with the expected thermal compression. The intensity and full width half maximum obtained from the fits to the (100) peak do not show any systematic changes with temperature (see Supporting Information, section S5, Fig. S12).

The broad peak at q ~ 18.5 nm^{-1} in the WAXS data (Fig. 3B) we associate with the π-π-stacking of the s-CBT molecules along the supramolecular nanofibers. Those broad peaks cannot be fitted with a single symmetric function and hence require a second function. Furthermore, the appropriate curve shape improves the fit quality when two Lorentzian curves are fitted, which is typical for the π-π-stacking of organic molecules[50]. When examining the temperature-dependence of the positions of these two peaks (Fig. 3E,F) the contraction of both contributions is independent of the fit functions used and only reaches about 0.5%. Hence, the reduction of the π-π-stacking distance is from the onset of cooling a factor of three to four less strong than the reduction of nearest neighbour distances within the solvent surrounding the supramolecular structures.

The presence of scattering peaks, indicating π–π-stacking of s-CBT within nanofibers and hexagonal packing of supramolecular nanofibers within bundles, over the entire temperature range clearly shows that a depolymerisation-polymerisation process cannot be responsible for the CD inversion, in accordance with results from optical spectroscopy. Notably, depolymerisation-polymerisation would imply that these densely packed bundles, comprising

more than 1000 nanofibers (Fig. S11), disassemble and reassemble, which is highly unlikely to occur. The observed contraction in the π-π-stacking distance is less strong than the contraction of the surrounding solvent with decreasing temperature, because the repulsion of the π-electrons of the H-type stacked s-CBT molecules within supramolecular nanofibers partially counteracts thermal compression. Despite being less pronounced, the decrease in the π-stacking distance supports our assignment of the continuous red-shift in absorption and PL spectra (Fig. 2C,E) to increasing non-resonant dispersive interactions between s-CBT molecules. Increasing van-der-Waals binding energies, that are different in the ground and excited states, continuously shift the optical transition to the red (see also Supporting Information, section S5)[46–48]. However, the trend of the decreasing π-π-stacking distance would also imply an increasing electronic coupling between transition dipole moments of stacked s-CBT molecules towards lower temperatures. This is not consistent with the increasing A_{485}/A_{460} absorption peak ratio (Fig. 2D), which can only result from a decreasing electronic coupling[45]. However, in helically arranged molecules a decreasing electronic coupling can be realised, if the compaction of the molecules is accompanied by a rotation of the s-CBT molecules (see below).

The absorption, PL, and scattering data upon cooling consistently show that the inversion of the CD signal at the critical temperature can only be caused by a rotation of monomers within the helical nanofibers. A rotation about large angles is sterically hindered by the bulky aliphatic side groups linked to the s-CBT cores. Given the column-column distances of ~3.9 nm within bundles (Fig. 3D) and the fully extended size of a s-CBT molecule of ~4.4 nm,[33,38] the side groups of adjacent nanofibers will interact within bundles[38], impeding substantial structural rearrangements upon cooling. Furthermore, our scattering data show only rather small structural changes in our temperature range. The change in rotation angle between neighbouring monomers along a nanofiber upon cooling can be estimated from the change in the absorption spectra (Fig. 2C, D): The absorption peak ratio A_{485}/A_{460} ~ 0.85 at 20°C is consistent with an electronic coupling between the transition dipole moments of adjacent monomers of about 700 cm^{-1} [38]. After cooling to 0°C the absorption peak ratio increased to ~1.05, which translates into a smaller electronic coupling of ~550 cm^{-1} (Supporting Information, section S6). Since the electronic coupling in helical arrangements of molecules depends on the cosine of the rotation angle[39], a rotation by ~10°, e.g. from 40° to 50°, is sufficient to account for this reduction of the electronic coupling (Supporting Information, section S6). Such rotation over a rather small angle is in line with steric constraints imposed

by the hydrogen bonds between the amide groups of next neighbours, resulting in three helical strands of hydrogen bonds along the columnar axis. During thermal compression of the π-stacking distance of the nanofibers, the limited length and tilting angle of the hydrogen-bonded amide groups allows for only a small and defined rotation of the cofacially stacked s-CBT molecules with respect to each other, since the structural integrity of the bundles of nanofibers is maintained. Note that the compression implies that the out-of-plane tilting angle of the amide groups reduces and thus the rotation must occur in a specific direction, i.e. towards larger angles upon cooling (see Supporting Information, Fig. S1).

In the CD spectra the bisignate signal originates from the stacked and rotated arrangement of electronically coupled transition dipole moments of s-CBT (note that e.g. optical rotation or CD involving magnetic dipole moments lead to odd-shaped, non-conservative CD spectra[40,44,51,52]). The helicity of the arrangement of the transition dipole moments determines the sign of the rotational line strength, which in turn determines the sign of the Cotton effect[39–41]. Although the helicity of stacked transition dipole moments is often identical to the structural helicity of a supramolecular polymer, for structurally C_3-symmetric molecules, such as s-CBT, the situation is more complex. The relevant optical π–π* transition of s-CBT around 450 – 500 nm is in fact due to two (near-)degenerate transitions with perpendicularly oriented (crossed) transition dipole moments[53,54], i.e., the arrangement of the transition dipole moments is C_4-symmetric (see Fig. 1D and Supporting Information, section S6, for a detailed description, including group theory considerations, of the electronic structure of the core of s-CBT). In this case, a rotation by 90° reproduces the arrangement of crossed transition dipole moments and the helicity in their arrangement inverts along a nanofiber when rotating over the critical angle of 45°. For instance, a change in the rotation angle of the molecules by 10°, e.g. from 40° to 50°, as derived from the observed change in the absorption spectra upon cooling, is therefore identical to a change in rotation angles of the crossed transition dipole moments from 40° to -40° (Fig. 1D and S15). Consequently, the sign of the rotational line strength changes and the CD spectra will feature a transition from a negative to a positive Cotton effect (Fig. 2A, B and Supporting Information, section S6). We note that this is a purely electronic effect when crossed transition dipole moments with their C_4-symmetry in a stacked configuration rotate over the critical angle of 45°. This rotation thus inverts *electronic helicity* (from an electronic M^E- to an P^E-helix, Fig. 1D), i.e., it changes the sign of the rotational line strength (Fig. S14). The *structural helicity* of the arrangement of s-CBT molecules along the nanofibers remains unaltered (i.e., a M^S-helix, Fig. 1C), determined by the chiral centres in the side groups. Due

to the structural C_3-symmetry of s-CBT, a rotation by 120° reproduces the structural arrangement of molecules within a nanofiber and a change in structural helicity of nanofibers requires to rotate over the critical angle of 60°. However, this requires a large change in rotation angles and is not consistent with our spectral and scattering data.

As a final note we emphasise that CD spectra and the sign of the rotational line strengths are very sensitive to non-nearest-neighbour electronic coupling between transition dipole moments[39,41]. The nearest-neighbour picture, assumed in the discussion above, is clearly an oversimplification. In fact, extracting a coherence length from the π–π-stacking signals from the WAXS data indicates that >17 s-CBT molecules along supramolecular nanofibers coherently contribute to the scattering peak (Fig. S12). This implies locally highly ordered supramolecular nanofibers within bundles in toluene dispersion, which is well in line with previous results found for benzene-trisamides[55]. These results support substantial delocalisation of vibronic excitons along nanofibers and highlights the relevance of non-nearest-neighbour electronic couplings. Moreover, due to π-stacking of s-CBT molecules within nanofibers, charge-transfer mediated (superexchange) interactions via orbital overlap of neighbouring s-CBTs may play a role, too. The precise evaluation of non-nearest-neighbour effects and superexchange interactions is computationally expensive[53,54] and beyond the scope of this work. Both effects might alter the critical inversion angle, i.e., this angle might be smaller than 45° [54], but a rotation by a few degrees over this angle still inverts electronic helicity. However, the main conclusions outlined above remain (see also Fig. 1), since structurally the C_3-symmetry still prevails, and thus an inversion of the structural helicity always requires rotating over an angle of 60°.

3. CONCLUSIONS

We studied the temperature-dependent inversion of the bisignate CD spectra of H-type supramolecular nanofibers based on the C_3-symmetric s-CBT molecule bearing (S)-chiral side groups. The common interpretation of this inversion at a critical temperature involves either a depolymerisation-polymerisation process or large intra-fiber rearrangements of molecules to invert fully from a structural M- to a P-helix, or vice versa, depending on the chiral side groups. Our combined optical and structural characterisation allowed us to demonstrate that only minor rotations of s-CBT monomers within nanofibers by just a few degrees are already sufficient to

switch the bisignate structure of the CD signal at the critical temperature. A slight rotation is consistent with the limited length and tilting angle that the three hydrogen-bonding amide groups of the C_3-symmetrical s-CBT molecules allow for, while maintaining the cofacial stacking within nanofibers. The bisignate CD signal of our supramolecular nanofibers arises from electronic coupling between transition dipole moments of adjacent molecules with a helical arrangement. Hence, the helicity of helically stacked transition dipole moments – the electronic helicity – must invert; a change in structural helicity is not required. Fundamentally, this difference in behaviour of electronic and structural helicity in our nanofibers arises from the fact that the structural C_3-symmetry of s-CBT translates into an electronic C_4-symmetry of two (nearly) degenerate, perpendicularly oriented transition dipole moments of the lowest energy electronic transition. We believe that this mechanism of inversion of electronic helicity also occurs in the supramolecular polymers based on other structurally C_3-symmetric molecules, for which the temperature-dependent inversion of the bisignate Cotton effect was reported, such as other N-heterotriangulenes[33], and tripenylene-2,6,10-tricarboxamides[16,17,20,27]. Those molecules have in common with our s-CBT compound that, apart from their structural C_3-symmetry, they possess bulky, chiral side groups, including hydrogen bonding amides; they assemble into bundles of H-type supramolecular nanofibers via hydrogen bonding and π-stacking, as evidenced by characteristic changes in the temperature-dependent UV/Vis spectra; they feature interactions of side groups of neighbouring supramolecular nanofibers, which sterically hinder large intra-fiber rotations of molecules. Hence, the structural helicity of nanofibers is not required to change as a function of temperature, since it is always determined by the chiral centres in the peripheral groups of the molecules, whereas the inversion of electronic helicity is responsible for the optical response. Since the chiral properties of the nanofibers are stable at a constant temperature, we anticipate that this mechanism will allow for structures with temperature-tuneable circularly polarised emission for nanophotonic applications.

Supporting Information

Materials and methods; additional optical investigations; additional WAXS investigations; temperature dependent WAXS data; discussion of electronic couplings, rotation angles and rotational line strengths.

Acknowledgements

A.C.H. and E.M.H. acknowledge funding from the Deutsche Forschungsgemeinschaft (DFG) through the TUM International Graduate School of Science and Engineering (IGSSE). Portions of this research were carried out at beamline 7.3.3 of the Advanced Light Source, which is supported by the Director of the Office of Science, Office of Basic Energy Sciences, of the U.S. Department of Energy under Contract No. DE-AC02-05CH11231. We also acknowledge financial support from the Bavarian State Ministry of Science and the Arts through the Collaborative Research Network "Solar Technologies go Hybrid". F.A.W. acknowledges support by the Elite Network of Bavaria (ENB) through the study program "Macromolecular Science". We are indebted to Prof. Birte Höcker and Sooruban Shanmugaratnam (Biochemistry III, University of Bayreuth) for support and help with CD spectroscopy measurements. R.H. is grateful to Profs. W. Barford (University of Oxford) and T. L. C. Jansen (University of Groningen) for helpful discussions on the electronic structure of CBT. We also thank Dr. B. Wittmann for his contribution in the initial phase of this project.

References

1. Adawy, A. Functional Chirality: From Small Molecules to Supramolecular Assemblies. *Symmetry* **14,** 292 (2022).
2. Scanga, R. A. & Reuther, J. F. Helical polymer self-assembly and chiral nanostructure formation. *Polym. Chem.* **12,** 1857–1897 (2021).
3. Dorca, Y., Greciano, E. E., Valera, J. S., Gómez, R. & Sánchez, L. Hierarchy of Asymmetry in Chiral Supramolecular Polymers: Toward Functional, Helical Supramolecular Structures. *Chem. Eur. J.* **25,** 5848–5864 (2019).
4. García, F., Gómez, R. & Sánchez, L. Chiral supramolecular polymers. *Chem. Soc. Rev.* **52,** 7524–7548 (2023).
5. Kim, Y.-H. *et al.* Chiral-induced spin selectivity enables a room-temperature spin light-emitting diode. *Science* **371,** 1129–1133 (2021).
6. Li, C., Jin, X., Han, J., Zhao, T. & Duan, P. Toward Large Dissymmetry Factor of Circularly Polarized Luminescence in Donor-Acceptor Hybrid Systems. *J. Phys. Chem. Lett.* **12,** 8566–8574 (2021).
7. Wan, L., Shi, X., Wade, J., Campbell, A. J. & Fuchter, M. J. Strongly Circularly Polarized Crystalline and β-Phase Emission from Poly(9,9-dioctylfluorene)-Based Deep-Blue Light-Emitting Diodes. *Adv. Opt. Mater.* **9** (2021).
8. Cheng, Q., Dai, C., Hao, A. & Xing, P. Self-Assembled Polyhedral Oligosilsesquioxane Dendrimers for Circularly Polarized Luminescence Energy Transfer. *J. Phys. Chem. C* **125,** 14141–14148 (2021).

9. Greaves, T. L. & Drummond, C. J. Protic ionic liquids: properties and applications. *Chem. Rev.* **108,** 206–237 (2008).
10. Warning, L. A. *et al.* Nanophotonic Approaches for Chirality Sensing. *ACS Nano* **15,** 15538–15566 (2021).
11. Hafner, R. J. *et al.* Unusually Long-Lived Photocharges in Helical Organic Semiconductor Nanostructures. *ACS Nano* **12,** 9116–9125 (2018).
12. Lin, M. *et al.* Flexible Polymer Device Based on Parylene-C with Memory and Temperature Sensing Functionalities. *Polymers* **9** (2017).
13. Lv, Z., Chen, Z., Shao, K., Qing, G. & Sun, T. Stimuli-Directed Helical Chirality Inversion and Bio-Applications. *Polymers* **8** (2016).
14. Kim, J. *et al.* Induction and control of supramolecular chirality by light in self-assembled helical nanostructures. *Nat. Commun.* **6,** 6959 (2015).
15. Bejagam, K. K., Kulkarni, C., George, S. J. & Balasubramanian, S. External electric field reverses helical handedness of a supramolecular columnar stack. *Chem. Commun.* **51,** 16049–16052 (2015).
16. Ślęczkowski, M. L., Mabesoone, M. F. J., Ślęczkowski, P., Palmans, A. R. A. & Meijer, E. W. Competition between chiral solvents and chiral monomers in the helical bias of supramolecular polymers. *Nat. Chem.* **13,** 200–207 (2021).
17. Ślęczkowski, M. L. *et al.* Helical bias in supramolecular polymers accounts for different stabilities of kinetically trapped states. *J. Polym. Sci.* **60,** 1871–1877 (2022).
18. Valera, J. S. *et al.* Solvent-Directed Helical Stereomutation Discloses Pathway Complexity on N-Heterotriangulene-Based Organogelators. *Chem. Eur. J.* **23,** 11141–11146 (2017).
19. Katayama, K., Hirata, S. & Vacha, M. Circularly polarized luminescence from individual microstructures of conjugated polymer aggregates with solvent-induced chirality. *Phys. Chem. Chem. Phys.* **16,** 17983–17987 (2014).
20. Adelizzi, B., Filot, I. A. W., Palmans, A. R. A. & Meijer, E. W. Unravelling the Pathway Complexity in Conformationally Flexible N-Centered Triarylamine Trisamides. *Chem. Eur. J.* **23,** 6103–6110 (2017).
21. George, S. J. *et al.* Asymmetric noncovalent synthesis of self-assembled one-dimensional stacks by a chiral supramolecular auxiliary approach. *J. Am. Chem. Soc.* **134,** 17789–17796 (2012).
22. Yang, D., Duan, P., Zhang, L. & Liu, M. Chirality and energy transfer amplified circularly polarized luminescence in composite nanohelix. *Nat. Commun.* **8,** 15727 (2017).
23. Dhiman, S., Jain, A. & George, S. J. Transient Helicity: Fuel-Driven Temporal Control over Conformational Switching in a Supramolecular Polymer. *Angew. Chem. Int. Ed.* **56,** 1329–1333 (2017).

24. George, S. J. *et al.* Helicity induction and amplification in an oligo(p-phenylenevinylene) assembly through hydrogen-bonded chiral acids. *Angew. Chem. Int. Ed.* **46,** 8206–8211 (2007).
25. Koenis, M. A. J. *et al.* Self-Assembly of Supramolecular Polymers of N-Centered Triarylamine Trisamides in the Light of Circular Dichroism: Reaching Consensus between Electrons and Nuclei. *J. Am. Chem. Soc.* **142,** 1020–1028 (2020).
26. Go, M. *et al.* Temperature-controlled helical inversion of asymmetric triphenylamine-based supramolecular polymers; difference of handedness at the micro- and macroscopic levels. *Org. Chem. Front.* **6,** 1100–1108 (2019).
27. Preuss, M. D., Jansen, S. A. H., Vantomme, G. & Meijer, E. W. Chirality and Supramolecular Copolymerizations – The Elusive Role of Subtle Solvation Effects. *Isr. J. Chem.* **61,** 622–628 (2021).
28. Kulkarni, C. *et al.* Solvent Clathrate Driven Dynamic Stereomutation of a Supramolecular Polymer with Molecular Pockets. *J. Am. Chem. Soc.* **139,** 13867–13875 (2017).
29. Osypenko, A. *et al.* Temperature Control of Sequential Nucleation-Growth Mechanisms in Hierarchical Supramolecular Polymers. *Chem. Eur. J.* **25,** 13008–13016 (2019).
30. Gopal, A., Hifsudheen, M., Furumi, S., Takeuchi, M. & Ajayaghosh, A. Thermally assisted photonic inversion of supramolecular handedness. *Angew. Chem. Int. Ed.* **51,** 10505–10509 (2012).
31. Huang, Z. *et al.* Pulsating tubules from noncovalent macrocycles. *Science* **337,** 1521–1526 (2012).
32. Korevaar, P. A. *et al.* Pathway complexity in supramolecular polymerization. *Nature* **481,** 492–496 (2012).
33. Haedler, A. T. *et al.* Pathway Complexity in the Enantioselective Self-Assembly of Functional Carbonyl-Bridged Triarylamine Trisamides. *J. Am. Chem. Soc.* **138,** 10539–10545 (2016).
34. Brixner, T., Hildner, R., Köhler, J., Lambert, C. & Würthner, F. Exciton Transport in Molecular Aggregates - From Natural Antennas to Synthetic Chromophore Systems. *Adv. Energy Mater.* **7,** 1700236 (2017).
35. Kreger, K., Schmidt, H.-W. & Hildner, R. Tailoring the excited-state energy landscape in supramolecular nanostructures. *Electron. Struct.* **3,** 23001 (2021).
36. Haedler, A. T. *et al.* Synthesis and photophysical properties of multichromophoric carbonyl-bridged triarylamines. *Chem. Eur. J.* **20,** 11708–11718 (2014).
37. Haedler, A. T. *et al.* Long-range energy transport in single supramolecular nanofibres at room temperature. *Nature* **523,** 196–199 (2015).
38. Wittmann, B. *et al.* Enhancing Long-Range Energy Transport in Supramolecular Architectures by Tailoring Coherence Properties. *J. Am. Chem. Soc.* **142,** 8323–8330 (2020).

39. Spano, F. C. Analysis of the UV/Vis and CD spectral line shapes of carotenoid assemblies: spectral signatures of chiral H-aggregates. *J. Am. Chem. Soc.* **131,** 4267–4278 (2009).
40. Berova, N., Di Bari, L. & Pescitelli, G. Application of electronic circular dichroism in configurational and conformational analysis of organic compounds. *Chem. Soc. Rev.* **36,** 914–931 (2007).
41. Renger, T. *et al.* Thermally activated superradiance and intersystem crossing in the water-soluble chlorophyll binding protein. *J. Phys. Chem. B* **113,** 9948–9957 (2009).
42. Pescitelli, G. *et al.* Theoretical analysis of the porphyrin-porphyrin exciton interaction in circular dichroism spectra of dimeric tetraarylporphyrins. *J. Am. Chem. Soc.* **125,** 7613–7628 (2003).
43. Shingu, K., Imajo, S., Kuritani, H., Hagishita, S. & Kuriyama, K. Optical activity due to exciton interaction between 1B transitions of benzene chromophores. *J. Am. Chem. Soc.* **105,** 6966–6967 (1983).
44. Albano, G., Pescitelli, G. & Di Bari, L. Chiroptical Properties in Thin Films of π-Conjugated Systems. *Chem. Rev.* **120,** 10145–10243 (2020).
45. Spano, F. C. Modeling disorder in polymer aggregates: the optical spectroscopy of regioregular poly(3-hexylthiophene) thin films. *J. Chem. Phys.* **122,** 234701 (2005).
46. Köhler, A. & Bässler, H. *Electronic processes in organic semiconductors. An introduction* (Wiley-VCH, Weinheim, 2015).
47. Schwoerer, M. & Wolf, H. C. *Organic molecular solids* (Wiley-VCH, Weinheim, 2007).
48. Spano, F. C. The spectral signatures of Frenkel polarons in H- and J-aggregates. *Acc. Chem. Res.* **43,** 429–439 (2010).
49. Sibillano, T. *et al.* Wide Angle X-Ray Scattering to Study the Atomic Structure of Polymeric Fibers. *Crystals* **10,** 274 (2020).
50. Peng, Z., Ye, L. & Ade, H. Understanding, quantifying, and controlling the molecular ordering of semiconducting polymers: from novices to experts and amorphous to perfect crystals. *Mater. Horiz.* **9,** 577–606 (2022).
51. Tinoco, I. *Theoretical Aspects of Optical Activity Part Two: Polymers* (Wiley, 1962).
52. DeVoe, H. Optical Properties of Molecular Aggregates. II. Classical Theory of the Refraction, Absorption, and Optical Activity of Solutions and Crystals. *J. Chem. Phys.* **43,** 3199–3208 (1965).
53. Saikin, S. K. *et al.* On the Long-Range Exciton Transport in Molecular Systems: The Application to H-Aggregated Heterotriangulene Chains. *J. Phys. Chem. C* **121,** 24994–25002 (2017).
54. Cerdá, J., Ortí, E., Beljonne, D. & Aragó, J. Optical Properties of H-Bonded Heterotriangulene Supramolecular Polymers: Charge-Transfer Excitations Matter. *J. Phys. Chem. Lett.* **15,** 7814–7821 (2024).
55. Zehe, C. S. *et al.* Mesoscale Polarization by Geometric Frustration in Columnar Supramolecular Crystals. *Angew. Chem. Int. Ed.* **56,** 4432–4437 (2017).

Supporting Information:

Temperature-induced inversion of circular dichroism in supramolecular polymers revisited: Structural vs. electronic helicity

Asena Cerhan-Haink[1,4,†], Felix A. Wenzel[2,†], Michael Buchhorn[1], Richard Kellnberger[1], Eric Schaible[3], Klaus Kreger[2], Hans-Werner Schmidt[2]*, Richard Hildner[4]*, Eva M. Herzig[1]*

[*] *Corresponding authors. Email: eva.herzig@uni-bayreuth.de, r.m.hildner@rug.nl, hans-werner.schmidt@uni-bayreuth.de*
[†] *Both authors contributed equally*

[1] *Dynamics and Structure Formation – Herzig Group, University of Bayreuth, 95447 Bayreuth, Germany*

[2] *Macromolecular Chemistry I and Bavarian Polymer Institute, University of Bayreuth, 95447 Bayreuth, Germany*

[3] *Lawrence Berkeley National Laboratory, 1 Cyclotron Road, Berkeley, CA 94720, USA*

[4] *Zernike Institute for Advanced Materials, University of Groningen, Nijenborgh 3, 9747 AG Groningen, The Netherlands*

S1: Packing model of N-heterotriangulene

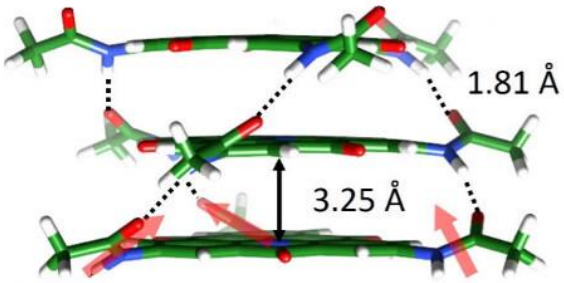

Fig. S1 | Side view of the cofacial stacking of a N-heterotriangulene derivative, namely a carbonyl-bridged triarylamine (CBT) linked to three acetamide side groups in 2,6,10 position of the CBT core. The structure is geometry optimized at the B3LYP-D3/6-31G** level. The π–π distance is 3.25 Å. Three strands of hydrogen bonds along the stacking direction form by rotation of the amides out of the CBT plane. Here, all amides are rotated in the same direction (red arrows pointing upwards yielding a so-called 3:0 configuration). To form stable hydrogen bonds, the distance between the amides of neighbouring molecules is 1.81 Å, which, together with the distance of the amide groups from the core, limits the rotation angle for the helical stacking imposed by additional chiral moieties in the side groups. Adapted from Cerda *et al.* [1].

S2: Materials and methods

Materials and sample preparation

Carbonyl-bridged triarylamine with (S)-chiral aliphatic side chains (s-CBT) was synthesised and purified as described in detail previously[2,3].

Self-assembly of s-CBT was performed in HPLC grade toluene (Sigma Aldrich), which was used as received. s-CBT in powder form was added to toluene and dispersed by ultrasonication for 15 minutes. The dispersion was stirred under reflux for 20 minutes and subsequently cooled to room temperature.

For WAXS measurements, dispersions were injected into a glass capillary with 2 mm in diameter (Hampton Research) and subsequently sealed with fast-drying epoxy resin (Weicon Epoxy Minute Adhesive).

Optical spectroscopy

CD measurements were carried out using a JASCO J-715 spectrophotometer. Photoluminescence measurements were carried out with an excitation wavelength of 380 nm using a JASCO FP8600 spectrofluorometer. UV/vis absorption spectroscopy was performed on a JASCO V-670 spectrophotometer. For each optical measurement, a fresh dispersion of s-CBT in toluene at a concentration of 40 µM (100 p.p.m.) were prepared unless otherwise stated. The dispersion was heated to 100°C, held for 10 min and then stepwise cooled to 0°C with intervals of 2°C (unless otherwise stated) and held for 10 minutes to allow for thermal equilibration of the system prior to each measurement. The dispersion was stirred during equilibration and throughout all measurements. Under these conditions no visual precipitation was observed.

WAXS measurements

X-ray scattering experiments in transmission geometry were performed at beamline 7.3.3 at the Advanced Light Source (ALS, Berkeley, USA) with an x-ray energy of 10 keV (Fig. S2). The transmission intensity was detected by a PILATUS3 X 2M at a sample detector distance of 430 mm. Silver behenate (AgBeh) powder was used as a calibration standard. Measurements were carried out in glass capillaries mounted in a temperature-controlled copper block with an opening for the X-ray beam. s-CBT in toluene was heated to 50°C and then gradually cooled to 20°C in steps of 10 °C. At a temperature of 20°C, the system was gradually cooled further in steps of 2°C or 1°C until 10 °C was reached. Each temperature was held for 10 minutes prior to measurement to allow for thermal equilibration of the system. This procedure was also performed with an empty capillary and a capillary filled with pure toluene. The 2D images obtained in the WAXS experiments were converted and reduced to 1D cuts using the GIXSGUI interface (version 1.7.1), a MATLAB based analysis program[4]. The reduced data were analysed using Python scripts carrying out background subtraction (glass capillary, solvent) for each temperature and the relevant peaks were fitted using a sum of Gaussian (for peaks in the low-q region <7 nm^{-1}) and Lorentzian functions (for peaks in the high-q region >7 nm^{-1}).

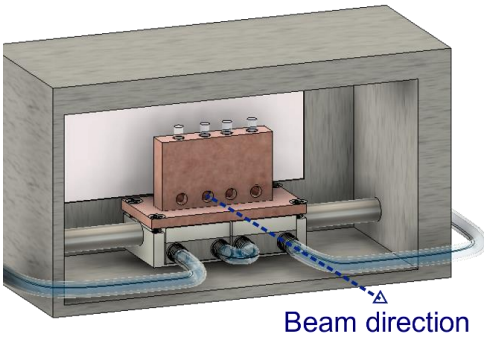

Fig. S2 | Schematic representation of the experimental setup used at the 7.3.3 beamline at the Advanced Light Source (ALS, Berkeley) for temperature controlled WAXS measurements.

Scanning electron microscopy

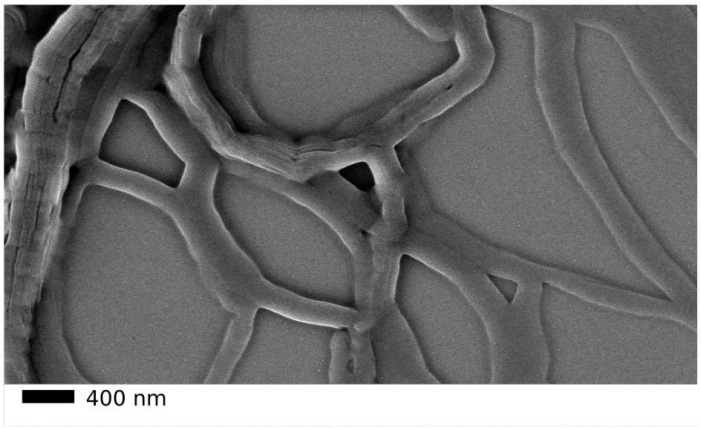

Fig. S3 | Scanning electron microscopy (SEM) image of a sample drop-cast from a toluene dispersion, showing the presence of bundles of nanofibers with a diameter of some 100 nm. Based on the bundles' diameter of ~200 nm and the column-column distance of 3.9 nm, each bundle can be estimated to comprise several 1000 hexagonally packed nanofibers. These measurements were performed with a Zeiss Leo 153 electron microscope.

S3: Additional optical investigations

Temperature-dependent CD spectroscopy

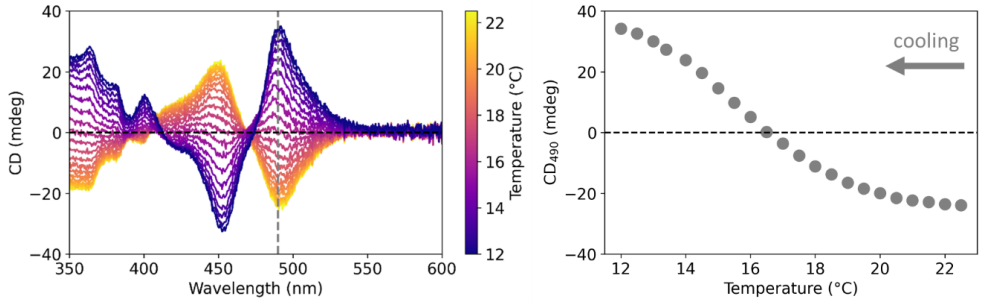

Fig. S4 | Left: CD spectra of bundles of supramolecular nanofibers as a function of temperature. CD spectra were recorded upon cooling in steps of 0.5°C from 22°C to 12°C, which is around the critical inversion temperature. Right: CD signal at 490 nm as a function of temperature showing an inversion temperature of 16.5°C. The concentration of s-CBT in toluene was 40 µM (100 p.p.m.).

Hysteresis of the CD signal at 490 nm

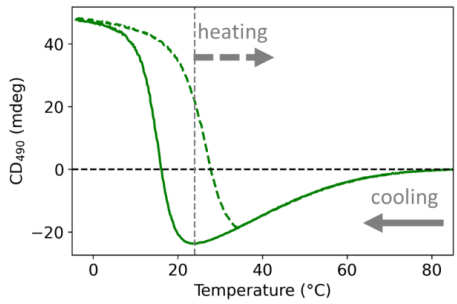

Fig. S5 | Hysteresis of the CD signal at 490 nm upon cooling and heating s-CBT in toluene at a concentration of ~40 µM (100 p.p.m.). The vertical grey dashed line at 24°C indicates a temperature where either positive or negative CD signals can be observed depending on the thermal history. The horizontal grey dashed line is a guide to the eye, indicating vanishing CD signal.

Absorption spectra at 24°C depending on the thermal history

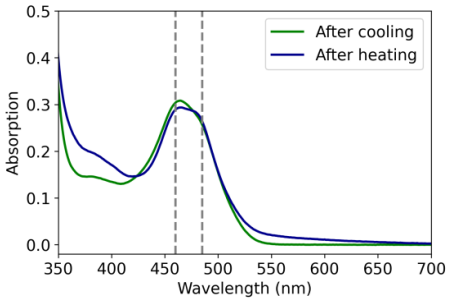

Fig. S6 | Absorption spectra of two distinct s-CBT dispersions in toluene at a concentration of ~40 µM (100 p.p.m.) applying different thermal protocols and after ageing at 24°C for 6 h. The green absorption spectrum is obtained after cooling the sample from 100°C to 24°C and aging for 6 h. The blue absorption spectrum is obtained after heating the sample from -5°C to 24°C and aging for 6 h. The electronic chirality is opposite at the same temperature depending on the thermal history (see also Fig. S5). Dashed lines refer to the absorption at 460 and 485 nm.

Stability of the supramolecular polymers

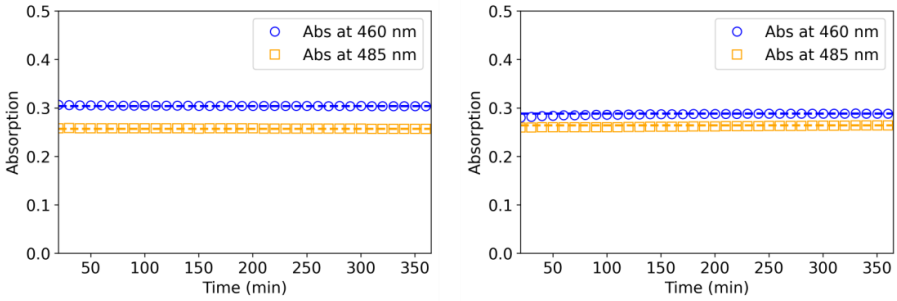

Fig. S7 | The absorption at 460 nm and 485 nm of s-CBT dispersions as a function of time at a concentration of 40 µM (100 p.p.m.) in toluene at 24°C treated with different thermal history. Left: sample is initially cooled from 100°C to 24 °C and aged for 6 h at this temperature; Right: sample is initially heated from -5°C to 24 °C and aged for 6 h. Both samples are (meta)stable under the given conditions, even though they have different electronic chirality (dashed line in Fig. S4), which indicates that an activation energy is required to convert between the two states.

Raw photoluminescence spectra

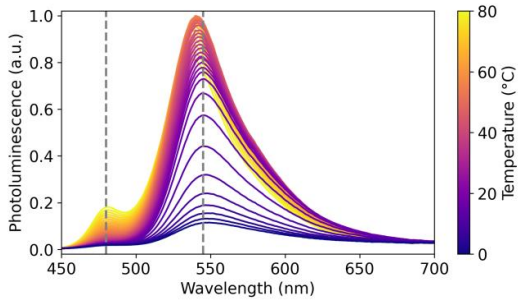

Fig. S8 | Raw temperature-dependent PL spectra of s-CBT in toluene at a concentration of 40 µM (100 p.p.m.). Grey dashed lines indicate the PL at 480 nm attributed to molecularly dissolved s-CBT and the PL at about 545 nm attributed to bundles of supramolecular nanofibres of s-CBT. The PL intensity at 480 nm is constantly decreasing with temperature, indicating a constant reduction in the concentration of s-CBT building blocks even around the critical inversion temperature T_{inv}.

CD, absorption and PL spectra at T_{inv}

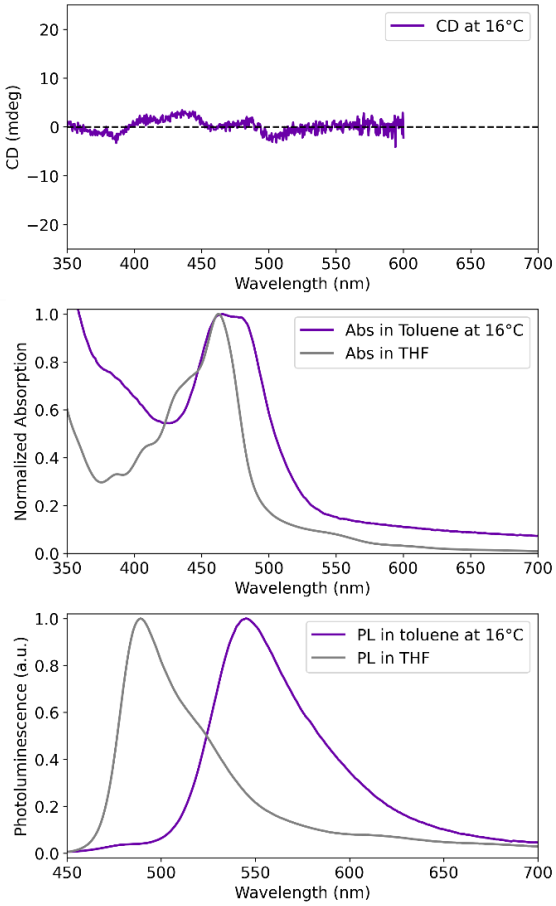

Fig. S9 | Optical spectra of s-CBT in toluene and THF at the critical temperature T_{inv} = 16°C. Top: CD spectrum of s-CBT in toluene. Middle: Normalised absorption. Bottom: Normalised photoluminescence (PL). For absorption and PL we overlaid the spectra measured on bundles of supramolecular nanofibres in toluene (violet) with those measured on molecularly dissolved s-CBT molecules in THF (grey). Particularly, the overlay of the PL spectra demonstrates that in toluene at T_{inv} only a very small fraction of molecularly dissolved s-CBT is present, as indicated by the weak relative PL signal at 480 nm. The relative PL signal at 480 nm in toluene is ~0.05 and given the PL quantum yield of 14% for molecularly dissolved s-CBT and ~ 3% for supramolecular nanofibers[2], the fraction of monomeric s-CBT in toluene can be estimated to be not more than 1% at 16°C. For all measurements the concentration of s-CBT was 40 μM (100 p.p.m.).

S4: Additional WAXS investigations

Concentration-dependent WAXS

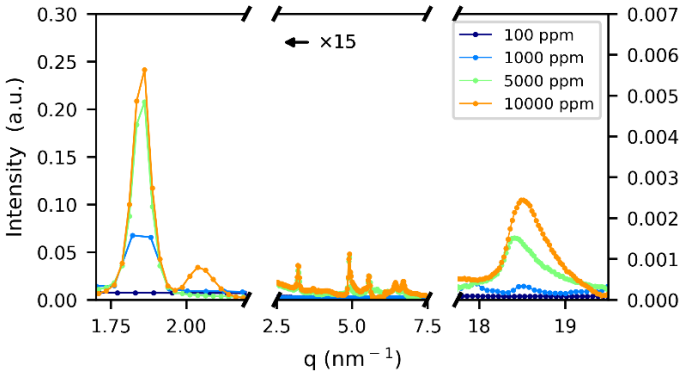

Fig. S10 | Concentration-dependent WAXS data of dispersions of s-CBT in toluene. Sufficiently high concentrations are necessary for examining the scattering signal. X-ray measurements were carried out in the lower third of the capillary for each concentration. Concentrations below 1000 p.p.m. do not show sufficient scattering signal in the range of the π-π-stacking feature (q ~ 18.5 nm^{-1}) for data evaluation. Concentrations below 5000 p.p.m. do not allow to retrieve the hexagonal packing in the low q-region. Therefore, the temperature study was carried out for the 5000 p.p.m. sample to maximize accessible information as a function of temperature.

Model for observed packing

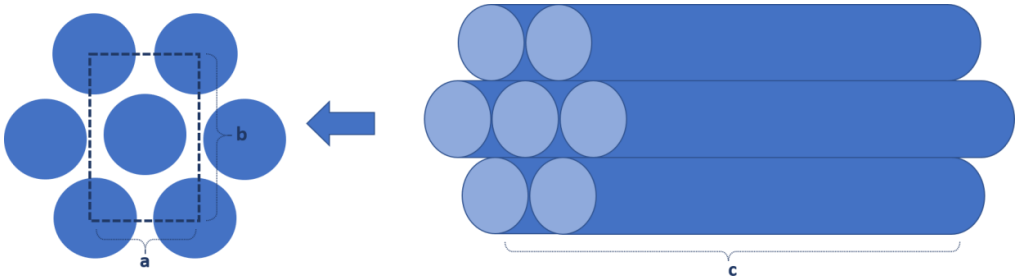

Fig. S11 | Sketch of hexagonally packed columns with (left) the relevant cell parameters a and b in top view and (right) the length c of the columns shown from the side.

Indexing of WAXS data

According to hexagonally packed columns, the observed peaks are indexed as follows:

$$\vec{q} = h\vec{a} + k\vec{b} = q_0 \quad (1)$$

$$q_{hk} = a\sqrt{h^2 + k^2 + 2hkcos60} = a\sqrt{h^2 + k^2 + hk} (2)$$

$$q_{10} = a = q_0 \quad (3)$$

$$q_{11} = q_0\sqrt{3} \quad (4)$$

.

.

.

$$q_{310} = q_0\sqrt{13} \quad (5)$$

where a and b are the lattice vectors. h and k are Miller indices of the hexagonally packed lattice[5]. The column-column distance between adjacent fibres is related to the positions of the first peak:

$$dc = \frac{4\pi}{\sqrt{3}q_0} \quad (6)$$

where q_0 and *dc* are the first peak position and column to column distance, respectively[6]. To more generally convert the momentum transfer value *q* into a real space distance *d*:

$$d = \frac{2\pi}{q} \quad (7)$$

Table S1: Experimental q positions (nm^{-1}) of the 5000 p.p.m. s-CBT dispersion in toluene measured with WAXS. For comparison, the theoretical peak positions for a hexagonally packed system are given based on the experimental 100 position.

	10 °C	12 °C	14 °C	15 °C	16 °C	17 °C	18 °C	20 °C	30 °C	40 °C	50 °C
experimental (100), q	1.858	1.856	1.854	1.853	1.854	1.853	1.852	1.851	1.845	1.839	1.833
theoric (110), q√3	3.218	3.215	3.212	3.21	3.211	3.209	3.208	3.206	3.195	3.185	3.174
experimental (110)	3.222	3.221	3.217	3.216	3.215	3.215	3.214	3.213	3.201	3.191	3.179
theoric (200), q√4	3.716	3.712	3.709	3.707	3.708	3.706	3.705	3.702	3.69	3.678	3.666
experimental (200)	3.725	3.71	3.715	3.712	3.715	3.713	3.729	3.711	3.697	3.697	3.684
theoric (210), q√7	4.915	4.91	4.906	4.904	4.905	4.902	4.901	4.897	4.881	4.865	4.849
experimental (210)	4.925	4.92	4.917	4.915	4.916	4.914	4.913	4.91	4.894	4.878	4.861
theoric (300), q√9	5.574	5.568	5.563	5.56	5.561	5.558	5.557	5.553	5.535	5.517	5.498
experimental (300)	5.578	5.577	5.573	5.57	5.568	5.566	5.566	5.562	5.545	5.526	5.509
theoric (220), q√12	6.436	6.429	6.424	6.421	6.422	6.418	6.416	6.412	6.391	6.37	6.349
experimental (220)	6.448	6.444	6.441	6.439	6.438	6.435	6.434	6.431	6.411	6.391	6.369
theoric (310), q√13	6.699	6.692	6.686	6.683	6.684	6.68	6.679	6.674	6.652	6.63	6.608
experimental (310)	6.719	6.714	6.709	6.709	6.706	6.704	6.703	6.698	6.676	6.655	6.631

switch the bisignate structure of the CD signal at the critical temperature. A slight rotation is consistent with the limited length and tilting angle that the three hydrogen-bonding amide groups of the C_3-symmetrical s-CBT molecules allow for, while maintaining the cofacial stacking within nanofibers. The bisignate CD signal of our supramolecular nanofibers arises from electronic coupling between transition dipole moments of adjacent molecules with a helical arrangement. Hence, the helicity of helically stacked transition dipole moments – the electronic helicity – must invert; a change in structural helicity is not required. Fundamentally, this difference in behaviour of electronic and structural helicity in our nanofibers arises from the fact that the structural C_3-symmetry of s-CBT translates into an electronic C_4-symmetry of two (nearly) degenerate, perpendicularly oriented transition dipole moments of the lowest energy electronic transition. We believe that this mechanism of inversion of electronic helicity also occurs in the supramolecular polymers based on other structurally C_3-symmetric molecules, for which the temperature-dependent inversion of the bisignate Cotton effect was reported, such as other N-heterotriangulenes[33], and tripenylene-2,6,10-tricarboxamides[16,17,20,27]. Those molecules have in common with our s-CBT compound that, apart from their structural C_3-symmetry, they possess bulky, chiral side groups, including hydrogen bonding amides; they assemble into bundles of H-type supramolecular nanofibers via hydrogen bonding and π-stacking, as evidenced by characteristic changes in the temperature-dependent UV/Vis spectra; they feature interactions of side groups of neighbouring supramolecular nanofibers, which sterically hinder large intra-fiber rotations of molecules. Hence, the structural helicity of nanofibers is not required to change as a function of temperature, since it is always determined by the chiral centres in the peripheral groups of the molecules, whereas the inversion of electronic helicity is responsible for the optical response. Since the chiral properties of the nanofibers are stable at a constant temperature, we anticipate that this mechanism will allow for structures with temperature-tuneable circularly polarised emission for nanophotonic applications.

Supporting Information

Materials and methods; additional optical investigations; additional WAXS investigations; temperature dependent WAXS data; discussion of electronic couplings, rotation angles and rotational line strengths.

S6: Electronic couplings and rotational line strength

Intermolecular electronic Coulomb coupling

The absorption spectra of bundles of supramolecular nanofibers in toluene at 20°C (Fig. 2C), especially the A_{485}/A_{460} absorption ratio (Fig. 2D), are identical to those that we reported recently[3]. Based on a theoretical framework developed by Spano and co-workers[7], we find via numerical simulations that the absorption spectra (at 20°C) are consistent with an electronic Coulomb coupling between transition dipole moments (TDMs) of neighbouring molecules of ~700 cm^{-1} [3]. For the bundles of nanofibers here we find that upon cooling to 0°C the ratio increases to A_{485}/A_{460} ~ 1.05 (Fig. 2D). To determine the electronic coupling for this low-temperature ratio, we consider the dependence of this ratio on the coupling V [7].

$$\frac{A_{485}}{A_{460}} = \frac{\left(1 - \frac{2V}{\omega_0} e^{-S} \sum_{n>0} \frac{S^n}{n!\, n}\right)^2}{S\left(1 - \frac{2V}{\omega_0} e^{-S} \sum_{n\neq 1} \frac{S^n}{n!\,(n-1)}\right)^2}$$

Here, ω_0 is the energy of an effective vibration coupling to the electronic transition (here the carbon-bond stretch with an energy of 1255 cm^{-1}), S = 0.54 is the Huang-Rhys factor of this vibration for non-interacting, molecularly dissolved s-CBT molecules, and n is the vibrational quantum number. From this expression we extrapolate that the electronic Coulomb coupling at 0°C is reduced to ~550 cm^{-1}.

The electronic Coulomb coupling in helically stacked molecules depends linearly on the cosine of the rotation angle,[8] around which nearest-neighbours are rotated with respect to each other. Using this dependence, the ratio of couplings from above $\frac{700}{550} \sim 1.2$ can be achieved by a change in rotation angle of only 10° in the range where the cosine function is 'steepest', i.e., around 45° since $\frac{\cos(40°)}{\cos(50°)} \sim 1.2$. Note that a C_4-symmetric system is "copied" onto itself after rotation by 90°. Hence, the angle of 45° is the critical angle to invert chirality in a C_4-symmetric system, to which the crossed arrangement of degenerate transition dipole moments in s-CBT corresponds, see the discussion further below.

A consequence of the electronic coupling between TDMs is the formation of an exciton band with a redistribution of oscillator strength to the highest-energy exciton states, i.e., only the highest energy states are optically allowed (notably, PL is still observed, since transitions from the bottom exciton states into vibrational levels in the ground state are still optically allowed)[9–11]. In a simple picture, this means that the absorption of H-aggregates is blue-shifted with respect to the absorption of the non-interacting, molecularly dissolved molecules. However, additional spectral shifts occur that are induced by a change in the local dielectric environment of each molecule upon aggregation. For our s-CBT molecules, this corresponds to a change from solvent molecules (toluene) surrounding s-CBT at high temperature (> 80°, non-aggregated, molecularly dissolved state) to s-CBT molecules cofacially stacked and fixated between s-CBT molecules within the nanofibers due to hydrogen-bond formation at lower temperatures. Within nanofibres the local environment of each s-CBT molecule is much more polar due to the extended π-electron system of the CBT core. Non-resonant (London) dispersive interactions give then rise to substantial additional van-der-Waals binding energies in ground and excited states of stacked molecules that cause a red-shift of the optical transition (sometimes referred to as “gas-to-crystal shift”)[11–13]. This red-shift can exceed the blue-shift induced by H-aggregation, i.e., an H-aggregate can feature a red-shifted absorption. Such red-shifted absorption of H-aggregates is observed for s-CBT, as we discussed in our recent work[3], as well as for the prototypical conjugated polymer P3HT[7,14].

Electronic structure of CBT monomers

To describe the electronic structure of the CBT core, in recent work Saikin *et al.*[15] and Cerda *et al.*[1] have performed density functional calculations on a geometry-optimised CBT molecule. To simplify calculations three short side groups were appended to the peripheries, here acetamides (i.e., an amide group linked to a methyl group). They found that the lowest-energy, optically allowed (HOMO-LUMO) transition is degenerate with perpendicularly oriented TDMs (Fig. S13).

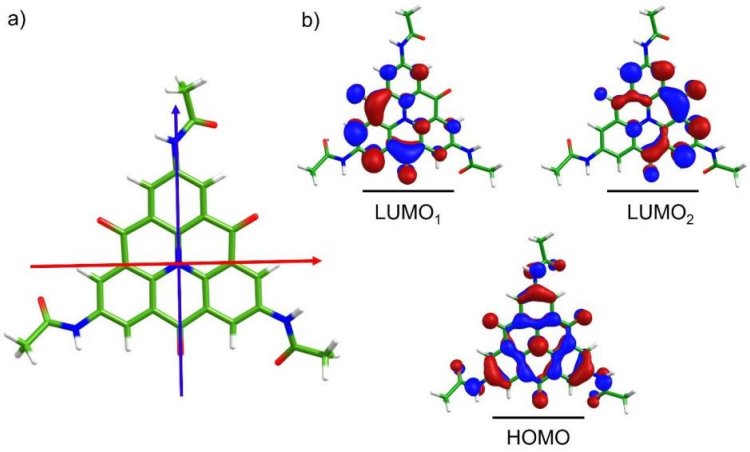

Fig. S13 | A) Geometry-optimised structure of a CBT core with appended acetamide groups. The blue and red arrows indicate the orientations of the TDMs of the (degenerate) lowest-energy optical (HOMO-LUMO) transition. B) Illustration of the nodal structures of HOMO and the two degenerate LUMO orbitals obtained from density functional theory. Taken from Cerda *et al.*[1].

To further demonstrate that the degenerate lowest-energy optically allowed transition in s-CBT is described by two independent, perpendicularly oriented TDMs, we also take into account group theory considerations following the approach outlined e.g. in Refs. [16,17]. In supramolecular nanofibres, the amides appended to the CBT cores are rotated out of the plane of the core to enable hydrogen bonding between adjacent building blocks (see Fig. S1). The amides are thus electronically decoupled from the core. For the symmetry of the core it is irrelevant, whether this out-of-plane rotation is symmetric for all three amides. We therefore only need to consider the CBT core without amides, which belongs to the point group D_{3h}:

- The core possesses a C_3 rotation axis through the central nitrogen, perpendicular to the plane of the core; this principal symmetry axis defines the z-axis of the coordinate system;
- It possesses three C_2 rotation axes in the CBT x-y-plane, perpendicular to the principal C_3 axis, each along the line connecting the central nitrogen and the carbonyls;
- It possesses a horizontal mirror plane σ_h, coinciding with the CBT plane, perpendicular to the C_3 axis.

Note that the presence of the principal C_3 rotation axis is the reason why such systems are often simply referred to as "C_3 symmetric" (it is *structurally C_3-symmetric*).

The character table for the D_{3h} point group is (TDM: transition dipole moment):

D_{3h}	E	$2C_3$	$3C_2$	σ_h	$2S_3$	$3\sigma_v$	TDM components
A_1`	1	1	1	1	1	1	
A_2`	1	1	-1	1	1	-1	
E`	2	-1	0	2	-1	0	x,y
A_1``	1	1	1	-1	-1	-1	
A_2``	1	1	-1	-1	-1	1	z
E``	2	-1	0	-2	1	0	

- A is the non-degenerate irreducible representation that is symmetric (character 1) with respect to a rotation about the principal axis;
- E is a doubly degenerate representation;
- Subscripts 1 and 2 indicate the symmetric and antisymmetric character of the representation with respect to a C_2 rotation;
- Prime (double-prime) indicates symmetry (antisymmetry) with respect to a reflection through the horizontal symmetry plane, in direct products (see below) to be evaluated as

  prime x prime = prime,

  prime x double-prime = double-prime x prime = double-prime, and

  double-prime x double-prime = prime;
- The symmetry of the three components of the electronic TDM is indicated in the last column; note that due to the planarity of the core the z-component (perpendicular to the CBT-plane) vanishes, i.e., only the x and y components are relevant here.

The direct products of the representations in the point group D_{3h} are given by:

D_{3h}	A_1	A_2	E
A_1	A_1	A_2	E
A_2		A_1	E
E			$A_1 + [A_2] + E$

The term in brackets [] is the antisymmetric component of the direct product.

As outlined above, in CBT the lowest-energy optically-allowed LUMO levels are doubly degenerate[1,15]. In this case, the LUMO orbitals must be of E`` symmetry, the only doubly degenerate representation in this point group (note that for convenience we do not follow the convention to label orbitals with the lower-case equivalents of the representations). The HOMO is of $A_2$`` symmetry, since the wavefunction inverts sign upon reflection at the σ_h plane (Fig. S12B).

The electronic ground state of the CBT molecule possesses the highest symmetry, i.e., the fully symmetric A_1` representation (all characters = 1, see the character table above). For the symmetry of the first electronically excited state, we need to evaluate the direct product of the HOMO and LUMO symmetries outlined above, i.e.,

$$A_2`` \times E`` = E`.$$

The symmetry selection rule for optical transitions states that the direct product of ground-state and excited-state symmetry as well as of the symmetry of the relevant components of the TDM must contain at least one element of A_1` symmetry to be optically allowed. Since the x- and y-components of the TDM have the same symmetry, E`, see the character table above, it reduces to (Γ(..) is the symmetry representation of the quantity in brackets):

$$\Gamma(\text{ground state}) \times \Gamma(\text{TDM}) \times \Gamma(\text{excited state}) = A_1` \times E` \times E` = \underline{A_1`} + A_2` + E.$$

Hence, the transition is <u>allowed</u> for both x- and y-components of the TDM, clearly showing that the TDM corresponding to the doubly degenerate lowest-energy transition in CBT possesses two independent, perpendicularly oriented components.

Importantly, for the calculation of the (sign of the) CD signal it is this arrangement of two perpendicularly oriented TDMs that is relevant here (see below). This arrangement of crossed TDMs belongs to the point group D_{4h} with a principal C_4 rotation axis perpendicularly oriented to the x-y-plane spanned by the TDMs. In our notation used and for the purposes of describing CD spectra, CBT cores represent thus <u>*electronically a C_4-symmetric system*</u>.

Rotational line strengths and the sign of the CD signal

Bisignate, conservative CD signals result from electronically interacting, helically stacked TDMs as outlined by many authors (see e.g. Refs. [8,18,19] for extensive descriptions, but the formalism dates back to the 1960s, see e.g. Refs. [20,21]). To obtain the sign of the CD signal the rotational line strength **R** is to be evaluated, as given by the vector cross product $\mathbf{R} \sim \mathbf{p}_i \times \mathbf{p}_j$ of the pair of interacting TDMs $\mathbf{p}_{i,j}$ on neighbouring molecules with a twist/rotation angle φ (see Fig. S14, for convenience we indicate vectorial quantities by letters in bold font, and the proportionality constants involve e.g. the wavevector of light and the distance between the TDMs, but those are irrelevant for this following discussion). Since electronically the CBT core represents a C_4-symmetric system with crossed, pairwise degenerate TDMs, we have in total four rotational line strength to evaluate: $\mathbf{R}_1 \sim \mathbf{p}_1 \times \mathbf{p}_3$, $\mathbf{R}_2 \sim \mathbf{p}_1 \times \mathbf{p}_4$, $\mathbf{R}_3 \sim \mathbf{p}_2 \times \mathbf{p}_3$, and $\mathbf{R}_4 \sim \mathbf{p}_2 \times \mathbf{p}_4$, see Fig. S14. The sign of the Cotton effect in CD spectra depends on the sign of the vector sum of all four rotational line strengths, the total rotational line strength $\mathbf{R}_{total} = \Sigma_{i=1-4} \mathbf{R}_i$, and the magnitude of the CD signal depends on the magnitude R_{total}.

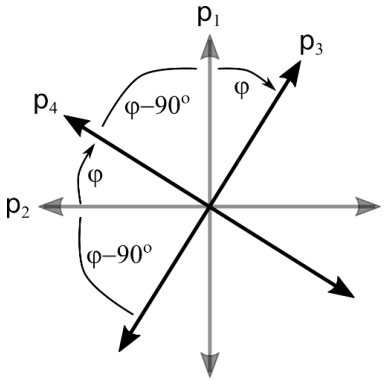

Fig. S14 | Illustration of the orientations and angles between TDMs that are important for the evaluation of the rotational line strength in a stacked arrangement (top view). The crossed TDMs of the bottom molecule ($\mathbf{p}_1$ and $\mathbf{p}_2$) are in grey and those of the top molecule are in black ($\mathbf{p}_3$ and $\mathbf{p}_4$), with the top molecule being rotated clockwise by an angle φ with respect to the bottom molecule.

To illustrate this evaluation of rotational line strengths and the change in CD sign at the critical angle of 45°, we consider four limiting situations in the following. Since all TDMs have the same strength, we can simplify by assuming that the magnitude of all TDMs is unity, i.e., each rotational line strength R_i is simply determined by the sinus of the relevant angle between the pairs of TDMs.

- **φ = 0°:** In this simplest case the TDMs just lie on top of each other, representing an achiral system. The magnitudes of all individual vector cross products vanish and for the total rotational line strength we get $R_{total} = 0$, i.e., no CD signal will be observed as expected for an achiral system.
- **φ = 45°:** This is another simple case, since a helicity cannot be defined here. Between p_1 and p_3 as well as p_2 and p_4 a clockwise rotation by 45° yields $R_1 = R_4 = \sin(45°) = 0.707$. But for the TDM pairs p_1 and p_4 as well as p_2 and p_3 the rotation is anti-clockwise, hence, $R_2 = R_3 = \sin(-45°) = -0.707$. We get $R_{total} = 0$ and there is no CD signal.
- **φ = 40°:** We used this angle as example for the situation above the inversion temperature of 16°C in the main text, corresponding to a clockwise rotation of 40° between p_1 and p_3 (p_2 and p_4). Hence, $R_1 = R_4 = 0.643$. However, for the pairs p_1 and p_4 (and p_2 and p_3) the angle to be used is then φ - 90° = -50°, i.e., $R_2 = R_3 = -0.766$. Thus, the total rotational line strength is negative, $R_{total} = -0.246$, i.e., a non-zero CD signal with a negative Cotton-effect results as we observe above the critical inversion temperature, see Fig. 2A in our manuscript.
- **φ = 50°:** This angle represents an example for the situation below the critical inversion temperature. This clockwise rotation between p_1 and p_3 (and thus p_2 and p_4) yields $R_1 = R_4 = 0.766$. For the pairs p_1 and p_4 (and p_2 and p_3) we get a rotation by φ - 90° = -40°, thus $R_2 = R_3 = -0.643$. Overall, the total rotational line strength is $R_{total} = 0.246$, i.e., again non-zero, but with positive sign, resulting in a CD signal with a positive Cotton effect, as we observe below the critical inversion temperature of 16°C, see Fig. 2A in our manuscript.

These simple considerations clearly show that for an electronically C_4-symmetric system with a pair of crossed electronic transition dipole moments the total rotational line strength inverts sign at the critical angle of 45°, i.e., the CD signal resulting from the electronic coupling of TDMs inverts.

In passing we note, that for a *structurally C_3-symmetric* system, corresponding to the structural symmetry of s-CBT, a rotation of 120° reproduces the system, i.e., the critical angle for a structural chirality inversion is 60° (see Fig 1C). Hence, if we assume that the rotation angle between neighbouring molecules along a nanostructure is initially 40° (Fig S15A), the structural helicity can be inverted either by changing this angle by +40° to +80° (Fig S15B, clockwise rotation of the top molecule). Alternatively, a much larger rotation of the top molecule by -80° (anticlockwise) to -40° is also possible (Fig S15C), but this is indistinguishable from the first option (the position of the molecules in Fig S15B and S15C is identical).

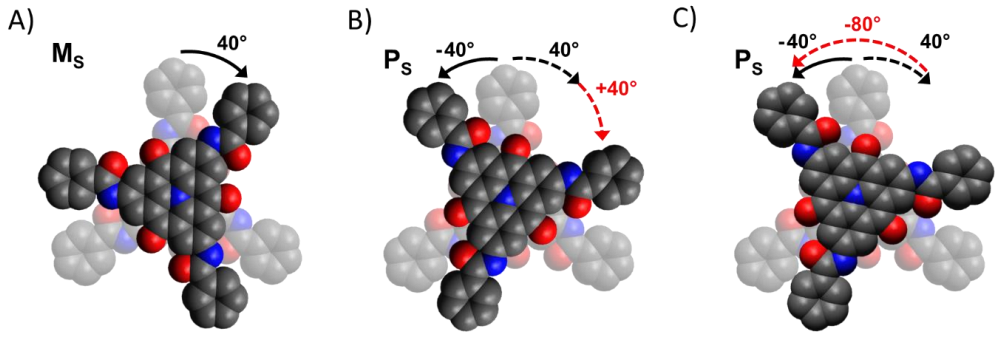

Fig. S15 | A) Sketch of helically stacked, structurally C_3-symmetric molecules with a rotation angle of 40°. B) A clockwise rotation of the top molecule by +40° to +80°. C) An anticlockwise rotation of the top molecule by -80°. The cases in B) and C) cannot be distinguished and result in the inversion of the structural helicity compared to the situation in A).

CD vs. optical rotation

The CD signal that we measure here is caused by the differential absorption of light with left- and right-handed circular polarisation, which is determined by the imaginary part of the (electronic) polarisability of CBT. Optical rotation refers to the rotation of the plane of polarisation of (linearly polarised) light when traversing a sample. This latter case is determined by the dispersion of the traversed medium, i.e., by the real part of the molecular polarisability. If, and only if, CBT were optically active, optical rotation

and CD are connected by the Kramers-Kronig relation. However, CBT can by symmetry not be optically active, since it belongs to the point group D_{3h} and thus possesses an S_3-axis of improper rotation[16,17].

The CD signal of the supramolecular polymers based on s-CBT shows a clear bisignate structure (Fig. 2A) and is largely conservative in the range of the lowest-energy (longest-wavelength) absorption. *Conservative* means that the integral over the wavelength-dependent bisignate CD signal vanishes in this relevant spectral region. Such conservative CD signals result from the collective response of electronically interacting TDMs that are helically stacked (no optical rotation and/or magnetic dipole moments are involved here)[19,21]. Hence, for the sign of the Cotton effect, the helicity of the stacked and interacting TDMs is relevant. As we have outlined above, the electronic symmetry of the TDMs is not identical to the structural symmetry of CBT. In this case, an inversion of the sign of the CD signal is not necessarily connected to a change in structural chirality.

S7: References

1. Cerdá, J., Ortí, E., Beljonne, D. & Aragó, J. Optical Properties of H-Bonded Heterotriangulene Supramolecular Polymers: Charge-Transfer Excitations Matter. *J. Phys. Chem. Lett.* **15,** 7814–7821 (2024).
2. Haedler, A. T. *et al.* Pathway Complexity in the Enantioselective Self-Assembly of Functional Carbonyl-Bridged Triarylamine Trisamides. *J. Am. Chem. Soc.* **138,** 10539–10545 (2016).
3. Wittmann, B. *et al.* Enhancing Long-Range Energy Transport in Supramolecular Architectures by Tailoring Coherence Properties. *J. Am. Chem. Soc.* **142,** 8323–8330 (2020).
4. Jiang, Z. *GIXSGUI*: a MATLAB toolbox for grazing-incidence X-ray scattering data visualization and reduction, and indexing of buried three-dimensional periodic nanostructured films. *J. Appl. Crystallogr.* **48,** 917–926 (2015).
5. Wang, G.-C. & Lu, T.-M. *RHEED Transmission Mode and Pole Figures. Thin Film and Nanostructure Texture Analysis.* 1st ed. (Springer New York; Springer International Publishing AG, New York, Cham, 2014).
6. Ghosh, S., Ramos, L. & Remita, H. Swollen hexagonal liquid crystals as smart nanoreactors: implementation in materials chemistry for energy applications. *Nanoscale* **10,** 5793–5819 (2018).
7. Spano, F. C. Modeling disorder in polymer aggregates: the optical spectroscopy of regioregular poly(3-hexylthiophene) thin films. *J. Chem. Phys.* **122,** 234701 (2005).
8. Spano, F. C. Analysis of the UV/Vis and CD spectral line shapes of carotenoid assemblies: spectral signatures of chiral H-aggregates. *J. Am. Chem. Soc.* **131,** 4267–4278 (2009).
9. Kreger, K., Schmidt, H.-W. & Hildner, R. Tailoring the excited-state energy landscape in supramolecular nanostructures. *Electron. Struct.* **3,** 23001 (2021).
10. Brixner, T., Hildner, R., Köhler, J., Lambert, C. & Würthner, F. Exciton Transport in Molecular Aggregates – From Natural Antennas to Synthetic Chromophore Systems. *Adv. Energy Mater.* **7** (2017).
11. Spano, F. C. The spectral signatures of Frenkel polarons in H- and J-aggregates. *Acc. Chem. Res.* **43,** 429–439 (2010).
12. Köhler, A. & Bässler, H. *Electronic processes in organic semiconductors. An introduction* (Wiley-VCH, Weinheim, 2015).
13. Schwoerer, M. & Wolf, H. C. *Organic molecular solids* (Wiley-VCH, Weinheim, 2007).

14. Stäter, S. *et al.* Directed Gradients in the Excited-State Energy Landscape of Poly(3-hexylthiophene) Nanofibers. *J. Am. Chem. Soc.* **145,** 13780–13787 (2023).
15. Saikin, S. K. *et al.* On the Long-Range Exciton Transport in Molecular Systems: The Application to H-Aggregated Heterotriangulene Chains. *J. Phys. Chem. C* **121,** 24994–25002 (2017).
16. Atkins, P. W., Paula, J. de & Keeler, J. J. *Atkins' physical chemistry* (Oxford University Press, Oxford, New York, 2018).
17. Harris, D. C. & Bertolucci, M. D. *Symmetry and spectroscopy. An introduction to vibrational and electronic spectroscopy* (Oxford University Press, Oxford, New York, 1978).
18. Albano, G., Pescitelli, G. & Di Bari, L. Chiroptical Properties in Thin Films of π-Conjugated Systems. *Chem. Rev.* **120,** 10145–10243 (2020).
19. Berova, N., Di Bari, L. & Pescitelli, G. Application of electronic circular dichroism in configurational and conformational analysis of organic compounds. *Chem. Soc. Rev.* **36,** 914–931 (2007).
20. Tinoco, I. *Theoretical Aspects of Optical Activity Part Two: Polymers* (Wiley, 1962).
21. DeVoe, H. Optical Properties of Molecular Aggregates. II. Classical Theory of the Refraction, Absorption, and Optical Activity of Solutions and Crystals. *J. Chem. Phys.* **43,** 3199–3208 (1965).

4.4 Publication III: Highly Efficient Supramolecular Nucleating Agents for Poly(3-hexylthiophene)

Macromolecules

pubs.acs.org/Macromolecules Article

Highly Efficient Supramolecular Nucleating Agents for Poly(3-hexylthiophene)

Felix A. Wenzel, Hannes Welz, Kasper P. van der Zwan, Sebastian Stäter, Klaus Kreger, Richard Hildner, Jürgen Senker, and Hans-Werner Schmidt*

Cite This: *Macromolecules* 2022, 55, 2861−2871 Read Online

ACCESS | Metrics & More | Article Recommendations | Supporting Information

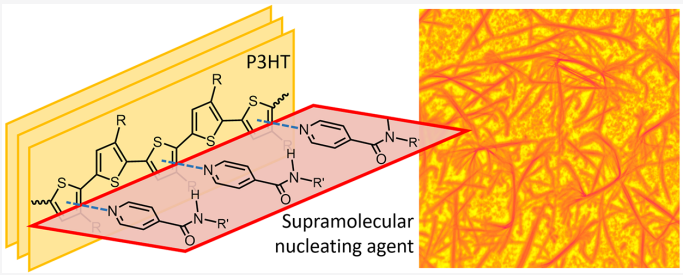

ABSTRACT: Controlling the solid-state morphology of semiconducting polymers is crucial for the function and performance of optoelectronic and photonic devices. Nucleation is a commonly used and straightforward approach to tailor the solid-state morphology of semi-crystalline polymers. However, efficient nucleating agents for semiconducting polymers are still rare. Here, we present a conceptual approach to tailor supramolecular nucleating agents for the semiconducting polymer, poly(3-hexylthiophene) (P3HT). Using this approach, we developed a class of supramolecular nucleating agents, which can achieve outstanding nucleation efficiencies of more than 95% at concentrations as low as 0.1 wt %. Such efficiencies can be achieved by combining an exceptionally high epitaxial match with highly regularly arranged donor−acceptor interactions between the nucleating agent and the polymer. Notably, the supramolecular agents do not induce trap states in thin films of P3HT and are beneficial for the film stability by controlling the solid-state morphology. We anticipate that this approach can be transferred to other semi-crystalline conjugated polymers, resulting in defined solid-state morphologies.

INTRODUCTION

Semiconducting semi-crystalline polymers are an established class of materials combining polymer science and technology with optoelectronics and photophysics.[1,2] These materials are of particular interest in thin-film architectures processed from solution.[3,4] Controlling the morphology, i.e., the relationship between the highly ordered crystalline domains and the entangled disordered amorphous phase, plays a decisive role in the optical and electronic characteristics and, ultimately, the device performance.[1,4−10] In general, the solid-state morphology can be controlled mainly by changes to the nucleation and crystal growth process. A multitude of approaches have evolved in this context, including thermal[11] and solvent vapor annealing,[12] solvent evaporation control[13] and antisolvent usage,[14] as well as processing additives[15,16] and nucleating agents.[17]

Poly(3-hexylthiophene) (P3HT), is one of the most investigated materials in the field of semiconducting polymers, rendering it an ideal model compound for fundamental studies.[3] In this context, different strategies to achieve morphology control during and after processing were widely investigated.[4,18] For example, multiple studies employed preformed P3HT nanofiber dispersions to improve device performances,[19,20] especially when the fibers are oriented under flow.[21] Different techniques have been used that include rubbing methods to orient the P3HT films[22,23] or nanostructured surfaces,[24,25] to name just a few. A common approach uses different small molecules as processing aids, such as 1,8-diiodooctane,[26] 4-bromoanisole,[27] or 2-hydroxypyridine.[15] Furthermore, nucleating agents, for example, based on carbon nanotubes,[28] graphene,[29,30] thiophene-containing copolymers,[31,32] as well as sorbitol and benzenetrisamide derivatives,[5,17,33] have been used to modify the crystallization process.

Received: November 5, 2021
Revised: February 18, 2022
Published: March 17, 2022

https://doi.org/10.1021/acs.macromol.1c02283
Macromolecules 2022, 55, 2861−2871

Heterogeneous nucleation, in general, is highly desirable because it controls the nucleation density during polymer processing.[34,35] As a result, nucleation reduces the average crystal size and size distribution and, in exceptional cases, allows to induce a specific crystal modification. Hence, heterogeneous nucleation can significantly alter the final property profile, including mechanical, electronic, and optical properties.[17,36−39]

Apart from often employed insoluble inorganic compounds such as talc, silica, and mica, supramolecular nucleating agents represent a recently established class of additives relying on the intrinsic reversibility of the structure formation.[36,40] These compounds dissolve at elevated temperatures, ensuring a homogeneous distribution in the polymer melt. Upon cooling, the building blocks self-assemble to highly regular solid nanostructures, which are finely dispersed in the polymer melt and induce polymer crystallization. Thus, these nucleating agents do not require elaborative dispersion additives and procedures.[17,36] For commodity polymers and engineering plastics, the use of inorganic and supramolecular nucleating agents are well investigated and widely established.[41,42] However, tailored and efficient supramolecular nucleating agents for semi-crystalline conjugated polymers are still rare.

Here, we report on a conceptual approach to design supramolecular nucleating agents for the semiconducting polymer, P3HT. We devised a class of molecular building blocks capable of forming supramolecular objects that act as efficient heterogeneous nucleation sites for the crystallization of P3HT. The synthesized series of bisamide building blocks, *N*,*N*′-1,4-phenylenebis[4-pyridinecarboxamide] (NA **1**) to N^1,N^4-di-4-pyridinyl-*trans*-1,4-cyclohexanedicarboxamide (NA **4**) is based on symmetrically substituted central units linked via amides to peripheral 4-pyridine units. We systematically varied both the central unit, either 1,4-substituted benzene or *trans*-1,4-cyclohexane, and the arrangement of the amide linkage (see Figure 1A). This design approach combines an attractive interaction between the donor thiophene groups of the polymer and the acceptor moieties of the nucleating agent, with a high epitaxial match encoded in the crystal structure of the nucleating agent (see Figure 1B). We demonstrate that this molecular design achieves excellent nucleation efficiencies for the semi-crystalline polymer P3HT, making it a promising candidate to control the P3HT solid-state morphology.

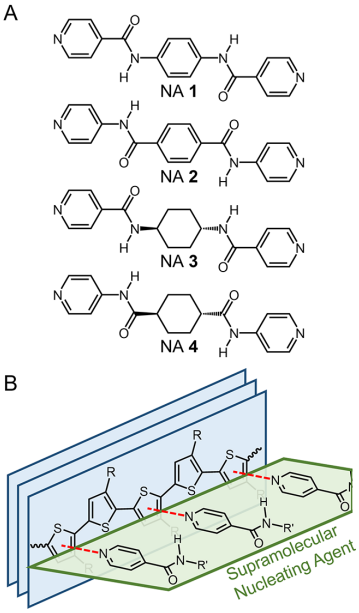

Figure 1. (A) Chemical structures of the four supramolecular building blocks: *N*,*N*′-1,4-phenylenebis[4-pyridinecarboxamide] (NA **1**), N^1,N^4-di-4-pyridinyl-1,4-benzenedicarboxamide (NA **2**), *N*,*N*′-*trans*-1,4-cyclohexanediylbis[4-pyridinecarboxamide] (NA **3**), and N^1,N^4-di-4-pyridinyl-*trans*-1,4-cyclohexanedicarboxamide (NA **4**). The molecules are based on substituted benzene or cyclohexane central unit and peripheral 4-pyridine moieties linked via different arrangements of the amide group. (B) Conceptual approach for supramolecular hydrogen-bonded nanostructures (green) providing efficient heterogeneous nucleation sites for the nucleation of P3HT (blue). We designed the supramolecular nucleating agent featuring an epitaxial match and attractive interactions between the pyridine acceptor moieties of the supramolecular nucleating agent and the thiophene donor moieties of the P3HT (indicated by dashed red lines).

EXPERIMENTAL SECTION

Materials. All solvents were purified according to standard procedures unless otherwise noted. The synthesis of pyridine-functionalized supramolecular nucleating agents NA **1**−NA **4** was conducted by amidation reactions as schematically depicted in the Supporting Information, Section S1. Details on the syntheses, purification, and characterization are given in the Supporting Information, Section S2. Regioregular poly(3-hexylthiophene) (grade: RMI-001-EE) was purchased from Rieke Metals and used as received. It features a weight average molecular weight M_w of 57 kg mol^{-1} and a dispersity Đ of 2.4 as determined by size exclusion chromatography. Size exclusion chromatography was performed with a Waters HPLC pump 515 and a WATERS 2998 as a UV detector. For separation, a guard column (PL, ResiPore, length: 5 cm, diameter: 0.8 cm) and two analytical columns (PL, ResiPore, length: 30 cm, diameter: 0.8 cm) were used. Tetrahydrofuran (THF) was used as eluent at a flow rate of 0.5 mL min^{-1}, and the molecular weight was reported with respect to narrowly distributed polystyrene standards.

Regioregular poly(3-butylthiophene) (grade: 4001-E) and regioregular poly(3-octylthiophene) (grade: 4003-E) were also purchased from Rieke Metals and used as received.

Differential Scanning Calorimetry. Differential scanning calorimetry (DSC) was conducted using Mettler Toledo DSC 3$^+$. For the preparation of bulk samples, a stock solution with 1 wt % of P3HT was prepared in chlorobenzene by dissolving the polymer at an elevated temperature until a clear solution was obtained. For samples with the different compounds NA **1**−NA **4**, amounts of 0.01 to 1 wt % with respect to the P3HT weight were dissolved in the stock solution. Prior to the DSC measurements, the solvent was completely removed under vacuum at 100 °C overnight. About 3−10 mg of the dried samples were weighed into the DSC pans and closed with a cover lid. A neat P3HT reference sample was prepared in the same manner by drying the pure stock solution.

Dynamic Differential Scanning Calorimetry Measurements. Prior to the dynamic experiments, all samples were heated from 100 to 300 °C under nitrogen and held for 5 min to erase the thermal history. Afterward, a first cooling, second heating, and second cooling run were performed. The cooling and heating rates were always 10 K min^{-1}. The values of the second cooling curves are reported. The reported thermal transition temperatures refer to peak temperatures in the DSC thermograms.

Isothermal Differential Scanning Calorimetry Measurements. Pretreatment of the sample was performed in a similar manner as described above to erase the thermal history. The sample was heated to 300 °C and held for 5 min at this temperature. It was subsequently cooled with a scan rate of 10 K min^{-1} to the isothermal temperature,

https://doi.org/10.1021/acs.macromol.1c02283
Macromolecules 2022, 55, 2861−2871

i.e., 212, 214, 216, 218, 220, and 222 °C, respectively, and held at this temperature for 60 to 180 min.

Polarized Light Microscopy. Polarized light microscopy was performed on a Nikon Invers Diaphot TMD 300 optical microscope. Thin films of neat P3HT and P3HT with 1 wt % of NA **1** were prepared via drop-casting a solution containing 1 wt % of P3HT in chlorobenzene on a glass slide. Contact samples were prepared by depositing a large amount of crystals of NA **1** on top of a thin film of neat P3HT. Temperature-dependent investigations on thin films and contact samples were performed using an HS82 hot-stage system from Mettler Toledo in the temperature range between room temperature and 300 °C under nitrogen flow. Optical micrographs were recorded using a Nikon DS-Ri2 digital camera and Nikon ACT-1 software.

Structure Elucidation. Single crystals of NA **1** were prepared by dissolving NA **1** in *N*,*N*-dimethylformamide (DMF) and exposing the solution to a heptane atmosphere. The heptane slowly diffuses into the DMF solution, and the crystals of NA **1** are formed. The solvents were slowly evaporated, and the larger crystals were collected. Single crystals were investigated using an STOE STADIVARI single-crystal diffractometer with Mo K_α radiation equipped with an Oxford Cryostream low-temperature unit. Data collection, indexing, and space group determination were done with the software package X-area (Stoe). Structure solution and refinement were done with ShelXL,[43] ShelXT,[44] and Olex.[45]

Powder X-ray diffraction data were collected on an STOE STADI P diffractometer equipped with a Ge(111) monochromator using Cu $K_{\alpha 1}$ radiation. The powder was filled in a 0.5 mm capillary tube and was measured in Debye−Scherrer geometry under ambient conditions. Indexing, simulated annealing, and Rietveld refinement were done with the software package TOPAS.[46]

Geometry optimization was done using the software package CASTEP[47] using the Perdew−Burke−Ernzerhof (PBE) functional and the Tkatchenko−Scheffler[48] dispersion correction scheme. Electronic cut-off energy of 900 eV and a Monkhorst k point grid spacing of 0.07 $Å^{-1}$ were used.[49]

Geometric models for the combination of the crystal structures of NA **1** and P3HT were built with Jmol.[50]

Hyperspectral Imaging. For hyperspectral imaging, thin films were prepared using solutions with 1 wt % of P3HT in chlorobenzene containing no or 0.1 wt % of NA **1** with respect to the polymer. Thin films were obtained by spin-coating with a Coros OP15 (Siemens) with a CONVAC 1001 onto glass slides at 1000 rpm for 60 s. The samples were heated under an inert atmosphere to 300 °C, held for 15 min at this temperature, and subsequently cooled to room temperature.

Hyperspectral photoluminescence imaging was performed with a home-built microscopy setup. To excite the sample, a pulsed white light laser system with a tunable wavelength filter (NKT SuperK EXTREME EXU-6 PP, SuperK SELECT), tuned to 560 nm, was used. In an inverted epi-illumination microscope layout, the excitation beam passes a 575 nm dielectric short-pass filter (Edmund, 84-709) and reflects off a 580 nm dichroic mirror (Semrock, FF580-FDi01-25 × 36) toward an oil-immersion objective (Olympus, PLAPON60-XOPH UIS2). To achieve widefield illumination, an additional lens in front of the dichroic mirror was inserted. The fluorescence signal is collected by the same objective, which then passes the dichroic mirror and a 568 nm long-pass filter (Semrock, BLP01-568R-25) to suppress residual laser light. The signal is then focused onto the slit of an imaging spectrograph (Princeton Instruments, IsoPlane 160, 150 g mm^{-1}) equipped with a cooled electron-multiplying charge-coupled device (emCCD) camera (Andor iXon Ultra 897). In an individual emCCD image, the photoluminescence signal is spectrally dispersed along rows (along the *x*-axis) of the chip, while spatial information is retained along columns, i.e., along the slit (*y*)-axis. The imaging quality of the spectrograph allows to retrieve and analyze 83 spectra along the *y*-axis, which corresponds to a distance of ∼40 μm using the magnification of the microscope of 67. After taking an image, the sample was moved by 500 nm in the *x*-direction with a piezo translation stage (piezosystems jena, TRITOR 102 CAP). These steps were repeated until an area of 40 × 40 μm^2 was scanned, corresponding to a total of 83 × 80 = 6640 individual photoluminescence spectra from each area.

RESULTS AND DISCUSSION

Apart from the numerous structural motifs which were used to achieve supramolecular (nano)objects and act as nucleating agents, we selected C2-symmetrical linear structures such as 1,4-benzenebisamides and 1,4-cycloehexanebisamide derivatives. These compounds are known to form a one-dimensional strand of hydrogen bonds, resulting in platelet or ribbon-like structures on the nano and mesoscale.[51,52] In particular, at least two opposite surfaces in these structures form a very regular and linear sequence of their used side groups, which may serve as nucleation sites for the extended P3HT backbone. For this, we explored a set of supramolecular nucleating agents for the semiconducting polymer, P3HT, consisting of four structurally similar bisamides NA **1**−NA **4**, each featuring two peripheral 4-pyridine moieties. The chemical structures of the four bisamides are shown in Figure 1A. The central unit of the bisamides is either based on 1,4-substituted benzene or *trans*-1,4-substituted cyclohexane moieties. The central units are connected with the pyridine moieties via different arrangements of amide linkages. These variations not only typically result in slightly different crystallographic parameters but also alter the strength of the directed hydrogen bond pattern. As a result, the thermal properties, as well as the solubility and self-assembly behavior of the molecules in the polymer melt, can be tuned. The syntheses of the four compounds, *N*,*N*′-1,4-phenylenebis[4-pyridinecarboxamide] (NA **1**), N^1,N^4-di-4-pyridinyl-1,4-benzenedicarboxamide (NA **2**), *N*,*N*′-*trans*-1,4-cyclohexanediylbis[4-pyridinecarboxamide] (NA **3**), and N^1,N^4-di-4-pyridinyl-*trans*-1,4-cyclohexanedicarboxamide (NA **4**), were performed via standard amidation reactions. Details on the synthetic route, the synthetic procedure, and the molecular characterization are given in the Supporting Information, Sections S1 and S2. All compounds feature melting points above 300 °C. These high phase transitions are required because dissolution and self-assembly of the compounds in the polymer melt strongly depend on, for instance, molecular structure, medium, concentration, and processing temperature. At elevated temperatures, the mandatory dissolution of the compounds to a molecular level in the P3HT melt results in a single homogeneous phase. Under appropriate conditions, this also allows for the self-assembly of well-dispersed solid nanoobjects before the polymer crystallization occurs.

The most common method to evaluate the performance of supramolecular nucleating agents is based on bulk studies of a polymer crystallization process. Here, the nucleating agents are evaluated using the difference (ΔT_c) between the maximum achievable crystallization temperature $T_{c,max}$ and the standard crystallization temperature T_{c0} of the neat polymer.[53] Standard crystallization temperatures T_{c0} are commonly obtained by dynamic differential scanning calorimetry (DSC) experiments. The maximal achievable crystallization temperature $T_{c,max}$ can be determined by self-nucleation experiments, as described in the literature.[54] In such self-nucleation experiments, a dynamic temperature protocol is used to melt the polymer partially. Tiny polymer crystals remain in the melt. These crystals eventually act as excellent nucleation sites for polymer crystallization because they have the same chemical composition and a perfectly epitaxial matching surface. For our studies, we selected the commercial P3HT grade RMI-001-EE

https://doi.org/10.1021/acs.macromol.1c02283
Macromolecules 2022, 55, 2861−2871

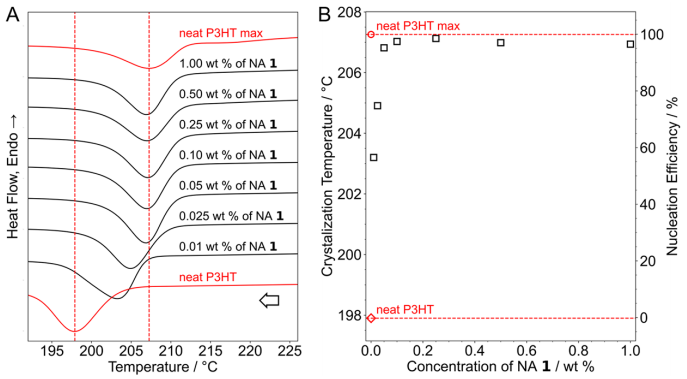

Figure 2. (A) Second DSC cooling curves of the standard and self-nucleated crystallization of neat P3HT (in red) and P3HT with NA **1** in the concentration range from 0.01 to 1 wt % (in black). The addition of NA **1** to P3HT shifts the polymer crystallization peak increasingly closer toward $T_{c,max}$, demonstrating the outstanding performance of this nucleation agent for P3HT. (B) Peak minima of the P3HT polymer crystallization and nucleation efficiency as a function of the concentration of NA **1**. The standard and self-nucleated crystallization temperatures for neat P3HT are shown as the lower and upper limits (in red).

(see Materials section). This polymer has a $T_{c,max}$ of 207.3 °C and a $T_{c,0}$ of 197.9 °C, resulting in a ΔT_c of 9.4 °C (Supporting Information, Section S3). This ΔT_c value provides a sufficiently large window to determine the nucleation efficiency of our supramolecular nucleating agents.

We have performed a series of dynamic DSC experiments using P3HT and the supramolecular building blocks NA **1**–NA **4** at different additive concentrations ranging from 0.01 to 1 wt %. In Figure 2A, the corresponding second DSC cooling scans comprising the polymer crystallization of P3HT with NA **1** at different concentrations as well as the neat and self-nucleated P3HT are shown. Details on the experimental procedure and DSC thermograms of NA **2**–NA **4** are presented in the Supporting Information, Section S4. The crystallization peak of P3HT notably shifts to higher temperatures at very low concentrations of NA **1** of only 0.01 wt %. With an increasing amount of NA **1**, the shift rapidly approaches a constant value close to the maximal achievable crystallization temperature $T_{c,max}$ of P3HT. A more straightforward presentation is provided by plotting the corresponding peak crystallization temperatures, as depicted in Figure 2B. For example, the addition of only 0.01 wt % of NA **1** already increases the crystallization temperature by 6.2 to 204.1 °C. The addition of 0.1 wt % of NA **1** increases the crystallization temperature of P3HT already by 9.2 to 207.1 °C, which is only slightly lower than the maximal achievable crystallization temperature $T_{c,max}$ of 207.3 °C.

Based on these values, the nucleation efficiency (NE) according to Lotz and Wittman was determined.[53] The nucleation efficiency is defined as the ratio of two temperature differences, namely, the crystallization temperature of the nucleated sample (T_c) to the standard crystallization of the neat polymer ($T_{c,0}$) and the self-nucleated sample ($T_{c,max}$) to the standard crystallization temperature (eq 1).

$$\mathrm{NE} = \frac{T_c - T_{c,0}}{T_{c,max} - T_{c,0}} \quad (1)$$

In this situation, $T_{c,0}$ represents the lower limit, and $T_{c,max}$ correlates to the upper limit of the crystallization temperature. Thus, it provides a measure to quantify and compare different nucleating agents with respect to their nucleation performance.

Figure 3 displays the nucleation efficiencies of all four nucleating agents as a function of concentration. Already at

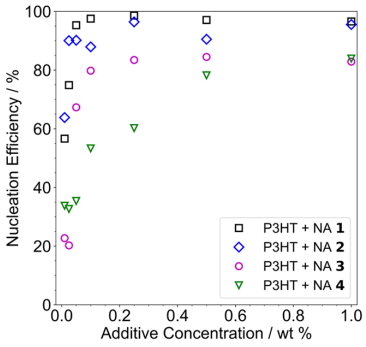

Figure 3. Nucleation efficiencies as a function of additive concentration: NA **1** (black squares), NA **2** (blue diamonds), NA **3** (magenta circles), and NA **4** (green triangles). Already at low concentrations, all four nucleating agents increase the polymer crystallization temperature significantly. NA **1** features an outstanding P3HT nucleation efficiency of 98% at already a concentration of 0.1 wt %.

concentrations of 0.1 wt %, all nucleating agents feature a significant nucleation efficiency of more than 50%. At a concentration of 0.5 wt %, the nucleating agents feature efficiencies of more than 75%. In general, with increasing concentration, the nucleation efficiency saturates and reaches a plateau. This plateau is very close to 100% for NA **1** and NA **2**, and in the case of NA **3** and NA **4**, still above 80%. In particular, the bisamides based on benzene as the central unit, NA **1** and NA **2**, exhibit outstanding performance at concentrations of 0.1 wt %. To the best of our knowledge, the determined nucleation efficiency of 98% for NA **1** at a concentration of 0.1 wt % is the highest reported value for the nucleation of P3HT. Therefore, we have focused in the following on this supramolecular nucleating agent, NA **1**.

With isothermal DSC measurements, it is possible to investigate the influence of nucleating agents on the

https://doi.org/10.1021/acs.macromol.1c02283
Macromolecules 2022, 55, 2861–2871

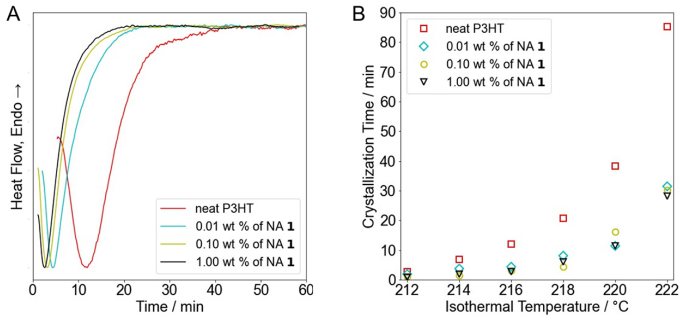

Figure 4. (A) Isothermal crystallization curves at 216 °C for 1 h for neat P3HT and P3HT with different concentrations of NA **1**. The heat flow is normalized to the minima of each sample and the baseline value at 60 min. (B) Time to reach the enthalpic minimum of the respective crystallization peaks at different isothermal temperatures. With increasing isothermal temperature from 212 to 222 °C, the time to reach the minimum is prolonged. In all cases, the addition of NA **1** results in a significant reduction of the crystallization time.

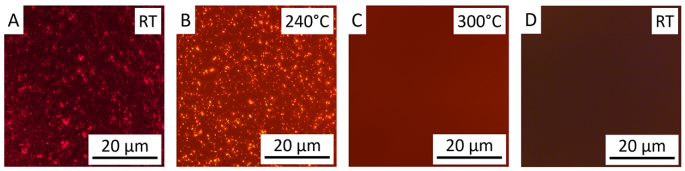

Figure 5. Optical light micrographs between crossed polarizers of P3HT films with 1 wt % of NA **1** before the first melting at RT (A) and after the P3HT melts at 240 °C (B). The birefringence in panels A and B is caused by the crystals of NA **1**. Upon further heating to 300 °C (C), NA **1** dissolves in the P3HT melt, visible by the disappearance of the birefringence. Cooling back to room temperature (D) results only in a uniform color change.

crystallization kinetics of the polymer by providing a tunable number of nucleation sites at a constant polymer crystallization growth rate. We performed isothermal DSC studies for different temperatures between 212 and 222 °C using samples of neat P3HT and P3HT with 0.01, 0.1, and 1.0 wt % of NA **1**. Exemplarily, DSC curves for such experiments at 216 °C, a temperature well above the standard crystallization temperature $T_{c,0}$, are depicted in Figure 4A. At these conditions, the enthalpic minimum for the neat P3HT is close to 12 min. Already with 0.01 wt % of NA **1**, the P3HT crystallization significantly accelerates, resulting in an enthalpic minimum at 4.3 min. Higher concentrations of NA **1** further reduce this time to 3.2 min with 0.1 wt % and to 2.6 min for the sample with 1.0 wt % of NA **1**. This data shows that even at low concentrations, NA **1** acts as an efficient nucleating agent, which is in line with the previous results for nucleation efficiencies. The isothermal DSC curves do not cover the entire crystallization process for the samples. Analyzing these data by the Avrami crystallization kinetic model is not applicable.[55]

As a qualitative guide for the kinetics of the crystallization process, we plotted the times to reach the minima of the crystallization enthalpy as a function of the isothermal temperature (Figure 4B). Expectedly, with increasing isothermal temperature, the crystallization time increases.[33] Notably, the crystallization times for the different concentrations of NA **1** at each temperature are essentially the same, demonstrating the effectiveness of the nucleating agent even at low concentrations. Moreover, the absolute difference between the P3HT samples with NA **1** and the neat P3HT becomes more significantly pronounced with an increasing isothermal temperature. For instance, at a high temperature of 222 °C, the enthalpic minima of the P3HT crystallization with NA **1** are reached within approximately 30 min, whereas for the neat P3HT, 85 min are required. In all cases shown in Figure 4B, the addition of NA **1** reduces the time to reach the enthalpic minimum by a factor of about three compared to the neat P3HT.

In a typical approach, the nucleation and crystallization process of semi-crystalline polymers with supramolecular nucleating agents is visualized by temperature-dependent polarized light microscopy. Here, we used polarized light microscopy to particularly demonstrate the homogeneous distribution of nanoscale supramolecular objects in a thin film of P3HT. For this, we prepared a drop-casted film comprising P3HT and 1 wt % of NA **1** crystals (see Figure 5). At room temperature (Figure 5A), the film shows birefringent features of finely dispersed NA **1** crystals. During heating to 240 °C, the P3HT starts to melt, as shown by the color change of the film, whereas the birefringent features are still present at this temperature (Figure 5B). Upon further heating to 300 °C, these structures vanish (Figure 5C), demonstrating the dissolution of NA **1** and its homogeneous distribution in the polymer melt. Upon cooling to room temperature, only a uniform color change of the thin film is observed, which is attributed to the crystallization of P3HT (Figure 5D). The absence of the birefringent structures indicates that supramolecular aggregates of NA **1** are finely dispersed with a size significantly below the diffraction limit of the optical light microscope.

In fact, the formation of supramolecular objects of NA **1** upon cooling can be seen with dynamic DSC experiments. Figure 6 shows dynamic DSC cooling curves using P3HT with different concentrations of NA **1** in the temperature range from 290 to 190 °C. The mixture comprising P3HT and 1 wt % of NA **1** shows a small but distinct exothermic peak at 274 °C, which is attributed to the crystallization of NA **1** in the

https://doi.org/10.1021/acs.macromol.1c02283
Macromolecules 2022, 55, 2861−2871

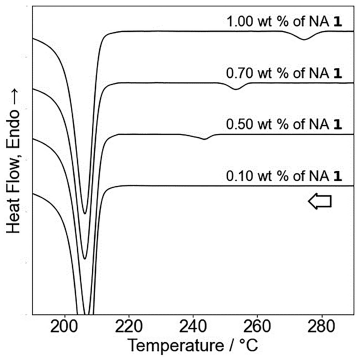

Figure 6. DSC cooling curves from 290 to 190 °C of P3HT with different concentrations of NA **1** (1.0, 0.7, 0.5, and 0.1 wt %). The samples with high concentrations of NA **1** feature an exothermic peak at elevated temperatures, which is attributed to the crystallization of NA **1**. The position of this peak shifts to lower temperatures, and the integral of this peak decrease with decreasing NA **1** concentration. All four DSC curves show a strong exothermic peak at about 207 °C, which is attributed to the crystallization of P3HT.

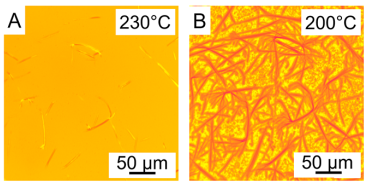

Figure 7. Optical light micrographs between crossed polarizers with a lambda-quarter plate of contact samples comprising fiber-like μm-sized objects of NA **1** on a thin film of P3HT. (A) At 230 °C, the P3HT film is molten, and birefringent structures of NA **1** are visible. (B) Upon cooling to 200 °C, trans-crystallization of P3HT from the structures of NA **1** takes place.

P3HT melt. This exothermic peak shifts for the sample with a lower concentration of 0.7 wt % of NA **1** to 253 °C. A further shift to lower temperatures of 244 °C is observed for the sample with only 0.5 wt % of NA **1**. Furthermore, the integral of these exothermic peaks also decreases as expected with decreasing additive concentration. The formation of supramolecular objects takes place in the melt clearly before P3HT starts to crystallize. Upon cooling, these three samples show a strong exothermic peak at about 207 °C, which is attributed to the crystallization of P3HT. For the concentration of 0.1 wt % of NA **1**, no exothermic peak for NA **1** was detected due to the low concentration and the sensitivity of the instrument. However, supramolecular objects, which act as heterogeneous nucleation sites, are present because the crystallization of P3HT also takes place at about 207 °C, well above the standard crystallization temperature $T_{c,0}$.

All data clearly suggests that self-assembly to solid objects of NA **1** must be present, giving rise to a nucleation effect. We note that as shown in Figure 5 above, the dimensions of the *in situ* formed supramolecular objects are well below the optical diffraction limit, and thus, the objects must be on the nanoscale. Since it is difficult to visualize the shape and size of these objects within the bulk film of P3HT by, e.g., electron microscopy, we visualize the trans-crystallization process of P3HT onto the nucleating agent by investigating contact samples. Contact samples were prepared by placing a large amount of μm-sized crystals of NA **1** on top of a P3HT film. The temperature-dependent crystallization behavior was studied by polarized light microscopy. These samples were heated to 240 °C. At this temperature, the P3HT is completely molten without dissolving the crystals of NA **1**, as already shown in Figure 5B. Upon cooling to 230 °C, only birefringent structures of NA **1** are present on top of the melt of P3HT, as shown in Figure 7A. Upon further cooling to 200 °C, additional birefringent features are formed, which occur close to the solid fiber-like structures of NA **1** (Figure 7B). This finding can be clearly assigned to the trans-crystallization process of P3HT on the nucleating agents. An additional series of micrographs under crossed polarizers showing a more detailed picture of the process is depicted in the Supporting Information, Section S5. Further evidence is provided by performing similar contact sample experiments using *N*,*N*′-1,4-phenylenebisbenzamide as a reference. This compound is very similar to that of NA **1**, but performing experiments revealed no additional birefringence, i.e., no trans-crystallization (see Supporting Information, Section S6).

To understand how the surface of NA **1** can nucleate P3HT on a molecular level, X-ray diffraction experiments were performed to elucidate the crystal structure of NA **1**, and the results were correlated with the crystal structure of P3HT. Single-crystal X-ray diffraction of NA **1** yielded a first structure model with the space group $P\bar{1}$. However, the unit cell parameters show a pseudo-monoclinic setting, and the structure model featured structural imperfections. Therefore, additional powder X-ray diffraction (PXRD) measurements were performed. Indexing of the powder X-ray diffractogram yielded a monoclinic unit cell in the space group $P2_1/c$. The model obtained from the single-crystal X-ray analysis was geometry-optimized by density functional theory (DFT) and placed in the unit cell obtained from PXRD. This model was refined using the Rietveld method, yielding a good agreement between the measured and simulated diffractogram as demonstrated by a small weighted discrepancy factor (R_{wp}) of 6.51%. The powder X-ray diffractogram is given in the Supporting Information, Section S7. Analyzing the results, we found that NA **1** crystallizes with one molecule in the asymmetric unit, leading to four molecules in the unit cell. The relevant crystallographic data are shown in the Supporting Information, Section S8.

The packing of the molecules along the *c*-axis and in the *ab*-plane (001) is shown in the Supporting Information, Section S9. Characteristic of the packing pattern is a hydrogen bond motif, where one molecule is connected to two other molecules by four hydrogen bonds. Consequently, the hydrogen bonds form a ribbon along the crystallographic *c*-axis. In each molecule, the pyridine rings are tilted by 70° toward the central benzene ring. The benzene rings of the molecules in neighboring ribbons along the *b*-axis are tilted by 60°, and only weak interactions between the molecules are present along the *a*-axis. Furthermore, Figure 8 provides a closer look at the packing by focusing on the *bc*-surface (100) of NA **1**. This surface features highly regular pyridine moieties along the *b*-axis, with the nitrogen atom facing outward.

Important for heterogeneous nucleation is an epitaxial match between the nucleating agent and the semi-crystalline polymer. For comparison, Table 1 provides the unit cell parameters of the crystal structures of NA **1** and P3HT.[56] In P3HT, the *c*-

https://doi.org/10.1021/acs.macromol.1c02283
Macromolecules 2022, 55, 2861−2871

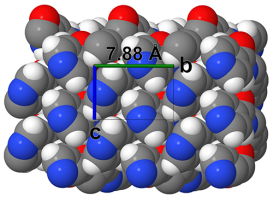

Figure 8. View on top of the *bc*-plane (100) of NA **1**. The spacing along the *b*-axis (green) of 7.88 Å is shown. The surface features a highly regular arrangement of the pyridine moieties, with the nitrogen atoms facing outward.

direction represents the direction of the polymer backbone, which has a characteristic periodic distance of 7.8 Å. In NA **1**, a periodic distance of 7.88 Å was found in the *b*-direction corresponding to the distance between neighboring nitrogen atoms of pyridine units of two molecules. This distance fits about 99% to the *c*-directions of the P3HT unit cell, demonstrating an excellent epitaxial match between the nucleating agent NA **1** and P3HT.

We also conducted nucleation experiments with P3HT using structurally very similar bisamides, where the pyridine moieties are replaced by benzene or cyclohexane groups. These reference compounds are *N*,*N*′-1,4-phenylenebisbenzamide, N^1,N^4-diphenyl-1,4-benzenedicarboxamide, and N^1,N^4-dicyclohexyl-1,4-benzenedicarboxamide (see Supporting Information, Section S10). Due to their structural similarities, they are expected to be highly efficient supramolecular nucleating agents for P3HT as well. In particular, the crystal structure of *N*,*N*′-1,4-phenylenebisbenzamide[57] shows the same packing pattern as NA **1** and also features a repeating distance of 7.88 Å, which matches the *c*-direction of P3HT (see Supporting Information, Section S10). However, the DSC experiments of the reference compounds at an additive concentration of 1 wt % reveal no or only a poor performance concerning the nucleation of P3HT. The fact that NA **1** is more efficient at a concentration two orders of magnitude lower than these reference compounds makes its performance even more impressive. Furthermore, these results strongly suggest that an epitaxial match alone is insufficient to achieve high nucleation performances in P3HT.

To explain why NA **1** exhibits such an outstanding nucleation performance, we combined the crystal structures of the nucleating agent NA **1** and P3HT. For this, we cleaved the crystallographic surface of NA **1** along the *bc*-plane (100) and positioned an extended P3HT chain from the crystal structure,[56] as depicted in Figure 9. The representation reveals that the nitrogen atoms of the pyridine units of the crystal structure of NA **1** can be arranged precisely with the centers of every second thiophene moiety along the P3HT backbone. This periodic sequence provides an attractive donor−acceptor interaction between the pyridine and the thiophene units. Thus, we conclude that the combination of the perfect donor−acceptor interactions with the high epitaxial match between the nucleating agent and the polymer backbone is responsible for the outstanding nucleation efficiency of NA 1 with respect to P3HT.°

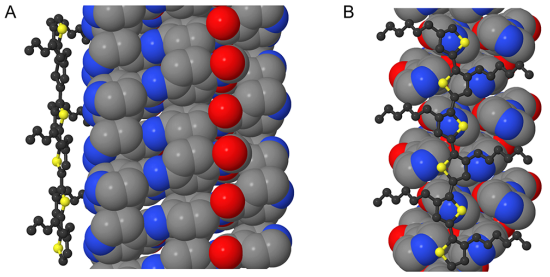

Figure 9. Geometric model combining the crystal structures of P3HT,[56] as depicted in a ball-and-stick model, and NA **1**, as depicted in a space-filling model. In both cases, the hydrogens are omitted for clarity. (A) View is on top of the *ab*-plane (001) of NA **1**. (B) View is rotated by 90° and is now on top of the *bc*-plane (100) of NA **1**. As depicted, the center of every second thiophene group almost perfectly matches the distance of the nitrogen atoms of the pyridine groups of NA **1**.

These data suggest that the P3HT crystallization proceeds perpendicularly to the bc surface of the nucleating agents. Consequently, the formation of P3HT lamella can be expected, resulting in a similar superstructure, as shown by multiple research groups.[56,58−60] The isolation and use of such so-called shish-kebab superstructures might be beneficial for directed energy or charge transport along the crystalline lamella of the P3HT.[61]

We also experimentally demonstrated the applicability of this nucleation concept to other poly(3-alkylthiophenes) such as poly(3-butylthiophene), P3BT, and poly(3-octylthiophene), P3OT. These polymers are chemically similar to P3HT but differ in their solubility and thermal behavior due to the different lengths of their aliphatic side groups. As shown in Supporting Information, Section S11, NA **1** is also a highly effective nucleating agent for P3BT and P3OT. We found that with 1 wt % of NA **1**, an outstanding nucleation efficiency of 98% for P3BT was obtained. For P3OT, a nucleation efficiency of 94% was obtained already at a concentration of only 0.1 wt %. These results also indicate that varying the length of the aliphatic side chain plays only a minor role in nucleation.

Photoluminescence imaging is a tool to assess the homogeneity of a film and its optical properties on microscopic scales. Therefore, we prepared a P3HT film with NA **1** and a neat P3HT film via spin-coating and employed a comparable temperature protocol as used in the previous DSC experiments. We collected spatially resolved photoluminescence (PL) spectra from a 40 × 40 μm^2 area of both films, each data set comprising 6640 individual spectra. Figure 10A shows the averaged and normalized PL spectra. Both averaged spectra

Table 1. Unit Cell Parameters for the Crystal Structure of P3HT from Literature and NA 1, as Obtained by PXRD in This Work

	space group	*a* [Å]	*b* [Å]	*c* [Å]	*α* [°]	*β* [°]	*γ* [°]
P3HT[a]	$P2_1/c$	16	7.8	7.8	90	90	86.5
NA **1**[b]	$P2_1/c$	35.4581(27)	7.8848(3)	5.2719(3)	90	90	99.792(6)

[a]Values taken from reference.[56] [b]As obtained by PXRD in this work.

https://doi.org/10.1021/acs.macromol.1c02283
Macromolecules 2022, 55, 2861−2871

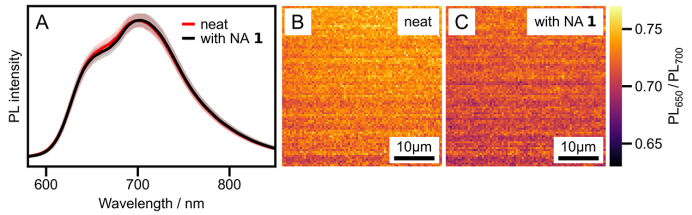

Figure 10. Hyperspectral imaging of thin films of neat P3HT and P3HT with NA **1**. (A) PL spectra of a neat P3HT film (red) and a P3HT film with 0.1 wt % NA **1** (black). Both PL spectra are averaged over an area of 40 × 40 μm^2 comprising 6640 individual spectra. The shaded area shows the degree of variation within the films. (B, C) Maps of the PL-ratio PL_{650}/PL_{700} for the neat P3HT film (B) and for the P3HT film with 0.1 wt % NA **1** (C).

feature the characteristic shape of P3HT film spectra with a weaker electronic 0−0 PL transition around 650 nm compared to the 0−1 transition at around 700 nm. Yet, the film with NA **1** shows a slightly more suppressed 0−0 PL transition, indicating a slight reduction of the intra-aggregate disorder of P3HT[62] when crystallized in the presence of a nucleating agent. From the individual spectra, we then extracted the ratio between the PL intensities at 650 and 700 nm (indicated by the arrows), PL_{650}/PL_{700}, and visualized it as maps in Figure 10B,C. On the length scale of the optical resolution limit (<300 nm), we detect no considerable variation of the ratio of PL_{650}/PL_{700} within both P3HT films, indicating that NA **1** is uniformly distributed, and the nucleation has occurred homogeneously within the film. Moreover, the PL spectra of P3HT films with NA **1** are slightly red-shifted with respect to neat P3HT films (Supporting Information, Section S12), indicating a slightly higher order of aggregates[62] and thus a slightly more controlled P3HT crystallization in the presence of the nucleating agent. Notably, the integrated PL signal from P3HT films with NA **1** increased by ca. 8% compared to that from neat P3HT films. This observation indicates that the nucleating agent does not introduce trap states quenching the PL. The optical homogeneity of the film is further confirmed by hyperspectral absorption imaging (Supporting Information, Section S13), which is in agreement with the previously discussed results of our polarized light microscopy data, where we observe no birefringent structures of NA **1** (see also Figure 5D). These data also suggest that these supramolecular nucleating agents can be used to prepare P3HT-based thin-film architectures without introducing microscale inhomogeneities by applying proper processing protocols.

Our observations during spatially resolved hyperspectral photoluminescence measurements suggest that in thin films of P3HT with NA **1**, the supramolecular nucleating agent does not induce trap states in P3HT that quench PL. To further elucidate the role of the nucleating agents in thin-film architectures, we have prepared thin films of neat P3HT and P3HT with 0.1 and 1 wt % of NA **1** on organic field effect transistors (OFET) silicon substrates and studied their film stability and their charge carrier mobility.

To investigate the film stability, all films were treated in the same manner, including a heating step to 300 °C after spin-coating and subsequent cooling to room temperature under an inert atmosphere. Under these conditions, we found that thin films of neat P3HT feature a significant surface roughness, which also comprises microcracks (Supporting Information, Section S14). This is in strong contrast to thin films of P3HT with 0.1 or 1 wt % of NA **1**. With increasing concentration of NA **1**, the homogeneity of the surface is maintained, and microcracks are not observed. Such findings may be attributed to the presence of networks of solid supramolecular objects of NA **1**. These networks are most likely formed upon rapid self-assembly when initiating the cooling step and may be beneficial in preserving the initial thin-film architecture.

Moreover, we measured the charge carrier mobilities[63] in the OFET geometry at room temperature using thin films of P3HT with and without NA **1**, which we determined from the transfer characteristics (Supporting Information, Section S15). After spin-coating, drying, heating to 300 °C, and cooling to room temperature, we found no significant difference in mobility between these films, indicating that the supramolecular nucleating agents do not act as traps for the charge carriers in P3HT-based OFETs. Interestingly, after a 4-week storage of the devices at room temperature, we found a further drop in the charge carrier mobility of the OFET for thin films with the neat P3HT, whereas the charge carrier mobilities for the devices with 0.1 and 1 wt % of NA **1** remain constant. This demonstrates the beneficial role of the nucleating agents during aging of the device, which may be attributed to a stabilized solid-state morphology.

CONCLUSIONS

We presented a successful approach for tailored supramolecular nucleating agents to induce the polymer crystallization of the family of semiconducting poly(3-alkylthiophenes). This approach combines a high epitaxial match with highly regular attractive interactions between the donor thiophene moieties of the polymer and the pyridine acceptor moieties of the nucleating agent.

We demonstrated that symmetrically substituted bisamides with peripheral 4-pyridine moieties are highly efficient supramolecular nucleating agents for poly(3-alkylthiophenes). By structure elucidation, we revealed supramolecular nucleating agents feature a directed hydrogen ribbon pattern and surfaces with highly regular arrangements of the pyridine moieties. These regular arrangements are responsible for the donor−acceptor interactions, as demonstrated for P3HT. With the best nucleating agent, we achieved outstanding nucleation efficiencies of 98% at a low concentration of 0.1 wt %. We also showed the applicability of this supramolecular nucleating agent to other poly(3-alkythiophenes) such as P3BT and P3OT, leading to nucleation efficiencies of more than 90% for both polymers.

Moreover, spatially resolved hyperspectral photoluminescence measurements suggest that in thin films of P3HT with NA **1**, the supramolecular nucleating agent does not induce trap states that quench photoluminescence. Similar results were found in OFETs, where the charge carrier mobility

https://doi.org/10.1021/acs.macromol.1c02283
Macromolecules 2022, 55, 2861−2871

remains constant upon increasing the concentration of NA **1** and upon aging of films. Our data therefore suggest that the use of these supramolecular nucleating agents is beneficial to control the solid-state morphology of P3HT films.

We anticipate that this approach can be transferred to design highly efficient supramolecular nucleating agents for other semi-crystalline semiconducting polymers. Such nucleating agents may ultimately allow controlling the processing and the morphology of thin-film architectures, thus optimizing the optical and electronic properties of conjugated polymers and leading to more reproducible device fabrications.

■ ASSOCIATED CONTENT

Supporting Information

The Supporting Information is available free of charge at https://pubs.acs.org/doi/10.1021/acs.macromol.1c02283.

> Synthesis and characterization of the nucleating agents, the self-nucleation experiment, further dynamic DSC studies, temperature-dependent polarized light microscopy studies, the elucidation and visualization of the crystal structure of NA **1**, DSC studies with reference compounds, DSC studies with different poly(3-alkylthiophenes), and further information about the hyperspectral imaging. The crystal structure data of NA **1** is deposited at the Cambridge Crystallographic Data Centre with the deposition number 2103040 (PDF)

■ AUTHOR INFORMATION

Corresponding Author

Hans-Werner Schmidt − *Macromolecular Chemistry I and Bavarian Polymer Institute, University of Bayreuth, 95447 Bayreuth, Germany;* orcid.org/0000-0002-1761-1153; Email: hans-werner.schmidt@uni-bayreuth.de

Authors

Felix A. Wenzel − *Macromolecular Chemistry I and Bavarian Polymer Institute, University of Bayreuth, 95447 Bayreuth, Germany*

Hannes Welz − *Macromolecular Chemistry I and Bavarian Polymer Institute, University of Bayreuth, 95447 Bayreuth, Germany*

Kasper P. van der Zwan − *Inorganic Chemistry III, University of Bayreuth, 95447 Bayreuth, Germany;* orcid.org/0000-0003-3568-5129

Sebastian Stäter − *Zernike Institute for Advanced Materials, University of Groningen, 9747 AG Groningen, The Netherlands*

Klaus Kreger − *Macromolecular Chemistry I and Bavarian Polymer Institute, University of Bayreuth, 95447 Bayreuth, Germany;* orcid.org/0000-0003-3021-1311

Richard Hildner − *Zernike Institute for Advanced Materials, University of Groningen, 9747 AG Groningen, The Netherlands;* orcid.org/0000-0002-7282-3730

Jürgen Senker − *Inorganic Chemistry III, University of Bayreuth, 95447 Bayreuth, Germany;* orcid.org/0000-0002-7278-7952

Complete contact information is available at: https://pubs.acs.org/10.1021/acs.macromol.1c02283

Author Contributions

The manuscript was written through contributions of all authors. All authors have given approval to the final version of the manuscript.

Notes

The authors declare no competing financial interest.

■ ACKNOWLEDGMENTS

The authors acknowledge financial support from the Bavarian State Ministry of Science and the Arts through the Collaborative Research Network "Solar Technologies go Hybrid" and by the German Research Foundation (DFG), Project Number 79971943: Collaborative Research Center SFB 840, Project B4. The authors also acknowledge support by the Elite Network of Bavaria (ENB) through the study program "Macromolecular Science" (F.A.W., K.P.v.d.Z.). The authors are grateful to Sandra Ganzleben (Macromolecular Chemistry, University of Bayreuth) for her help with the synthesis of the additives. The authors thank Florian Meissner (Macromolecular Chemistry, University of Bayreuth) for help with the SEC measurement and Robin Freitag (Inorganic Chemistry II, University of Bayreuth) for the assistance in setting up the single-crystal X-ray measurement. The authors thank Adrian Hochgesang and Prof. Mukundan Thelakkat for their support with OFET device fabrication and valuable discussions. The authors acknowledge the KeyLab Device Engineering of the Bavarian Polymer Institute, the University of Bayreuth, for support.

■ REFERENCES

(1) Noriega, R.; Rivnay, J.; Vandewal, K.; Koch, F. P. V.; Stingelin, N.; Smith, P.; Toney, M. F.; Salleo, A. A general relationship between disorder, aggregation and charge transport in conjugated polymers. *Nat. Mater.* **2013**, *12*, 1038−1044.

(2) Botiz, I.; Durbin, M. M.; Stingelin, N. Providing a Window into the Phase Behavior of Semiconducting Polymers. *Macromolecules* **2021**, *54*, 5304−5320.

(3) Ludwigs, S. *P3HT Revisited − From Molecular Scale to Solar Cell Devices*; Springer Berlin Heidelberg: 2014; Vol. *265*.

(4) Brinkmann, M. Structure and morphology control in thin films of regioregular poly(3-hexylthiophene). *J. Polym. Sci., Part B: Polym. Phys.* **2011**, *49*, 1218−1233.

(5) Diao, Y.; Shaw, L.; Bao, Z.; Mannsfeld, S. C. B. Morphology control strategies for solution-processed organic semiconductor thin films. *Energy Environ. Sci.* **2014**, *7*, 2145−2159.

(6) Hildner, R.; Köhler, A.; Müller-Buschbaum, P.; Panzer, F.; Thelakkat, M. π-Conjugated Donor Polymers: Structure Formation and Morphology in Solution, Bulk and Photovoltaic Blends. *Adv. Energy Mater.* **2017**, *7*, No. 1700314.

(7) Zhao, F.; Wang, C.; Zhan, X. Morphology Control in Organic Solar Cells. *Adv. Energy Mater.* **2018**, *8*, No. 1703147.

(8) Choi, D.; Chang, M.; Reichmanis, E. Controlled Assembly of Poly(3-hexylthiophene): Managing the Disorder to Order Transition on the Nano- through Meso-Scales. *Adv. Funct. Mater.* **2015**, *25*, 920−927.

(9) Lee, H.; Park, C.; Sin, D. H.; Park, J. H.; Cho, K. Recent Advances in Morphology Optimization for Organic Photovoltaics. *Adv. Mater.* **2018**, *30*, No. 1800453.

(10) Dolynchuk, O.; Schmode, P.; Fischer, M.; Thelakkat, M.; Thurn-Albrecht, T. Elucidating the Effect of Interfacial Interactions on Crystal Orientations in Thin Films of Polythiophenes. *Macromolecules* **2021**, *54*, 5429−5439.

(11) Verploegen, E.; Mondal, R.; Bettinger, C. J.; Sok, S.; Toney, M. F.; Bao, Z. Effects of Thermal Annealing Upon the Morphology of Polymer-Fullerene Blends. *Adv. Funct. Mater.* **2010**, *20*, 3519−3529.

https://doi.org/10.1021/acs.macromol.1c02283
Macromolecules 2022, 55, 2861−2871

(12) Verploegen, E.; Miller, C. E.; Schmidt, K.; Bao, Z.; Toney, M. F. Manipulating the Morphology of P3HT−PCBM Bulk Heterojunction Blends with Solvent Vapor Annealing. *Chem. Mater.* **2012**, *24*, 3923−3931.
(13) Goto, O.; Tomiya, S.; Murakami, Y.; Shinozaki, A.; Toda, A.; Kasahara, J.; Hobara, D. Organic single-crystal arrays from solution-phase growth using micropattern with nucleation control region. *Adv. Mater.* **2012**, *24*, 1117−1122.
(14) Minemawari, H.; Yamada, T.; Matsui, H.; Tsutsumi, J.; Haas, S.; Chiba, R.; Kumai, R.; Hasegawa, T. Inkjet printing of single-crystal films. *Nature* **2011**, *475*, 364−367.
(15) Xu, B.; Sai-Anand, G.; Unni, G. E.; Jeong, H.-M.; Kim, J.-S.; Kim, S.-W.; Kwon, J.-B.; Bae, J.-H.; Kang, S.-W. Pyridine-based additive optimized P3HT:PC61BM nanomorphology for improved performance and stability in polymer solar cells. *Appl. Surf. Sci.* **2019**, *484*, 825−834.
(16) Stingelin-Stutzmann, N.; Smits, E.; Wondergem, H.; Tanase, C.; Blom, P.; Smith, P.; Leeuw, D. de. Organic thin-film electronics from vitreous solution-processed rubrene hypereutectics. *Nat. Mater.* **2005**, *4*, 601−606.
(17) Treat, N. D.; Nekuda Malik, J. A.; Reid, O.; Yu, L.; Shuttle, C. G.; Rumbles, G.; Hawker, C. J.; Chabinyc, M. L.; Smith, P.; Stingelin, N. Microstructure formation in molecular and polymer semiconductors assisted by nucleation agents. *Nat. Mater.* **2013**, *12*, 628−633.
(18) Persson, N. E.; Chu, P.-H.; McBride, M.; Grover, M.; Reichmanis, E. Nucleation, Growth, and Alignment of Poly(3-hexylthiophene) Nanofibers for High-Performance OFETs. *Acc. Chem. Res.* **2017**, *50*, 932−942.
(19) McBride, M.; Bacardi, G.; Morales, C.; Risteen, B.; Keane, D.; Reichmanis, E.; Grover, M. A. Control of Nucleation Density in Conjugated Polymers via Seed Nucleation. *ACS Appl. Mater. Interfaces* **2019**, *11*, 37955−37965.
(20) Oh, J. Y.; Shin, M.; Lee, T. I.; Jang, W. S.; Min, Y.; Myoung, J.-M.; Baik, H. K.; Jeong, U. Self-Seeded Growth of Poly(3-hexylthiophene) (P3HT) Nanofibrils by a Cycle of Cooling and Heating in Solutions. *Macromolecules* **2012**, *45*, 7504−7513.
(21) Chu, P.-H.; Kleinhenz, N.; Persson, N.; McBride, M.; Hernandez, J. L.; Fu, B.; Zhang, G.; Reichmanis, E. Toward Precision Control of Nanofiber Orientation in Conjugated Polymer Thin Films: Impact on Charge Transport. *Chem. Mater.* **2016**, *28*, 9099−9109.
(22) Hamidi-Sakr, A.; Biniek, L.; Fall, S.; Brinkmann, M. Precise Control of Lamellar Thickness in Highly Oriented Regioregular Poly(3-Hexylthiophene) Thin Films Prepared by High-Temperature Rubbing: Correlations with Optical Properties and Charge Transport. *Adv. Funct. Mater.* **2016**, *26*, 408−420.
(23) Untilova, V.; Biskup, T.; Biniek, L.; Vijayakumar, V.; Brinkmann, M. Control of Chain Alignment and Crystallization Helps Enhance Charge Conductivities and Thermoelectric Power Factors in Sequentially Doped P3HT:F4TCNQ Films. *Macromolecules* **2020**, *53*, 2441−2453.
(24) Brinkmann, M.; Contal, C.; Kayunkid, N.; Djuric, T.; Resel, R. Highly Oriented and Nanotextured Films of Regioregular Poly(3-hexylthiophene) Grown by Epitaxy on the Nanostructured Surface of an Aromatic Substrate. *Macromolecules* **2010**, *43*, 7604−7610.
(25) Johnston, D. E.; Yager, K. G.; Hlaing, H.; Lu, X.; Ocko, B. M.; Black, C. T. Nanostructured surfaces frustrate polymer semiconductor molecular orientation. *ACS Nano* **2014**, *8*, 243−249.
(26) Reichenberger, M.; Baderschneider, S.; Kroh, D.; Grauf, S.; Köhler, J.; Hildner, R.; Köhler, A. Watching Paint Dry: The Impact of Diiodooctane on the Kinetics of Aggregate Formation in Thin Films of Poly(3-hexylthiophene). *Macromolecules* **2016**, *49*, 6420−6430.
(27) Liu, X.; Huettner, S.; Rong, Z.; Sommer, M.; Friend, R. H. Solvent additive control of morphology and crystallization in semiconducting polymer blends. *Adv. Mater.* **2012**, *24*, 669−674.
(28) Dias, Y.; Yerushalmi-Rozen, R. Entropic effects in carbon nanotubes-templated crystallization of Poly(3-alkyl thiophenes, P3HT, P3OT). *Polymer* **2013**, *54*, 6399−6405.
(29) Acevedo-Cartagena, D. E.; Zhu, J.; Trabanino, E.; Pentzer, E.; Emrick, T.; Nonnenmann, S. S.; Briseno, A. L.; Hayward, R. C. Selective Nucleation of Poly(3-hexyl thiophene) Nanofibers on Multilayer Graphene Substrates. *ACS Macro Lett.* **2015**, *4*, 483−487.
(30) Yang, Z.; Lu, H. Nonisothermal crystallization behaviors of poly(3-hexylthiophene)/reduced graphene oxide nanocomposites. *J. Appl. Polym. Sci.* **2013**, *128*, 802−810.
(31) Bechara, R.; Leclerc, N.; Lévêque, P.; Richard, F.; Heiser, T.; Hadziioannou, G. Efficiency enhancement of polymer photovoltaic devices using thieno-thiophene based copolymers as nucleating agents for polythiophene crystallization. *Appl. Phys. Lett.* **2008**, *93*, No. 013306.
(32) Deribew, D.; Pavlopoulou, E.; Fleury, G.; Nicolet, C.; Renaud, C.; Mougnier, S.-J.; Vignau, L.; Cloutet, E.; Brochon, C.; Cousin, F.; Portale, G.; Geoghegan, M.; Hadziioannou, G. Crystallization-Driven Enhancement in Photovoltaic Performance through Block Copolymer Incorporation into P3HT:PCBM Blends. *Macromolecules* **2013**, *46*, 3015−3024.
(33) Yuan, N.; Huo, H. 1,2,3,4-Bis(p-methylbenzylidene sorbitol) accelerates crystallization and improves hole mobility of poly(3-hexylthiophene). *Nanotechnology* **2016**, *27*, No. 06LT01.
(34) Wang, B.; Utzeri, R.; Castellano, M.; Stagnaro, P.; Müller, A. J.; Cavallo, D. Heterogeneous Nucleation and Self-Nucleation of Isotactic Polypropylene Microdroplets in Immiscible Blends: From Nucleation to Growth-Dominated Crystallization. *Macromolecules* **2020**, *53*, 5980−5991.
(35) Gahleitner, M.; Grein, C.; Kheirandish, S.; Wolfschwenger, J. Nucleation of Polypropylene Homo- and Copolymers. *Int. Polym. Process.* **2011**, *26*, 2−20.
(36) Blomenhofer, M.; Ganzleben, S.; Hanft, D.; Schmidt, H.-W.; Kristiansen, M.; Smith, P.; Stoll, K.; Mäder, D.; Hoffmann, K. "Designer" Nucleating Agents for Polypropylene. *Macromolecules* **2005**, *38*, 3688−3695.
(37) Liu, L.; Zhao, Y.; Zhang, C.; Dong, Z.; Wang, K.; Wang, D. Morphological Characteristics of *β*-Nucleating Agents Governing the Formation of the Crystalline Structure of Isotactic Polypropylene. *Macromolecules* **2021**, *54*, 6824−6834.
(38) Kersch, M.; Schmidt, H.-W.; Altstädt, V. Influence of different beta-nucleating agents on the morphology of isotactic polypropylene and their toughening effectiveness. *Polymer* **2016**, *98*, 320−326.
(39) Yue, Y.; Yi, J.; Wang, L.; Feng, J. Toward a More Comprehensive Understanding on the Structure Evolution and Assembly Formation of a Bisamide Nucleating Agent in Polypropylene Melt. *Macromolecules* **2020**, *53*, 4381−4394.
(40) Kristiansen, M.; Werner, M.; Tervoort, T.; Smith, P.; Blomenhofer, M.; Schmidt, H.-W. The Binary System Isotactic Polypropylene/Bis(3,4-dimethylbenzylidene)sorbitol: Phase Behavior, Nucleation, and Optical Properties. *Macromolecules* **2003**, *36*, 5150−5156.
(41) Karger-Kocsis, J.; Bárány, T. *Polypropylene Handbook [electronic resource]:Morphology, Blends and Composites*; Karger-Kocsis, J.; Bárány, T., Eds.; Springer, 2019.
(42) Zweifel, H.; Maier, R. D.; Schiller, M. *Plastics Additives Handbook*, 6th ed.; Hanser Publications, 2009.
(43) Sheldrick, G. M. Crystal structure refinement with SHELXL. *Acta Crystallogr., Sect. C: Struct. Chem.* **2015**, *71*, 3−8.
(44) Sheldrick, G. M. SHELXT - integrated space-group and crystal-structure determination. *Acta Crystallogr., Sect. A: Found. Crystallogr.* **2015**, *71*, 3−8.
(45) Dolomanov, O. V.; Bourhis, L. J.; Gildea, R. J.; Howard, J. A. K.; Puschmann, H. OLEX2: a complete structure solution, refinement and analysis program. *J. Appl. Crystallogr.* **2009**, *42*, 339−341.
(46) Coelho, A. A. TOPAS and TOPAS-Academic: an optimization program integrating computer algebra and crystallographic objects written in C++. *J. Appl. Crystallogr.* **2018**, *51*, 210−218.
(47) Clark, S. J.; Segall, M. D.; Pickard, C. J.; Hasnip, P. J.; Probert, M. I. J.; Refson, K.; Payne, M. C. First principles methods using CASTEP. *Z. Kristallogr. - Cryst. Mater.* **2005**, *220*, 567−570.

https://doi.org/10.1021/acs.macromol.1c02283
Macromolecules 2022, 55, 2861−2871

(48) Tkatchenko, A.; Scheffler, M. Accurate molecular van der Waals interactions from ground-state electron density and free-atom reference data. *Phys. Rev. Lett.* **2009**, *102*, No. 073005.
(49) Monkhorst, H. J.; Pack, J. D. Special points for Brillouin-zone integrations. *Phys. Rev. B* **1976**, *13*, 5188−5192.
(50) Jmol: an open-source Java viewer for chemical structures in 3D. http://www.jmol.org/ (accessed 2022-3-14).
(51) Schmidt, M.; Zehe, C. S.; Siegel, R.; Heigl, J. U.; Steinlein, C.; Schmidt, H.-W.; Senker, J. NMR-crystallographic study of two-dimensionally self-assembled cyclohexane-based low-molecular-mass organic compounds. *CrystEngComm* **2013**, *15*, 8784.
(52) Zwan, K. P.; Steinlein, C.; Kreger, K.; Schmidt, H.-W.; Senker, J. Crystal Engineering of Supramolecular 1,4-Benzene Bisamides by Side-Chain Modification - Towards Tuneable Anisotropic Morphologies and Surfaces. *ChemPhysChem* **2021**, *22*, 2585−2593.
(53) Fillon, B.; Thierry, A.; Lotz, B.; Wittmann, J. C. Efficiency scale for polymer nucleating agents. *J. Therm. Anal.* **1994**, *42*, 721−731.
(54) Fillon, B.; Wittmann, J. C.; Lotz, B.; Thierry, A. Self-nucleation and recrystallization of isotactic polypropylene (α phase) investigated by differential scanning calorimetry. *J. Polym. Sci., Part B: Polym. Phys.* **1993**, *31*, 1383−1393.
(55) Lorenzo, A. T.; Arnal, M. L.; Albuerne, J.; Müller, A. J. DSC isothermal polymer crystallization kinetics measurements and the use of the Avrami equation to fit the data: Guidelines to avoid common problems. *Polym. Test.* **2007**, *26*, 222−231.
(56) Brinkmann, M.; Rannou, P. Effect of Molecular Weight on the Structure and Morphology of Oriented Thin Films of Regioregular Poly(3-hexylthiophene) Grown by Directional Epitaxial Solidification. *Adv. Funct. Mater.* **2007**, *17*, 101−108.
(57) Cheng, N.; Yan, Q.; Liu, S.; Zhao, D. Probing the intermolecular interactions of aromatic amides containing N-heterocycles and triptycene. *CrystEngComm* **2014**, *16*, 4265−4273.
(58) Brinkmann, M.; Chandezon, F.; Pansu, R. B.; Julien-Rabant, C. Epitaxial Growth of Highly Oriented Fibers of Semiconducting Polymers with a Shish-Kebab-Like Superstructure. *Adv. Funct. Mater.* **2009**, *19*, 2759−2766.
(59) Zhang, X.; Yuan, N.; Ding, S.; Wang, D.; Li, L.; Hu, W.; Bo, Z.; Zhou, J.; Huo, H. Growth and carrier-transport performance of a poly(3-hexylthiophene)/1,2,3,4-bis(p-methylbenzylidene) sorbitol hybrid shish-kebab nanostructure. *J. Mater. Chem. C* **2017**, *5*, 3983−3992.
(60) Liu, J.; Zou, J.; Zhai, L. Bottom-up Assembly of Poly(3-hexylthiophene) on Carbon Nanotubes: 2D Building Blocks for Nanoscale Circuits. *Macromol. Rapid Commun.* **2009**, *30*, 1387−1391.
(61) Kreger, K.; Schmidt, H.-W.; Hildner, R. Tailoring the excited-state energy landscape in supramolecular nanostructures. *Electron. Struct.* **2021**, *3*, No. 023001.
(62) Spano, F. C.; Clark, J.; Silva, C.; Friend, R. H. Determining exciton coherence from the photoluminescence spectral line shape in poly(3-hexylthiophene) thin films. *J. Chem. Phys.* **2009**, *130*, No. 074904.
(63) Krauss, G.; Meichsner, F.; Hochgesang, A.; Mohanraj, J.; Salehi, S.; Schmode, P.; Thelakkat, M. Polydiketopyrrolopyrroles Carrying Ethylene Glycol Substituents as Efficient Mixed Ion-Electron Conductors for Biocompatible Polydiketopyrrolopyrroles Carrying Ethylene Glycol Substituents as Efficient Mixed Ion-Electron Conductors for Biocompatible Organic Electrochemical Transistors. *Adv. Funct. Mater.* **2021**, *31*, No. 2010048.

https://doi.org/10.1021/acs.macromol.1c02283
Macromolecules 2022, 55, 2861−2871

Supporting Information to

Highly Efficient Supramolecular Nucleating Agents for Poly(3-hexylthiophene)

*Felix A. Wenzel[1], Hannes Welz[1], Kasper P. van der Zwan[2], Sebastian Stäter[3], Klaus Kreger[1], Richard Hildner[3], Jürgen Senker[2], Hans-Werner Schmidt[*1]*

[1]Macromolecular Chemistry I and Bavarian Polymer Institute, University of Bayreuth, Universitätsstraße 30, 95447 Bayreuth, Germany.

[2] Inorganic Chemistry III, University of Bayreuth, Universitätsstraße 30, 95447 Bayreuth, Germany.

[3] Zernike Institute for Advanced Materials, University of Groningen, Nijenborgh 4, 9747 AG Groningen, The Netherlands.

Table of contents

S1. Synthetic routes to pyridine-functionalized trans-1,4-cyclohexane- and 1,4-benzene-bisamides NA 1 – NA 4

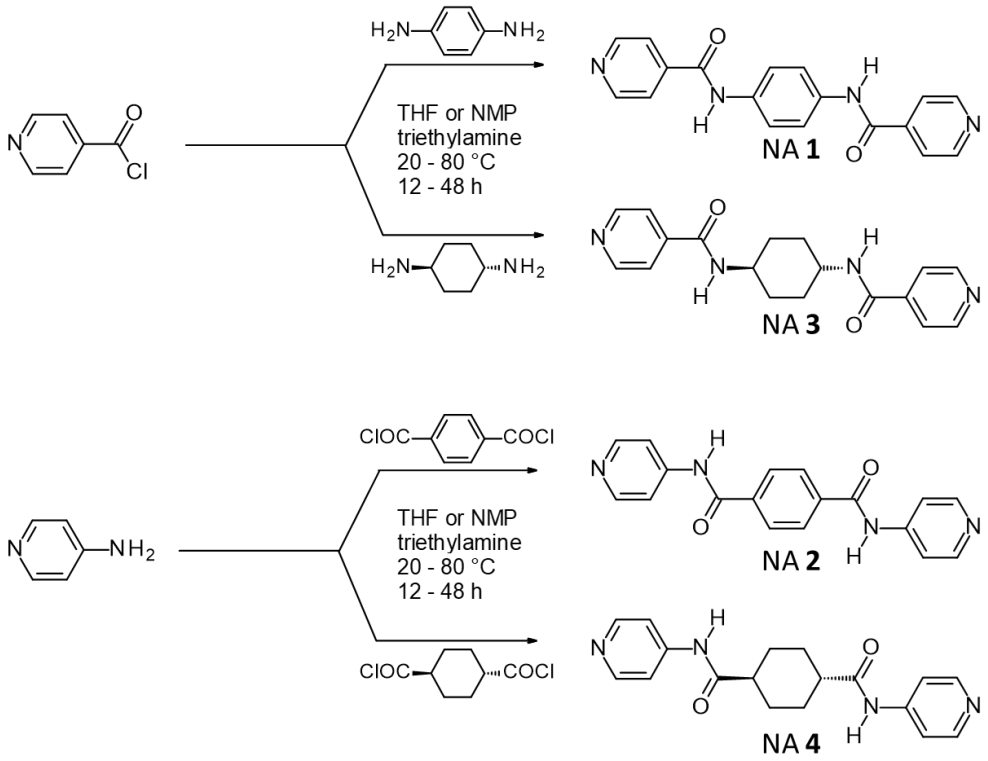

Figure S1. Schematic representation of the synthetic routes to pyridine-functionalized *trans*-1,4-cyclohexane- and 1,4-benzene-bisamides NA **1** – NA **4**.

S2. Synthetic procedures and characterization of pyridine-functionalized *trans*-1,4-cyclohexane- and 1,4-benzene-bisamides NA 1 – NA 4

Molecular characterization

^{1}H-NMR spectra in solution were recorded on a Bruker Avance Ultrashield 300 (300 MHz) at room temperature. For the preparation of the NMR samples, approx. 5 mg of the compounds were dissolved in 1.2 mL of DMSO-d_6.

Mass spectra (MS) were carried out on a FINNIGAN MAT 8500 spectrometer from Thermo-Fisher Scientific using electron spray ionization.

Infrared (IR) spectra were recorded on a PerkinElmer Spectrum 100 FT-IR spectrometer in ATR mode in the range from 4000 cm^{-1} to 650 cm^{-1}.

Melting points (Mp) of the as-synthesized compounds were determined with a melting point system MP 90 from Mettler Toledo. Approx. 10 mg of the compounds were filled in a measuring tube. Data were recorded with a heating rate of 10 $K \cdot min^{-1}$ in a temperature range from 30 °C to 400 °C. Melting points were determined at the transmission of 5 %. Three measurements were performed simultaneously, and the mean value of the measurements was reported.

*Synthesis of N,N′-1,4-phenylene bis[4-pyridinecarboxamide] NA **1** (CAS: 55119-42-1)*

5.0 g of 1,4-phenylenediamine and 50 ml of triethylamine were placed in a Schlenk flask together with 300 mL of dried tetrahydrofuran under nitrogen. 18.87 g of isonicotinoyl chloride hydrochloride was then added under ice-cooling. The reaction was stirred and refluxed for 48 hours. The solvents were removed, and the crude product was recrystallized in DMSO. The resulting powder was filtered off and washed with acetone. Finally, the product was dissolved in DSMO and precipitated in water. The product was washed with acetone and dried under vacuum, yielding 48% of a whitish powder.

^{1}H-NMR (DMSO-d_6, δ in ppm): 10.55 (2H, s); 8.74-8.84 (4H, m); 7.83-7.93 (4H, m); 7.78 (4H, s).
MS (m/z in %): 318 (100, [M]+); 240 (12); 212 (12); 106 (99); 78 (84); 51 (20).
IR ($\tilde{\upsilon}$ in cm^{-1}): 3330; 1645; 1545; 1520; 1410.
Mp: >300°C.

*Synthesis of N^1,N^4-di-4-pyridinyl-1,4-benzenedicarboxamide NA **2** (CAS:* 216079-39-9)

2.53 g of 4-aminopyridine, 10 mL of triethylamine, and approx. 10 mg of LiCl were placed in a Schlenk flask together with 50 mL of N-methylpyrollidone under nitrogen. 2.53 g of terephthaloyl dichloride was then added under ice-cooling. The reaction mixture was stirred at 80 °C for 48 hours. After cooling to room

temperature, the mixture was precipitated in ice water. The solid was filtered off and then dissolved in a small amount of dimethylsulfoxide and precipitated again in 500 mL of water. The final product was dried at 60 °C under a high vacuum yielding 54% of a greyish powder.

^{1}H-NMR (DMSO-d_6, δ in ppm): 10.77 (2H, s); 8.51 (4H, dd); 8.13 (4H, s); 7.81 (4H, dd).
MS (m/z in %): 318 (72, [M]+); 225 (100); 198 (25); 104 (45); 76 (23).
IR ($\tilde{\upsilon}$ in cm^{-1}): 1689; 1593; 1513; 1418; 1328.
Mp: >300°C.

Synthesis of N,N´-trans-1,4-cyclohexanediyl bis[*4-pyridinecarboxamide] NA* ***3*** *(CAS:* 306766-51-8)

1.0 g of trans-cyclohexane-1,4-diamine, 10 mL of triethylamine, and approximately 10 mg of LiCl were placed in a Schlenk flask together with 100 mL of dried THF under nitrogen. 3.42 g of isonicotinoyl chloride hydrochloride was then added under ice-cooling. The reaction mixture was stirred at room temperature for 48 hours. The mixture was precipitated in ice water; the solid was filtered off and dried. The crude product was then recrystallized in 30 mL of DMSO, filtered, and dried under a high vacuum to obtain a white powder in 27% yield.

^{1}H-NMR (DMSO-d_6, δ in ppm): 8,72 (4H, dd); 8,59 (2H, d); 7,74 (4H, dd); 3,65-2,90 (2H, m); 1,80- 2,05 (4H, m); 1,35-1,60 (4H, m).
MS (m/z in %): 324 (6, [M]+); 218 (15); 202 (100); 123 (99); 106 (95); 78 (75); 51 (20).
IR ($\tilde{\upsilon}$ in cm^{-1}): 3312; 2947; 1640; 1529; 1490; 1412.
Mp: >300°C.

Synthesis of N^1,N^4-di-4-pyridinyl-trans-1,4-cyclohexanedicarboxamide NA ***4*** *(CAS:* 1367879-00-2)

2.31 g of 4-aminopyridine, 10 mL of triethylamine, and LiCl were placed in a Schlenk flask to a mixture of 50 mL of N-methylpyrollidone and 100 mL of tetrahydrofuran under nitrogen. 2.34 g of trans-cyclohexane-1,4-dicarbonyl dichloride was then added under ice-cooling. The reaction mixture was stirred at room temperature for 12 hours and subsequently precipitated in ice water. The solid was filtered off and dried in a vacuum. The crude product was recrystallized DMSO, filtered off, and dried under vacuum to get a white powder in 64% yield.

^{1}H-NMR (DMSO-d_6, δ in ppm): 10.29 (2H, s); 8.40 (4H, dd); 8.57 (4H, dd); 2.25-2.45 (2H, m); 1.80- 2.10 (4H, m); 1.35-1.60 (4H, m).
MS (m/z in %): 324 (51, [M]+); 231 (16); 203 (100); 121 (52); 95 (77); 81 (43).
IR ($\tilde{\upsilon}$ in cm^{-1}): 1695; 1594; 1512; 1418; 1376.
Mp: >300°C.

S3. Self-nucleation studies of P3HT

The maximal achievable crystallization temperature utilizing the own P3HT crystal as an ideal nucleation site can be revealed by self-nucleation studies utilizing dynamic DSC experiments. In a typical procedure, the sample is heated with 10 K min^{-1} to a maximal temperature, which is at the upper end of the melting range to maintain tiny P3HT crystals and is subsequently isothermally held for 5 min. Afterward, the sample was cooled down to 150°C with 10 K min^{-1}. Here, 248°C was selected as the maximal heating temperature. The maximal temperature was decreased by one Kelvin steps for each following scan. The last measurement was conducted with 239°C as maximal temperature. The resulting cooling curves for the self-nucleation measurements and standard cooling curves are shown in Figure S2.

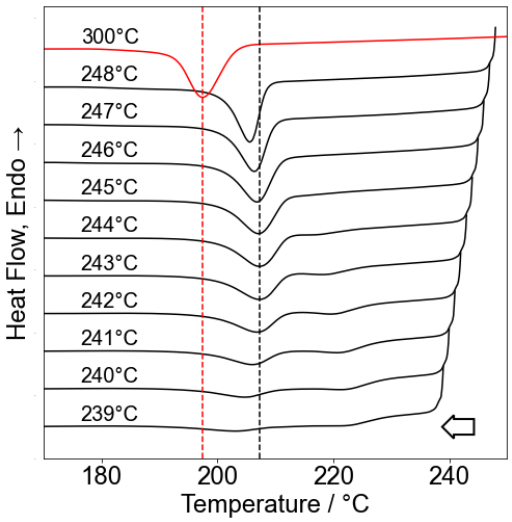

Figure S2. DSC curves of neat P3HT at various starting temperatures for the cooling process with a rate of 10 K min^{-1} under an inert atmosphere. The red curve represents a typical scan at standard conditions where the thermal history of the sample was eliminated. The black curves represent conditions to reveal maximal achievable crystallization temperature. Due to an incomplete melting of the P3HT upon the applied heating step, the remaining P3HT crystallites act as ideal nucleation sites upon cooling, causing an increase in the crystallization temperatures. The maximum achievable crystallization temperature is found to be at about 207°C if the initial heating process is stopped at 244°C.

S4. Dynamic crystallization studies of P3HT with supramolecular nucleating agents

Temperature protocol for nucleation experiments by dynamic DSC

Prior to all nucleation experiments by dynamic DSC, the thermal history was erased by heating the sample from 100°C to 300°C with a heating rate of 10 K min^{-1} and keeping the sample isothermally for 5 min at 300°C. Afterward, the sample was cooled again to 100°C. All DSC scans of such thermally pretreated samples were performed with a heating and cooling rate of 10 K min^{-1} in the temperature range from 150°C to 300°C. The corresponding cooling thermograms for the samples containing different amounts of nucleation agent NA **2** – NA **4** are depicted in Figure S3.

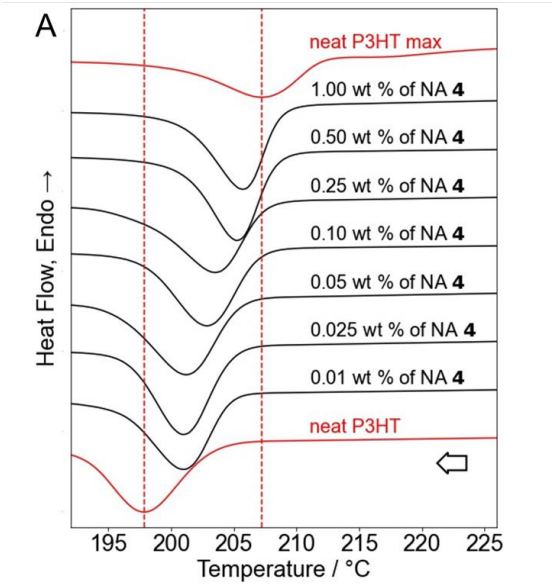

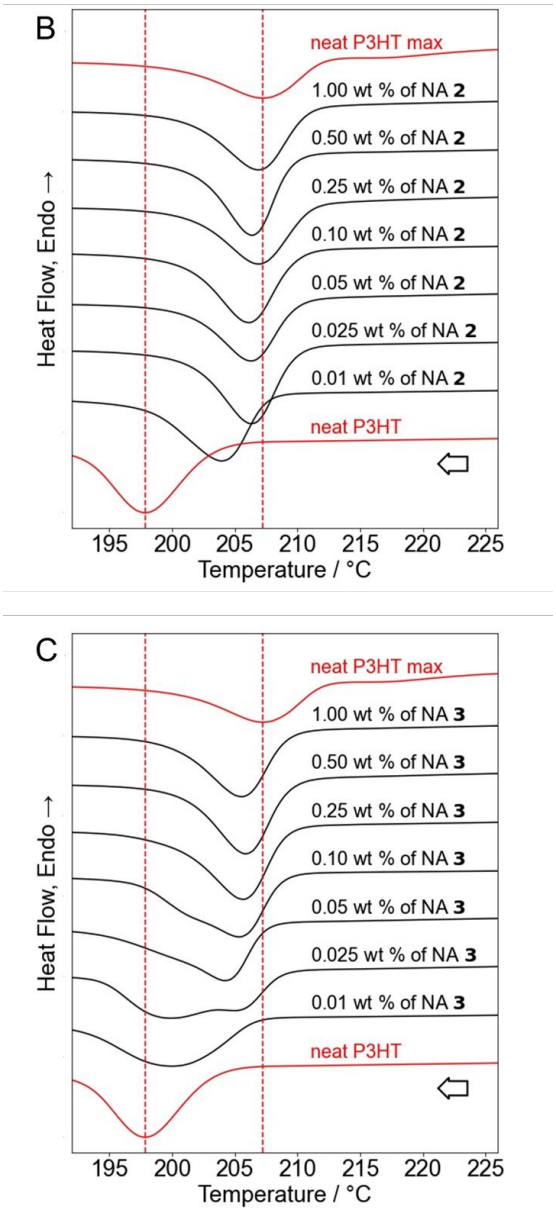

Figure S3. Second cooling curves of P3HT with different concentrations of NA **2** (A), NA **3** (B), or NA **4** (C). The neat and self-nucleated P3HT cooling scans are shown in red as references. The addition of the nucleating agents significantly shifts the polymer crystallization to higher temperatures.

S5. Temperature-dependent polarized light microscopy on contact samples of P3HT with NA 1

For the contact sample preparation, thin films of neat P3HTwere prepared via drop-casting a solution containing 1 wt % of P3HT in chlorobenzene on a glass slide. Subsequently, µm-sized crystals of NA 1 were placed on top of the thin film and covered with a coverslip. Temperature-dependent polarized light microscopy was performed using a Nikon Invers Diaphot TMD 300 optical microscope and a HS82 hot-stage system from Mettler Toledo under nitrogen flow. Optical micrographs were recorded using a Nikon DS-Ri2 digital camera and Nikon ACT-1 software. For these experiments, the contact samples were heated to 240°C and subsequently cooled to the temperature as indicated in Figure S4.

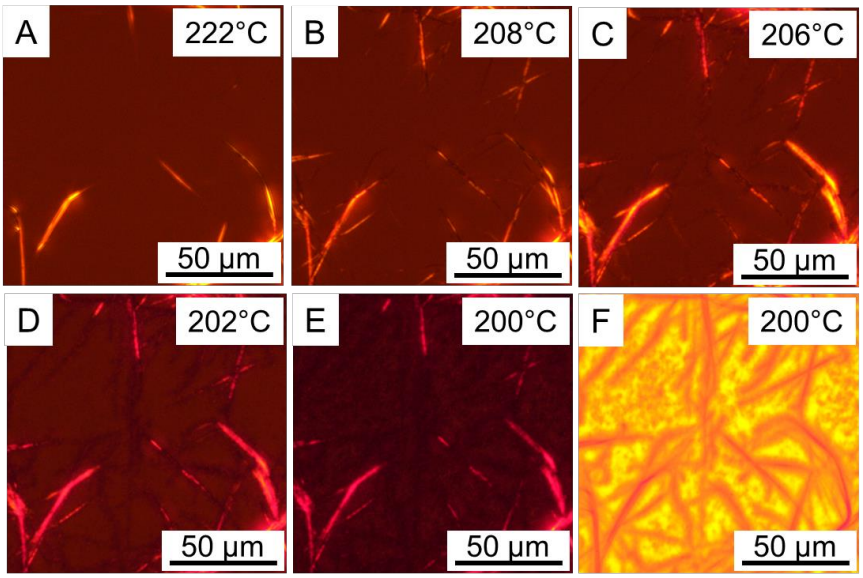

Figure S4. Optical light micrographs between crossed polarizers of contact samples comprising fiber-like objects of NA **1** in P3HT. A) Upon cooling to 222°C, fiber-like structures of NA **1** can be seen in the molten film of P3HT. Upon further cooling to 208°C (B), 206 °C (C) 202°C (D) and 200°C (E) additional birefringent signals next to the structures of nucleating agent can be observed. These additional signals are attributed to the trans-crystallization process of P3HT on the surface of NA **1** and become increasingly pronounced upon cooling. F) Represents the same image as shown in E) but is taken using an additional lambda quarter plate.

S6. Temperature-dependent polarized light microscopy on contact samples of P3HT with reference compound 1

Similar temperature-dependent polarized light microscopy experiments were performed using *N*,*N*′-1,4-phenylenebisbenzamide (CAS: 5467-04-9) as a reference, which is referred to as reference compound 1 (Ref **1**) in the following. The chemical structure of Ref **1** is very similar to that of NA **1** with the peripheral 4-pyridine units being replaced by benzene units. Notably, Ref **1** exhibits a poor nucleation efficiency for P3HT (see Section S10). However, the thermal behavior of Ref **1** is comparable to that of NA **1** as demonstrated by its melting point being above 300 °C.

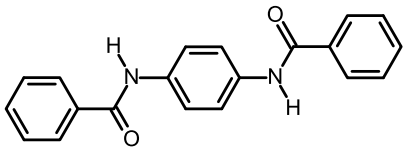

Contact samples of P3HT and Ref **1** were prepared in the same manner as described in Section S5. Similarly, µm-sized crystals of Ref **1** were placed on top of the thin film of P3HT and covered with a coverslip. The film with Ref **1** was heated to 240 °C to ensure a complete melting of the thin film of P3HT and subsequently cooled to room temperature (see Figure S5).

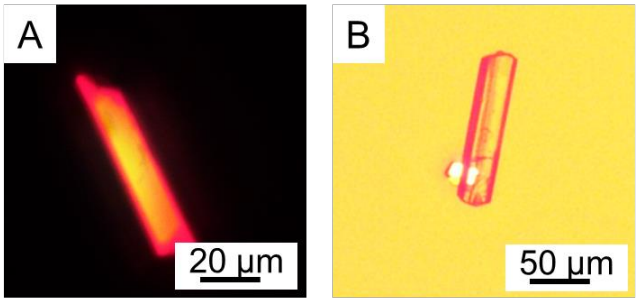

Figure S5. Optical light micrographs of thin films of P3HT with µm-sized crystals of Ref **1** on top after heating to 240 °C and subsequent cooling to room temperature. A) Image is taken between crossed polarizers B) Image is taken using an additional lambda-quarter plate. In both images no indication of a trans-crystallization can be seen.

S7. Powder X-ray diffractogram of NA 1

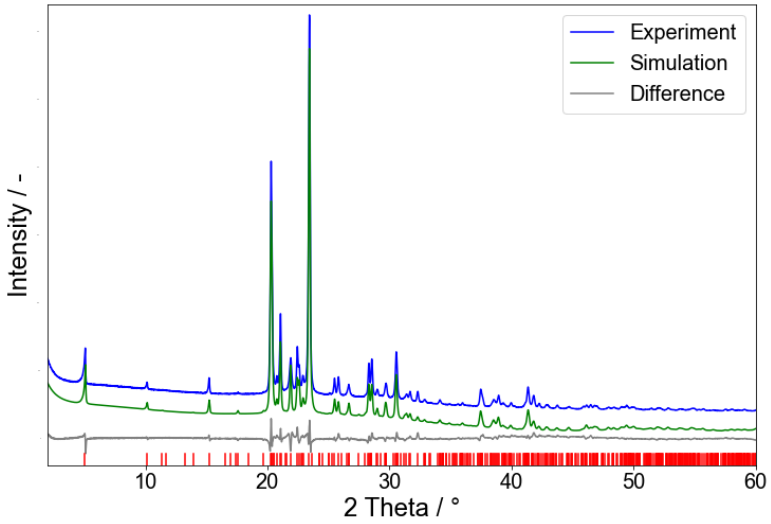

Figure S6. Measured (blue) and simulated (green) PXRD of NA **1** as well as the difference plot (grey). The red bars indicate all possible reflections for the space group $P2_1/c$.

S8. Unit cell and relevant crystallographic information of NA 1

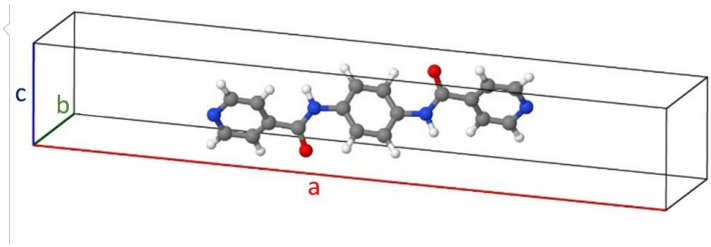

Compound	NA **1**
Molecular formula	$C_{18}H_{14}N_4O_2$
M/g mol^{-1}	318.33
Crystal system	monoclinic
Space group	$P2_1/c$
a/Å	35.45805(274)
b/Å	7.88484(32)
c/Å	5.27197(27)
α/°	90.0000
β/°	90.0000
γ/°	99.791(6)
V/Å^3	1452.5(5)
Z'/Z	1/4
ρ/g cm^{-3}	0.877
T/ K	293(2)
R_p	0.046
R_{wp}	0.065

Figure S7. Visualization of the asymmetric unit placed in the unit cell (top). The other three molecules of the unit cell are created by the symmetry operations of the space group $P2_1/c$ and are omitted in the figure for clarity. Relevant crystallographic data of NA **1** are shown at the bottom.

S9. Visualization of the crystal packing of NA 1

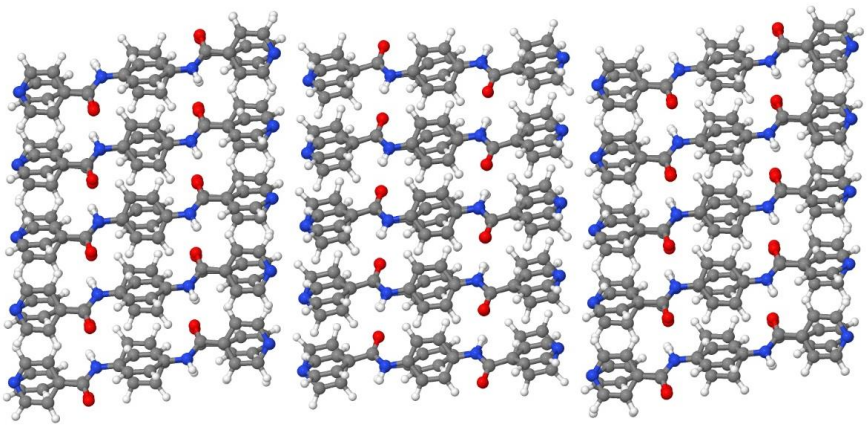

Figure S8. Packing of NA **1**. The hydrogen bond pattern propagates from top to bottom along the crystallographic *c*-axis.

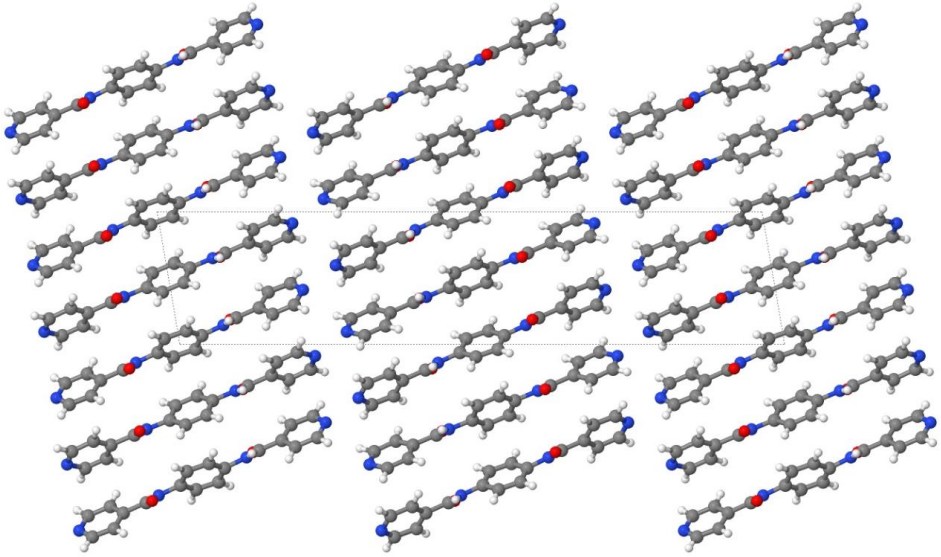

Figure S9. Packing of NA **1** in the ab-plane (100). The pyridine units point in a regular fashion to the bc-plane (100).

S10. Dynamic crystallization studies of P3HT with reference compounds

Reference compounds 1-3

For a comparative study, we have selected three reference compounds (Ref **1** - **3**), which are structurally very similar to the highly efficient supramolecular nucleating agents NA **1** and NA **2**. As reference compound Ref **1**, we have selected *N*,*N*′-1,4-phenylenebisbenzamide (CAS: 5467-04-9) which is very similar to NA **1**. As reference compound Ref **2**, we selected N^1,N^4-diphenyl-1,4-benzenedicarboxamide (CAS: 7154-31-6) which is very similar to NA **2**. Both structures differ compared to NA **1** and NA **2** by the use of benzene units instead of pyridine as peripheral units. In addition, the reference compound Ref **3**, N^1,N^4-dicyclohexyl-1,4-benzenedicarboxamide (CAS: 15088-29-6) with non-aromatic side groups with similar bulkiness in the periphery was investigated.

Nucleation experiments by dynamic DSC

Comparative nucleation experiments by DSC were carried out with P3HT and an additive concentration of 1 wt %, as described in the experimental section. The resulting cooling curves, including the one of neat P3HT and self-nucleated P3HT, are compared in Figure S10.

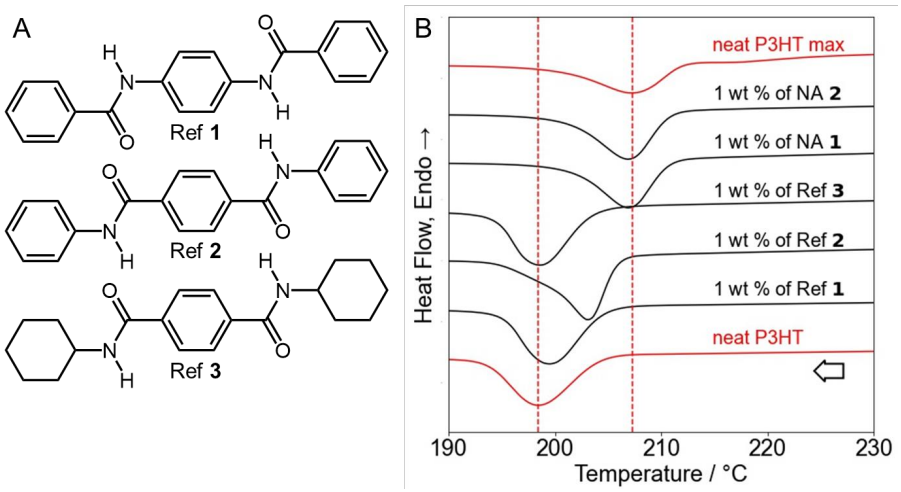

Figure S10. A) Molecular structures of the reference compounds Ref **1** – Ref **3**. B) Second cooling curves of neat and self-nucleated P3HT (red curves) and P3HT with 1 wt % of NA **1** (97%), NA **2** (96%), Ref **1** (12%), Ref **2** (53%) and Ref **3** (2%). The determined nucleation efficiencies of the additives are given in brackets.

*Crystal structure visualization of reference compound Ref **1** compared to NA **1***

Based on the structure solution of reference compound Ref **1**, which is known from literature[1], a view of the bc-plane (100) was constructed (Figure S11A). For comparison, the same view is shown for the crystal structure of NA **1** (Figure S11B). Both compounds feature identical packing patterns. The distance between the phenyl groups of Ref **1** features a distance of 7.88 Å. This distance also matches the c-axis of P3HT almost perfectly.

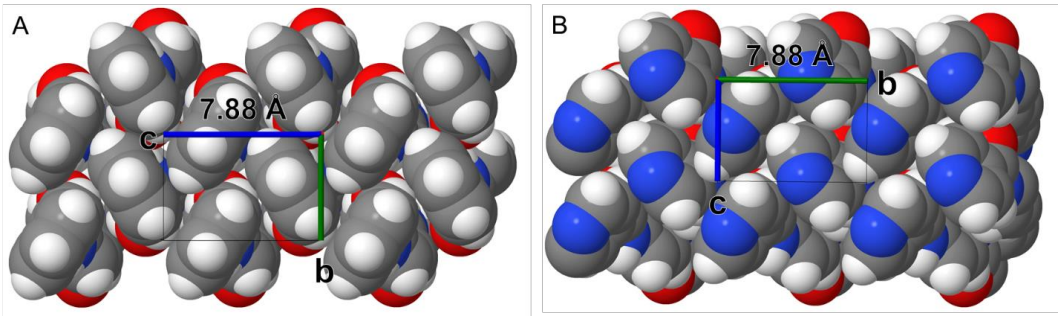

Figure S11*:* A) View on top of the bc-plane (100) of Ref **1**, *N*,*N*′-1,4-phenylenebisbenzamide as taken from reference[1]. B) For comparison, the crystal structure of NA **1** is shown in the same view.

[1] Cheng, N.; Yan, Q.; Liu, S.; Zhao, D. Probing the intermolecular interactions of aromatic amides containing N-heterocycles and triptycene. *CrystEngComm* **2014**, *16* (20), 4265–4273.

S11. Applicability of this class of nucleation agents to other poly(3-alkylthiophenes)

Nucleation experiments with poly(3-butylthiophenes) (P3BT) and poly(3-octylthiophenes) (P3OT) with selected concentrations of NA **1** were performed via dynamic DSC in a similar manner as described before (see Section 3 and Section 4). The investigated temperature range was adjusted to the respective poly(3-alkylthiophenes) due to the different melting properties. For P3BT, the measurements were performed between 100 and 300 °C, and for P3OT, between 75 and 225 °C. Also, self-nucleation experiments and the determination of $T_{c,max}$ were carried out for both polymers.

Figure S12 depicts the second cooling curves of P3BT and P3OT samples with different concentrations of NA **1** (black curves) as well as a neat and self-nucleated sample as references (red curves). The addition of NA **1** significantly shifts the polymer crystallization peak in both cases to higher temperatures. We found that with 1 wt % of NA **1,** an outstanding nucleation efficiency of 98% for P3BT was obtained. For P3OT, a nucleation efficiency of 94% was obtained already at a concentration of only 0.1 wt %.

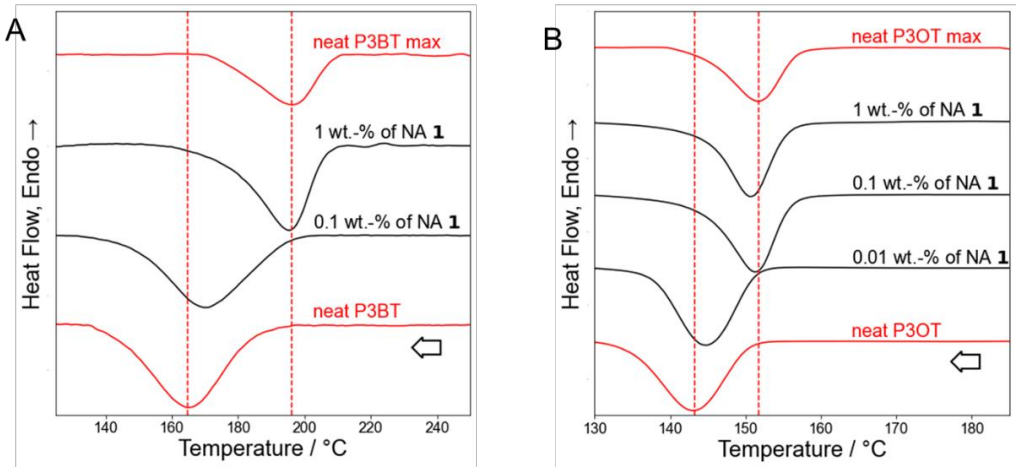

Figure S12. A) Second cooling curves of neat and self-nucleated poly(3-butylthiophenes) (P3BT) (red curves) and P3BT with 0.1 and 1 wt % of NA **1**. B) Second cooling curves of neat and self-nucleated poly(3-octylthiophenes) (P3OT) (red curves) and P3OT with 0.01, 0.1, and 1 wt % of NA **1**. The addition of NA **1** shifts the polymer crystallization peak to higher temperatures close to the respective $T_{c,max}$.

S12. Hyperspectral imaging of neat P3HT and P3HT with NA 1

In P3HT films with the nucleating agent NA **1**, we observed a slight decrease of the relative 0-0 PL peak intensity at around 650 nm, compared to neat P3HT films (as explained in the main text). Furthermore, analyzing the same data, we observe a slight red-shift of the low-energy (high wavelength) flank of the PL spectrum. This shift is visible in the averaged spectrum (black line) in Figure S13 A, at around 750 nm (indicated by the arrow). We visualize this shift by evaluating the PL intensity at 60 % of the maximum intensity (around 750 nm) for each individual spectrum of the 40x40 μm^2 area and plot a map of the wavelengths at which this intensity is obtained. Figure S13 B and C show those maps of the extracted flank positions for a neat P3HT film and for a P3HT film with 0.1 wt % NA **1**, respectively. As with the maps in Figure 10, we also observe no inhomogeneities.

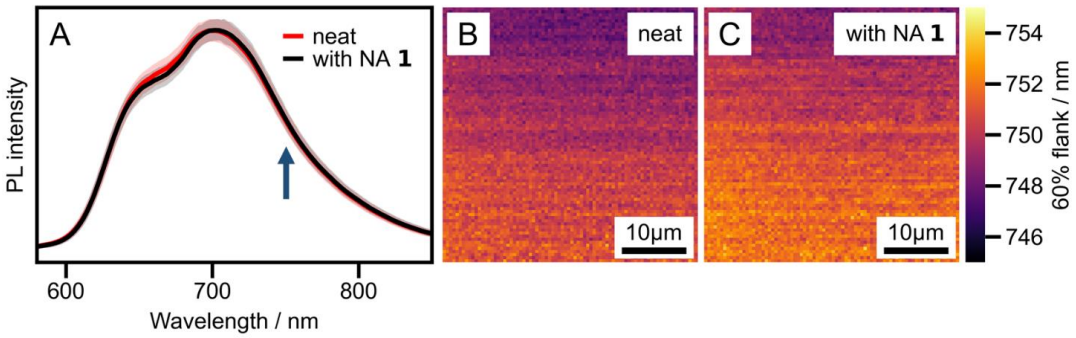

Figure S13. Hyperspectral imaging of thin films of neat P3HT and P3HT with NA **1**. A) PL spectra of a neat P3HT film (red) and a P3HT film with 0.1 wt % NA **1** (black). Both PL spectra are averaged over an area of 40x40 μm^2 each comprising 6640 individual spectra. The shaded area shows the degree of variation within the films. B) and C) Maps of the spectral position of the low-energy (high-wavelength) flank, retrieved at 60 % of the maximum intensity for the neat P3HT film (B) and the P3HT film with 0.1 wt % NA **1** (C).

S13. Hyperspectral absorption imaging of neat P3HT and P3HT with NA 1

To further investigate the optical properties of P3HT films with nucleating agent NA **1**, we analyzed the samples shown in Figure 10 of the main text via hyperspectral absorption spectroscopy. We followed the experimental procedure outlined in the *Experimental Section* of the main text, except we replaced the laser with a white light source (Thorlabs OSL1) in a trans-illumination configuration and removed the optical filters. Both hyperspectral PL imaging and hyperspectral absorption imaging have been performed on the same samples and the same sample area, allowing us to correlate the results in Figure S14 and Figure 10 of the main text.

Comparing the average absorption spectra (solid lines in Figure S14 A), we see no substantial differences between the absorption properties of the neat P3HT film and a P3HT film with NA **1**. In particular, the amorphous contribution to the absorbance signal, which dominates below ~500nm, barely differs between both samples, indicating no fundamental difference in the degree of crystallinity, i.e, in the relative fractions of amorphous and crystalline domains.[2] Moreover, the low-energy part of the absorption spectrum (ca. 550nm-650nm) contains information on the electronic interaction between polymer chains within crystallites, giving valuable insight into the electronic landscape of the film.[3,4] Here, this low-energy part of the absorption spectra shows no substantial difference between both samples, indicating that the electronic interaction is barely affected by the nucleating agent. Since the electronic interaction between P3HT chains is determined e.g. by the planarity of the chains within crystallites, the chain conformation can only be influenced on a very small level.[5]

For each recorded spectrum we extracted the ratio between the absorbance signal at 600nm and 540nm, which roughly quantifies the shape of the low-energy part of the absorbance spectra. Visualizing this ratio as maps (Figure 14 B and C), we confirm that preparation with NA **1** does not introduce substantial spatial inhomogeneities in the film. This confirms the results from PL studies presented in Figure 10 of the main text.

---

[2] Clark, J.; Chang, J.-F.; Spano, F. C.; Friend, R. H.; Silva, C. Determining Exciton Bandwidth and Film Microstructure in Polythiophene Films Using Linear Absorption Spectroscopy. *Appl Phys Lett* **2009**, *94* (16), 163306.

[3] Spano, F. C. Modeling Disorder in Polymer Aggregates: The Optical Spectroscopy of Regioregular Poly(3-Hexylthiophene) Thin Films. *J Chem Phys* **2005**, *122* (23), 234701.

[4] Gierschner, J.; Huang, Y.-S.; Van Averbeke, B.; Cornil, J.; Friend, R. H.; Beljonne, D. Excitonic versus Electronic Couplings in Molecular Assemblies: The Importance of Non-Nearest Neighbor Interactions. *J Chem Phys* **2009**, *130* (4), 044105.

[5] P. Beer, P. M. Reichstein, K. Schoetz, D. Raithel, M. Thelakkat, J. Köhler, F. Panzer, R. Hildner. Disorder in P3HT nanoparticles probed by optical spectroscopy on P3HT-*b*-PEG micelles. *J Phys Chem A* **2021**, *125* (47), 10165–10183.

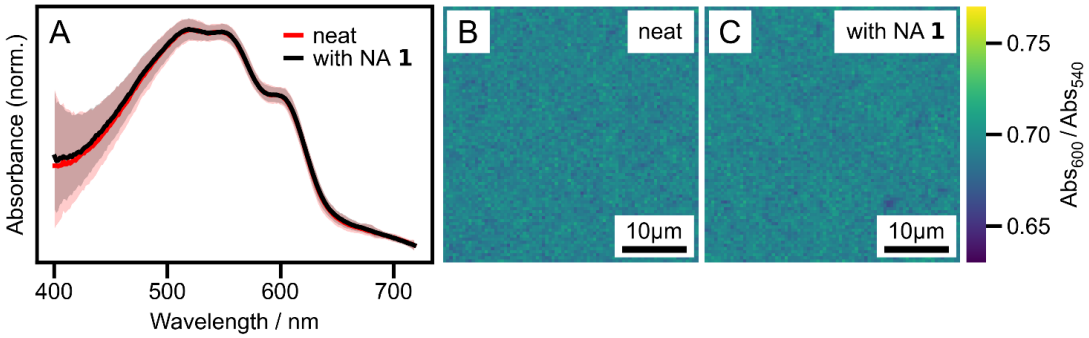

Figure S14. Hyperspectral imaging of thin films of neat P3HT and P3HT with NA **1**. A) Absorption spectra of a neat P3HT film (red) and a P3HT film with 0.1 wt % NA **1** (black). Both absorption spectra are averaged over an area of 40x40 μm^2 comprising 6640 individual spectra each. The shaded area shows the degree of variation within the films. B) and C) Maps of the ratio Abs_{600}/Abs_{540} of the absorbance at 600 nm (Abs_{600}) and at 540 nm (Abs_{540}) for the neat P3HT film (B) and the P3HT film with 0.1 wt % NA **1** (C).

S14. Thin film stability neat P3HT and P3HT with NA 1 on silicon substrates

To study the film stability of the P3HT with and without NA **1**, thin films were spin-coated on OFET silicon substrates with a silicon oxide surface (Fraunhofer IPMS Dresden, OFET Gen. 4). The substrates were rinsed and sonicated for five minutes with acetone and subsequently treated with ozone plasma for 15 minutes. Thin films were prepared by spin-coating with a Coros OP15 (Siemens) with a CONVAC 1001 at 1000 rpm for 60 s using solutions of 1 wt % of P3HT in chlorobenzene containing no, 0.1 wt % or 1.0 wt % of NA **1** with respect to the polymer and dried at ambient conditions for 24 h. The samples were heated to 300°C with a rate of 10 K/min using a Linkam TMS 92 hot stage and kept for 5 min at his temperature to ensure complete melting of the P3HT and dissolution of NA **1** in the P3HT melt. Subsequently the samples were cooled to room temperature and stored under inert atmosphere. For further investigations, these samples were stored for four weeks at room temperature. The quality of the films was investigated with a light microscopy, using an Olympus BX60 microscope, and images were recorded using a a Moticam Pro 282B.

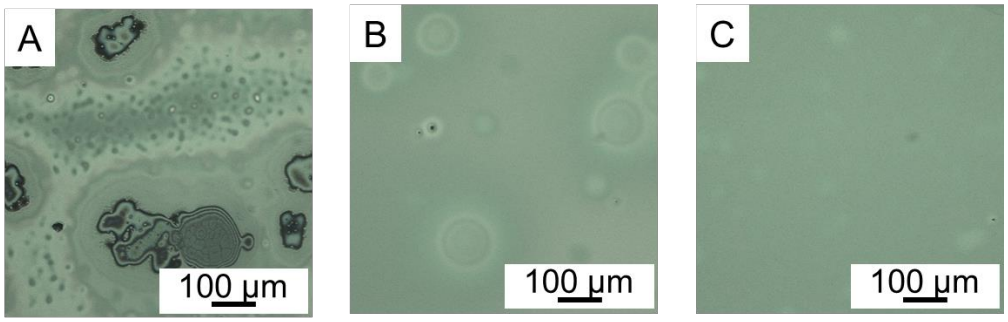

Figure S15. Optical micrographs of spin-coated thin films of P3HT on silicon substrates with a silicon oxide surface. The micrographs show A) neat P3HT, B) P3HT with 0.1wt % of NA **1** and C) P3HT with 1 wt % of NA **1** after applying the heating step to 300 °C and a four-week storage of the films under inert atmosphere at room temperature. The neat P3HT film (A) features a very inhomogeneous appearance including microcracks. In contrast, thin films of P3HT with NA **1** are highly uniform and show only some inhomogeneities (B), which are further reduced with increasing concentration of NA **1** (C).

S15. Charge carrier mobilities in OFETs of thin films of P3HT with and without NA 1

To study the influence of NA **1** on the charge carrier mobility, experiments in OFET geometry were performed. As substrates, 4th generation OFET substrates were purchased from Fraunhofer IPMS Dresden. Thin films of P3HT with and without NA **1** on OFET substrates were prepared and treated as described in Section 14. An Agilent Technologies B1500A Semiconductor Device Analyzer in a nitrogen-filled glovebox were used to measure the transistor characteristics. To calculate the charge carrier mobility, transfer characteristics were recorded according to literature procedures and analyzed in the saturation regime.[6] In a first set of experiments, the charge carrier mobilities were determined after spin-coating and drying under ambient conditions for 24h. Subsequently, the charge carrier mobilities were determined after applying a heating step to 300 °C and cooling to room temperature as described in Section S14. Finally, transistor measurements were performed and the mobilities were calculated after a four-week storage at ambient conditions. The averaged mobilities for each sample for at least three measurements each after drying for 24 h, after annealing at 300°C and after a four-week storage are depicted in Figure S16.

The averaged charge carrier mobilities determined from the transfer characteristics of the thin films after drying (red crosses) are in the range of approximately $1x10^{-2}$ $cm^2V^{-1}s^{-1}$. We find no significant loss in charge carrier mobility if the supramolecular nucleating agents are used. Moreover, different concentrations do not have an influence on the mobility. Thus, we conclude that objects of NA **1** do not act as traps for the charge carriers in P3HT-based OFETs. After applying the heating step, the charge carrier mobilities of all thin films (green squares) drop to the same level of approximately $5x10^{-5}$ $cm^2V^{-1}s^{-1}$. This supports the above-mentioned finding that the presence of NA **1** objects is not detrimental to the charge carrier mobility. Interestingly, after a four-week storage of the devices at room temperature, we found a further drop in the charge carrier mobility of the OFET with the neat P3HT, whereas the charge carrier mobilities for the devices with 0.1 wt % or 1 wt % of NA **1** remains constant (blue circles).

[6] Krauss, G.; Meichsner, F.; Hochgesang, A.; Mohanraj, J.; Salehi, S.; Schmode, P.; Thelakkat, M. Polydiketopyrrolopyrroles Carrying Ethylene Glycol Substituents as Efficient Mixed Ion-Electron Conductors for Biocompatible Organic Electrochemical Transistors . *Adv Funct Mater* **2021**, *31* (20), 2010048.

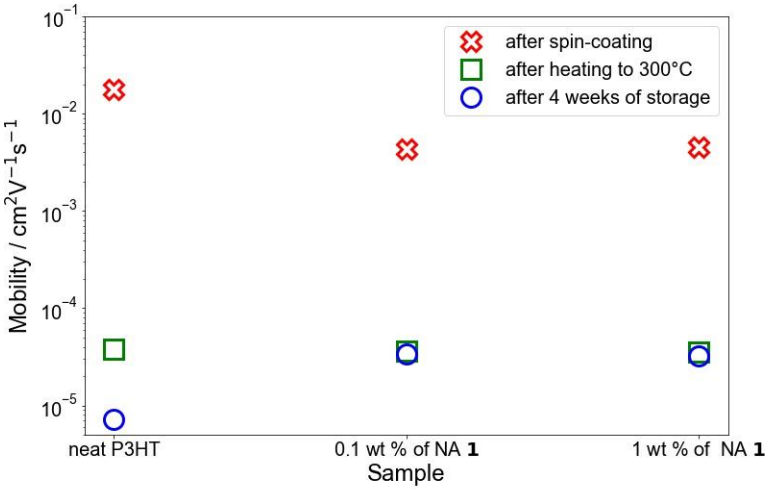

Figure S16. Averaged charge carrier mobilities of OFETs based on thin films of neat P3HT, P3HT with 0.1 wt % of NA **1** and P3HT with 1 wt % of NA **1** after different processing steps and storage. Red crosses: Charge carrier mobilities after spin-coating and drying for 24h under ambient conditions. Green squares: Charge carrier mobilities after heating to 300°C and cooling to room temperature. Blue circles: After storing the samples for four weeks under inert atmosphere and at room temperature.

4.5 Publication IV: Directed Gradients in the Excited-State Energy Landscape of Poly(3-hexylthiophene) Nanofibers

JACS
JOURNAL OF THE AMERICAN CHEMICAL SOCIETY
pubs.acs.org/JACS
Article

Directed Gradients in the Excited-State Energy Landscape of Poly(3-hexylthiophene) Nanofibers

Sebastian Stäter, Felix A. Wenzel, Hannes Welz, Klaus Kreger, Jürgen Köhler, Hans-Werner Schmidt, and Richard Hildner*

Cite This: J. Am. Chem. Soc. 2023, 145, 13780−13787
Read Online
ACCESS | Metrics & More | Article Recommendations | Supporting Information

ABSTRACT: Funneling excitation energy toward lower energy excited states is a key concept in photosynthesis, which is often realized with at most two chemically different types of pigment molecules. However, current synthetic approaches to establish energy funnels, or gradients, typically rely on Förster-type energy-transfer cascades along many chemically different molecules. Here, we demonstrate an elegant concept for a gradient in the excited-state energy landscape along micrometer-long supramolecular nanofibers based on the conjugated polymer poly(3-hexylthiophene), P3HT, as the single component. Precisely aligned P3HT nanofibers within a supramolecular superstructure are prepared by solution processing involving an efficient supramolecular nucleating agent. Employing hyperspectral imaging, we find that the lowest-energy exciton band edge continuously shifts to lower energies along the nanofibers' growth direction. We attribute this directed excited-state energy gradient to defect fractionation during nanofiber growth. Our concept provides guidelines for the design of supramolecular structures with an intrinsic energy gradient for nanophotonic applications.

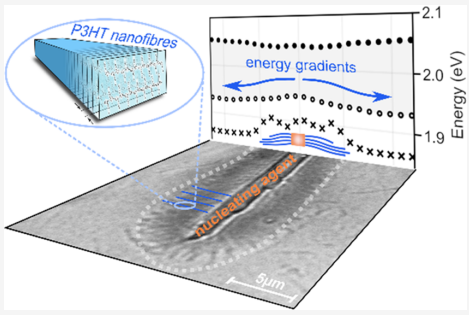

INTRODUCTION

The precise flow of excitation energy between nanoscopic functional units is a key step in the initial light-driven steps in photosynthesis. Those functional units comprise light-harvesting complexes that act as antennae and reaction centers that act as transducers. Both units are often complex superstructures with very few chemically different pigment molecules densely packed and precisely arranged within a protein scaffold.[1−4] Electronic Coulomb interactions between pigments and noncovalent interactions between pigments and the protein scaffold create a funnel, or gradient, in the excited-state energy landscape, i.e., a decreasing energy of the lowest-energy excited states toward the reaction center. This energy gradient provides the driving force to steer excitation energy in a directed and highly efficient way toward the reaction center, where excitation energy is converted into chemical energy.[1,2,5]

Several approaches have been developed to establish (step) gradients in artificial systems. The aim is to transfer energy between molecules or assemblies of molecules in a cascade-type fashion from higher to lower transition energies. Such systems are based on, e.g., thin films comprising different conjugated polymers[6] or laser dyes,[7] or a series of up to five chemically different chromophores with decreasing transition energies, which are covalently linked to a strand of DNA.[8] Supramolecular assemblies have recently attracted great attention as artificial light-harvesting systems as well. For instance, donor−acceptor-type assemblies with various morphologies were designed, such as wire-like structures forming organogels[9] or sheet-like structures of clay−dye-based hydrogels,[10] micelles,[11,12] vesicles,[13,14] spherical aggregates,[15] nanofibers and nanotubes.[16−18] Moreover, distinct BODIPY derivatives that self-assemble into sheet-like morphologies with specific packing and order of the molecules were used to create a "cascaded" excited-state energy landscape between the supramolecular assemblies.[19]

However, concepts that employ only a single chemical species of functional molecules to establish a continuous excited-state energy gradient have not been realized yet to the best of our knowledge. In principle, along one-dimensional supramolecular nanofibers, a continuous shift of the lowest-energy excited state can be achieved by a (increasing or decreasing) trend in intermolecular Coulomb interaction. Using small, rigid, conjugated molecules as building blocks, however, such variation in interaction may be challenging to achieve. The required continuous change in intermolecular distance and/or mutual orientation is impeded by the supramolecular motif(s) and the self-assembly conditions,

Received: March 2, 2023
Published: June 14, 2023

both of which determine the mutual arrangement of molecules in thermodynamic equilibrium.[20] In contrast, the crystallization of conjugated polymers from solution results in the incorporation of an increasing number of defects along a nanostructure, thus providing a gradient in defect density. Defects that are relevant in this context are regio-defects of polymer chains, chain ends incorporated within a nanostructure, and intra-chain torsional disorder. Intra-chain torsional disorder refers to a deviation from backbone planarity by a rotation of monomers out of plane. A regio-defect is a local chemical deviation from the polymer structure, typically a mis-attached side chain. Such regio-defects typically increase torsional disorder along polymer chains due to steric hindrance, which influences the polymers' packing within nanostructures.[21,22] Similarly, the end of a polymer chain being incorporated into a nanostructure impacts the overall packing;[23] often, the chain end involves a regio-defect, too. Importantly, such defects do not act as (emissive) trap states for electronic excitations; yet, an increasing defect density can be expected to modulate the excited-state energy landscape along the growth direction of conjugated polymer nanostructures via an increasing degree of disorder in chain packing, thus modulating inter-chain electronic interactions. For instance, Roehling et al. and Oosterbaan et al. showed for polythiophenes such fractionation according to molecular weight and probably regio-defects, implying an increasing number of defects, during growth of supramolecular nanofibers.[24,25] However, an energy gradient could not be demonstrated.

Here, we exploit defect fractionation during the growth of nanofibers based on a conjugated polymer to realize a gradient in the excited-state energy landscape over micrometer distances. We employ a highly efficient ribbon-like supramolecular nucleating agent (NA)[26] for the controlled crystallization of the extensively studied and well-understood poly(3-hexylthiophene), P3HT,[27−33] into nanofibers. The resulting NA/P3HT superstructures, resembling shish-kebab-like structures,[34,35] with their highly aligned and oriented micrometer-long P3HT nanofibers allow us to use hyperspectral imaging, i.e., spatially resolved absorption and emission spectroscopy. We reveal a continuous red shift of the lowest-energy exciton states exceeding thermal energy at room temperature along the growth direction of the P3HT nanofibers.

RESULTS AND DISCUSSION

To demonstrate the concept of defect fractionation on the excited-state energy landscape of supramolecular P3HT nanofibers, knowledge of the starting point and growth direction of nanofibers is essential. Heterogeneous nucleating agents (NAs) are known to provide an epitaxial surface from which the polymer crystallization is initiated, and subsequently, crystal growth proceeds in a defined manner.[36,37] Achieving very densely packed and oriented nanofibers of P3HT requires NAs with a highly regular surface and a large number of nucleation sites. In our recent work, we have shown that a supramolecular NA based on *N*,*N*′-1,4-phenylenebis[4-pyridinecarboxamide] (compound **1**, see Scheme 1) is an excellent nucleating agent for the oriented crystallization of P3HT.[26]

We employ a two-step protocol to grow P3HT nanofibers as part of a supramolecular superstructure (as detailed in the Supporting Information (SI), Section S1). In the first step, we grow ribbon-like supramolecular NAs based on compound **1**.

Scheme 1. Chemical Structure of *N*,*N*′-1,4-Phenylenebis[4-pyridinecarboxamide], Compound 1[a]

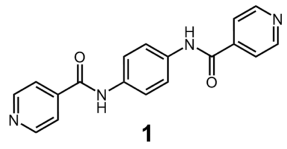

1

[a]The molecular design combines the ability to form stable supramolecular aggregates via hydrogen bonding of the amide linkages, resulting in epitaxial surfaces with the ability to form attractive pyridine−thiophene interactions to nucleate P3HT.[26]

The self-assembly of compound **1** into supramolecular structures is achieved by controlled heating and cooling of compound **1** in chlorobenzene. The formation of ribbon-like structures with lengths of several tens of μm and widths of 1−5 μm is confirmed by electron microscopy (see SI Figure S2a). In the second step, we add P3HT to a dispersion of the supramolecular NA. The sample is kept for several days at room temperature, allowing P3HT to trans-crystallize from the epitaxial surface of the ribbon-like supramolecular NA into oriented nanofibers. The presence of oriented P3HT nanofibers grown from supramolecular NAs is confirmed via electron microscopy (see SI Figure S2c). Importantly, the P3HT nanofibers are densely packed and highly oriented, with known starting point and growth direction, and lengths of several micrometers. This allows for the straightforward and unambiguous investigation of the nanofibers' optical and electronic properties as a function of position along their growth direction.

The morphology of NA/P3HT superstructures was characterized by correlative electron and optical microscopy (SI, Section S1). Figure 1a shows a scanning electron microscopy (SEM) image of a representative example of a superstructure. The ribbon-like supramolecular NA is oriented vertically in this figure and features a length exceeding 40 μm and a width of 3 μm. The P3HT nanofibers are oriented horizontally with a dense packing and extend on both sides up to 5 μm away from the central supramolecular NA. The area covered by P3HT nanofibers is indicated with the dotted line in Figure 1a. Figure 1b shows a magnified view of the boxed area in Figure 1a close to the supramolecular NA. Individual P3HT nanofibers are clearly discernible and are arranged with a high degree of parallel alignment with respect to each other (although some nanofibers on the surface are not perfectly aligned). A grayscale profile across the P3HT nanofibers reveals an average distance of 33 nm between signal maxima, as indicated by the blue dots in Figure 1c. This lamellar distance comprises the width of the crystalline P3HT nanofibers, as well as the width of amorphous interlamellar zones between nanofibers. For high-molecular-weight P3HT, as used here, the width of the interlamellar zones is in the range of 10−15 nm. Hence, we estimate that the P3HT nanofibers have a crystalline width of about 20 nm, in agreement with literature data.[27,34,38−41] A schematic illustration of the NA/P3HT superstructure's cross section is shown in Figure 1d with the supramolecular NA in orange and the P3HT nanofibers in blue; the π-stacking of P3HT within nanofibers is displayed in Figure 1e (see also SI, Section S2). Residual molecularly dissolved P3HT in solution leads to the formation of a polycrystalline P3HT film (Figure 1d, red) surrounding the

https://doi.org/10.1021/jacs.3c02117
J. Am. Chem. Soc. 2023, 145, 13780−13787

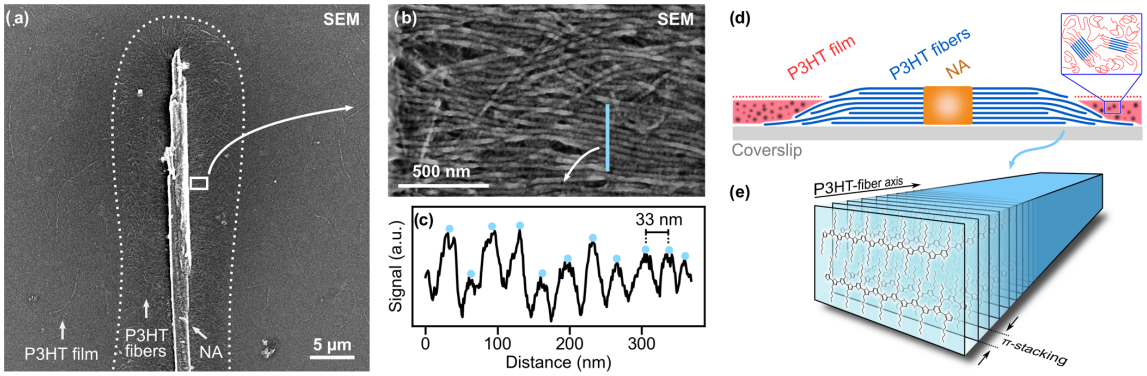

Figure 1. Structural characterization of P3HT nanofibers within a nucleating agent (NA)/P3HT superstructure. (a) Scanning electron microscopy (SEM) image of a NA/P3HT superstructure with a vertically oriented supramolecular NA and P3HT nanofibers that grew perpendicularly from the NA. The dotted white line indicates the area covered by P3HT nanofibers. (b) Magnified view of the P3HT nanofibers within the boxed area in panel (a), highlighting their high degree of orientation. (c) Gray scale profile along the blue line in panel (b); the blue dots indicate the interlamellar distances of ~33 nm between P3HT nanofibers. (d) Schematic cross section of the NA/P3HT superstructure. The inset illustrates the structure of the semicrystalline P3HT film surrounding the P3HT nanofibers. (e) Schematic view of the packing of P3HT chains into an individual P3HT nanofiber.

NA/P3HT superstructure upon deposition. The optical bright-field microscopy image of the same superstructure in Figure 2a

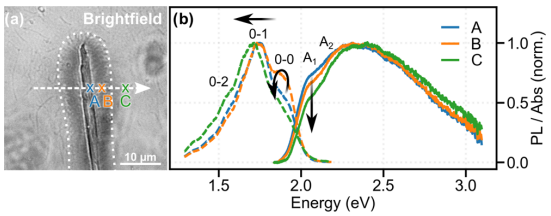

Figure 2. Optical microscopy and spectroscopy of the NA/P3HT superstructure shown in Figure 1. (a) Optical bright-field image. The dotted white line indicates the area covered by P3HT nanofibers as in Figure 1a; the white arrow indicates the direction of scanning for hyperspectral imaging. (b) Examples of spatially resolved PL (dashed lines) and absorption spectra (solid lines) taken at spot A (beginning of P3HT nanofibers), B (middle of P3HT nanofibers), and C (surrounding P3HT film). The arrows indicate spectral changes for increasing distance to the supramolecular NA: a decrease in the lowest-energy absorption A_1 around 2.1 eV, a red shift of the PL spectra, and the complex behavior of the electronic (0−0) PL peak intensity.

closely matches the SEM image (Figure 1a). Even though individual P3HT nanofibers cannot be resolved optically, the area covered by nanofibers (indicated by the dotted line) is clearly discernible by the lower (but constant) transmission in this region. While the end of P3HT nanofibers may be immersed in or under the P3HT film, the good agreement between the electron and optical microscopy images ensures an accurate assessment of the nanofiber length of about 5 μm.

We reconstruct the excited-state energy landscape along the highly oriented P3HT nanofibers by hyperspectral imaging of the 40 × 40 μm^2 area shown in Figures 1a and 2a[26,42] (see the SI, Section S1). Collecting absorption and photoluminescence (PL) spectra with diffraction-limited resolution and moving the sample both horizontally and vertically results in a set of 1680 absorption and 1680 PL spectra fully characterizing our sample. To introduce the analysis procedure and to discuss the qualitative trends, we start with three representative positions: At the beginning (spot A), in the middle of the P3HT nanofibers (spot B), as well as within the surrounding P3HT film, remote from the superstructure (spot C, see Figure 2a). We will later extend this discussion to a horizontal line scan along the P3HT nanofibers as well as to a full representation of the excited-state energy landscape in 2-dimensional 40 × 40 μm^2 maps. We note that the supramolecular NA does not absorb in the visible range and, thus, the absorption and PL spectra stem exclusively from P3HT.

The absorption spectra from positions A, B, and C (Figure 2b, solid lines) share the same general shape that is characteristic of semicrystalline P3HT.[43] The structured shoulder in the low-energy part (1.9−2.2 eV), labeled with A_1 and A_2, stems from absorption into exciton states delocalized along π-stacks of P3HT chains forming H-aggregates. The broad, featureless shape in the high-energy region (2.3−3.1 eV) results from the absorption of amorphous P3HT chains. These spectra thus confirm the coexistence of crystalline and amorphous P3HT both in the nanofiber region and the surrounding P3HT film. The main difference in the absorption spectra is the relative intensity of the lowest-energy shoulder A_1 at 2.1 eV, which indicates variations in the electronic Coulomb interaction V between π-stacked chains as a function of position.[43] Specifically, when going from the beginning (spot A) toward the middle of the P3HT nanofibers (spot B) and into the surrounding P3HT film (spot C), the decreasing relative intensity of this shoulder suggests an increasing inter-chain electronic interaction.

To quantify the change in electronic interaction between π-stacked P3HT chains as a function of position, we exploit the Frenkel Polaron model.[44] This model describes the optical properties of molecular H-aggregates in the presence of intramolecular vibrations and has been widely applied to aggregates of conjugated polymers, such as P3HT.[43] By fitting the low-energy part of the absorption spectra (SI, Section S3), we extract the free exciton bandwidth W, which relates to the electronic interaction V between P3HT chains via $W = 4V$. When going from the beginning of the P3HT nanofibers (spot A) toward their middle (spot B) and into the P3HT film (spot

https://doi.org/10.1021/jacs.3c02117
J. Am. Chem. Soc. 2023, 145, 13780−13787

Table 1. Free Exciton Bandwidth W and Spectral Position of the Lowest-Energy Absorption Peak E_{A1}^{Abs} and of the Electronic 0−0 PL Peak E_{00}^{PL} for the Spectra of P3HT Aggregates in Figure 2b[a]

	spot A (start of nanofibers)	spot B (middle of nanofibers)	spot C (surrounding film)
W (meV)	193	211	248
E_{A1}^{Abs} (eV)	2.043	2.044	2.054
E_{00}^{PL} (eV)	1.903	1.904	1.862

[a]The positions of spots A, B, and C are indicated in Figure 2a.

C), we find from the fits to the spectra in Figure 2b that the free exciton bandwidth increases from 193 to 248 meV (Table 1). While this range of values is in agreement with literature data,[29,31,43] the substantial change of this parameter within the same sample (in fact, within a few micrometers of our sample) is remarkable. Along the same direction (from A to C), the spectral position of the lowest-energy absorption peak A_1 of the crystalline phase E_{A1}^{Abs} blue-shifts by 10 meV, starting from 2.043 eV at spot A (Table 1).

A straightforward explanation for the increasing trend of the exciton bandwidth, and thus of the increasing inter-chain electronic interaction along P3HT nanofibers, would be a decrease in the $\pi-\pi$-stacking distance between P3HT chains. However, selected-area electron diffraction (SAED; see the SI, Section S2) demonstrates that this distance does not change substantially along our P3HT nanofibers. In π-stacked, H-type aggregates of conjugated oligomers and polymers a further effect plays a strong role for the exciton bandwidth. For a given π-stacking distance, the inter-chain electronic interaction increases if the delocalization of electronic excitations within a chain decreases.[24,31,45] Such decreasing intra-chain delocalization can be caused by the presence of more and more torsionally disordered chain segments. This disorder, in turn, originates from an incorporation of an increasing number of chain-end and regio-defects during nanofiber growth, i.e., from the start (spot A) toward the end of our P3HT nanofibers. The increasing defect density thus leads to H-aggregation with an increasing degree of disorder along the nanofiber.

Evidence for the increasing disorder toward the P3HT nanofiber ends comes from the PL spectra at the different spots (Figure 2b, dashed lines). All PL spectra feature a distorted vibronic progression with a partially suppressed highest-energy peak around 1.9 eV, the electronic 0−0 transition, relative to the lower energy 0−1 transition around 1.7 eV. This spectral shape is typical for PL from H-aggregated P3HT.[46] The absence of PL signal from the amorphous part above 2.0 eV is expected due to the relatively low absorbance of amorphous P3HT at the excitation wavelength (532 nm, corresponding to 2.33 eV). Moreover, rapid and efficient energy transfer from amorphous toward aggregated regions may occur prior to PL.[47,48] The PL spectra exhibit systematic variations as a function of position, in particular, the relative intensity of the 0−0 peak changes, which implies different degrees of disorder.[46] The increasing trend of the relative 0−0 PL intensity from spot A toward spot B demonstrates increasing disorder along P3HT nanofibers, corroborating our interpretation of the changes in absorption spectra. Notably, the spectral shape of the PL spectra with the suppressed 0−0 PL peaks highlights that the emission always stems from (vibronic) exciton states delocalized along the π-stacking direction, despite an increasing defect density toward nanofiber ends. In other words, such defects do not introduce (emissive and highly localized) trap states that modify emission properties; they rather modulate the overall excited-state energy landscape of delocalized vibronic excitons.

The spectral shift of the PL spectra as a function of position shows the opposite trend compared to the shift observed in absorption. Since some reabsorption may occur, we retrieve spectral shifts by extracting the spectral position E_{01}^{PL} of the 0−1 PL peak with a simple peak tracking algorithm (SI, Section S4). The position of the 0−0 transition is then determined via $E_{00}^{PL} = E_{01}^{PL} + E_{vib}$, with E_{vib} = 0.18 eV being the energy of the dominant carbon-bond stretch vibration coupling to the electronic transition.[49] We find that the 0−0 PL peak position E_{00}^{PL} red-shifts by ca. 40 meV starting from 1.90 eV at spot A (see Table 1). This opposite trend in spectral shifts between absorption and PL indicates complex structural and electronic relaxation processes related to the H-aggregation of P3HT that will be discussed in detail further below.

To visualize the continuous variation in the excited-state energy landscape along our P3HT nanofiber, we performed the analysis outlined above for all 40 absorption and PL spectra along the dashed arrow in Figure 2a. For illustration, Figure 3a schematically shows the vibronic exciton bands of an H-aggregate (right) and how those relate to the corresponding energy levels of isolated noninteracting molecules (left) in the case of a single effective vibrational mode (here: carbon-bond stretch) coupling to the electronic transition.[4,20,44,50] We limit

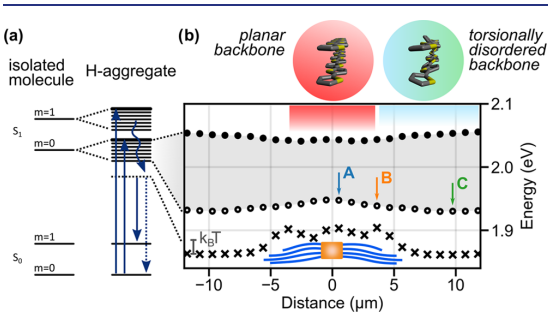

Figure 3. Excited-state energy landscape along P3HT nanofibers within a NA/P3HT superstructure. (a) Energy level schemes of isolated (left) and H-aggregated (right) molecules. Arrows indicate absorption, relaxation, and emission, and m represents the vibrational quantum number. (b) Excited-state energy landscape along the dashed white arrow in Figure 2a retrieved from optical spectra. The gray shaded area indicates the lowest-energy (m = 0) vibronic exciton band determined from spatially resolved absorption spectra. Filled and open circles indicate the upper and lower band edge, respectively. Crosses indicate the torsionally relaxed, lowest-energy exciton state from where emission occurs. The red and blue-green-filled circles and boxes (top) highlight the suggested planar and increasingly torsionally disordered P3HT backbones within P3HT nanofibers and into the surrounding P3HT film. The blue, orange, and green labels (A, B, C) refer to the same positions marked in Figure 2a.

https://doi.org/10.1021/jacs.3c02117
J. Am. Chem. Soc. 2023, 145, 13780−13787

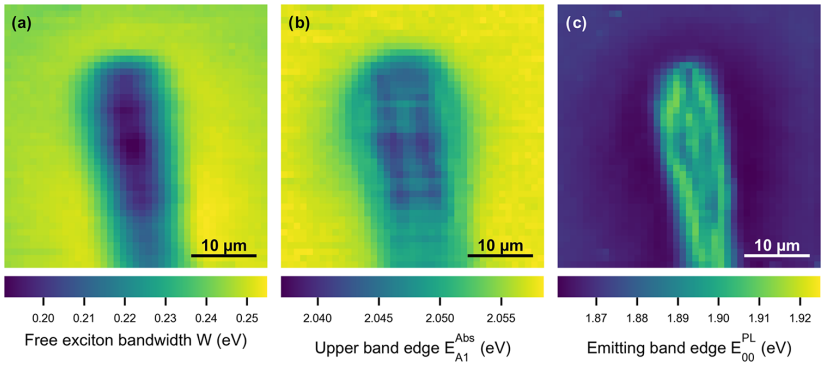

Figure 4. Hyperspectral maps of the NA/P3HT superstructure based on 1680 individual spectra. (a) Free exciton bandwidth W. (b) Upper band edge E_{A1}^{Abs}. (c) Emitting band edge E_{00}^{PL}. The 40 × 40 μm^2 area is identical to that shown in Figures 1a and 2a.

ourselves to the bands with vibrational quantum numbers m = 0 and 1 for clarity. In an H-aggregate, only the top state of each band carries oscillator strength.[44] Hence, the lowest-energy peak position E_{A1}^{Abs} of the absorption spectra corresponds to the upper band edge of the lowest-energy (m = 0) vibronic exciton band. This upper band edge, determined from 24 spectra around the central supramolecular NA, is displayed as a function of the position along P3HT nanofibers in Figure 3b by filled circles, with the supramolecular NA being located at 0 μm. We find a minimum in the energy position of the upper band edge at the beginning of the P3HT nanofibers at the nucleating agent, a continuous increase (blue shift) toward the nanofibers' ends, and finally, a leveling off to a constant value within the surrounding P3HT film.

The full shape of the (m = 0) vibronic exciton band is obtained by calculating the energy position of its lower band edge via subtraction of the bandwidth W_0 from the energy of the upper band edge. W_0 is related to the free exciton bandwidth W determined above via $W_0 = W * \exp(-S)$.[44,46] S refers to the Huang–Rhys factor for noninteracting P3HT chains, which we determined previously by single-molecule spectroscopy to be S = 0.7[30,51] (see also the SI, Section S3). This lower band edge (labeled with open circles in Figure 3b) has its highest energy at the beginning of the P3HT nanofibers, decreases in energy (red-shifts) along the nanofibers, and again levels off to a constant energy within the P3HT film. Hence, an energy gradient is imprinted in the bottom of the lowest-energy (m = 0) vibronic exciton band along P3HT nanofibers, which amounts to about thermal energy at room temperatures.

The spatially resolved PL spectra along the P3HT nanofibers show a red shift of the electronic 0–0 PL peak E_{00}^{PL} (Figure 3b, crosses) similar to that of the lower band edge E_{00}^{Abs} determined from absorption data. Yet, the behavior of the red shift at the position between the nanofiber region and the surrounding film is much steeper, as seen in the strong change of E_{00}^{PL} at around ±5 μm, close to the P3HT nanofibers' end. In this context, it is instructive to look at the energy difference between E_{00}^{PL} and E_{00}^{Abs}. In the region of the P3HT nanofibers, we find an energy difference of about 20 meV, which significantly increases to 50 meV in the surrounding P3HT film due to the more pronounced change in E_{00}^{PL} at the end of the nanofibers. Two effects can be responsible for this energy gap. First, energy transfer between crystalline domains within the P3HT nanofibers or the surrounding semicrystalline film can cause the emission to originate from crystallites with energetically very low-lying excited states. Such low-energy emitting crystallites, however, should be preferentially found close to the supramolecular NA at the beginning of the P3HT nanofibers. At that position, the relative 0–0 PL intensity is lowest (see Figure 2b), and thus the P3HT nanofibers possess a high degree of order with a larger intra-chain delocalization of electronic excitations, as discussed above. Since this is in contrast to our observation of higher energy emission at the beginning of P3HT nanofibers, we believe that this energy transfer cannot be the main effect. Second, structural relaxation, e.g., along the configuration coordinate of torsional modes of the P3HT backbone (planarization), can occur prior to the emission process. Such torsional relaxation takes place within picoseconds and was observed in P3HT aggregates.[33,52−54] Our data thus suggest that torsional relaxation, after absorption and intra-band relaxation, becomes more and more pronounced when going along the P3HT nanofibers. In other words, the torsional disorder is smallest (chain planarity is highest) at the beginning of the nanofibers, and the disorder increases (planarity decreases) along the nanofiber growth direction (see the illustration in Figure 3b, top).

Based on our hyperspectral data set, the origin of the excited-state energy gradient along the growth direction of the P3HT nanofibers can thus be traced back to a decreasing degree of order caused by fractionation during polymer crystallization into nanofibers. During crystallization, an increasing number of defects are incorporated into P3HT nanofibers. Both regio and chain-end defects can give rise to an increasing torsional disorder of P3HT chains due to steric hindrance of hexyl side chains of neighboring chains within a crystalline domain. Since this increasing torsional disorder along the P3HT nanofibers limits intra-chain delocalization of electronic excitations, the electronic Coulomb interaction between π-stacked P3HT backbones (and thus the exciton bandwidth) increases along the nanofibers' growth direction (see Figure 3b, gray shaded area). Ultimately, fractionation imprints a gradient into the excited-state energy landscape of P3HT nanofibers grown under controlled conditions. We note that in the surrounding P3HT film, comprising randomly oriented crystalline nanostructures, we do not find variations in the energy landscape, thus providing a direct control experiment for our approach.

The intrinsic energy gradient *along* the growth direction of P3HT nanofibers is most clearly seen in the lower band edge of the lowest-energy (m = 0) vibronic exciton band.

https://doi.org/10.1021/jacs.3c02117
J. Am. Chem. Soc. 2023, 145, 13780–13787

Importantly, we observe this gradient not only for the specific "horizontal" direction along the dashed arrow in Figure 2a. Analyzing our full hyperspectral data set of the 40 × 40 μm^2 area results in 2-dimensional maps of the parameters W (free exciton bandwidth), E_{A1}^{Abs} (upper band edge), and E_{00}^{PL} (emitting band edge). These 2-dimensional maps, shown in Figure 4 (see also the energy landscape cross sections in Figure S8), demonstrate that the presence of the observed gradients is not limited to one specific "horizontal" line, but gradients are imprinted consistently along the P3HT nanofibers' growth direction, independent of the starting position at the supramolecular NA. In particular, small imperfections in the (otherwise rod-like) supramolecular NA, as visible in Figure 1a, do not significantly affect the formation of a defined gradient in the excited-state energy landscape. The robustness and reproducibility of our concept are confirmed by hyperspectral measurements in another NA/P3HT superstructure (see the SI, Figure S9).

CONCLUSIONS

Creating a gradient in the excited-state energy landscape along well-defined supramolecular nanostructures is an intriguing approach toward steering exciton diffusion. To create such gradients, a variation of (photophysical) parameters along nanostructures is required, for instance, a change in stacking distance, in intermolecular electronic interaction, and/or in (electronic and structural) order. In supramolecular nanoobjects based on conjugated polymers with broad molecular weight distribution including regio-defects, such intrinsic variation is induced by fractionation during polymer crystallization. We demonstrated this concept of a gradient in the excited-state landscape on a model system that comprises nanofibers of the prototypical conjugated polymer P3HT as part of a supramolecular superstructure. Exploiting an efficient supramolecular NA, P3HT nanofiber growth starts from a well-defined position, and P3HT nanofibers are highly oriented with lengths of several μm. This unique superstructure geometry is a prerequisite to allow investigations by hyperspectral optical imaging. Fractionation during the crystallization of P3HT incorporates an increasing number of defects (regio-defects, chain-end defects, and torsionally disordered chains) toward nanofiber ends. This leads to an increase in electronic inter-chain interaction of π-stacked P3HT chains along nanofibers. Thus, a "downhill" gradient of more than thermal energy at room temperature is imprinted in the bottom of the exciton band along the P3HT nanofibers. We emphasize that regio-defects, chain ends, and (intra-chain) torsional disorder do not introduce (emissive and strongly localized) traps for electronic excitations. The presence of such defects rather modulates the overall excited-state energy landscape of delocalized vibronic excitons to create an energy gradient over distances of several micrometers.

In principle, intrinsic energy gradients in the lowest-energy exciton states could promote directed energy transport along the nanofibers toward their ends, i.e., toward lower energies, because relaxed excitons are responsible for long-range transport.[55] The absence of directed long-range transport in our P3HT nanofibers might be related to the relatively small crystalline domain size of only about 10 nm, which introduces inter-crystallite disorder and is detrimental to transport. However, we believe that our concept of fractionation-induced excited-state energy gradients is transferable to other combinations of nucleating agents and conjugated polymers that crystallize into fibrillar (nano-)structures. This approach may thus pave the way to achieving directed long-range energy transport and may find use in novel photonic nanodevices or as antennae for the guided transport of excitation energy in artificial light-harvesting systems.

ASSOCIATED CONTENT

Supporting Information

The Supporting Information is available free of charge at https://pubs.acs.org/doi/10.1021/jacs.3c02117.

Sample preparation and reference experiments, experimental section, structural characterization of P3HT nanofibers, analysis of spectroscopic data, and hyperspectral images (PDF)

AUTHOR INFORMATION

Corresponding Author

Richard Hildner − *Zernike Institute for Advanced Materials, University of Groningen, 9747 AG Groningen, The Netherlands; Spectroscopy of Soft Matter, University of Bayreuth, 95440 Bayreuth, Germany;* orcid.org/0000-0002-7282-3730; Email: r.m.hildner@rug.nl

Authors

Sebastian Stäter − *Zernike Institute for Advanced Materials, University of Groningen, 9747 AG Groningen, The Netherlands; Spectroscopy of Soft Matter, University of Bayreuth, 95440 Bayreuth, Germany*

Felix A. Wenzel − *Macromolecular Chemistry I and Bavarian Polymer Institute, University of Bayreuth, 95440 Bayreuth, Germany*

Hannes Welz − *Macromolecular Chemistry I and Bavarian Polymer Institute, University of Bayreuth, 95440 Bayreuth, Germany*

Klaus Kreger − *Macromolecular Chemistry I and Bavarian Polymer Institute, University of Bayreuth, 95440 Bayreuth, Germany;* orcid.org/0000-0003-3021-1311

Jürgen Köhler − *Spectroscopy of Soft Matter, University of Bayreuth, 95440 Bayreuth, Germany; Bavarian Polymer Institute and Bayreuther Institut für Makromolekülforschung (BIMF), University of Bayreuth, 95440 Bayreuth, Germany;* orcid.org/0000-0002-4214-4008

Hans-Werner Schmidt − *Macromolecular Chemistry I and Bavarian Polymer Institute, University of Bayreuth, 95440 Bayreuth, Germany;* orcid.org/0000-0002-1761-1153

Complete contact information is available at: https://pubs.acs.org/10.1021/jacs.3c02117

Author Contributions

All authors were involved in the design of the research and the discussion of the results. The manuscript was written through the contributions of all authors. All authors have given approval to the final version of the manuscript.

Notes

The authors declare no competing financial interest.

ACKNOWLEDGMENTS

The authors acknowledge financial support from the German Research Foundation (DFG) through the research training group GRK1640 and from the Bavarian State Ministry of Science and the Arts through the Collaborative Research Network "Solar Technologies go Hybrid." The authors

https://doi.org/10.1021/jacs.3c02117
J. Am. Chem. Soc. 2023, 145, 13780−13787

acknowledge support by the Elite Network of Bavaria (ENB) through the study programs "Macromolecular Science" (F.A.W.) and "Biological Physics" (R.H.). The authors are grateful to Werner Reichstein and Markus Drechsler (KeyLab Electron and Optical Microscopy of the Bavarian Polymer Institute) for support with the SEM and SAED measurements.

REFERENCES

(1) Brédas, J.-L.; Sargent, E. H.; Scholes, G. D. Photovoltaic Concepts Inspired by Coherence Effects in Photosynthetic Systems. *Nat. Mater.* **2017**, *16*, 35−44.
(2) Strümpfer, J.; Şener, M.; Schulten, K. How Quantum Coherence Assists Photosynthetic Light-Harvesting. *J. Phys. Chem. Lett.* **2012**, *3*, 536−542.
(3) Cogdell, R. J.; Gall, A.; Köhler, J. The Architecture and Function of the Light-Harvesting Apparatus of Purple Bacteria: From Single Molecules to *in Vivo* Membranes. *Q. Rev. Biophys.* **2006**, *39*, 227−324.
(4) Brixner, T.; Hildner, R.; Köhler, J.; Lambert, C.; Würthner, F. Exciton Transport in Molecular Aggregates - From Natural Antennas to Synthetic Chromophore Systems. *Adv. Energy Mater.* **2017**, *7*, No. 1700236.
(5) Scholes, G. D.; Mirkovic, T.; Turner, D. B.; Fassioli, F.; Buchleitner, A. Solar Light Harvesting by Energy Transfer: From Ecology to Coherence. *Energy Environ. Sci.* **2012**, *5*, 9374.
(6) Kim, J.; McQuade, D. T.; Rose, A.; Zhu, Z.; Swager, T. M. Directing Energy Transfer within Conjugated Polymer Thin Films. *J. Am. Chem. Soc.* **2001**, *123*, 11488−11489.
(7) Berggren, M.; Dodabalapur, A.; Slusher, R. E.; Bao, Z. Light Amplification in Organic Thin Films Using Cascade Energy Transfer. *Nature* **1997**, *389*, 466−469.
(8) Sánchez-Mosteiro, G.; van Dijk, E. M. H. P.; Hernando, J.; Heilemann, M.; Tinnefeld, P.; Sauer, M.; Koberlin, F.; Patting, M.; Wahl, M.; Erdmann, R.; van Hulst, N. F.; García-Parajó, M. F. DNA-Based Molecular Wires: Multiple Emission Pathways of Individual Constructs. *J. Phys. Chem. B* **2006**, *110*, 26349−26353.
(9) Ajayaghosh, A.; Praveen, V. K.; Vijayakumar, C.; George, S. J. Molecular Wire Encapsulated into π Organogels: Efficient Supramolecular Light-Harvesting Antennae with Color-Tunable Emission. *Angew. Chem., Int. Ed.* **2007**, *46*, 6260−6265.
(10) Rao, K. V.; Datta, K. K. R.; Eswaramoorthy, M.; George, S. J. Light-Harvesting Hybrid Hydrogels: Energy-Transfer-Induced Amplified Fluorescence in Noncovalently Assembled Chromophore-Organoclay Composites. *Angew. Chem., Int. Ed.* **2011**, *50*, 1179−1184.
(11) Li, C.; Zhang, J.; Zhang, S.; Zhao, Y. Efficient Light-Harvesting Systems with Tunable Emission through Controlled Precipitation in Confined Nanospace. *Angew. Chem., Int. Ed.* **2019**, *58*, 1643−1647.
(12) Liu, Y.; Jin, J.; Deng, H.; Li, K.; Zheng, Y.; Yu, C.; Zhou, Y. Protein-Framed Multi-Porphyrin Micelles for a Hybrid Natural-Artificial Light-Harvesting Nanosystem. *Angew. Chem., Int. Ed.* **2016**, *55*, 7952−7957.
(13) Zhang, X.; Rehm, S.; Safont-Sempere, M. M.; Würthner, F. Vesicular Perylene Dye Nanocapsules as Supramolecular Fluorescent PH Sensor Systems. *Nat. Chem.* **2009**, *1*, 623−629.
(14) Calver, C. F.; Schanze, K. S.; Cosa, G. Biomimetic Light-Harvesting Antenna Based on the Self-Assembly of Conjugated Polyelectrolytes Embedded within Lipid Membranes. *ACS Nano* **2016**, *10*, 10598−10605.
(15) Acharyya, K.; Bhattacharyya, S.; Lu, S.; Sun, Y.; Mukherjee, P. S.; Stang, P. J. Emissive Platinum(II) Macrocycles as Tunable Cascade Energy Transfer Scaffolds. *Angew. Chem., Int. Ed.* **2022**, *61*, No. e202200715.
(16) Bösch, C. D.; Langenegger, S. M.; Häner, R. Light-Harvesting Nanotubes Formed by Supramolecular Assembly of Aromatic Oligophosphates. *Angew. Chem., Int. Ed.* **2016**, *55*, 9961−9964.
(17) Winiger, C. B.; Li, S.; Kumar, G. R.; Langenegger, S. M.; Häner, R. Long-Distance Electronic Energy Transfer in Light-Harvesting Supramolecular Polymers. *Angew. Chem., Int. Ed.* **2014**, *53*, 13609−13613.
(18) Winiger, C. B.; Langenegger, S. M.; Calzaferri, G.; Häner, R. Formation of Two Homo-Chromophoric H-Aggregates in DNA-Assembled Alternating Dye Stacks. *Angew. Chem., Int. Ed.* **2015**, *54*, 3643−3647.
(19) Das, G.; Cherumukkil, S.; Padmakumar, A.; Banakar, V. B.; Praveen, V. K.; Ajayaghosh, A. Tweaking a BODIPY Spherical Self-Assembly to 2D Supramolecular Polymers Facilitates Excited-State Cascade Energy Transfer. *Angew. Chem., Int. Ed.* **2021**, *60*, 7851−7859.
(20) Kreger, K.; Schmidt, H.-W.; Hildner, R. Tailoring the Excited-State Energy Landscape in Supramolecular Nanostructures. *Electron. Struct.* **2021**, *3*, No. 023001.
(21) Kim, Y.; Cook, S.; Tuladhar, S. M.; Choulis, S. A.; Nelson, J.; Durrant, J. R.; Bradley, D. D. C.; Giles, M.; McCulloch, I.; Ha, C.-S.; Ree, M. A Strong Regioregularity Effect in Self-Organizing Conjugated Polymer Films and High-Efficiency Polythiophene:Fullerene Solar Cells. *Nat. Mater.* **2006**, *5*, 197−203.
(22) Adachi, T.; Brazard, J.; Ono, R. J.; Hanson, B.; Traub, M. C.; Wu, Z.-Q.; Li, Z.; Bolinger, J. C.; Ganesan, V.; Bielawski, C. W.; Vanden Bout, D. A.; Barbara, P. F. Regioregularity and Single Polythiophene Chain Conformation. *J. Phys. Chem. Lett.* **2011**, *2*, 1400−1404.
(23) Tatum, W. K.; Resing, A. B.; Flagg, L. Q.; Ginger, D. S.; Luscombe, C. K. Defect Tolerance of π-Conjugated Polymer Crystal Lattices and Their Relevance to Optoelectronic Applications. *ACS Appl. Polym. Mater.* **2019**, *1*, 1466−1475.
(24) Roehling, J. D.; Arslan, I.; Moulé, A. J. Controlling Microstructure in Poly(3-Hexylthiophene) Nanofibers. *J. Mater. Chem.* **2012**, *22*, 2498−2506.
(25) Oosterbaan, W. D.; Vrindts, V.; Berson, S.; Guillerez, S.; Douhéret, O.; Ruttens, B.; D'Haen, J.; Adriaensens, P.; Manca, J.; Lutsen, L.; Vanderzande, D. Efficient Formation, Isolation and Characterization of Poly(3-Alkylthiophene) Nanofibres: Probing Order as a Function of Side-Chain Length. *J. Mater. Chem.* **2009**, *19*, 5424.
(26) Wenzel, F. A.; Welz, H.; van der Zwan, K. P.; Stäter, S.; Kreger, K.; Hildner, R.; Senker, J.; Schmidt, H.-W. Highly Efficient Supramolecular Nucleating Agents for Poly(3-Hexylthiophene). *Macromolecules* **2022**, *55*, 2861−2871.
(27) Brinkmann, M. Structure and Morphology Control in Thin Films of Regioregular Poly(3-Hexylthiophene). *J. Polym. Sci., Part B: Polym. Phys.* **2011**, *49*, 1218−1233.
(28) Noriega, R.; Rivnay, J.; Vandewal, K.; Koch, F. P. V.; Stingelin, N.; Smith, P.; Toney, M. F.; Salleo, A. A General Relationship between Disorder, Aggregation and Charge Transport in Conjugated Polymers. *Nat. Mater.* **2013**, *12*, 1038−1044.
(29) Beer, P.; Reichstein, P. M.; Schötz, K.; Raithel, D.; Thelakkat, M.; Köhler, J.; Panzer, F.; Hildner, R. Disorder in P3HT Nanoparticles Probed by Optical Spectroscopy on P3HT-b-PEG Micelles. *J. Phys. Chem. A* **2021**, *125*, 10165−10173.
(30) Raithel, D.; Baderschneider, S.; de Queiroz, T. B.; Lohwasser, R.; Köhler, J.; Thelakkat, M.; Kümmel, S.; Hildner, R. Emitting Species of Poly(3-Hexylthiophene): From Single, Isolated Chains to Bulk. *Macromolecules* **2016**, *49*, 9553−9560.
(31) Scharsich, C.; Lohwasser, R. H.; Sommer, M.; Asawapirom, U.; Scherf, U.; Thelakkat, M.; Neher, D.; Köhler, A. Control of Aggregate Formation in Poly(3-Hexylthiophene) by Solvent, Molecular Weight, and Synthetic Method. *J. Polym. Sci., Part B: Polym. Phys.* **2012**, *50*, 442−453.
(32) Panzer, F.; Bässler, H.; Lohwasser, R.; Thelakkat, M.; Köhler, A. The Impact of Polydispersity and Molecular Weight on the Order−Disorder Transition in Poly(3-Hexylthiophene). *J. Phys. Chem. Lett.* **2014**, *5*, 2742−2747.
(33) Banerji, N.; Cowan, S.; Vauthey, E.; Heeger, A. J. Ultrafast Relaxation of the Poly(3-Hexylthiophene) Emission Spectrum. *J. Phys. Chem. C* **2011**, *115*, 9726−9739.
(34) Brinkmann, M.; Chandezon, F.; Pansu, R. B.; Julien-Rabant, C. Epitaxial Growth of Highly Oriented Fibers of Semiconducting

https://doi.org/10.1021/jacs.3c02117
J. Am. Chem. Soc. 2023, 145, 13780−13787

Polymers with a Shish-Kebab-Like Superstructure. *Adv. Funct. Mater.* **2009**, *19*, 2759−2766.
(35) Agbolaghi, S.; Charoughchi, S.; Aghapour, S.; Abbasi, F.; Bahadori, A.; Sarvari, R. Bulk Heterojunction Photovoltaics with Improved Efficiencies Using Stem-Leaf, Shish-Kebab and Double-Fibrillar Nano-Hybrids Based on Modified Carbon Nanotubes and Poly(3-Hexylthiophene). *Sol. Energy* **2018**, *170*, 138−150.
(36) Liu, J.; Zou, J.; Zhai, L. Bottom-up Assembly of Poly(3-Hexylthiophene) on Carbon Nanotubes: 2D Building Blocks for Nanoscale Circuits. *Macromol. Rapid Commun.* **2009**, *30*, 1387−1391.
(37) Bu, L.; Pentzer, E.; Bokel, F. A.; Emrick, T.; Hayward, R. C. Growth of Polythiophene/Perylene Tetracarboxydiimide Donor/Acceptor Shish-Kebab Nanostructures by Coupled Crystal Modification. *ACS Nano* **2012**, *6*, 10924−10929.
(38) Samitsu, S.; Shimomura, T.; Heike, S.; Hashizume, T.; Ito, K. Effective Production of Poly(3-Alkylthiophene) Nanofibers by Means of Whisker Method Using Anisole Solvent: Structural, Optical, and Electrical Properties. *Macromolecules* **2008**, *41*, 8000−8010.
(39) Brinkmann, M.; Rannou, P. Effect of Molecular Weight on the Structure and Morphology of Oriented Thin Films of Regioregular Poly(3-Hexylthiophene) Grown by Directional Epitaxial Solidification. *Adv. Funct. Mater.* **2007**, *17*, 101−108.
(40) Liu, J.; Arif, M.; Zou, J.; Khondaker, S. I.; Zhai, L. Controlling Poly(3-Hexylthiophene) Crystal Dimension: Nanowhiskers and Nanoribbons. *Macromolecules* **2009**, *42*, 9390−9393.
(41) Wu, Z.; Petzold, A.; Henze, T.; Thurn-Albrecht, T.; Lohwasser, R. H.; Sommer, M.; Thelakkat, M. Temperature and Molecular Weight Dependent Hierarchical Equilibrium Structures in Semiconducting Poly(3-Hexylthiophene). *Macromolecules* **2010**, *43*, 4646−4653.
(42) Ye, G.; Liu, J.; Qiu, X.; Stäter, S.; Qiu, L.; Liu, Y.; Yang, X.; Hildner, R.; Koster, L. J. A.; Chiechi, R. C. Controlling N-Type Molecular Doping via Regiochemistry and Polarity of Pendant Groups on Low Band Gap Donor−Acceptor Copolymers. *Macromolecules* **2021**, *54*, 3886−3896.
(43) Clark, J.; Chang, J.-F.; Spano, F. C.; Friend, R. H.; Silva, C. Determining Exciton Bandwidth and Film Microstructure in Polythiophene Films Using Linear Absorption Spectroscopy. *Appl. Phys. Lett.* **2009**, *94*, No. 163306.
(44) Spano, F. C. The Spectral Signatures of Frenkel Polarons in H- and J-Aggregates. *Acc. Chem. Res.* **2010**, *43*, 429−439.
(45) Gierschner, J.; Huang, Y.-S.; Van Averbeke, B.; Cornil, J.; Friend, R. H.; Beljonne, D. Excitonic versus Electronic Couplings in Molecular Assemblies: The Importance of Non-Nearest Neighbor Interactions. *J. Chem. Phys.* **2009**, *130*, No. 044105.
(46) Spano, F. C. Modeling Disorder in Polymer Aggregates: The Optical Spectroscopy of Regioregular Poly(3-Hexylthiophene) Thin Films. *J. Chem. Phys.* **2005**, *122*, No. 234701.
(47) Reichenberger, M.; Baderschneider, S.; Kroh, D.; Grauf, S.; Köhler, J.; Hildner, R.; Köhler, A. Watching Paint Dry: The Impact of Diiodooctane on the Kinetics of Aggregate Formation in Thin Films of Poly(3-Hexylthiophene). *Macromolecules* **2016**, *49*, 6420−6430.
(48) Shaw, P. E.; Ruseckas, A.; Samuel, I. D. W. Exciton Diffusion Measurements in Poly(3-Hexylthiophene). *Adv. Mater.* **2008**, *20*, 3516−3520.
(49) Louarn, G.; Trznadel, M.; Buisson, J. P.; Laska, J.; Pron, A.; Lapkowski, M.; Lefrant, S. Raman Spectroscopic Studies of Regioregular Poly(3-Alkylthiophenes). *J. Phys. Chem. A* **1996**, *100*, 12532−12539.
(50) Spano, F. C.; Silva, C. H- and J-Aggregate Behavior in Polymeric Semiconductors. *Annu. Rev. Phys. Chem.* **2014**, *65*, 477−500.
(51) Raithel, D.; Simine, L.; Pickel, S.; Schötz, K.; Panzer, F.; Baderschneider, S.; Schiefer, D.; Lohwasser, R.; Köhler, J.; Thelakkat, M.; Sommer, M.; Köhler, A.; Rossky, P. J.; Hildner, R. Direct Observation of Backbone Planarization via Side-Chain Alignment in Single Bulky-Substituted Polythiophenes. *Proc. Natl. Acad. Sci. U.S.A.* **2018**, *115*, 2699−2704.
(52) Westenhoff, S.; Beenken, W. J. D.; Friend, R. H.; Greenham, N. C.; Yartsev, A.; Sundström, V. Anomalous Energy Transfer Dynamics Due to Torsional Relaxation in a Conjugated Polymer. *Phys. Rev. Lett.* **2006**, *97*, No. 166804.
(53) Parkinson, P.; Müller, C.; Stingelin, N.; Johnston, M. B.; Herz, L. M. Role of Ultrafast Torsional Relaxation in the Emission from Polythiophene Aggregates. *J. Phys. Chem. Lett.* **2010**, *1*, 2788−2792.
(54) Gallaher, J. K.; Chen, K.; Huff, G. S.; Prasad, S. K. K.; Gordon, K. C.; Hodgkiss, J. M. Evolution of Nonmirror Image Fluorescence Spectra in Conjugated Polymers and Oligomers. *J. Phys. Chem. Lett.* **2016**, *7*, 3307−3312.
(55) Vlaming, S. M.; Malyshev, V. A.; Eisfeld, A.; Knoester, J. Subdiffusive Exciton Motion in Systems with Heavy-Tailed Disorder. *J. Chem. Phys.* **2013**, *138*, No. 214316.

https://doi.org/10.1021/jacs.3c02117
J. Am. Chem. Soc. 2023, 145, 13780−13787

Supporting Information:

Directed Gradients in the Excited-State Energy Landscape of Poly(3-hexylthiophene) Nanofibres

[1, 2]Sebastian Stäter, [3]Felix A. Wenzel, [3]Hannes Welz, [3]Klaus Kreger,[2,4] Jürgen Köhler, [3]Hans-Werner Schmidt and [1,2]Richard Hildner*

[1] Zernike Institute for Advanced Materials, University of Groningen, Nijenborgh 4, 9747 AG Groningen, The Netherlands

[2] Spectroscopy of Soft Matter, University of Bayreuth, Universitätsstrasse 30, 95440 Bayreuth, Germany

[3] Macromolecular Chemistry I and Bavarian Polymer Institute, University of Bayreuth, Universitätsstrasse 30, 95440 Bayreuth, Germany

[4] Bavarian Polymer Institute and Bayreuther Institut für Makromolekülforschung (BIMF), University of Bayreuth, 95440 Bayreuth, Germany

S1: Materials and Methods

Materials

Poly(3-hexylthiophene), P3HT, with a molecular weight M_w = 57 kg/mol, a dispersity Đ = 2.4 as determined by size exclusion chromatography [1], and a regioregularity of >96% was purchased from Rieke and used as received. The synthesis and characterisation of compound **1** (N,N'-1,4-phenylenebis[4-pyridinecarboxamide]) was described in a recent publication [1]. Chlorobenzene was purchased from abcr (HPLC grade, 99.5%).

P3HT crystallization in solution

Recently, we highlighted the outstanding nucleation performance of the supramolecular nucleating agent (NA) consisting of N,N'-1,4-phenylenebis[4-pyridinecarboxamide] (compound **1**) in the P3HT melt [1]. To show its nucleating abilities *in solution*, we first performed temperature-dependent UV-VIS spectroscopy of 1wt% P3HT-chlorobenzene solutions with different amounts of compound **1** added. All solutions were slowly cooled from 90°C to -5°C (with a cooling rate of roughly 1 K/h), resulting in a reduction of the absorption signal in the range of 400-550 nm, where amorphous P3HT absorbs, and the emergence of spectral features around 550-650 nm, where crystalline P3HT absorbs[2]. Figure S1 shows the P3HT crystallization process by plotting the absorption of crystalline P3HT at 620nm in the temperature range from 16°C to -2°C. At elevated temperatures, the absorption at this wavelength is low because the P3HT is completely dissolved. Upon cooling, the absorbance at 620nm rises steeply due to crystallisation of P3HT. In the solution without NA (blue line), this steep increase (the crystallisation) occurs at temperatures below 3°C. The addition of the NA (at concentrations of 0.01wt%, 0.1wt%, or 1wt%, see dashed and dotted lines) increases the crystallization temperature to around 4°C, clearly indicating a nucleation effect. Therefore, the supramolecular NA based on compound **1** can be readily used to initialise the crystallisation of P3HT in solution.

We note that the dynamic nature of the measurement in figure S1 means that only crystallization processes over time intervals of minutes to hours can be detected reliably, a situation similar to dynamic DSC measurements. As shown in figure S2, nucleation at room temperature is possible as well, but requires several days of crystallization time.

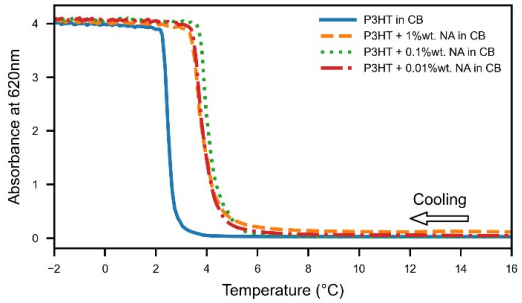

Figure S1: *Temperature-dependent absorption signal from P3HT-chlorobenzene (CB) solutions taken at a wavelength of 620 nm, corresponding to the absorption of crystalline P3HT without (blue) and with the addition of different amounts of compound* ***1*** *(orange: 1wt%, green: 0.1wt%, red: 0.01wt%). The presence of the supramolecular NA based on compound* ***1*** *increases the crystallization temperature, indicating nucleation of P3HT in the solution. All data were obtained while cooling the solutions from 90°C to -5°C.*

Preparation of NA/P3HT supramolecular superstructures

The P3HT nanofibres were grown as part of a supramolecular superstructure in a two-step protocol. At first, a solution of compound **1** in chlorobenzene at a concentration of 0.01wt% was heated to 130°C and cooled down to room temperature, resulting in the formation of ribbon-like supramolecular NA structures (**Figure S2a**). Subsequently, P3HT was added to the NA dispersion to reach a concentration of 1wt% (resulting in a concentration of 1wt% of compound **1** in relation to P3HT). The mixture was heated to 50°C, then cooled down to room temperature and aged for different times (main text: 11 days, figure S2c: 1 day, figure S9: 7 days). After ageing the superstructures were deposited on a glass coverslip by spin-coating.

Figure S2 demonstrates that the supramolecular NA enables the formation of the superstructures. Figure S2a shows a typical example of a SEM image of the ribbon-like supramolecular NA without the addition of P3HT, i.e., after the first step of the protocol. **Figure S2b** shows the SEM image of a thin film of P3HT without the addition of compound **1**. Only a grainy structure is observed, as expected for semicrystalline P3HT, and no defined structures can be found. Finally, NA/P3HT superstructures can be reliably formed by following the complete two-step protocol, as shown in **Figure S2c**. This demonstrates that the supramolecular NA is essential to achieve highly aligned, oriented and densely packed P3HT nanofibres as part of the NA/P3HT superstructures. In other words, the solvent chlorobenzene *requires* the use of the supramolecular NA to achieve nanofibre growth at room temperature.

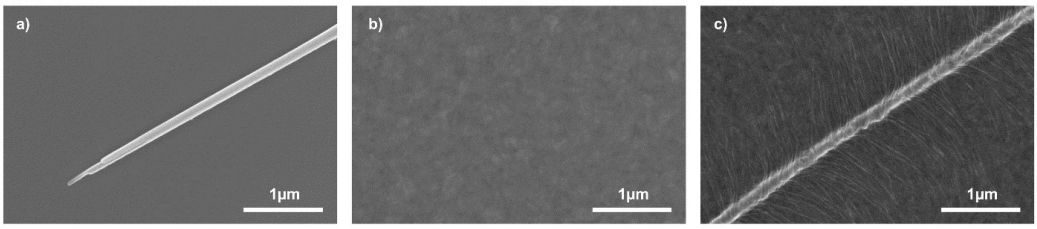

Figure S2: *Scanning electron microscopy images of (a) the supramolecular NA (without P3HT), (b) a semicrystalline P3HT film without compound* ***1****, and (c) the NA/P3HT superstructure prepared by the two-step process outlined in the text.*

Experimental setup for spatially resolved spectroscopy

For optical and spectroscopic experiments, 25µl of the NA/P3HT superstructure dispersion was spin-coated (Coros OP15, Siemens, with CONVAC 1001) onto glass slides at 1000rpm for 60s.

Optical imaging and spectroscopy were performed with a home-built inverted optical scanning microscope that can be operated in confocal and widefield mode. For PL measurements, the sample was excited with an unpolarized pulsed laser at 532 nm (NKT Fianium SC-400) through an oil-immersion objective (Olympus PlanApo, NA 1.45). The time-averaged excitation power was 40µW/cm^2 in widefield mode, and 1.5kW/cm^2 in confocal mode. Scanning was performed by moving the sample with a computer-controlled piezo stage (Piezosystem Jena Tritor 102SG). The PL signal was collected with the same objective and directed through a dichroic mirror (540nm, AHF) and a longpass filter (545nm, AHF) to suppress residual laser light. In confocal mode, the PL signal was focused onto the slit of an imaging spectrograph (Princeton Instruments IsoPlane 160, 150g/mm) and detected with a cooled emCCD camera (Andor iKon M DU934N-BR-DD, -80°C). In widefield mode, the PL signal was directed onto a sCMOS camera (pco PixelFly USB) for imaging. For brightfield microscopy and absorption spectroscopy, the sample was illuminated from above (trans-illumination) in widefield mode with a tungsten white light source (Streppel halolux 150), and filters were removed. Absorption spectra were calculated according to the Beer-Lambert-law, using reference spectra collected without a sample. The spectral resolution is limited to 0.4nm due to the pixel size of our detector. Based on the slit width of the spectrometer (100 µm), the microscope's magnification (67x), pixel size of emCCD, and hardware binning, the spatial resolution is 1µm by 1.6µm. The step size during sample scanning was, therefore, chosen to 1µm accordingly. We note that due to the nanoscopic dimensions of the investigated P3HT nanofibers (width ~20 nm), our optical experiments inevitably probe the average spectral response of several nanofibres as well as of along the nanofibres' growth direction.

Experimental details for Electron Microscopy and SAED

Scanning Electron Microscopy (SEM) measurements were performed with a Zeiss Ultra Plus (3kV, InLens detector) after sputter-coating the sample with a thin platinum layer. The relevant sample part containing a NA/P3HT superstructure was identified with an optical microscope (Zeiss Axio Imager.A2m) and transferred to the SEM using a universal sample holder for correlative optical and electron microscopy.

Selected area electron diffraction (SAED) was performed with a Zeiss / LEO EM922 Omega with an aperture diameter of 1 µm. The sample was prepared by filtering the NA/P3HT dispersion and depositing the redispersed filter cake onto a carbon-coated TEM copper grid. Finally, the samples were dried under vacuum.

S2: Structural Characterization of P3HT Nanofibres

To obtain structural information of P3HT nanofibres via TEM imaging and SAED, we deposited the final dispersion containing NA/P3HT superstructures, after filtration and redispersion, onto a carbon-coated TEM grid. In the first step, we located a NA/P3HT superstructure within the accessible squares of the grid, as shown in the overview image in **Figure S3**.

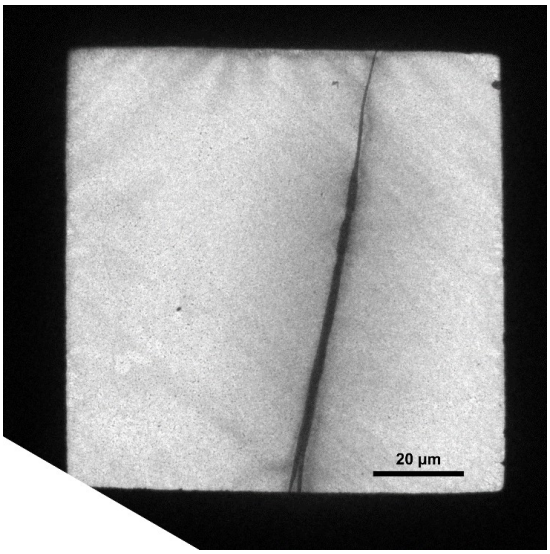

Figure S3*: Overview TEM image of the investigated NA/P3HT superstructure. The supramolecular NA lies vertically in the image. The black frame is caused by the copper grid with 100µm wide openings.*

We then followed a systematic approach to perform both imaging and selected area electron diffraction along the P3HT nanofibres that extend from the supramolecular NA: Using a high magnification and moving the sample stepwise by around 1µm, we recorded 28 TEM images and SAED patterns along the P3HT nanofibers. We started at a position close to the supramolecular NA and moved towards the ends of the P3HT nanofibres. The aperture diameter for both imaging and SAED was 1µm.

Figures S4a and **c** are TEM images of an array of P3HT nanofibres located approximately 2µm and 7µm, respectively, from the supramolecular NA. As in Fig. 1b of the main text, the P3HT-fibers are oriented horizontally in the image, parallel with respect to each other, and show a homogeneous width.

Figure S4b and **d** show the SAED patterns of the same areas as shown in the TEM images. In general, this data agrees well with known diffraction data of P3HT nanofibres with edge-on

orientation [3–5]. The horizontal axis corresponds to the long fiber axis in real space, along which P3HT is stacked in a π-π-fashion. We identify the 020 and 040 diffraction signals of P3HT at scattering vectors q = 2.6 1/nm and q = 5.3 1/nm, with the 020 signal being the strongest signal observed. This corresponds to a stacking distance d = 0.38nm along the nanofibres' long axis. In the vertical direction, we identify the 002 signal at q = 2.6 1/nm. This corresponds to a distance d = 0.38nm along the axis defined by the conjugated P3HT backbones, which is the distance between thiophene monomers along a P3HT-chain. We note that separating the 020 and 002 signals would not be possible in isotropic samples, as both signals share the same q-value.

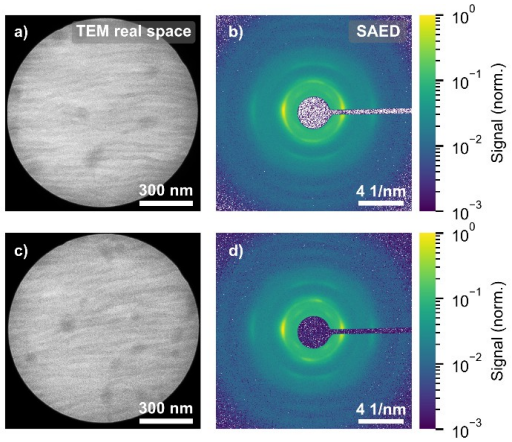

Figure S4*: Structural analysis of P3HT nanofibres within a NA/P3HT superstructure.* ***(a, c)*** *TEM images of P3HT nanofibres with parallel alignment.* ***(b, d)*** *SAED patterns of the areas in (a, c). The two investigated spots were 2µm (a, b) and 7µm (c, d) away from the supramolecular NA.*

To rule out that a variation in the π-π-stacking distance along P3HT nanofibres causes the variation of the exciton bandwidth that we present in table 1 and figure 3 of the main text, we extract the position of the 020 peak for each of the 28 SAED patterns that we recorded systematically along the P3HT nanofibres. **Figure S5** shows that, along the P3HT nanofibres, the 020 peak appears in the range between 2.64/nm and 2.59/nm, corresponding to stacking distances d of 0.379nm and 0.387nm. In other words, the stacking distance d fluctuates by approximately 2%. Using the point-dipole-approximation with parallel transition dipole moments, the interaction energy V between two chromophores is given by $V = \frac{1}{4\pi\,\epsilon_0}\frac{p_1 p_2}{r^3}$, with p_1 and p_2 being the associated transition dipole moments, and r the distance between their centres of mass. For constant magnitudes of transition dipole moments, a 2% change of the π-π-stacking distance to $r_{long} = 1.02\, r_{short}$ changes the interaction V by about 6%: $\frac{V_{long}}{V_{short}} = \frac{r_{short}^3}{r_{long}^3} = \frac{1}{1.02^3} = 0.942.$ In the main text however, we observe a decrease of the exciton bandwidth by up to 23%:

$\frac{193\,meV}{248\,meV}=0.77$, which thus cannot be explained by the observed variation of the π-π-stacking distance. We further emphasise that, compared to the point-dipole-approximation, quantum chemical calculations on polythiophene stacks predict an even lower influence of the stacking distance on the interaction energy [6], so that our estimate represents an upper bound for the distance-related change in inter-chain interactions.

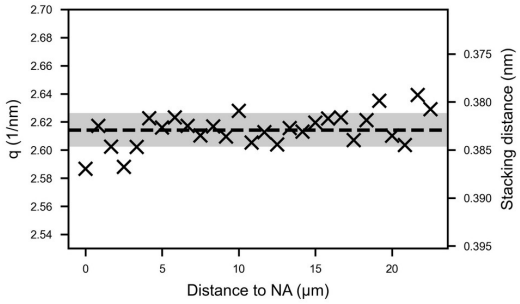

***Figure S5**: π-π-stacking distance along the long axis of P3HT nanofibres. Data points correspond to the centre of a Gaussian 2D fit to the 020 peak in SAED patterns. The black dashed line highlights the mean value, and the shaded area indicates the standard deviation.*

Our structural analysis thus confirms that the P3HT nanofibres are highly crystalline along their long axis with minimal structural variations, as evidenced by the diffraction pattern as a function of the spatial position.

S3: Analysis of Absorption Spectra

For the analysis of the absorption spectra of P3HT nanofibres, we use the Frenkel Polaron model that describes the optical properties of molecular H-aggregates in the presence of intra-molecular vibrations and that has been widely applied to conjugated polymers such as P3HT [7,8].We fit the low-energy part (1.87eV - 2.25 eV) of each absorption spectrum with equation (1), which models the energy-dependent absorption *A(E)* of crystalline P3HT as a distorted vibronic progression using a single (effective) vibrational mode:

$$\frac{A(E)}{E} \propto \sum_m \frac{S^m}{m!} \cdot \left(1 - \frac{W e^{-S}}{2 E_{vib}} G_m\right) \cdot \Gamma_m(E) \quad \text{with} \quad G_m = \sum_{n(\neq m)} \frac{S^n}{n!(n-m)} \qquad (1)$$

Here, *m* and *n* are vibrational quantum numbers, $\Gamma_m(E)$ is a Gaussian line-shape function centred around an energy E_m with $E_m = E^{Abs}_{A1} + m * E_{vib}$. The parameter E^{Abs}_{A1} describes the spectral position of the lowest-energy transition at around 2.1 eV, and E_{vib}=0.18 eV is the fixed energy of the (effective) vibrational mode (carbon-bond stretch) coupling to the electronic transition. The Huang-Rhys parameter *S* is a measure for the electron-phonon coupling strength and has to be taken from molecularly dissolved, non-interacting P3HT. Based on our recent single-molecule work, we keep the Huang-Rhys parameter constant at *S*=0.7 [9]. *W* is the free-exciton bandwidth and is related to the electronic interaction *V* between P3HT chains by *W=4V* in the nearest-neighbour approximation. For *W*=0, the vibronic progression of the non-interacting P3HT is recovered, while for $W \geq 0$, the lowest-energy peak at 2.1 eV is reduced in relative intensity. Hence, W is the main fit parameter to describe the changes in the shape of the low-energy absorption.

Related to the choice of the Huang-Rhys parameter for our analysis we note that in Raithel et al. (2016) we reported S = 0.84 for a disordered P3HT film [9]. In films, however, inter-chain interactions are always present that lead to H-type coupling between chains and thus to an overestimation of the Huang-Rhys parameter via a suppression of the 0-0 PL peak relative to the 0-1 PL peak. In Raithel et al. (2018) we reported a value of S = 0.77 derived from single chains of a thiophene-derivative (PDOPT) with bulky side groups [10]. Single PDOPT chains are more planar than single P3HT chains and show a slightly higher electron-phonon coupling to effective carbon-bond stretch modes, and thus a slightly larger S-value. Hence, we chose S = 0.7 (unpublished results).

Figure S6 shows the best fits to the absorption spectra at positions A, B, and C (see Figure 2 of the main text). We fixed the linewidth of the lowest-energy transition (around 2.1 eV) at 80% of the (variable) overall linewidth for all transitions. This is justified since the vibronic transitions in bulk P3HT are, in fact, a superposition of several closely spaced individual vibrational modes, which gives rise to additional line broadening[9,10]. The residuals (difference between the data and best fit, green curves) nicely reproduce the absorption of amorphous P3HT with a maximum absorption slightly above 2.5 eV.

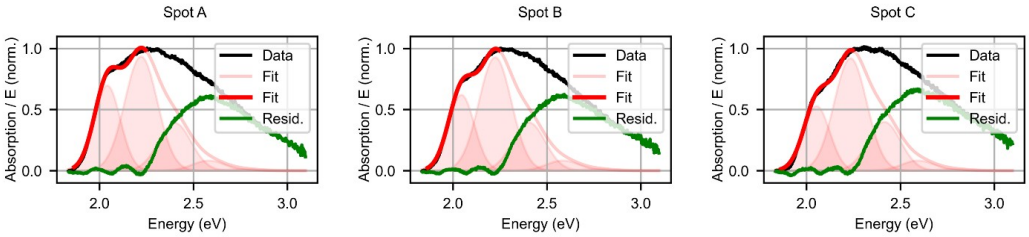

Figure S6: *Fitting of spatially resolved absorption spectra of P3HT nanofibres at spots A (left), B (centre), and C (right) from figure 2 of the main text. The black lines represent data, the red lines show the best fits to the low-energy region (1.87 eV - 2.25 eV), and the green lines are the residuals. The red-shaded areas represent the individual peaks of the vibronic progression. The residuals (green) in the high-energy region reproduce the absorption of amorphous P3HT.*

S4: Analysis of PL Spectra

PL spectra of crystalline P3HT can in principle be modelled with a distorted Franck-Condon progression[2,11]. Since our PL spectra may be affected by some reabsorption in the spectral region of the electronic 0-0 transition (1.9 to 2.0 eV), induced by a substantial optical density of around 1.0 of our sample, we refrain of a quantitative analysis of the shape of PL spectra. We note, however, that reabsorption has only a minor effect: E.g. the PL spectrum at spot C (Fig. S7) features the smallest relative intensity of the 0-0 PL peak; at the same time the corresponding absorption spectrum (Fig. S6) has the smallest absorbance in the spectral range where absorption overlaps with PL. This trend is inconsistent with reabsorption processes.

As only quantitative parameter we extract here the spectral shifts of the PL spectra as a function of position. We employ a simple peak tracking analysis. We fit the peak of the PL spectra (in the range 1.65eV to 1.80eV), which corresponds to the 0-1 transition E_{01}, with a parabola and extract its apex. **Figure S7** shows examples for this peak tracking for positions A, B, and C in Figure 2 of the main text. The position of the 0-0 PL peak is then calculated by $E^{PL}_{00} = E_{01} - E_{vib}$, with E_{vib} = 0.18 eV, see section S3.

For both the analysis of absorption and PL spectra, the employed Levenberg-Marquard fitting algorithm, directly yields the estimated standard-error of the best-fit values. For the values reported in Table 1 and figure 3 of the main text, these errors are in the range of 0.0004 eV (for E^{Abs}_{00} and E^{PL}_{00}) and 1 meV (for W). Because these errors are smaller than the symbols in figure 3, we refrain from showing error bars.

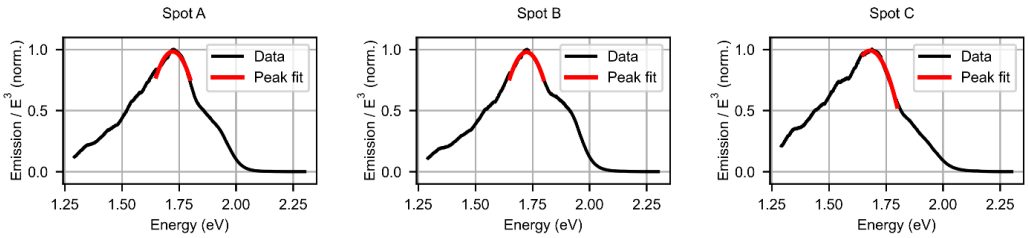

Figure S7: *Tracking of the 0-1 PL peak in spatially resolved PL spectra of P3HT nanofibres. The data correspond to the spots A (left), B (centre), and C (right) from figure 2 of the main text.*

S5: Additional energy landscape cross-sections

Analyzing the hyperspectral dataset, which covers an area of 40x40 µm² (and thus the whole area shown in figures 1a and 2a of the main text), allows us to extract the excited-state energy landscape at arbitrary positions along the direction of the supramolecular NA (perpendicularly to the P3HT nanofibres).

In analogy to Figure 3 of the main text, **Figure S8** shows the extracted shape of the *m*=0 vibronic exciton band (circles) and the position E_{PL}^{00} of the 0-0 PL peak (crosses) along additional horizontal axes, marked with the colored lines A (blue), B (orange, corresponds to the axis chosen in the main text and shown in Figure 3), and C (green) in Figure S8a. The corresponding excited-state energy landscapes, shown in Figure S8b, are essentially identical, demonstrating that the observed energy gradients are imprinted consistently into our NA/P3HT superstructure. Note that the NA/P3HT superstructure was not perfectly vertically oriented (see Figure S8a), and the energy profiles in Figure S8b have been slightly shifted horizontally so that the distance of 0 µm always corresponds to the centre of the supramolecular NA.

The dataset D (violet) corresponds to average values extracted from the violet hatched area in figure S8a. This area averages over 20 individual line scans.

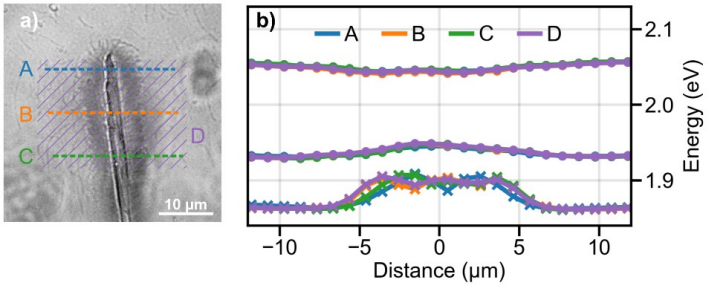

Figure S8: (a) Optical brightfield image of the NA/P3HT superstructure discussed in the main text. **(b)** Excited-state energy landscapes, analogous to figure 3b of the main text. Circles indicate the upper and lower band edge, respectively, of the *m*=0 vibronic exciton band. Crosses indicate the relaxed, lowest-energy exciton state from where emission occurs. Energy profiles were extracted along the colored lines A (blue), B (orange), and C (green) as marked in figure (a). Profile B corresponds to the data shown in figure 3b of the main text. The energy profile D (violet) corresponds to the average profile extracted from the hatched area marked with D (violet) in figure (a), corresponding to an average over 20 individual line-scans.

S6: Additional dataset

In **Figure S9**, we show the data recorded on *a different* NA/P3HT superstructure, which was prepared with a crystallisation time of 7 days. P3HT nanofibers are shorter in this sample, and the effects on free exciton bandwidth *W*, 0-0 transition energy E^{Abs}_{00}, and E^{PL}_{00} occur closer to the supramolecular NA. Yet, the gradient is again reproducibly imprinted into all nanofibres.

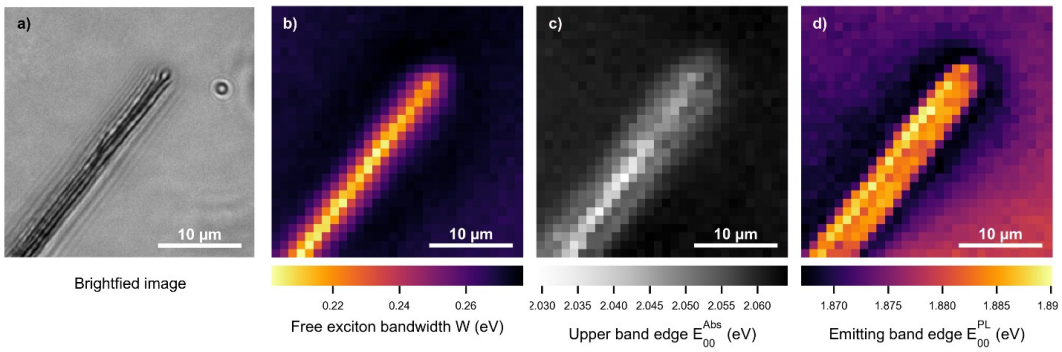

Figure S9: *Analysis of 40x40µm hyperspectral images of another NA/P3HT superstructure. a) Brightfield microscopy image. b) Map of the free exciton bandwidth W, as extracted from absorption fits. c) Map of the spectral position of the 0-0 transition* E^{Abs}_{00}*, as extracted from absorption fits. d) Map of the 0-0 position* E^{PL}_{00} *as extracted from PL fits.*

S7: References

(1) Wenzel, F. A.; Welz, H.; van der Zwan, K. P.; Stäter, S.; Kreger, K.; Hildner, R.; Senker, J.; Schmidt, H.-W. Highly Efficient Supramolecular Nucleating Agents for Poly(3-Hexylthiophene). *Macromolecules* **2022**, *55* (7), 2861–2871. https://doi.org/10.1021/acs.macromol.1c02283.

(2) Panzer, F.; Sommer, M.; Bässler, H.; Thelakkat, M.; Köhler, A. Spectroscopic Signature of Two Distinct H-Aggregate Species in Poly(3-Hexylthiophene). *Macromolecules* **2015**, *48* (5), 1543–1553. https://doi.org/10.1021/acs.macromol.5b00129.

(3) Brinkmann, M.; Wittmann, J.-C. Orientation of Regioregular Poly(3-Hexylthiophene) by Directional Solidification: A Simple Method to Reveal the Semicrystalline Structure of a Conjugated Polymer. *Advanced Materials* **2006**, *18* (7), 860–863. https://doi.org/10.1002/adma.200501838.

(4) Brinkmann, M. Structure and Morphology Control in Thin Films of Regioregular Poly(3-Hexylthiophene). *Journal of Polymer Science Part B: Polymer Physics* **2011**, *49* (17), 1218–1233. https://doi.org/10.1002/polb.22310.

(5) Liu, J.; Arif, M.; Zou, J.; Khondaker, S. I.; Zhai, L. Controlling Poly(3-Hexylthiophene) Crystal Dimension: Nanowhiskers and Nanoribbons. *Macromolecules* **2009**, *42* (24), 9390–9393. https://doi.org/10.1021/ma901955c.

(6) Gierschner, J.; Huang, Y.-S.; Van Averbeke, B.; Cornil, J.; Friend, R. H.; Beljonne, D. Excitonic versus Electronic Couplings in Molecular Assemblies: The Importance of Non-Nearest Neighbor Interactions. *The Journal of Chemical Physics* **2009**, *130* (4), 044105. https://doi.org/10.1063/1.3065267.

(7) Clark, J.; Chang, J.-F.; Spano, F. C.; Friend, R. H.; Silva, C. Determining Exciton Bandwidth and Film Microstructure in Polythiophene Films Using Linear Absorption Spectroscopy. *Applied Physics Letters* **2009**, *94* (16), 163306. https://doi.org/10.1063/1.3110904.

(8) Spano, F. C. The Spectral Signatures of Frenkel Polarons in H- and J-Aggregates. *Accounts of Chemical Research* **2010**, *43* (3), 429–439. https://doi.org/10.1021/ar900233v.

(9) Raithel, D.; Baderschneider, S.; de Queiroz, T. B.; Lohwasser, R.; Köhler, J.; Thelakkat, M.; Kümmel, S.; Hildner, R. Emitting Species of Poly(3-Hexylthiophene): From Single, Isolated Chains to Bulk. *Macromolecules* **2016**, *49* (24), 9553–9560. https://doi.org/10.1021/acs.macromol.6b02077.

(10) Raithel, D.; Simine, L.; Pickel, S.; Schötz, K.; Panzer, F.; Baderschneider, S.; Schiefer, D.; Lohwasser, R.; Köhler, J.; Thelakkat, M.; Sommer, M.; Köhler, A.; Rossky, P. J.; Hildner, R. Direct Observation of Backbone Planarization via Side-Chain Alignment in Single Bulky-Substituted Polythiophenes. *Proceedings of the National Academy of Sciences* **2018**, *115* (11), 2699–2704. https://doi.org/10.1073/pnas.1719303115.

(11) Parkinson, P.; Müller, C.; Stingelin, N.; Johnston, M. B.; Herz, L. M. Role of Ultrafast Torsional Relaxation in the Emission from Polythiophene Aggregates. *J. Phys. Chem. Lett.* **2010**, *1* (19), 2788–2792. https://doi.org/10.1021/jz101026g.

4.6 Publication V: Micrometer-Long Highly Oriented P3HT Nanofibers in Isolated Hierarchical Superstructures

Macromolecules

pubs.acs.org/Macromolecules Article

Isolated Hierarchical Superstructures with Highly Oriented P3HT Nanofibers

Felix A. Wenzel, Sebastian Stäter, Padraic O'Reilly, Klaus Kreger, Jürgen Köhler, Richard Hildner, and Hans-Werner Schmidt*

Cite This: *Macromolecules* 2024, 57, 10389−10398 Read Online

ACCESS | Metrics & More | Article Recommendations | Supporting Information

ABSTRACT: The preparation of supramolecular mesoscale structures with high intrinsic order and orientation based on π-conjugated systems is of fundamental interest for studying their photophysical characteristics as well as for potential applications in (nano)photonics. However, the preparation, isolation and transfer of individual structures to substrates without compromising their structural integrity is challenging. Here we report on the controlled formation of hierarchical superstructures based on poly(3-hexylthiophene) (P3HT) comprising highly ordered and oriented P3HT nanofibers with lengths of up to 20 μm via a two-step self-assembly process. In the first step, we prepare defined supramolecular ribbons of *N*,*N*′-1,4-phenylenebis[4-pyridinecarboxamide]. In the second step, these ribbons act as efficient nucleation sites for the transcrystallization of P3HT into μm-long nanofibers from solution. The resulting shish-kebab-like superstructures can be purified and deposited on substrates without compromising their structural integrity. The densely packed and well-arranged P3HT nanofibers within the isolated superstructures feature a high orientational order parameter close to one up to a distance of 15 μm away from the initial nucleation sites. A systematic variation of photoluminescence spectra along the P3HT nanofibers in isolated superstructures indicates an increasing defect density toward the nanofiber end due to fractionation during growth. We anticipate that these findings can be transferred to designing and realizing superstructures as components for nanophotonic devices or light-harvesting antennae.

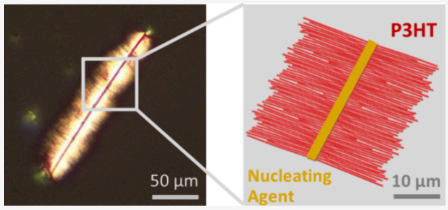

1. INTRODUCTION

Poly(3-hexylthiophene) (P3HT) is a prototypical and one of the best studied conjugated polymers.[1,2] The optoelectronic characteristics of P3HT films are largely dominated by their semicrystalline morphology, i.e., by the interplay between the ordered and highly anisotropic crystalline domains and the (interconnected) isotropic amorphous phases.[3−5] Manipulation of the final morphology and thus solid-state properties not only depends on the polymer structure, including molecular weight, dispersity and structural defects, but also on the processing conditions and methods.[6−9] Early findings demonstrated that P3HT self-assembles from solution into randomly distributed crystalline nanofibers formed by $\pi-\pi$ stacking of the polymer backbones.[10] Oriented and aligned P3HT-nanofibers in thin film architectures were realized later by various processing techniques such as brush coating,[11] preformed P3HT-nanofibers under shear flow[12] or spin-coating,[13] melt-processing under shear forces such as strain alignment,[14] friction transfer technique[15,16] and high temperature rubbing of thin films.[6,17,18] These large-scale processing techniques resulting in oriented P3HT nanofibers have been proven to be beneficial for device performance of, e.g., OFETs and OPVs.[6,11,19,20]

Another way to obtain and study ordered P3HT nanofibers on the mesoscale is epitaxial crystallization of P3HT grown in a directional manner away from nanostructures. Such mesoscale objects, which are also referred to as (hybrid) shish-kebab-like superstructures, offer an interesting perspective for the development of light-harvesting antenna systems, nanophotonic devices[21] and nanoscale electronics.[22] In a typical procedure, dissolved P3HT is transcrystallized from solid-state objects based on nonpolar species, providing an epitaxial surface with weak van-der-Waals interactions. For instance, Brinkmann et al. demonstrated the use of solid 1,3,5-trichlorobenzene (TCB) fibers, which leads initially to thread-like growth of P3HT fibers along the TCB fiber. On this P3HT-TCB fiber ("shish") densely packed small P3HT nanofibers ("kebab") grow perpendicularly from the 'shish' with lengths of some hundreds of nanometers resembling a shish-kebab-like superstructure.[23] Liu et al. made use of single and multiwall carbon nanotubes (CNTs) as heterogeneous nucleating agents for the transcrystallization of P3HT.[22] They found that P3HT nanofibers with lengths of several hundreds

Received: July 12, 2024
Revised: October 15, 2024
Accepted: October 23, 2024
Published: October 30, 2024

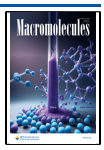

https://doi.org/10.1021/acs.macromol.4c01618
Macromolecules 2024, 57, 10389−10398

of nanometers, but with less dense packing, grow perpendicularly from the CNTs. Later on, Zhang et al. reported the formation of hybrid shish-kebab-like superstructures using nanofibers of 1,2,3,4-bis(*p*-methylbenzylidene) sorbitol (MDBS) as heterogeneous nucleating agent in solution of P3HT.[24] Bu et al. showed an in situ two-step process based on self-assembled nanofibers of a perylene tetracarboxydiimide (PDI) derivative and the subsequent formation of P3HT nanofibers on the PDI-fibers.[25] A similar approach was reported by Li et al. using *N*,*N*-(dicyclopentyl)perylene-3,4,9,10-tetracarboxylic diimide (C5-PTCDI) which forms nanobelts from solution. These nanobelts were subsequently added to a solution of P3HT resulting in shish-kebab-like superstructures.[26] Apart from such templated or heterogeneous nucleation-based approaches, P3HT superstructures with similar morphologies can also be realized by using solvent mixtures[27] or P3HT and P3HT block copolymers,[28] where initially formed P3HT nanofibers act as nucleus for branched small P3HT nanofibers.

Recently, we have demonstrated that supramolecular fibers or ribbon-like objects of *N*,*N*′-1,4-phenylenebis[4-pyridinecarboxamide] (**1**) induce the crystallization of P3HT in the polymer melt with nucleation efficiencies up to 98%.[29] This supramolecular material is composed of a central benzene unit and substituted in 1,4-position with two amide groups and two peripheral 4-pyridene moieties. The amide groups of the C_2-symmetric building blocks form two strands of hydrogen bonds, whereas the resulting ribbon-like objects provide an epitaxial match. More importantly, the extraordinary nucleating efficiency is attributed to the peripheral pyridine moieties, which enable attractive interactions with every second thiophene repeating unit of the extended P3HT backbone.[29] Ultimately, the P3HT nucleation leads to the formation of superstructures based on the ribbon-like nucleating agents and P3HT nanofibers. Since structure formation is initiated by the polymer crystallization from the P3HT melt upon cooling, numerous and overlapping hierarchical superstructures exist within a P3HT film at room temperature. These embedded P3HT superstructures cannot be easily isolated anymore, rendering detailed studies and exploitation of individual superstructures unfeasible. Later, we have therefore developed a processing approach from solution, that has allowed for the preparation of separated superstructures featuring unique photophysical properties.[30] In particular, we have demonstrated by hyperspectral imaging that a continuous gradient in the excited-state energy landscape is present, i.e., the lowest-energy excited state continuously shifts toward lower energy by more than thermal energy at room temperature when moving along the growth direction of the P3HT nanofibers. This gradient is due to defect fractionation, which results in the incorporation of an increasing number of defects (regio and chain-end defects) into the nanofibers during growth. These superstructures, however, are still surrounded by a P3HT film hampering detailed structural investigations.

Here, we report on a comprehensive investigation of the preparation and isolation of hierarchical superstructures comprising a central supramolecular ribbon based on *N*,*N*′-1,4-phenylenebis[4-pyridinecarboxamide] (**1**) and perpendicularly oriented P3HT nanofibers with lengths of up to 20 μm (see Figure 1), using a two-step self-assembly approach. The first step comprises a seeded growth process of **1** in chlorobenzene yielding defined supramolecular ribbons. The second step includes the addition of dissolved P3HT, which

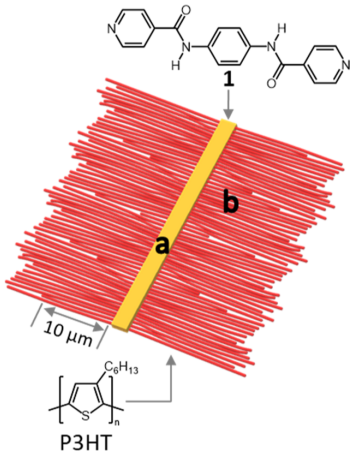

Figure 1. Schematic representation of hierarchical superstructures based on supramolecular ribbons (yellow, a) of *N*,*N*′-1,4-phenylenebis[4-pyridinecarboxamide] (**1**) with perpendicularly oriented, micrometer-long nanofibers (red, b) of poly(3-hexylthiophene) (P3HT).

transcrystallizes from the epitaxial surface of ribbons of **1**. Aging of the dispersion allows for the controlled preparation of defined superstructures with densely packed and highly oriented μm-long P3HT nanofibers. These superstructures can be isolated by removing the remaining dissolved P3HT without significantly dissolving the aggregated P3HT nanofibers. The superstructures can be transferred to substrates without introducing severe structural damage. We find that the P3HT nanofibers feature a nearly perfect orientational order over distances of more than 15 μm.

2. EXPERIMENTAL SECTION

2.1. Materials. Chlorobenzene was received from abcr (HPLC grade, 99.5%). Regioregular P3HT (RMI-001-EE) with a regioregularity of >96% was purchased from Rieke Metals and used as received. The average molecular weight M_w of P3HT was determined by size exclusion chromatography and yielded 57 kg mol^{-1} with a dispersity $Đ$ of 2.4.[29] *N*,*N*′-1,4-phenylenebis[4-pyridinecarboxamide] (**1**) was synthesized as described previously.[29]

2.2. Two-Step Self-Assembly Procedure and Superstructure Purification. In a typical procedure, the first step comprises dispersion of 0.005 wt % (50 ppm) of **1** in chlorobenzene and sonication for 15 min. The dispersion was subsequently heated to 125 °C using a Biotage Initiator+ Microwave System, kept for 5 min at 125 °C and subsequently cooled to room temperature yielding a dispersion with defined supramolecular ribbons.

In the second step, 1 wt % (10,000 ppm) of P3HT relative to chlorobenzene was added to the dispersion. P3HT is dissolved by heating the dispersion to about 50 °C under stirring at 300 rpm. The mixture was cooled to room temperature and aged for a given time from 4 h up to 50 days to yield a dispersion with P3HT superstructures.

For the purification procedure, 100 μL of dispersions containing P3HT superstructures were passed through a mountable syringe filter (Teflon, 0.2 μm pore size) to remove most of the dissolved P3HT. Subsequently, the filter was washed with 10 mL of chlorobenzene. Already after a few mL of washing a colorless washing solution was observed indicating the removal of the remaining dissolved P3HT. The Teflon filter features a dark-brownish color indicating the presence of superstructures. The deposited superstructures on the filter were redispersed in 2 mL of chlorobenzene. This dispersion was

https://doi.org/10.1021/acs.macromol.4c01618
Macromolecules 2024, 57, 10389−10398

then stored at room temperature before it was transferred to substrates by drop casting.

2.3. Polarized Light Microscopy. Polarized light microscopy was performed on a Nikon Invers Diaphot TMD 300 optical microscope. A drop of a dispersion at different stages of the superstructure preparation procedure was cast on a glass slide and dried under ambient conditions. Optical micrographs of such samples were recorded using a Nikon DS-Ri2 digital camera and Nikon ACT-1 software. Different colors in polarization microscopy images result from different thicknesses of the samples and the required changes of the brightness of the light source.

2.4. Absorption Spectroscopy. Absorption spectroscopy was performed on a Jasco V670. All measurements were performed in HPLC-grade chlorobenzene. Dispersions of **1** were investigated in the concentration range of 10−30 ppm. Using an ETC-815 heating device, the samples were heated to 103 °C and cooled to −6 °C with a cooling rate of 2 °C h^{-1}. Dispersions of superstructures before purification were diluted with chlorobenzene by a factor of 100 prior to measurement.

2.5. Electron Microscopy. Scanning electron microscopy (SEM) was conducted using a Fei Quanta FEG 250 (Zeiss). For sample preparation, 50 μL of a dispersion was spin-coated onto silicon wafers using a Coros OP15 (Siemens) with a CONVAC 1001 (1000 rpm for 60 s) and dried overnight under vacuum. The samples were then sputtered with a 2 nm thick layer of platinum using a Sputter Coater 208HR (Cressington). In addition, scanning transmission electron microscopy (STEM) was performed with the same instrument. Samples for STEM were prepared by drop casting 10 μL of a dispersion on copper grids coated with a carbon foil.

Transmission electron microscopy (TEM) and selected area electron diffraction (SAED) were performed using a Zeiss/LEO EM922 Omega and a JEOL JEM-2200FS energy filtering transmission electron microscope (EFTEM). Both systems were operated at 200 kV in bright-field and diffraction mode. For the zero-loss filtered micrographs ($\Delta E \sim 0$ eV) a bottom-mounted camera system was utilized. For the Zeiss microscope a CCD camera system (Ultrascan 1000, Gatan) and for the JEOL microscope a CMOS camera system (OneView, Gatan) were used. For image acquisition and processing Digital Micrograph DM 1.9 was used for both systems. For sample preparation, dispersions of the redispersed superstructures were spin-coated onto the TEM grids and dried overnight in vacuum.

2.6. Photoinduced Force IR Spectroscopy. Photoinduced Force Microscopy (PiFM) combines noncontact bimodal Atomic Force Microscopy (AFM) with a light source to simultaneously acquire topographical and chemical information with sub-5-nm resolution.[31] A Vista One microscope (Molecular Vista, USA), using a 300 kHz NCH-Au cantilever (Nanosensors, Switzerland), was coupled with a LaserTune mid-IR QCL laser (Block Engineering, USA) with a tuning range of 1850−800 cm^{-1} and spectral resolution of 0.5 cm^{-1}. A parabolic mirror with a focal length of 3 mm was used to focus the laser at the AFM tip−sample interface, resulting in an averaged power of 0.1 mW at the surface. Each PiFM and topography image was acquired with a scan speed of 0.89 Hz and 256 × 256 resolution; spectra were recorded with a 15 s sweep time. SurfaceWorks (Molecular Vista, USA) was used for all PiFM-related data analysis.

2.7. Spatially Resolved Photoluminescence Spectroscopy. Spatially resolved photoluminescence (PL) spectroscopy was performed with a home-built setup as described elsewhere.[30] The samples were prepared as described above for electron microscopy on a TEM grid. The TEM grid was placed on a glass coverslip and mounted on a piezo stage (Piezosystem Jena Tritor 102SG) that allows to scan an 80 × 80 μm^2 area on the sample. Excitation was performed in widefield mode through an oil immersion objective (Olympus PlanApo, NA 1.45) with a pulsed laser at 532 nm (PicoQuant LDH-P-FA-530L), which was circularly polarized by a quarter-wave plate and attenuated to a power of 2.1 μW. The PL signal was collected by the same objective, passed a dichroic mirror (540 nm, AHF) and a long-pass filter (545 nm, AHF) to suppress residual laser light. The signal was detected by a cooled emCCD camera (Andor iXon DV887-DCS-BV, −80 °C) attached to an imaging spectrograph (Princeton Instruments IsoPlane 160, 50 g/mm). The spectral resolution is 0.4 nm, limited by the pixel size of our detector. To avoid photobleaching during acquisition of the PL spectra, we moved the sample with a rather large step size of 1 μm between subsequent spectra using the piezo stage.

3. RESULTS AND DISCUSSION

Figure 2 depicts the schematic procedure for the preparation and isolation of hierarchical superstructures with oriented

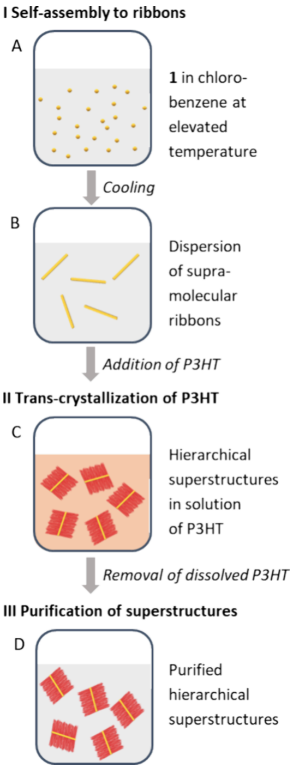

Figure 2. Schematic illustration of the controlled two-step self-assembly and purification processes to obtain isolated hierarchical superstructures with oriented P3HT nanofibers. *N*,*N*′-1,4-Phenylenebis[4-pyridinecarboxamide] (**1**) in chlorobenzene at elevated temperatures (A) is cooled to room temperature, resulting in the self-assembly into well-defined supramolecular ribbons (B). After the addition of P3HT, transcrystallization of P3HT on the surface of the supramolecular ribbons to defined P3HT nanofibers occurs, leading to hierarchical superstructures in a solution containing dissolved P3HT (C). Dissolved P3HT is removed by filtration and the purified hierarchical superstructures can be dispersed in chlorobenzene (D).

P3HT nanofibers comprising two self-assembly steps followed by a purification step. The first step is a seeded growth approach for the controlled formation of defined ribbon-like supramolecular structures of *N*,*N*′-1,4-phenylenebis[4-pyridinecarboxamide] (**1**) in chlorobenzene. Upon cooling a dispersion with seeds, supramolecular ribbons are formed (Figure 2A,B). In the second step we dissolve P3HT in the dispersion with the supramolecular ribbons at elevated temperature. Chlorobenzene is a good solvent for P3HT, in

https://doi.org/10.1021/acs.macromol.4c01618
Macromolecules 2024, 57, 10389−10398

which the polymer remains dissolved, and homonucleation and aggregation of the polymer is largely prevented at ambient conditions. Thus, upon cooling the dispersion with P3HT to room temperature, transcrystallization of P3HT is only initiated on the epitaxial surface of the ribbons (Figure 2C). Since the number of the used seeds is very small, only a small fraction of P3HT is consumed during superstructure formation and the remaining dissolved P3HT in chlorobenzene must be removed in the subsequent purification step by filtration. Redispersion of the hierarchical superstructures in chlorobenzene (Figure 2D) allows for investigations of the purified superstructures in the dispersed form or after the transfer to substrates in an isolated form.

In the following, we describe all steps including the controlled self-assembly to supramolecular ribbons (I), transcrystallization of P3HT to superstructures (II) and the purification of the superstructures (III), which we used for detailed structural and photophysical studies.

3.1. Controlled Self-Assembly of *N*,*N*′-1,4-Phenylenebis[4-Pyridinecarboxamide] (1). The first step involves self-assembly studies of **1** in solution to obtain well-defined nanostructures under a given set of conditions. To gain insight into the mechanistic aspects of the self-assembly process of **1**, we investigated the temperature-dependent aggregation behavior by absorption spectroscopy in the concentration range between 10 and 30 ppm in chlorobenzene (see Section S1.1 of the Supporting Information). At these concentrations, **1** is molecularly dissolved at temperatures of ∼100 °C, as shown by the absorption of the molecular building block at around 320 nm. Upon cooling, a steady decrease of the absorbance at 320 nm is observed due to the formation of aggregates (Figure S1), from which we calculate the temperature-dependent degree of aggregation α. At a concentration of 20 ppm, self-assembly occurs mainly between 95 and 30 °C (Figure 3A). Fitting the temperature-dependence of α with an Arrhenius-type function[32] yields a cooperative self-assembly mechanism for the aggregation of **1** with an enthalpy of aggregation H_{agg} of −58.8 kJ/mol and a critical temperature T_m of 94 °C (Figure S2A). Experiments performed with the different concentrations of 10, 20−30 ppm show the same trend, with the critical temperature being shifted to higher values with increasing concentration. For the degree of aggregation α at a concentration of 30 ppm and at elevated temperature, a plateau near zero is hardly achievable, indicating that the solubility limit is reached under these conditions (Figure S2B). This finding shows that at higher concentrations insoluble ribbon-like objects (seeds) remain at higher temperatures.

The presence of seeds at higher concentrations at elevated temperature together with a cooperative mechanism during the self-assembly process allows us to gain control over formation and size of ribbon-like objects of **1** via a temperature-induced seeded growth approach. In general, the seeded growth approach is a well-established method,[33,34] in which the seeds are added to a solution of molecularly dissolved building blocks and the self-assembly is then initiated. Here we control the number of seeds by using a selected maximum temperature at concentrations of more than 30 ppm. The remaining number of seeds determines the number of aggregates during the self-assembly in a nucleation-elongation-type process and therefore the average size of the formed structures. We used dispersions with a concentration of 50 ppm of **1**, heated them to selected maximum temperatures, such as 110, 115, 120, or

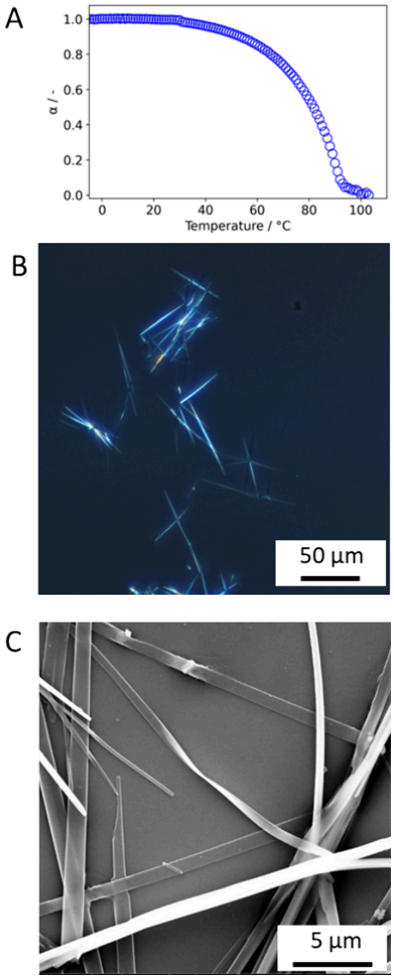

Figure 3. Self-assembly of **1** into well-defined ribbon-like supramolecular structures. (A) Temperature-dependent degree of aggregation α of **1** determined by absorption spectroscopy for a concentration of 20 ppm. (B) Polarized light microscopy image of elongated structures of **1** with average lengths of about 50 μm. The sample was prepared by drop-casting a dispersion (conc.: 50 ppm) on a glass slide. (C) Scanning electron microscopy (SEM) image of a sample drop-cast from dispersion (conc.: 50 ppm) on a silicon wafer revealing a ribbon-like structure of **1** with widths in the μm-range.

125 °C, and subsequently cooled them to room temperature (see Section S1.2 of the Supporting Information). Analysis of the supramolecular objects drop-cast on glass substrates using polarized optical microscopy revealed that the objects' length increases from about 7 to 50 μm when the maximum temperature is increased from 110 to 125 °C. At temperatures higher than 125 °C, the 50 ppm dispersion of **1** is completely dissolved resulting in supramolecular structures initiated by homogeneous nucleation. Figure 3B shows as an example a microscopy image of structures obtained from dispersions initially heated to 125 °C featuring an average length of (52 ± 25) μm. Details of the supramolecular structures were visualized by scanning electron microscopy (Figure 3C and Section S1.3 of the Supporting Information), as well as by

https://doi.org/10.1021/acs.macromol.4c01618
Macromolecules 2024, 57, 10389−10398

AFM studies (Figure S5), both clearly indicating a ribbon-like morphology with widths in the μm range and below, and heights in the range of a few 100 nm.

3.2. Controlled Formation of P3HT Superstructures in Solution. Using 50 ppm dispersions of **1** in chlorobenzene, we investigated the controlled formation of superstructures based on μm-scaled supramolecular ribbons and transcrystallized nanofibers of P3HT. At low concentration the supramolecular objects with their size on the μm scale lead to only a limited number of nucleation sites, which will be efficiently occupied by P3HT. This small number of superstructures therefore enables the investigation of individual, well-separated shish-kebab-like structures. To prepare these superstructures, we dissolved 1 wt % of P3HT in such dispersions of **1** at a temperature of 50 °C, since only fully dissolved polymer chains are mobile enough to contribute to the transcrystallization process. We note that chlorobenzene is a good solvent for P3HT hampering spontaneous P3HT crystallization at this temperature as well as at room temperature.[35] Also, a short exposure to 50 °C does not dissolve the supramolecular ribbons. Consequently, at room temperature P3HT crystallization is preferably initiated at the ribbons' surface and the length of the transcrystallized P3HT nanofibers can be controlled by aging. Figure 4A shows a SEM image of a drop-cast sample obtained after 28 days of aging. The superstructure comprises a central ribbon of **1**, which is densely and symmetrically surrounded by uniformly grown P3HT nanofibers with lengths of about 20 μm. The nanofibers are perpendicularly grown away from the epitaxial surface of the supramolecular ribbon in a highly ordered manner. Compound **1** crystallizes in a monoclinic unit cell in the space group P_21/c. It exhibits a high lattice matching for P3HT, combined with attractive interactions due to the pyridine groups along the crystallographic *b*-axis, which corresponds to the lateral ribbon direction. Thus, P3HT nucleation is only initiated at the two opposing sides of the ribbon.[29] The SEM image also indicates that the superstructure is surrounded by a P3HT film due to the large excess of P3HT in the dispersion. These findings are confirmed by polarized light microscopy images as depicted in Figure 4B that shows a central ribbon of **1** and two about 20 μm wide fiber mats with a strong homogeneous birefringence resulting from densely aligned P3HT nanofibers. The P3HT superstructures are surrounded by a semicrystalline P3HT film with less strong birefringence, caused by the amorphous part as well as the randomly distributed small-sized crystals in the film. The zones without birefringence separating the superstructures and film are probably related to an excess of amorphous P3HT at this interface.

To demonstrate that prolonged aging enables control over the length of the P3HT nanofibers, we performed nucleation experiments in solution with varying aging time from 4 to 24 h to 7 days. SEM images of drop-cast samples of the differently aged dispersions reveal in all cases highly aligned and uniformly grown P3HT nanofibers but with increasing fiber lengths from 0.6 to 1.5 to 14.5 μm (see Section S2.1 of the Supporting Information). This clear trend, i.e., the increasing length of the P3HT fibers during aging in solution, indicates that drying effects do not play a significant role.

3.3. Purification of Superstructures. To investigate structural features, such as order and degree of orientation of the P3HT nanofibers, purification and isolation steps of individual superstructures are essential. For instance, in a dispersion with superstructures that is aged for 50 d, only a small fraction of less than 5% of the overall amount of P3HT in the dispersion is consumed for the transcrystallization process into "kebab"-like nanofibers (see Section S2.2 of the Supporting Information). Equally important, the use of chlorobenzene prevents homonucleation and aggregation of P3HT at ambient conditions, so that aggregated P3HT is mostly present as part of the superstructures in the dispersion. We therefore developed a straightforward purification and isolation procedure. The dispersion with the superstructures was filtered through a standard Teflon filter with 0.2 μm pores, whereby the much larger superstructures are deposited on the filter in contrast to the dissolved P3HT. Washing with chlorobenzene efficiently removes the dissolved P3HT from the superstructures, as shown by the increasingly colorless solution. Subsequently, the purified superstructures on the filter can be dispersed in clean chlorobenzene. Although neat P3HT is soluble in chlorobenzene at room temperature, the

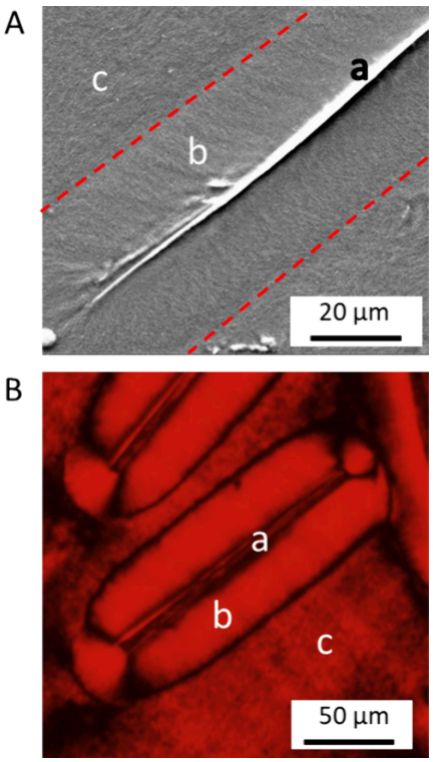

Figure 4. Hierarchical superstructures after transcrystallization of a 1 wt % solution of P3HT in a 50 ppm dispersion of **1** in chlorobenzene aged for 28 days. (A) SEM micrograph of a drop-cast superstructure on a silicon wafer revealing a central supramolecular ribbon of **1** (a) with highly oriented P3HT nanofibers with a length of about 20 μm (b) transcrystallized perpendicularly from the ribbon. Superstructure is embedded in a film of semicrystalline P3HT (c). (B) Polarized light microscopy image of identically prepared superstructures on a glass slide showing the same features and dimensions as found in the SEM micrograph. Birefringence is visible for the central supramolecular ribbons of **1** (a), which is symmetrically surrounded by highly birefringent fiber mats of aligned P3HT nanofibers (b) of the superstructure. The birefringent surrounding area demonstrates the presence of a semicrystalline film of P3HT (c).

https://doi.org/10.1021/acs.macromol.4c01618
Macromolecules 2024, 57, 10389−10398

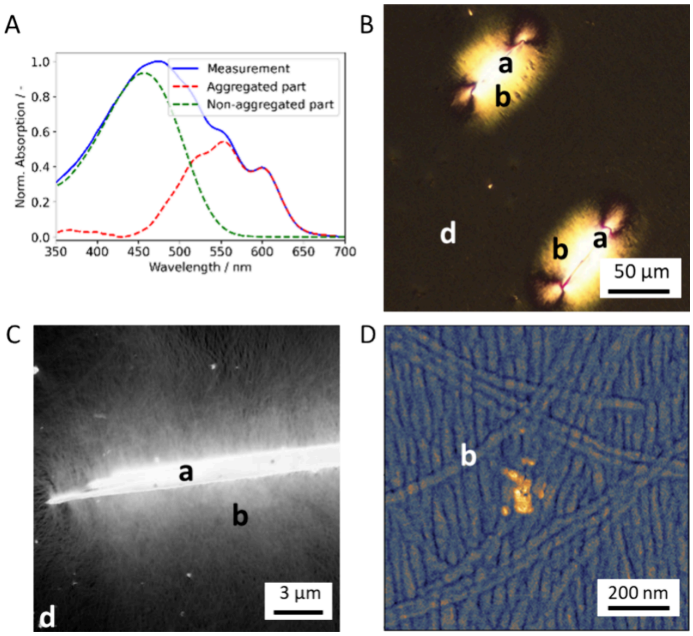

Figure 5. Purified and isolated superstructures after trans-crystallization of a 1 wt % solution of P3HT in a 50 ppm dispersion of **1** in chlorobenzene aged for 50 d. (A) Absorption spectrum of the dispersion of purified superstructures (blue) together with the absorption of dissolved P3HT (green) in chlorobenzene and the difference between both spectra (red), reflecting only the aggregated fraction of P3HT within nanofibers. (B) Polarized light microscopy image of isolated superstructures on a glass slide showing strong birefringence from the supramolecular ribbon (a) and the P3HT nanofibers (b). Almost no other birefringence (d) can be observed indicating the absence of a thin semicrystalline film of P3HT. The width of the isolated superstructure is similar to the superstructure shown in Figure 4B. (C) Scanning transmission electron microscopy (STEM) image of an isolated superstructure reveals densely packed P3HT nanofibers (b) perpendicularly oriented from the central supramolecular ribbon (a). (D) PiFM image of densely packed P3HT nanofibers about 400 nm away from the ribbon of **1**, highlighting the absorption at 1470 cm^{-1} (the absorption increases from blue to orange).

highly aggregated P3HT nanofibers in the superstructures are stable under these conditions. This stability in chlorobenzene after purification is demonstrated by absorption spectroscopy, which remains largely unchanged when monitored over a period of 60 min (see Figure S8A of the Supporting Information). The absorption spectra of purified and dispersed superstructures are shown in Figures 5A and S8B of the Supporting Information. As reference, we used a solution of homogeneously dissolved P3HT in chlorobenzene (Figure 5A, green), which features its well-known broad and structureless absorption with a maximum at 450 nm.[3] The absorption spectrum of the purified superstructures is significantly broader with a structureless absorption around 450 nm and structured shoulders at longer wavelength that result from absorption of aggregated P3HT in nanofibers.[36] We note that the absorption around 450 nm stems from a small fraction of residual molecularly dissolved P3HT chains and from amorphous interlamellar P3HT chains between nanofibers, which both share the same spectral characteristics.[30] To retrieve the spectrum of aggregated P3HT in the superstructures (Figure 5A, red), we can therefore scale the absorption of the dissolved P3HT (green) to the short-wavelength tail of the absorption spectrum of the sample containing the superstructures (blue) and subtract it. Integrating and weighting the spectra of dissolved/amorphous and aggregated P3HT according to their different oscillator strengths (see also Section 2.2 of the Supporting Information), we find for the isolated superstructures that they comprise about 30% aggregated P3HT and 70% amorphous P3HT. Thus, the fraction of the aggregated part is at least increased by a factor of 6 with respect to the nonpurified samples. Moreover, these values are reasonably close to those of thin semicrystalline P3HT films.[37] This strongly indicates that a large part of the remaining dissolved P3HT is removed by the purification and dispersion step.

We can now transfer the superstructures from dispersion to substrates and characterize individual isolated species. Figure 5B shows a representative polarized light microscopy image of a drop-cast dispersion on a glass slide. In contrast to Figure 4B, we now find a significantly increased contrast in birefringence between the P3HT superstructures and the background demonstrating that barely P3HT film is present. It was found that the length of the P3HT nanofibers is about 20 μm growing from the central ribbon. Notably, the superstructures' shape and the length of the P3HT nanofibers is similar to that of the structures embedded in the P3HT film, which also indicates that the P3HT-kebab fibers remain intact in the chlorobenzene dispersion. Since there are only isolated P3HT superstructures present, we were able to perform scanning transmission electron microscopy (STEM) to visualize the central supramolecular ribbon of **1** and dense P3HT nanofibers (Figure 5C). The very dense packing and alignment of P3HT nanofibers are further visualized by the PiFM image in Figure 5D, showing the absorption at 1470 cm^{-1} due to aromatic C=C vibrations of the thiophene backbone.[38,39] Full IR spectra taken from the ribbon of **1** and from P3HT nanofibers are shown in Figure S9 in the Supporting Information. The STEM

https://doi.org/10.1021/acs.macromol.4c01618
Macromolecules 2024, 57, 10389−10398

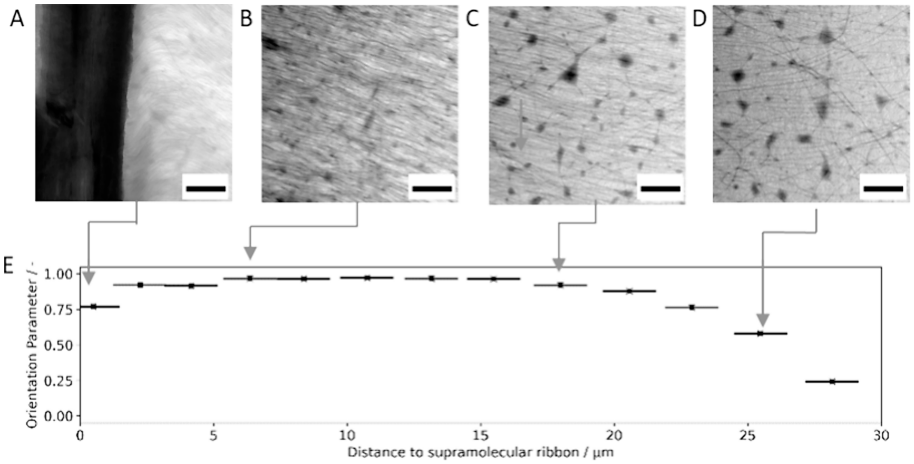

Figure 6. Spatially resolved transmission electron microscopy shows a high orientation of the P3HT nanofibers in isolated superstructures. (A–D) Representative TEM images at different positions relative to the central ribbon of **1** (black feature to the left in A). The scale bar corresponds to 0.5 μm. (E) The orientational order parameter at different distance to the supramolecular ribbon for the nanofibers extracted from a series of TEM images as for instance shown in A–D. Orientational order parameter was determined using an algorithm by Persson et al.[40] (also see Figures S14 and S15).

image indicates that the P3HT nanofibers are more densely packed close to the central ribbon and the high degree of orientation of the P3HT nanofibers is clearly visible and largely preserved even at a distance of about 10 μm from the ribbon. Note that the P3HT nanofibers also feature the same length as shown in Figure 4A.

3.4. Structural Order and Orientation of P3HT Nanofibers in Isolated Superstructures. Isolated P3HT superstructures allow us to study their structural features without deterioration by surrounding P3HT films using transmission electron microscopy (TEM) and selective area electron diffraction (SAED). First, we take a closer look at selected positions of the superstructures, i.e., the supramolecular ribbon, the interface of the ribbon and P3HT nanofibers, and P3HT nanofibers alone (see Section S3.3 of the Supporting Information). The SAED of the ribbon features a series of sharp reflexes demonstrating the crystalline nature of the supramolecular ribbon of **1** (Figure S10).[29] At the interface of the ribbon of **1** to the P3HT nanofibers we find the same sharp reflexes of **1** in addition to the typical broader reflexes of nanofibers corresponding to the π-stacking distance of P3HT backbones (Figure S11). Importantly, these SAED data indicate the presence of a defined joint contact plane between the ribbon of **1** and the plane of P3HT backbones that are oriented perpendicularly to the nanofibers' growth direction. Finally, the SAED data of P3HT nanofibers alone yield a series of diffraction reflexes (Figure S12), which is uncommon for P3HT nanofibers, but demonstrates a significant degree of order and orientation. This high alignment is most likely attributed to the ribbon's rigid shape and the epitaxial match of the surface of **1**.[29] Hence, not only is a defined starting point provided by the rigid surface of **1**, but it also allows for a very dense nanofiber growth, resulting in the growth of a highly defined and aligned P3HT nanofiber mat held together via amorphous tie-chains.

To study the extent to which this P3HT alignment is preserved over the length of the nanofibers, we took a series of transmission electron microscopy images of an isolated superstructure starting from the ribbon's interface up to a distance of 30 μm (Figure 6A–D, see also Figures S13 and S14). At the interface, the P3HT nanofibers are directly connected to the ribbon (Figure 6A). At a distance of 6 μm away from the ribbon, a dense and highly aligned network of P3HT nanofibers is observed (B). Although the nanofiber network is getting less dense, at distances of 15 μm still a significant alignment can be seen (C). Only at still larger distance the nanofibers become less oriented and aligned (D). To quantify the alignment, we applied an algorithm by Persson et al.[40] to calculate an orientational order parameter S for the nanofibers from each TEM image. An orientational order parameter of 1 means perfectly ordered and aligned nanofibers, while a parameter of 0 reflects an isotropic orientation (for detailed information see Section S3.4 of the Supporting Information). The orientational order parameter for each position along the P3HT superstructure is shown in Figure 6E. Except for the first TEM image, which we attribute to the interface of the ribbon and the starting point of P3HT fiber growth, the orientational order parameter for the P3HT nanofiber alignment is close to 1. This exceptionally high alignment is preserved over more than 15 μm before it drops.

3.5. Photophysical Properties of P3HT Nanofibers in Isolated Superstructures. In aggregates of functional materials, such as the P3HT nanofibers in the hierarchical superstructures, the structural properties on the nanoscale have a significant impact on the optical properties. We thus investigated the PL properties of the P3HT nanofibers with spatially resolved photoluminescence (PL) spectroscopy (see Section 2). Figure 7A shows the TEM image of an isolated superstructure (as indicated by the dotted line) on a TEM grid with the supramolecular ribbon of **1** oriented diagonally and P3HT nanofibers with a length of ~15 μm grown perpendicularly to the ribbon. On the same superstructure we scanned an area of 80 × 80 μm^2 with a step width of 1 μm and recorded a PL spectrum at each position, resulting in a total of 6561 PL spectra. The spectrally integrated PL signal at each position is displayed in Figure 7B (the area of the TEM

https://doi.org/10.1021/acs.macromol.4c01618
Macromolecules 2024, 57, 10389–10398

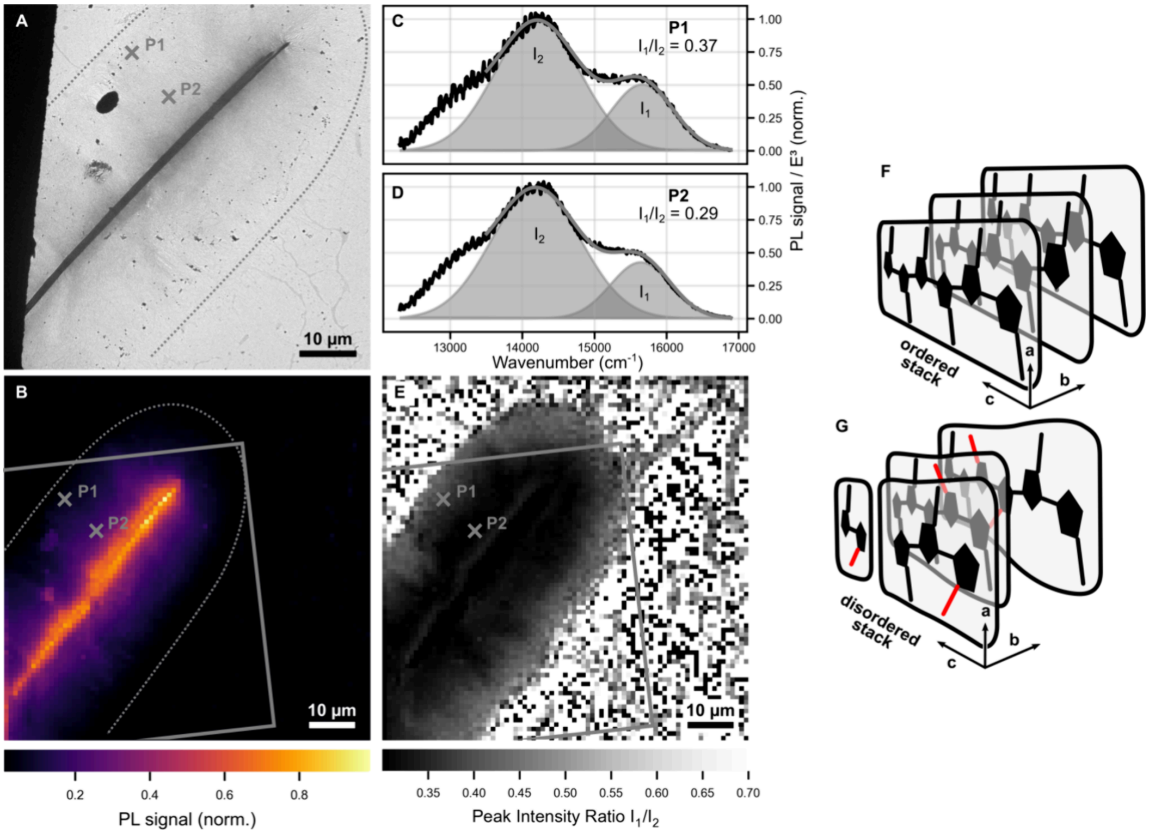

Figure 7. Photophysical characterization of isolated superstructure by spatially resolved PL spectroscopy. (A) TEM image of an isolated superstructure. The dotted line indicates the ends of the nanofibers. (B) Total PL intensity at each point measured on the same superstructure as in (A). The dotted line indicates the ends of the nanofibers (as in A) and the solid gray rectangle indicates the area imaged by TEM in A. (C) PL spectrum measured on the periphery of the isolated P3HT superstructure (spot P1 in A and B). PL signal (black line) is fitted with two Gaussian peaks (gray) with intensities I_1 and I_2. (D) PL spectrum measured in the inner part of an isolated P3HT superstructure (spot P2 in A and B). (E) Map of the PL peak intensity ratio I_1/I_2, based on the analysis of 6561 individual PL spectra. (F,G) Sketch of a perfectly ordered π-stack of P3HT chains (F) and of a disordered stack with chain-end and regio defects incorporated into the stack (G).

image in Figure 7A is indicated by the gray box). We observe exclusively PL signal from the area where P3HT nanofibers exist, while there is barely P3HT surrounding the superstructure as expected after the purification and isolation procedure.

For a more detailed insight into the relationship between structure and optical properties, we analyze the shapes of all acquired PL spectra, since those are very sensitive to the local disorder within P3HT nanofibers. Two examples of PL spectra at different positions within the superstructure (P1 and P2, indicated in Figures 7A,B) are shown in Figure 7C,D. The spectra feature a distorted vibronic progression that is characteristic of emission of well-ordered π-stacks of P3HT.[41−43] The high-energy peak (I_1) around 15800 cm^{-1} is always weaker with respect to the peak at 14,200 cm^{-1} (I_2). Yet, the peak ratio I_1/I_2 increases along the nanofibers' growth direction (I_1/I_2 = 0.29 at P2 close to the ribbon, and I_1/I_2 = 0.37 at P1 close to the nanofibers' ends), indicating an increase in disorder when going toward the nanofibers' ends (see Section S4 in the Supporting Information for details on this analysis). We extracted the ratio I_1/I_2 from all 6561 PL spectra, see Figure 7E, confirming that this ratio systematically increases along the growth direction of all nanofibers with values close to 0.3 at the center of the superstructure and values around 0.5 at the edges. We note that the strong noise visible around the superstructure in Figure 7E results from a lack of P3HT (i.e., from noisy PL spectra that cannot be fitted sensibly). The consistent and systematic increase in peak ratio and thus of disorder along the growth direction of the P3HT nanofibers is in line with our recent work on nonpurified superstructures surrounded by a P3HT film.[30] We found that the origin of this disorder is defect fractionation during nanofiber growth: Initially only the longest chains and those with highest regioregularity are incorporated into nanofibers, which leads to ordered π-stacks of P3HT chains (Figure 7F); during continued growth the number of regio defects and chain-end defects incorporated into nanofibers increases, resulting in increasingly disordered stacks (Figure 7G). Both defects can give rise to an increase in torsional disorder of P3HT chains along nanofibers (see Figure 7G), and ultimately to the characteristic and systematic changes in the shapes of the spatially resolved PL spectra. Remarkably, not only the size

https://doi.org/10.1021/acs.macromol.4c01618
Macromolecules 2024, 57, 10389−10398

of the superstructures is maintained during the purification step, but also the defect composition and defect density along the P3HT nanofibers remain largely intact,[30] demonstrating that the P3HT molecules are tightly integrated into the superstructure regardless of their defects.

4. SUMMARY

We presented a two-step self-assembly approach to achieve mesoscaled hierarchical superstructures based on P3HT and *N*,*N*′-1,4-phenylenebis[4-pyridinecarboxamide] **1**. Supramolecular ribbons of **1** with tailored dimensions were straightforwardly prepared in a seeded-growth approach. These objects were subsequently used to efficiently transcrystallize P3HT in form nanofibers from solution yielding such shish-kebab-like superstructures. Purification and deposition on substrates of such isolated shish-kebab-like superstructures revealed highly ordered and oriented P3HT nanofibers with lengths of up to 20 μm without compromising their structural integrity. Within the superstructures, P3HT nanofibers feature an exceptional orientational order parameter close to one over almost the entire fiber length. PL imaging along the P3HT nanofibers reveal that more defects are included in the superstructure toward the nanofiber end as a result of defect (regio and chain-end defects) fractionization during the P3HT fiber growth. This finding agrees with our previous results, demonstrating that our two-step self-assembly and purification concept is a suitable approach to design and realize mesoscale components, which can be used in nanophotonic devices or as light-harvesting antennae.

■ ASSOCIATED CONTENT

Supporting Information

The Supporting Information is available free of charge at https://pubs.acs.org/doi/10.1021/acs.macromol.4c01618.

Details on mechanistic studies of the self-assembly of **1**, seeded growth studies, SEM and AFM images of the ribbon morphology, SEM images of embedded deposited P3HT superstructures after different aging times, absorption spectra of dispersions with P3HT superstructures, absorption spectra, photoinduced force IR spectra, TEM and SAED images of isolated superstructures, visualization of the orientational order parameter of P3HT nanofibers, and information on the analysis of spatially resolved PL spectra on P3HT nanofibers (PDF)

■ AUTHOR INFORMATION

Corresponding Author

Hans-Werner Schmidt − *Macromolecular Chemistry I and Bavarian Polymer Institute, University of Bayreuth, 95447 Bayreuth, Germany*; orcid.org/0000-0002-1761-1153; Email: hans-werner.schmidt@uni-bayreuth.de

Authors

Felix A. Wenzel − *Macromolecular Chemistry I and Bavarian Polymer Institute, University of Bayreuth, 95447 Bayreuth, Germany*

Sebastian Stäter − *Zernike Institute for Advanced Materials, University of Groningen, 9747 AG Groningen, The Netherlands*

Padraic O'Reilly − *Molecular Vista, San Jose, California 95119, United States*

Klaus Kreger − *Macromolecular Chemistry I and Bavarian Polymer Institute, University of Bayreuth, 95447 Bayreuth, Germany*; orcid.org/0000-0003-3021-1311

Jürgen Köhler − *Spectroscopy of Soft Matter and Bavarian Polymer Institute, University of Bayreuth, 95447 Bayreuth, Germany*; orcid.org/0000-0002-4214-4008

Richard Hildner − *Zernike Institute for Advanced Materials, University of Groningen, 9747 AG Groningen, The Netherlands*; orcid.org/0000-0002-7282-3730

Complete contact information is available at: https://pubs.acs.org/10.1021/acs.macromol.4c01618

Notes

The authors declare no competing financial interest.

■ ACKNOWLEDGMENTS

The authors acknowledge financial support from the Bavarian State Ministry of Science and the Arts through the Collaborative Research Network "Solar Technologies go Hybrid." FAW also acknowledge support by the Elite Network of Bavaria through the study program "Macromolecular Science." The authors are grateful to Hannes Welz (Macromolecular Chemistry, University of Bayreuth) for his help during the initial steps of this work. The authors acknowledge support of the facility in the Keylab Electron and Optical Microscopy of the Bavarian Polymer Institute and in particular Dr. Markus Drechsler for help with the TEM and SAED measurements.

■ REFERENCES

(1) Noriega, R.; Rivnay, J.; Vandewal, K.; Koch, F. P. V.; Stingelin, N.; Smith, P.; Toney, M. F.; Salleo, A. A general relationship between disorder, aggregation and charge transport in conjugated polymers. *Nat. Mater.* **2013**, *12* (11), 1038−1044.

(2) Brinkmann, M. Structure and morphology control in thin films of regioregular poly(3-hexylthiophene). *J. Polym. Sci., Part B: Polym. Phys.* **2011**, *49* (17), 1218−1233.

(3) Tremel, K.; Ludwigs, S. *Morphology of P3HT in Thin Films in Relation to Optical and Electrical Properties*. In P3HT Revisited—from Molecular Scale to Solar Cell Devices; Ludwigs, S.; Andrienko, D., Eds.; Advances in Polymer Science, Vol. *265*; Springer, 2014; pp 39−82.

(4) Choi, D.; Chang, M.; Reichmanis, E. Controlled Assembly of Poly(3-hexylthiophene): Managing the Disorder to Order Transition on the Nano- through Meso-Scales. *Adv. Funct. Mater.* **2015**, *25* (6), 920−927.

(5) Hildner, R.; Köhler, A.; Müller-Buschbaum, P.; Panzer, F.; Thelakkat, M. π-Conjugated Donor Polymers: Structure Formation and Morphology in Solution, Bulk and Photovoltaic Blends. *Adv. Energy Mater.* **2017**, *7* (16), No. 1700314.

(6) Guchait, S.; Zhong, Y.; Brinkmann, M. High-Temperature Rubbing: An Effective Method to Fabricate Large-Scale Aligned Semiconducting and Conducting Polymer Films for Applications in Organic Electronics. *Macromolecules* **2023**, *56* (17), 6733−6757.

(7) Kline, R. J.; McGehee, M. D.; Kadnikova, E. N.; Liu, J.; Fréchet, J. M. J.; Toney, M. F. Dependence of Regioregular Poly(3-hexylthiophene) Film Morphology and Field-Effect Mobility on Molecular Weight. *Macromolecules* **2005**, *38* (8), 3312−3319.

(8) Brinkmann, M.; Rannou, P. Effect of Molecular Weight on the Structure and Morphology of Oriented Thin Films of Regioregular Poly(3-hexylthiophene) Grown by Directional Epitaxial Solidification. *Adv. Funct. Mater.* **2007**, *17* (1), 101−108.

(9) Wu, Z.; Petzold, A.; Henze, T.; Thurn-Albrecht, T.; Lohwasser, R. H.; Sommer, M.; Thelakkat, M. Temperature and Molecular Weight Dependent Hierarchical Equilibrium Structures in Semi-

https://doi.org/10.1021/acs.macromol.4c01618
Macromolecules 2024, 57, 10389−10398

conducting Poly(3-hexylthiophene). *Macromolecules* **2010**, *43* (10), 4646−4653.
(10) Ihn, K. J.; Moulton, J.; Smith, P. Whiskers of poly(3-alkylthiophene)s. *J. Polym. Sci., Part B: Polym. Phys.* **1993**, *31* (6), 735−742.
(11) Guo, C.; Gao, X.; Lin, F.-J.; Wang, Q.; Meng, L.; Bian, R.; Sun, Y.; Jiang, L.; Liu, H. In Situ Characterization of the Triphase Contact Line in a Brush-Coating Process: Toward the Enhanced Efficiency of Polymer Solar Cells. *ACS Appl. Mater. Interfaces* **2018**, *10* (46), 39448−39454.
(12) Chu, P.-H.; Kleinhenz, N.; Persson, N.; McBride, M.; Hernandez, J. L.; Fu, B.; Zhang, G.; Reichmanis, E. Toward Precision Control of Nanofiber Orientation in Conjugated Polymer Thin Films: Impact on Charge Transport. *Chem. Mater.* **2016**, *28* (24), 9099−9109.
(13) Kleinhenz, N.; Persson, N.; Xue, Z.; Chu, P. H.; Wang, G.; Yuan, Z.; McBride, M. A.; Choi, D.; Grover, M. A.; Reichmanis, E. Ordering of Poly(3-hexylthiophene) in Solutions and Films: Effects of Fiber Length and Grain Boundaries on Anisotropy and Mobility. *Chem. Mater.* **2016**, *28* (11), 3905−3913.
(14) O'Connor, B.; Kline, R. J.; Conrad, B. R.; Richter, L. J.; Gundlach, D.; Toney, M. F.; DeLongchamp, D. M. Anisotropic Structure and Charge Transport in Highly Strain-Aligned Regioregular Poly(3-hexylthiophene). *Adv. Funct. Mater.* **2011**, *21* (19), 3697−3705.
(15) Nagamatsu, S.; Takashima, W.; Kaneto, K.; Yoshida, Y.; Tanigaki, N.; Yase, K.; Omote, K. Backbone Arrangement in "Friction-Transferred" Regioregular Poly(3-alkylthiophene)s. *Macromolecules* **2003**, *36* (14), 5252−5257.
(16) Hosokawa, Y.; Misaki, M.; Yamamoto, S.; Torii, M.; Ishida, K.; Ueda, Y. Molecular orientation and anisotropic carrier mobility in poorly soluble polythiophene thin films. *Appl. Phys. Lett.* **2012**, *100* (20), 203305.
(17) Hamidi-Sakr, A.; Biniek, L.; Fall, S.; Brinkmann, M. Precise Control of Lamellar Thickness in Highly Oriented Regioregular Poly(3-Hexylthiophene) Thin Films Prepared by High-Temperature Rubbing: Correlations with Optical Properties and Charge Transport. *Adv. Funct. Mater.* **2016**, *26* (3), 408−420.
(18) Untilova, V.; Biskup, T.; Biniek, L.; Vijayakumar, V.; Brinkmann, M. Control of Chain Alignment and Crystallization Helps Enhance Charge Conductivities and Thermoelectric Power Factors in Sequentially Doped P3HT:F 4 TCNQ Films. *Macromolecules* **2020**, *53* (7), 2441−2453.
(19) Persson, N. E.; Chu, P.-H.; McBride, M.; Grover, M.; Reichmanis, E. Nucleation, Growth, and Alignment of Poly(3-hexylthiophene) Nanofibers for High-Performance OFETs. *Acc. Chem. Res.* **2017**, *50* (4), 932−942.
(20) Khim, D.; Luzio, A.; Bonacchini, G. E.; Pace, G.; Lee, M.-J.; Noh, Y.-Y.; Caironi, M. Uniaxial Alignment of Conjugated Polymer Films for High-Performance Organic Field-Effect Transistors. *Adv. Mater.* **2018**, *30* (20), No. e1705463.
(21) Kreger, K.; Schmidt, H.-W.; Hildner, R. Tailoring the excited-state energy landscape in supramolecular nanostructures. *Electron. Struct.* **2021**, *3* (2), 23001.
(22) Liu, J.; Zou, J.; Zhai, L. Bottom-up Assembly of Poly(3-hexylthiophene) on Carbon Nanotubes: 2D Building Blocks for Nanoscale Circuits. *Macromol. Rapid Commun.* **2009**, *30* (16), 1387−1391.
(23) Brinkmann, M.; Chandezon, F.; Pansu, R. B.; Julien-Rabant, C. Epitaxial Growth of Highly Oriented Fibers of Semiconducting Polymers with a Shish-Kebab-Like Superstructure. *Adv. Funct. Mater.* **2009**, *19* (17), 2759−2766.
(24) Zhang, X.; Yuan, N.; Ding, S.; Wang, D.; Li, L.; Hu, W.; Bo, Z.; Zhou, J.; Huo, H. Growth and carrier-transport performance of a poly(3-hexylthiophene)/1,2,3,4-bis(p-methylbenzylidene) sorbitol hybrid shish-kebab nanostructure. *J. Mater. Chem. C* **2017**, *5* (16), 3983−3992.
(25) Bu, L.; Pentzer, E.; Bokel, F. A.; Emrick, T.; Hayward, R. C. Growth of polythiophene/perylene tetracarboxydiimide donor/acceptor shish-kebab nanostructures by coupled crystal modification. *ACS Nano* **2012**, *6* (12), 10924−10929.
(26) Li, L.; Jacobs, D. L.; Bunes, B. R.; Huang, H.; Yang, X.; Zang, L. Anomalous high photovoltages observed in shish kebab-like organic p−n junction nanostructures. *Polym. Chem.* **2014**, *5* (2), 309−313.
(27) Yan, H.; Yan, Y.; Yu, Z.; Wei, Z. Self-Assembling Branched and Hyperbranched Nanostructures of Poly(3-hexylthiophene) by a Solution Process. *J. Phys. Chem. C* **2011**, *115* (8), 3257−3262.
(28) Kamps, A. C.; Fryd, M.; Park, S.-J. Hierarchical self-assembly of amphiphilic semiconducting polymers into isolated, bundled, and branched nanofibers. *ACS Nano* **2012**, *6* (3), 2844−2852.
(29) Wenzel, F. A.; Welz, H.; van der Zwan, K. P.; Stäter, S.; Kreger, K.; Hildner, R.; Senker, J.; Schmidt, H.-W. Highly Efficient Supramolecular Nucleating Agents for Poly(3-hexylthiophene). *Macromolecules* **2022**, *55* (7), 2861−2871.
(30) Stäter, S.; Wenzel, F. A.; Welz, H.; Kreger, K.; Köhler, J.; Schmidt, H.-W.; Hildner, R. Directed Gradients in the Excited-State Energy Landscape of Poly(3-hexylthiophene) Nanofibers. *J. Am. Chem. Soc.* **2023**, *145* (25), 13780−13787.
(31) Nowak, D.; Morrison, W.; Wickramasinghe, H. K.; Jahng, J.; Potma, E.; Wan, L.; Ruiz, R.; Albrecht, T. R.; Schmidt, K.; Frommer, J.; Sanders, D. P.; Park, S. Nanoscale chemical imaging by photoinduced force microscopy. *Sci. Adv.* **2016**, *2* (3), No. e1501571.
(32) Smulders, M. M. J.; Nieuwenhuizen, M. M. L.; de Greef, T. F. A.; van der Schoot, P.; Schenning, A. P. H. J.; Meijer, E. W. How to distinguish isodesmic from cooperative supramolecular polymerisation. *Chem.—Eur. J.* **2010**, *16* (1), 362−367.
(33) Jarrett-Wilkins, C.; He, X.; Symons, H. E.; Harniman, R. L.; Faul, C. F. J.; Manners, I. Living Supramolecular Polymerisation of Perylene Diimide Amphiphiles by Seeded Growth under Kinetic Control. *Chem.—Eur. J.* **2018**, *24* (58), 15556−15565.
(34) Wehner, M.; Würthner, F. Supramolecular polymerization through kinetic pathway control and living chain growth. *Nat. Rev. Chem.* **2020**, *4* (1), 38−53.
(35) Raithel, D.; Baderschneider, S.; de Queiroz, T. B.; Lohwasser, R.; Köhler, J.; Thelakkat, M.; Kümmel, S.; Hildner, R. Emitting Species of Poly(3-hexylthiophene): From Single, Isolated Chains to Bulk. *Macromolecules* **2016**, *49* (24), 9553−9560.
(36) Clark, J.; Chang, J.-F.; Spano, F. C.; Friend, R. H.; Silva, C. Determining exciton bandwidth and film microstructure in polythiophene films using linear absorption spectroscopy. *Appl. Phys. Lett.* **2009**, *94* (16), 163306.
(37) Scharsich, C.; Lohwasser, R. H.; Sommer, M.; Asawapirom, U.; Scherf, U.; Thelakkat, M.; Neher, D.; Köhler, A. Control of aggregate formation in poly(3-hexylthiophene) by solvent, molecular weight, and synthetic method. *J. Polym. Sci., Part B: Polym. Phys.* **2012**, *50* (6), 442−453.
(38) Louarn, G.; Trznadel, M.; Buisson, J. P.; Laska, J.; Pron, A.; Lapkowski, M.; Lefrant, S. Raman Spectroscopic Studies of Regioregular Poly(3-alkylthiophenes). *J. Phys. Chem.* **1996**, *100* (30), 12532−12539.
(39) Milani, A.; Brambilla, L.; Del Zoppo, M.; Zerbi, G. Raman dispersion and intermolecular interactions in unsubstituted thiophene oligomers. *J. Phys. Chem. B* **2007**, *111* (6), 1271−1276.
(40) Persson, N. E.; McBride, M. A.; Grover, M. A.; Reichmanis, E. Automated Analysis of Orientational Order in Images of Fibrillar Materials. *Chem. Mater.* **2017**, *29* (1), 3−14.
(41) Clark, J.; Silva, C.; Friend, R. H.; Spano, F. C. Role of intermolecular coupling in the photophysics of disordered organic semiconductors: aggregate emission in regioregular polythiophene. *Phys. Rev. Lett.* **2007**, *98* (20), No. 206406.
(42) Spano, F. C. Modeling disorder in polymer aggregates: the optical spectroscopy of regioregular poly(3-hexylthiophene) thin films. *J. Chem. Phys.* **2005**, *122* (23), 234701.
(43) Spano, F. C.; Clark, J.; Silva, C.; Friend, R. H. Determining exciton coherence from the photoluminescence spectral line shape in poly(3-hexylthiophene) thin films. *J. Chem. Phys.* **2009**, *130* (7), 74904.

https://doi.org/10.1021/acs.macromol.4c01618
Macromolecules 2024, 57, 10389−10398

Supporting Information

Isolated Hierarchical Superstructures with Highly Oriented P3HT Nanofibers

*Felix A. Wenzel[1], Sebastian Stäter[2], Padraic O'Reilly[3], Klaus Kreger[1], Jürgen Köhler[4], Richard Hildner[2], and Hans-Werner Schmidt[1]**

[1]Macromolecular Chemistry I and Bavarian Polymer Institute, University of Bayreuth, Universitätsstraße 30, 95447 Bayreuth, Germany.

[2]Zernike Institute for Advanced Materials, University of Groningen, Nijenborgh 3, 9747 AG Groningen, The Netherlands.

[3]Molecular Vista, 6840 Via del Oro, Suite 110, San Jose, CA 95119, USA.

[4] Spectroscopy of soft Matter and Bavarian Polymer Institute, University of Bayreuth, Universitätsstraße 30, 95447 Bayreuth, Germany.

*Corresponding author: hans-werner.schmidt@uni-bayreuth.de

Table of contents

S1 Self-assembly of N,N′-1,4-phenylenebis [4-pyridinecarboxamide]

S1.1 Mechanistic studies of the self-assembly process

To gain insight into the mechanistic process of the self-assembly of N,N′-1,4-phenylenebis [4-pyridinecarboxamide] (**1**), we performed temperature-dependent UV-vis studies. In a typical procedure, a dispersion in chlorobenzene was heated to 103°C and kept at this temperature for 30 min. Absorption spectra were recorded upon cooling the samples from 103 to -6°C with a cooling rate of about 2 °C h^{-1}. In this way, a series of measurements were conducted using various concentrations ranging from 10 to 20 to 30 ppm.

Exemplary, **Figure S1 A** shows the evolution of the temperature-dependent absorption spectra of **1** from 300 to 500 nm at a concentration of 20 ppm. At high temperatures, a peak with a maximum at about 310 nm is observed, which is attributed to the molecularly dissolved compound **1**. To follow the temperature-dependent absorption of **1**, we selected the absorption at 320 nm to avoid an additional contribution from the solvent, chlorobenzene, which features a maximum at 280 nm. Upon cooling, the absorbance of the peak is steadily decreasing due the aggregation of **1** until the absorption at 320 nm almost vanished at around 30°C. At low temperatures, the absorption deviates from zero within the investigated region due to scattering of the formed aggregates.

In **Figure S1 B**, the intensity of the absorption at 320 nm and at 450 nm are plotted versus the temperature. Upon cooling from 103 to 95°C, only a slight decrease of the absorption at 320 nm is found, followed by a rapid decrease. At about 30°C a plateau is reached. This suggests that under these conditions self-assembly of the molecularly dissolved compound **1** is initiated at 95°C and completed at 30°C. The absorption around 450 nm was found to be 0 at 103°C. At about 95°C a slight increase is observed due to the scattering of the formed supramolecular objects. This goes in line with the observed initiation of the aggregation at 320 nm. Upon further cooling, only a minor change of the absorbance at 450 nm is observed.

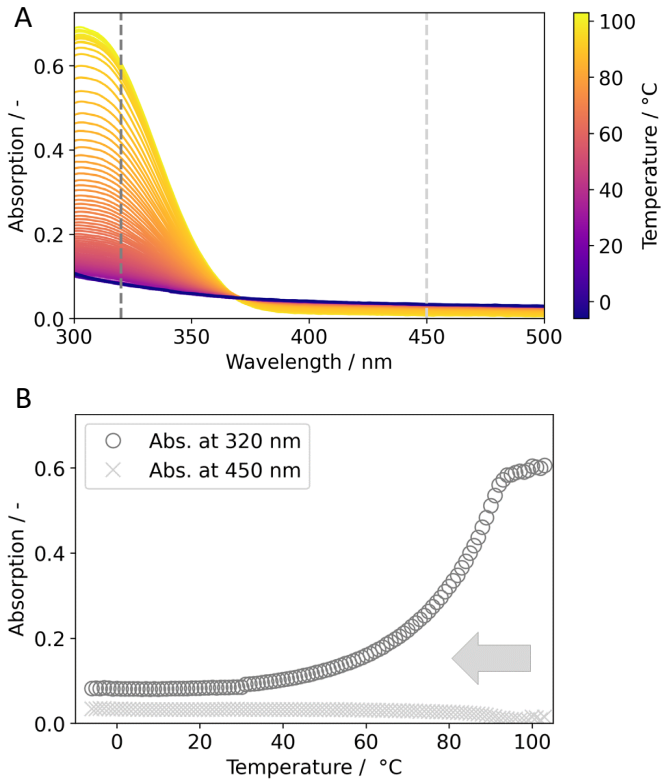

Figure S1 A) Temperature-dependent absorption spectra of N,N′-1,4-phenylenebis [4-pyridinecarboxamide] (**1**) in chlorobenzene at a concentration of 20 ppm upon cooling from 103 to -6 °C. B) Temperature-dependent progression of the absorbance at 320 nm and at 450 nm upon cooling.

Based on the data in **Figure S1 B**, we determine the degree of aggregation α of the self-assembly process from the UV-vis measurements at 320 nm. The degree of aggregation is defined as

$$\alpha = \frac{A_{monomeric\ state} - A(T)}{A_{monomeric\ state} - A_{aggregated\ state}}$$

where $A_{monomeric\ state}$ refers to the absorbance of the molecularly dissolved state, $A_{aggregated\ state}$ to the absorbance of the fully aggregated state and $A(T)$ to the absorbance at a given temperature T. For $A_{monomeric\ state}$, we selected the absorbance of the high temperature plateau (~103°C) and for $A_{aggregated\ state}$ the absorbance of the low temperature plateau (below 30°C). Consequently, α can hold values between 0 and 1. **Figure S2 A** shows the temperature-dependent degree of aggregation of **1** at a concentration of 20 ppm.

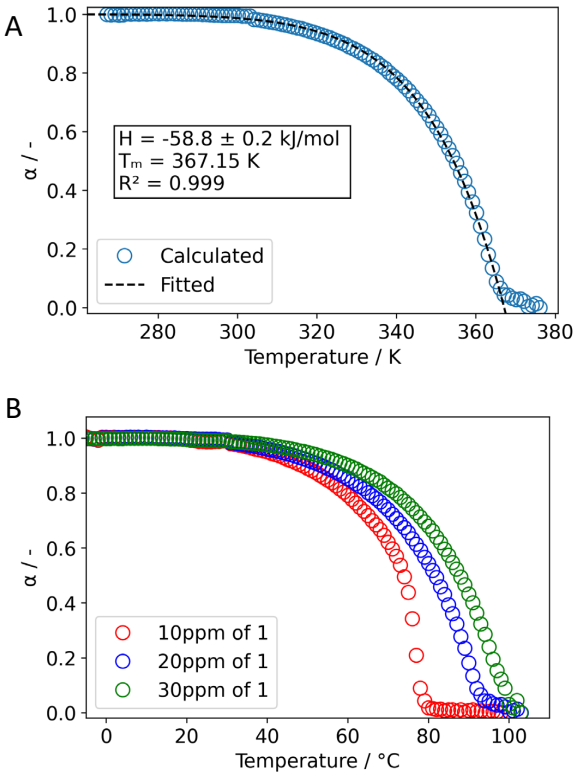

Figure S2 A) Calculated degree of aggregation of **1** at 20 ppm in chlorobenzene based on the absorption at 320 nm (open blue circles). The corresponding Arrhenius-type fit (dashed line) yields an enthalpy of aggregation of -58.8 kJ/mol and a critical temperature T_m of 94°C. The very good value of 0.999 for the coefficient of determination R^2 highly suggests that aggregation proceeds via a cooperative mechanism. B) Temperature-dependent degrees of aggregation of **1** for the concentrations 10 ppm (open red circles), 20 ppm (open blue circles) and 30 ppm (open green circles) in chlorobenzene. The critical temperature T_m shifts to higher values with increasing concentrations. Under these conditions, the high temperature plateau of α, indicative for molecularly dissolved species, is not fully reached anymore at a concentration of 30 ppm.

The temperature-dependence of α, starting with a plateau at high temperature followed by a rapid aggregation upon cooling below a critical temperature is, in general, highly indicative for a cooperative mechanism. Therefore, we used the following Arrhenius-type function to fit the degree of aggregation: [1]

$$\alpha(T) = 1 - e^{\frac{H_{agg.}}{R \cdot T_m} \cdot \left(\frac{T_m}{T} - 1\right)}$$

with $H_{agg.}$ being the enthalpy of aggregation, R the molar gas constant and T_m the critical temperature. We found an $H_{agg.}$ of -58.8 ± 0.2 kJ/mol, which is comparable with literature values found for similar building blocks such as 1,3,5-benzenetricarboxamides[2,3], and a T_m of 367 K (94°C). The coefficient of determination R^2 was found to be 0.999 and strongly suggests a cooperative mechanism for the aggregation of **1** (**Figure S2 A**). It should be noted that a fit for an isodesmic mechanism results in a significantly poorer coefficient of determination and thus does not satisfactorily describe the degree of aggregation.

Figure S2 B shows the degree of aggregation for different concentrations of **1**. The temperature-dependence is maintained with the critical temperature being shifted to higher temperatures with increasing concentration, a behavior in agreement with literature for a cooperative mechanism. [1] Note that at concentrations of more than 30 ppm the high temperature plateau, i.e., the completely dissolved state cannot be reached under these conditions. These findings imply that using compound **1**, supramolecular objects can be prepared in a controlled manner by a seeded-growth approach.

S1.2 Seeded growth studies

Seeded growth to supramolecular objects is well an established approach [4,5] typically relying on the addition of defined seeds to a solution with molecularly dissolved building blocks. The number of seeds added allows controlling the number of growing aggregates and thus the average size of the formed structures.

Here, we control the number of seeds by applying a protocol to selectively dissolve seeds in a dispersion upon heating. The temperature-dependent control over seeds is based on the work of Wittmann and Lotz[6], who developed a temperature protocol, in which polymer crystals in bulk were only partially molten upon heating. Upon cooling, the remaining seeds facilitate the self-nucleation of the polymer crystallization. We applied the temperature protocol to a solution-based process with small molecular building blocks. Heating to a given temperature controls the number of remaining nuclei. When cooled at a relatively low cooling rate of less than 5 K min^{-1}, self-assembly proceeds rapidly on the existing nuclei, while sporadic formation of homonuclei is avoided. This results in the formation of a few large supramolecular objects with a small number of remaining nuclei and many small supramolecular objects with a large number of remaining nuclei, featuring a well-defined distribution of the objects' dimensions.

As shown in **Section S1.1**, **1** is not completely dissolved at 103°C at a concentration of 30 ppm. Thus, by varying the maximal temperature of the heating process, the number of seeds and in turn the size of the growing aggregates can be tuned. For the seeded growth approach, we used sonicated dispersions of **1** at a concentration of 50 ppm in chlorobenzene and heated them to selected maximal temperatures, such as 110, 115, 120 or 125°C. After cooling to room temperature, the dispersions were drop-cast on glass slides and dried at ambient conditions. The supramolecular aggregates were analyzed by polarized light microscopy. To establish statistics of the aggregates' length, at least 50 aggregates per sample were evaluated.

Figure S3 shows representative optical micrographs of dried samples based on dispersions with 50 ppm of **1** heated to various maximal temperatures. With increasing maximal temperature, the solubility of **1** increases and the number of remaining seeds decreases. Upon cooling those samples from higher maximal temperatures, the comparably lower number of seeds results in larger aggregates. For samples cooled from 110°C, the aggregates have an average length of 7.3 ± 3.0 µm, from 115 °C an average length of 32.6 ± 10.2 µm and from 120 °C an average length of 44.9 ± 16.5 µm. The largest aggregates are formed upon cooling from 125 °C featuring an average length of 51.9 ± 25.1 µm. Further increasing the maximal temperature results in slightly smaller aggregates with lengths in the range of 40 – 50 µm. At such high temperatures, no seeds are present and aggregated objects were formed upon cooling by homogeneous nucleation and elongation.

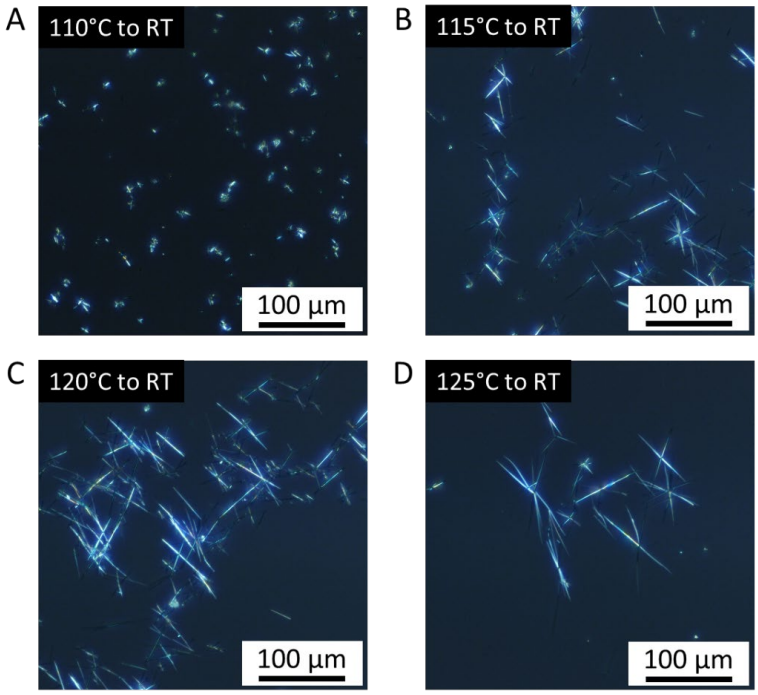

Figure S3: Polarized light microscopy images of drop-cast dispersions of **1** (50 ppm) in chlorobenzene after heating to various maximal temperatures of 110, 115, 120 and 125 °C and subsequent cooling to room temperature. The maximal temperature has a significant impact on the dimensions of the aggregates due to the seeded growth approach. At higher maximal temperatures the number of seeds and thus the number of objects is lower, but the size of the aggregates is larger and *vice versa*.

S1.3 Morphology of supramolecular ribbons

A more detailed picture of the morphology of objects of **1** can be obtained with scanning electron microscopy (SEM) and atomic force microscopy (AFM). For SEM, 50 µL of a dispersion was spin-coated onto silicon wafers, dried overnight under vacuum and sputtered with a 2 nm thick layer of platinum. For AFM, samples were prepared in a similar manner without subsequent sputtering. **Figure S4** provides an overview and different magnifications of the aggregates of **1** obtained from dispersions with a concentration of 50 ppm cooled from 125°C to room temperature. SEM micrographs reveal that **1** form supramolecular ribbons with lengths in the range of 50 µm and widths typically below 1 µm (**Figure S4**). The width and in particular the height of the supramolecular ribbons can be determined by AFM as shown in **Figure S5** for a supramolecular ribbon with a width of ~ 2 µm. The height is ~ 350 nm and is thus significantly smaller than the width.

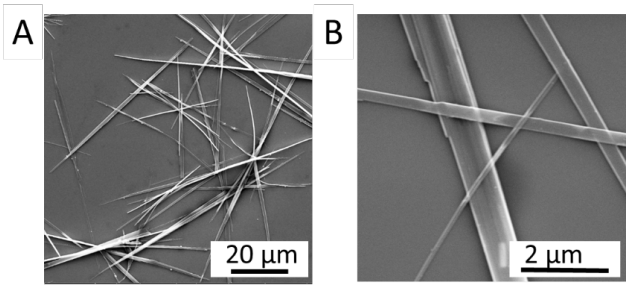

Figure S4: SEM micrographs at different magnifications of a drop-cast dispersion of **1** (50 ppm) after heating to 125°C and cooling to room temperature. The supramolecular ribbons feature lengths in the range of 50 µm (A) and ribbon widths are typically in the range of ~1 µm and below (B).

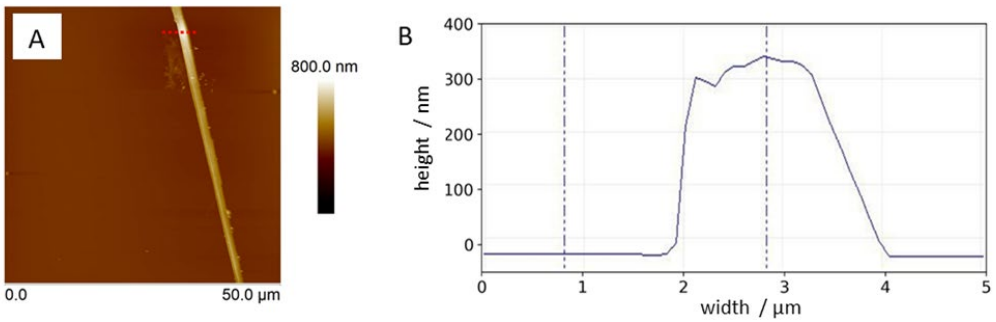

Figure S5: Atomic force microscopy of drop-cast aggregates of **1**. A) Topological image of a supramolecular ribbon and B) height scan at the position indicated in A by a red dotted line. Here, the supramolecular ribbon features a width of ~2 µm and a height of ~ 350 nm.

S2 Controlled formation of P3HT superstructures in solution

S2.1 SEM studies of embedded P3HT superstructures

To demonstrate control over the P3HT transcrystallization process on the supramolecular ribbons of **1**, we have performed different aging experiments in chlorobenzene containing supramolecular ribbons of **1** and dissolved P3HT at room temperature. For this, we dissolved 1 wt.% of P3HT at 50°C in chlorobenzene containing 50 ppm of supramolecular aggregates of 1. After cooling to room temperature, the dispersions were stored for 4 h up to 50 days. Here, samples were taken after 4h, 24h and 7d and studied by SEM. SEM samples were prepared as described in the experimental section. **Figure S6** shows SEM micrographs after different aging time comprising central fibrillar structures of **1** surrounded by highly ordered perpendicularly grown P3HT nanofibers of different lengths depending on the aging time.

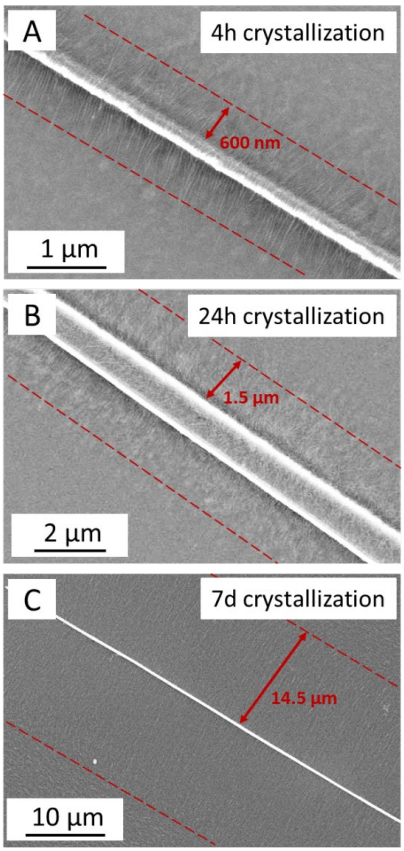

Figure S6: SEM micrographs of drop-cast dispersions of P3HT superstructures after aging dispersions for 4h (A), 24 h (B) and 7d (C). Note that the superstructures are surrounded by a thin film of the initially dissolved P3HT. The dashed red lines indicate the length of the P3HT nanofibers perpendicularly grown away from the fibrillar object of **1**. The P3HT nanofiber lengths are highly uniform and range from several hundreds of nm up to tens of µm depending on the aging time.

S2.2 Absorption spectroscopy of P3HT superstructure dispersions

To estimate the fraction of P3HT transcrystallizing into nanofibers from ribbons of **1**, we performed UV-vis spectroscopy. Dispersions were aged for 50 d at room temperature and subsequently diluted by a factor of 100 to establish a proper optical density of the dispersion. As reference, a homogeneous solution of P3HT in chlorobenzene was prepared by heating it to 50°C and cooling to room temperature. **Figure S7** shows the absorption spectra of both the aged dispersion with the P3HT superstructures and the solution comprising dissolved P3HT. The P3HT-chlorobenzene solution features a broad, structureless absorption with a maximum at 450 nm characteristic of dissolved P3HT.[7] For the aged sample containing the superstructures, the absorption below 525 nm is very similar to that of dissolved P3HT; however, an additional weak absorption in the long-wavelength region around 600 nm is present. Those spectra indicate that samples containing superstructures mostly comprise dissolved P3HT and that only a small fraction of P3HT crystallizes into nanofibers. Scaling the absorption of the dissolved P3HT to the absorption spectrum containing the superstructures allows us to extract the absorption of the aggregated P3HT species of the superstructures. The non-aggregated and aggregated P3HT spectra are shown in **Figure 5C** of the main text. By integrating the spectra, the ratio of non-aggregated and aggregated P3HT can be obtained, if we consider that chains in a more planar configuration (as in an aggregate) possess an oscillator strength that is larger by a factor of 1.39 compared to the oscillator strength of a more twisted chain dissolved in solution.[7] The share of aggregated P3HT is the integral of the aggregated P3HT spectrum divided by the ratio of oscillator strengths,[7] divided by the total, i.e., the sum of the weighted integral of the aggregated part and the integral of the non-aggregated part.[8] We find that about 4.7 % of the P3HT is aggregated in the dispersion. Note that the non-aggregated fraction of P3HT includes dissolved chains in solution as well as the amorphous interlamellar zones between nanofibers.[8,9]

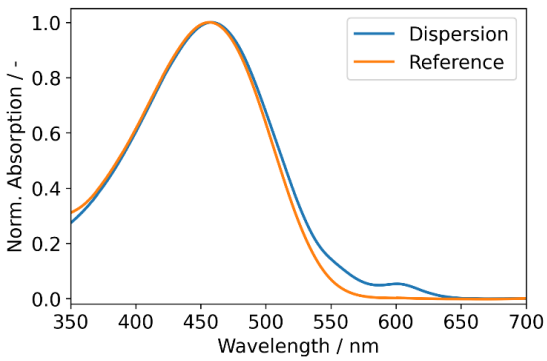

Figure S7: Normalized absorption spectra of a diluted dispersion of superstructures after 50 d of aging (blue) and a solution of dissolved P3HT (orange) as reference.

S3 Characterization of isolated P3HT superstructures

S3.1 Absorption spectroscopy

The P3HT superstructures can be purified from most of the excessive dissolved P3HT and redispersed in chlorobenzene with the superstructures remaining intact. **Figure S8A** shows absorption spectra of a freshly prepared dispersion, which were monitored after 0 min (blue), 20 min (orange) and 60 min (green). The absorption spectra show that after redispersion in chlorobenzene, the spectral features are the same and no significant dissolution of the transcrystallized P3HT kebab fibers on the shish can be observed.

To determine the fraction of aggregated P3HT nanofibers, we applied the same procedure as described in the previous section. **Figure S8B** shows the absorption spectra of a redispersed sample containing isolated P3HT superstructures (blue) and a dissolved sample of P3HT (orange). By fitting the non-aggregated and aggregated part of the absorption spectra of the redispersed sample (see **Figure 5C**) we find that a fraction of about 28.2% of the P3HT in the sample is aggregated. This corresponds to a six time increase of the aggregated P3HT species to the non-aggregated species compared to the non-purified dispersions. This value is now also closer to the typical ratio of aggregated P3HT to amorphous P3HT in thin films.[9]

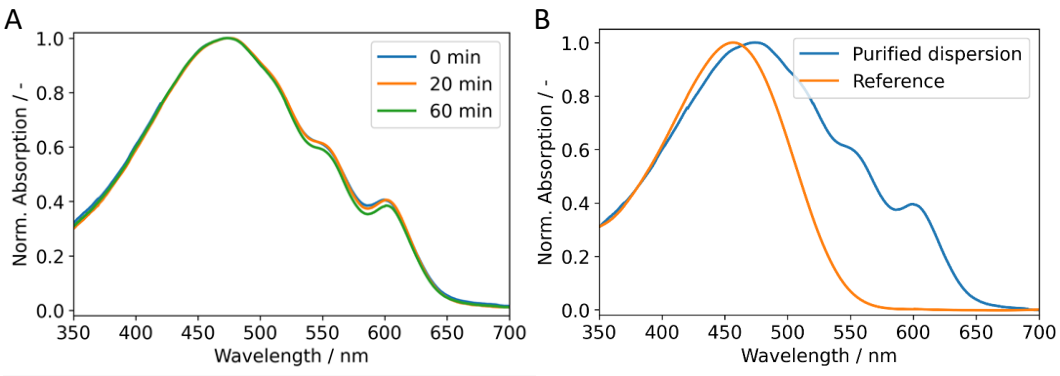

Figure S8: A) Normalized absorption spectra of a purified dispersion of superstructures after aging for 50 days acquired after 0 min, 20 min and 60 min. B) Normalized absorption spectrum of a purified dispersion of superstructures after aging for 50 days (blue) and a solution of P3HT in chlorobenzene (orange) as reference.

S3.2 Photo-induced force IR spectroscopy on isolated superstructures

Transfer of isolated P3HT superstructures to substrates allows for the characterization by high-resolution techniques such as photo-induced force IR spectroscopy. Thus, we can study the superstructure properties only, i.e., in the absence of a surrounding P3HT film. Photo-induced force IR spectroscopy on isolated superstructures was performed as described in the experimental section in the manuscript. IR spectra taken at the ribbon of **1** and ca. 400 nm away from the ribbon are shown in **Figure S9**. The IR spectra show in general a complex structure and are dominated by carbon-bond stretch vibrations between 1450 cm^{-1} and 1570 cm^{-1}. Notably, the peak at 1645 cm^{-1}, reflecting the C=O stretch of the amide group of **1** is only present in the IR spectrum from the ribbon of **1**, thus verifying that the degree of aggregation α of **1** is indeed close to 1 (see also Figure S2).

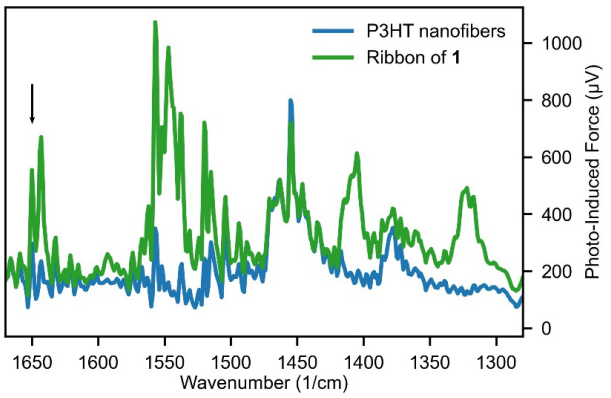

Figure S9: IR spectra taken by photo-induced force IR spectroscopy at the ribbon of **1** and at P3HT nanofibres about 400 nm away from the ribbon. The downward arrow highlights the C=O stretch vibration of the amide groups at ~1645 cm^{-1} that is only present at the central ribbon.

S3.3 Electron microscopy and diffraction on isolated P3HT superstructures

Figure S10 A shows a transmission electron microscopy (TEM) image of the supramolecular ribbon of **1** in an isolated superstructure. In **Figure S10 B** the corresponding selected area electron diffraction (SAED) pattern of the same region is shown. The SAED pattern exhibits a significant number of sharp diffraction peaks, which result from the highly crystalline nature of **1**, as shown recently.[10]

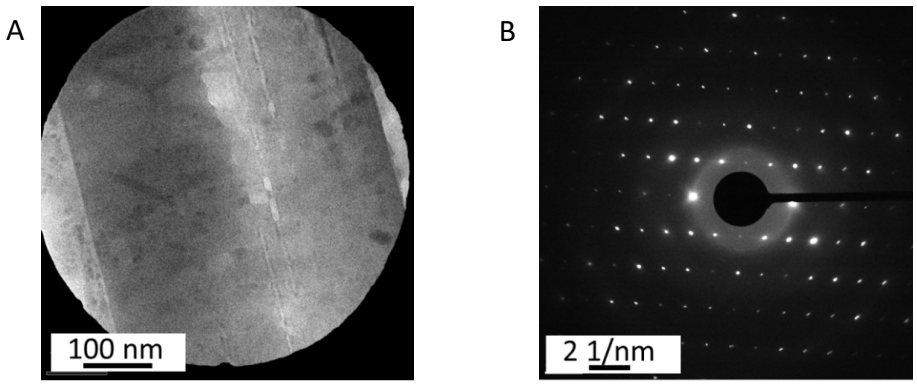

Figure S10 A) TEM image and B) SAED of a supramolecular ribbon of **1** in an isolated superstructure demonstrating its highly crystalline nature.

Figure S11 A shows a transmission electron microscopy (TEM) image of an isolated superstructure at the interface between the supramolecular ribbon of **1** and the P3HT nanofibers. From the central ribbon, the P3HT nanofibers transcrystallize perpendicularly to the ribbon's long axis. In **Figure S11 B**, the corresponding SAED of the same spot is shown. The SAED exhibits a significant number of sharp diffraction patterns of **1** as shown in **Figure S10 B**. Apart from these sharp reflections, some broad and more diffuse signatures can be seen that are attributed to diffraction from the P3HT nanofibers. In particular, the reflection at 2.6 1/nm is clearly visible, which we assign to the 020 reflection (indicated by arrows in **Figure S11 B**). The 020 reflection corresponds to the π-π distance of the thiophene moieties in the oriented P3HT nanofibers. The orientation of the 020 reflection of P3HT is perpendicularly oriented to lattice planes of **1**, indicating a joint contact plane between the ribbon of **1** and P3HT nanofibers that enables efficient transcrystallization of P3HT. [10]

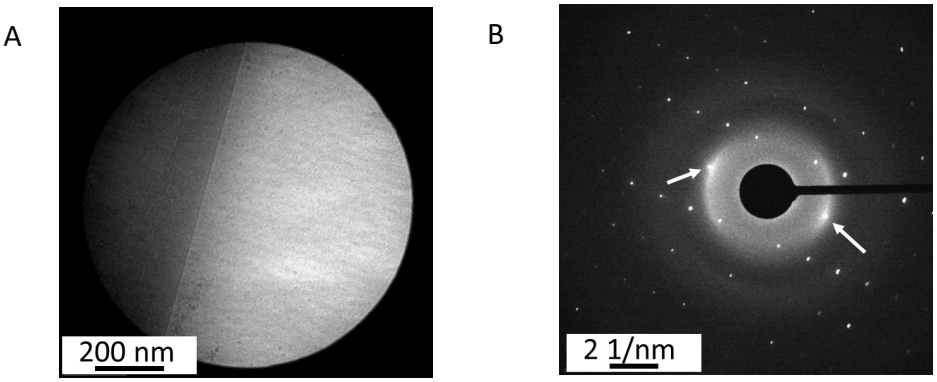

Figure S11 A) TEM image of an isolated superstructure close to middle center showing (from left) the supramolecular ribbon of **1**, the defined ribbon-nanofiber interface and perpendicularly grown P3HT nanofibers. B) SAED of the same position as shown in A. The sharp reflexes stem from the crystalline structure of **1** and the broad reflexes from the P3HT nanofibers. The arrows indicate the position of the 020 peak (π-stacking distance) of the P3HT nanofibers.

We also performed TEM and SAED around 2 µm away from the central ribbon of **1** in the region with P3HT nanofibers only, as shown in **Figure S 12**. The TEM image reveals that the P3HT nanofibers are highly aligned. This is also reflected by SAED showing a series of reflexes indicating a significant degree of order of the P3HT nanofibers with respect to each other. Five different reflections were identified and assigned. We find two 020 reflections arising from the π – π distance of 0.38 nm, labelled with b in **Figure S12 B** following the common nomenclature for crystalline P3HT. Moreover, two 002 reflections (c) resulting from the monomer-monomer distance of 0.38 nm along P3HT chains. Importantly, these 020 and 002 reflections can only be distinguished due to the very high degree of orientation of the P3HT nanofibers. The reflections labelled (d) correspond to the 040 peak, i.e., higher order reflexes of the π – π distance. The four 011 reflections (e) correspond to around 0.51 nm in real space and relate to the diagonal direction between the π-π direction and the direction of the backbone.[11] Note that scattering peaks of crystalline P3HT, commonly labelled with a, are not visible here, since this corresponds to the chain-chain distance out of the image plane in **Figure S12 A**. Additional reflexes (f) are visible that have, to the best of our knowledge, not been reported so far and cannot be assigned.

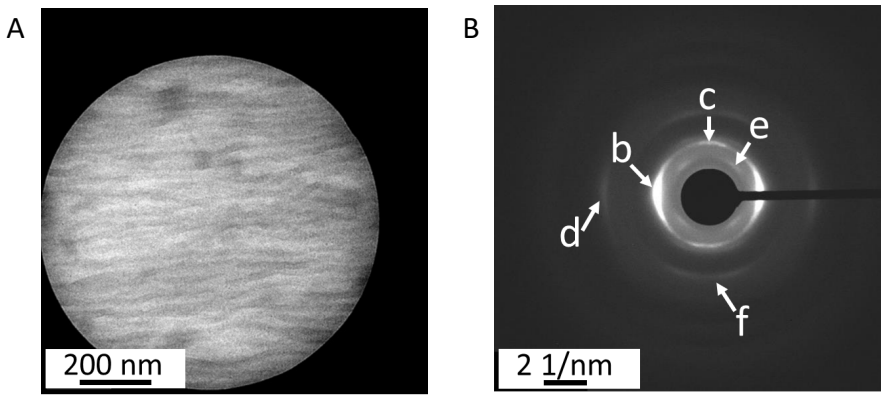

Figure S12 A) TEM image of highly aligned P3HT nanofibers in an isolated superstructure. B) SAED of highly aligned P3HT nanofibers shown in A). For the assignment of the reflections labelled b-f, see text.

S3.4 Orientation of the P3HT nanofibers in isolated superstructures

Overview of the P3HT nanofibers orientation in isolated superstructures

Within the superstructures, the P3HT nanofibers are grown perpendicularly to the supramolecular ribbons of **1** in a highly oriented manner both in superstructures covered with excess of P3HT (**Figure S6**) and in isolated superstructures (**Figure S11**). As demonstrated, the length of the P3HT nanofibers is determined by the aging time (**Figure S6**). Thus, interesting questions are how the transfer of the mesoscale-objects affects the orientation of nanofibers, and over which distances this orientation is preserved in isolated superstructures. **Figure S13** shows two representative TEM images taken from an isolated superstructure at different positions demonstrating that the orientation of nanofibers mostly maintains their initial orientation over distances significantly larger than 20 µm.

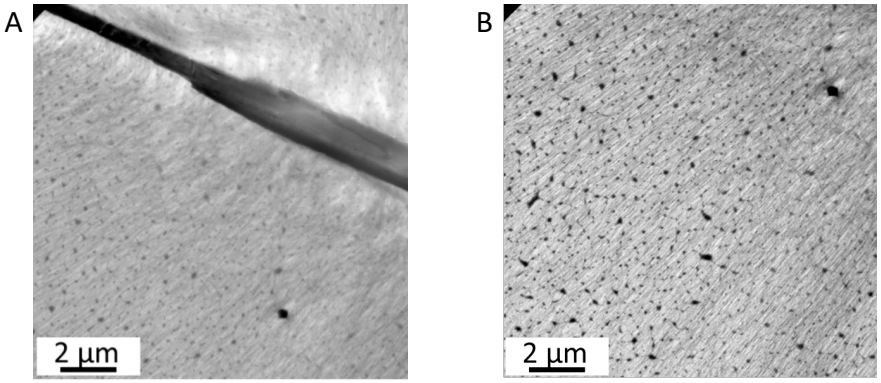

Figure S13: TEM images of an isolated superstructure deposited by spin-coating. The images were taken at two different positions, close to the supramolecular ribbon (A) and several µm away from the ribbon (B), showing the high orientation of the nanofibers over a long range of over 20 µm. Note that the P3HT fibers near the supramolecular ribbon are mechanically deformed due to the spin-coating process.

Determination of the orientational order parameter over distances up to 30 µm

To quantify the degree of orientation as well as the spatial limits of the orientation of nanofibers, multiple TEM images were recorded along the growth direction of P3HT nanofibers. The first image was taken directly next to a supramolecular ribbon of **1** (see **Figure S14** leftmost image). For the other images, the distance to the supramolecular ribbon was increased by a few micrometers such that subsequent images overlap, allowing us to stitch them together as shown in **Figure S14**. Thus, we can determine the average distance for each image relative to the ribbon. Close to the supramolecular ribbon, the P3HT nanofibers are highly oriented and densely packed. At distances above 20 µm to the ribbon, the density of nanofibers as well as the orientation decrease.

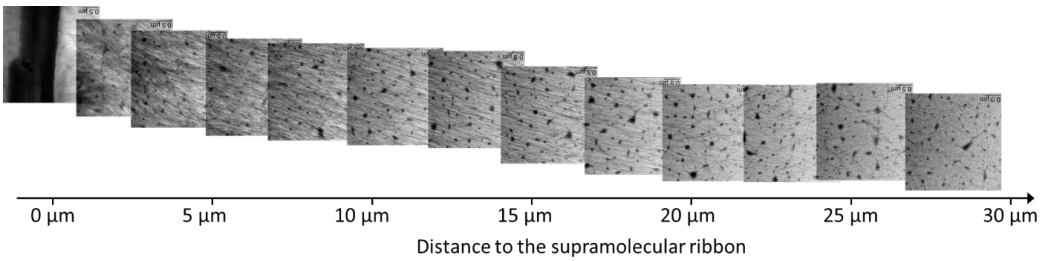

Figure S14: Overlapping TEM images recorded from an isolated superstructure with an increasing distance to the supramolecular ribbon of **1** shown in the leftmost image. The orientational order parameter of the nanofibers in each image was analyzed separately and is shown in **Figure 6** in the main text.

To quantify the orientation of the nanofibers, we used an algorithm by Persson et al. [12]. The algorithm recognizes fiber fragments in the images and calculates the orientational order parameter S based on the orientation of the fiber fragments [12]:

$$S = 2 < cos^2\theta_n > -1$$

Here, θ_n is the angle of each fiber fragment relative to the director of the image, i.e. the average orientation of the nanofibers or, in other words, their preferential alignment within the image. The parameter S can have values from zero, for randomly oriented fibers, to one, for perfectly aligned fibers. We used this algorithm to determine the orientational order parameter for each image shown in **Figure S14**. The parameter S as a function of the distance to the supramolecular ribbon is shown in **Figure 6**. An exemplary image at a distance of around 6 µm from the supramolecular ribbon is shown in **Figure 15 A**. The algorithm recognizes most of the fiber fragments and colors them according to their orientation. As shown in **Figure 15 B,** the fibers show a very similar orientation resulting in a high orientational order parameter S of 0.97.

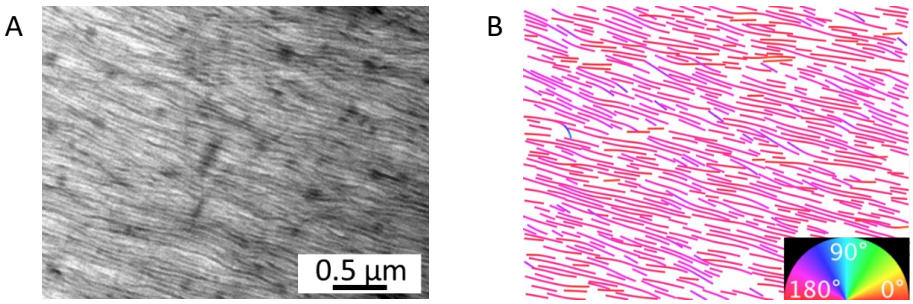

Figure S15 A) TEM image of highly aligned P3HT nanofibers in an isolated superstructure around 6 µm away from the supramolecular ribbon. B) The image of A was fitted using an algorithm by Persson et al. [12] to quantify the orientation of nanofibers. The recognized fiber fragments are colored according to their orientation. The color code is shown in the bottom right corner.

S4 Analysis of spatially resolved PL spectra on P3HT nanofibers

To fit the dataset of 6561 individual PL spectra recorded from the superstructure shown in **Figure 7** of the main text, we used a function of three independent Gaussians in the range between 13500 cm^{-1} and 17000 cm^{-1} describing a distorted vibronic progression characteristic for aggregated P3HT:

$$\frac{I}{E^3}(E) = \frac{I_1}{\sigma_1\sqrt{2\pi}} \times \exp\left(-\frac{1}{2}\frac{(E-E_{00})^2}{{\sigma_1}^2}\right) + \frac{I_2}{\sigma_2\sqrt{2\pi}} \times \exp\left(-\frac{1}{2}\frac{(E-E_{00}-E_{vib})^2}{{\sigma_2}^2}\right) + \frac{I_3}{\sigma_3\sqrt{2\pi}} \times \exp\left(-\frac{1}{2}\frac{(E-E_{00}-2\times E_{vib})^2}{{\sigma_3}^2}\right)$$

The peak position E_{00} of the electronic 0-0 peak, the linewidths σ_1 and σ_2, and the peak intensities I_1, I_2 and I_3 are fit parameters (here the subscript '1' refers to the 0-0 transition, '2' to the 0-1, and '3' to the 0-2 transition of the PL spectra). The energy of the vibrational mode was fixed to E_{vib}=1450 cm^{-1} reflecting an effective carbon-bond stretch coupling to the electronic transition, and the linewidth was kept constant at σ_3 = 500 cm^{-1}. The 0-0 and 0-1 peaks (with intensities I_1 and I_2) are essential to reproduce the high-energy part of the PL spectra and to extract information on (structural) disorder within the P3HT nanofibers, whereas the 0-2 peak is only required to prevent fit deviations close to the edge of the fitting range (~13500 cm^{-1}).

S5 References

(1) Smulders, M. M. J.; Nieuwenhuizen, M. M. L.; Greef, T. F. A. de; van der Schoot, P.; Schenning, A. P. H. J.; Meijer, E. W. How to distinguish isodesmic from cooperative supramolecular polymerisation. *Chem. Eur. J.* **2010**, *16* (1), 362–367.

(2) Das, A.; Vantomme, G.; Markvoort, A. J.; Eikelder, H. M. M. ten; Garcia-Iglesias, M.; Palmans, A. R. A.; Meijer, E. W. Supramolecular Copolymers: Structure and Composition Revealed by Theoretical Modeling. *J. Am. Chem. Soc.* **2017**, *139* (20), 7036–7044.

(3) Kulkarni, C.; Meijer, E. W.; Palmans, A. R. A. Cooperativity Scale: A Structure-Mechanism Correlation in the Self-Assembly of Benzene-1,3,5-tricarboxamides. *Acc. Chem. Res.* **2017**, *50* (8), 1928–1936.

(4) Jarrett-Wilkins, C.; He, X.; Symons, H. E.; Harniman, R. L.; Faul, C. F. J.; Manners, I. Living Supramolecular Polymerisation of Perylene Diimide Amphiphiles by Seeded Growth under Kinetic Control. *Chem. Eur. J.* **2018**, *24* (58), 15556–15565.

(5) Wehner, M.; Würthner, F. Supramolecular polymerization through kinetic pathway control and living chain growth. *Nat. Rev. Chem.* **2020**, *4* (1), 38–53.

(6) Fillon, B.; Wittmann, J. C.; Lotz, B.; Thierry, A. Self‐nucleation and recrystallization of isotactic polypropylene (α phase) investigated by differential scanning calorimetry. *J. Polym. Sci., Part B: Polym. Phys.* **1993**, *31* (10), 1383–1393.

(7) Clark, J.; Chang, J.-F.; Spano, F. C.; Friend, R. H.; Silva, C. Determining exciton bandwidth and film microstructure in polythiophene films using linear absorption spectroscopy. *Appl. Phys. Lett.* **2009**, *94* (16), 163306.

(8) Panzer, F.; Sommer, M.; Bässler, H.; Thelakkat, M.; Köhler, A. Spectroscopic Signature of Two Distinct H-Aggregate Species in Poly(3-hexylthiophene). *Macromolecules* **2015**, *48* (5), 1543–1553.

(9) Scharsich, C.; Lohwasser, R. H.; Sommer, M.; Asawapirom, U.; Scherf, U.; Thelakkat, M.; Neher, D.; Köhler, A. Control of aggregate formation in poly(3‐hexylthiophene) by solvent, molecular weight, and synthetic method. *J. Polym. Sci., Part B: Polym. Phys.* **2012**, *50* (6), 442–453.

(10) Wenzel, F. A.; Welz, H.; van der Zwan, K. P.; Stäter, S.; Kreger, K.; Hildner, R.; Senker, J.; Schmidt, H.-W. Highly Efficient Supramolecular Nucleating Agents for Poly(3-hexylthiophene). *Macromolecules* **2022**, *55* (7), 2861–2871.

(11) Brinkmann, M.; Chandezon, F.; Pansu, R. B.; Julien‐Rabant, C. Epitaxial Growth of Highly Oriented Fibers of Semiconducting Polymers with a Shish‐Kebab‐Like Superstructure. *Adv. Funct. Mater.* **2009**, *19* (17), 2759–2766.

(12) Persson, N. E.; McBride, M. A.; Grover, M. A.; Reichmanis, E. Automated Analysis of Orientational Order in Images of Fibrillar Materials. *Chem. Mater.* **2017**, *29* (1), 3–14.

Danksagung

Zuerst möchte ich mich bei meinem Doktorvater, Herrn Prof. Dr. Hans-Werner Schmidt, für die Möglichkeit danken die vorliegende Doktorarbeit anfertigen und die damit verbundene Forschung an dem Lehrstuhl Makromolekulare Chemie I der Universität Bayreuth durchführen zu dürfen. Dabei möchte ich mich besonders für seine Offenheit bezüglich neuer Themen und Vorschläge und die Unterstützung, sowohl von fachlicher als auch persönlicher Seite, herzlich bedanken.

Für die finanzielle Unterstützung bedanke ich mich beim Bayerischen Staatsministerium für Wissenschaft und Kunst im Rahmen des Verbundprojektes „*Solar Technology go Hybrid*“ und für die Förderung durch den Elitestudiengang „*Macromolecular Science*“ im Rahmen des Elitenetzwerks Bayern.

Ganz besonderer Dank gilt Dr. Klaus Kreger, der mich fortwährend von meiner Zeit als Masterstudent bis zum Ende meiner Promotion begleitet hat und mir immer bei fachlichen Fragen weitergeholfen hat. Ohne unsere vielen gemeinsamen Diskussionen im Laufen oder beim Rauchen über fachliche, sprachliche und weitere Themen wäre ich heute nicht der gleiche.

Sehr möchte ich mich auch bei Prof. Dr. Richard Hildner bedanken, der mir bei allen physikalischen Fragestellungen während meiner Promotion geholfen hat. Nur durch die Kooperation mit ihm und seiner Arbeitsgruppe konnte diese Arbeit entstehen.

In diesem Zusammenhang möchte ich mich herzlich bei Dr. Bernd Wittmann und Sebastian Stäter bedanken. Mit denen ich eine enge und hervorragende Zusammenarbeit bei meinen Themen genießen durfte. Ich freue mich sehr, dass wir gemeinsam forschen konnten.

An dieser Stelle möchte ich auch bei Prof. Bert Meijer und seiner Gruppe danken, die während meines Forschungsaufenthaltes im Masterstudium kennenlernen durfte. Danke, dass ihr mir bei fachlichen Fragen geholfen habt und ich Konferenzen gemeinsam mit euch erleben durfte.

Ebenfalls möchte ich mich bei Prof. Eva Herzig und ihrer Gruppe für die gute Zusammenarbeit bedanken. Bei Asena Cerhan-Haink bedanke ich mich für die gemeinsame Arbeit am CBT-Paper. Meike Kuhn danke ich für die gemeinsame Entwicklung eines Konzepts zur Perowskit Nukleierung und die gemeinsamen Arbeiten in diese Richtung. Mein Dank richtet sich auch an Fabian Eller und unsere gemeinsamen Arbeiten zur P3HT Aggregation. Nicht zuletzt möchte ich mich bei Christopher Greve bedanken mit dem ich neben fachlichen Diskussionen auch Bücher besprechen konnte und hoffentlich auch weiter werde.

Ich bedanke mich bei Prof. Jürgen Senker und Dr. Kasper van der Zwan für die Strukturaufklärungen und gemeinsamen Überlegungen bezüglich der Wechselwirkungen von Nukleierungsmitteln mit P3HT.

Besonders möchte ich mich auch bei Prof. Natalie Stingelin und ihrer Gruppe bedanken, die mich in Atlanta, USA, für drei Monate aufgenommen haben und mit denen ich eine unvergessliche Zeit verbringen durfte.

Dr. Beate Förster, Dr. Ulrich Mansfeld und Martina Heider möchte ich für die Einweisung und stete Unterstützung im Bereich der Rasterelektronenmikroskopie danken. Und Dr. Markus Drechsler für die Einweisung und Unterstützung bezüglich der Transmissionselektronenmikroskopie.

Ich möchte mich auch bei Dr. Christian Neuber und Dr. Reiner Giesa für die Betreuung und Einweisung der Geräte am Lehrstuhl bedanken. Bei den technischen Angestellten Sandra Opel und Jutta Failner bedanke ich mich ganz herzlich für die Unterstützung bei der Analytik und Synthese der vorgestellten supramolekularen Bausteine. An dieser Stelle bedanke ich mich auch bei Alexander Kern für seine Unterstützung bei IT-Fragestellungen. Einen besonderen Dank möchte ich an Petra Weiss und Christina Wunderlich aussprechen, die mir durch ihre unermüdliche Unterstützung bei verwaltungstechnischen, organisatorischen und vielen weiteren Aufgaben geholfen haben.

Des Weiteren möchte ich mich bei allen Kooperationspartner bedanken mit den ich das Vergnügen hatte während meiner Promotion arbeiten zu dürfen.

Natürlich möchte mich auch bei allen weiteren Mitarbeitern und Ehemaligen des Lehrstuhls Makromolekulare Chemie I bedanken, die mich durch den fachlichen Austausch und die Freundschaft unterstützt haben. Diesen Dank möchte ich auch an alle Praktikanten aussprechen, die ich während meiner Zeit betreuen durfte.

Besonders muss ich natürlich Dennis Schröder erwähnen mit dem ich das große Vergnügen hatte jahrelang ein Labor zu teilen. Ohne unseren intensiven Austausch auf fachlicher, wie persönlicher Ebene und unserer hervorragenden Musikauswahl wäre meine Promotion nicht die gleiche gewesen. Vielen Dank für alles und ich hoffe, dass wir uns auch weiterhin so prächtig verstehen.

Des Weiteren möchte ich mich bei meinen Bayreuther Studienfreunden bedanken. Zuerst bei den “Dudes“, Daniel Keim, Dr. Thomas Tran und Dr. Yannick Jännsch. Ohne unser gemeinschaftliches Mittagessen sowie die gemeinsame Freizeitgestaltung wäre meine Zeit viel langweiliger gewesen. Natürlich möchte ich auch Dr. Anton Weissbach und Timon Schönauer danken mit denen ich mich

jederzeit austauschen konnte. Ein großer Dank geht auch an alle weiteren Freunde, mit denen ich während meiner Promotion Zeit verbringen durfte.

Besonders möchte ich abschließend meiner Familie und Freundin danken, die mich immer unterstützt haben – *Danke!*

(Eidesstattliche) Versicherungen und Erklärungen

(§ 9 Satz 2 Nr. 3 PromO BayNAT)

Hiermit versichere ich eidesstattlich, dass ich die Arbeit selbstständig verfasst und keine anderen als die von mir angegebenen Quellen und Hilfsmittel benutzt habe (vgl. Art. 97 Abs. 1 Satz 8 BayHIG).

(§ 9 Satz 2 Nr. 3 PromO BayNAT)

Hiermit erkläre ich, dass ich die Dissertation nicht bereits zur Erlangung eines akademischen Grades eingereicht habe und dass ich nicht bereits diese oder eine gleichartige Doktorprüfung endgültig nicht bestanden habe.

(§ 9 Satz 2 Nr. 4 PromO BayNAT)

Hiermit erkläre ich, dass ich Hilfe von gewerblichen Promotionsberatern bzw. -vermittlern oder ähnlichen Dienstleistern weder bisher in Anspruch genommen habe noch künftig in Anspruch nehmen werde.

(§ 9 Satz 2 Nr. 7 PromO BayNAT)

Hiermit erkläre ich mein Einverständnis, dass die elektronische Fassung meiner Dissertation unter Wahrung meiner Urheberrechte und des Datenschutzes einer gesonderten Überprüfung unterzogen werden kann.

(§ 9 Satz 2 Nr. 8 PromO BayNAT)

Hiermit erkläre ich mein Einverständnis, dass bei Verdacht wissenschaftlichen Fehlverhaltens Ermittlungen durch universitätsinterne Organe der wissenschaftlichen Selbstkontrolle stattfinden können.

…….
Ort, Datum, Unterschrift